Giant radio galaxies in the LOFAR deep fields: old and lonely?

Dissertation

zur Erlangung des Doktorgrades
an der Fakultät für Mathematik, Informatik und Naturwissenschaften
Fachbereich Physik
der Universität Hamburg

vorgelegt von

Marco Simonte

Hamburg
2024

Eidesstattliche Versicherung

Hiermit versichere ich an Eides statt, die vorliegende Dissertationsschrift selbst verfasst und keine anderen als die angegebenen Hilfsmittel und Quellen benutzt zu haben.

Hamburg, den 08.02.2024

Marco Simonte

II

Zusammenfassung

Die Untersuchung von Radiogalaxien (RGs) bietet wertvolle Einblicke in die komplexe Dynamik zwischen aktiven Galaxienkernen (*active galactic nuclei,* AGN), deren Heimatgalaxien und dem diese umgebenden Medium. Unter der vielfältigen Population von RGs haben Riesenradiogalaxien (*giant radio galaxies*, GRGs) eine lineare Ausdehnung von über 700 kpc und sind im Vergleich zu kleineren RGs relativ selten. Darüber hinaus sind die Faktoren die zu ihrer außergewöhnlichen Größe führen noch nicht genau bekannt. In dieser Doktorarbeit konzentriere ich mich darauf, das komplexe Zusammenspiel zwischen verschiedenen Aspekten wie den Eigenschaften der Heimatgalaxie, der Umgebung und dem Alter der Radioquelle zu entwirren und ihren gemeinsamen Beitrag zur Entstehung von GRGs zu verstehen. Als primäres Beobachtungswerkzeug verwendete ich das Low-Frequency Array (LOFAR), das eine hohe Sensitivität und räumliche Auflösung mit einem weiten Sichtfeld und einzigartigen Niedrigfrequenzfähigkeiten kombiniert.

Im Verlauf meiner Doktorarbeit erstellte ich eine vollständige Stichprobe von GRGs durch eine sorgfältige visuelle Inspektion der LOFAR Tiefenfelder (Boötes, ELAIS-N1 und Lockman Hole), ergänzt durch tiefe Himmelsdurchmusterungen im optischen und infraroten Bereich zur genauen Identifizierung der Heimatgalaxien. Die endgültige Stichprobe umfasst etwa 1600 RGs, von denen 280 GRGs sind. Die Stichprobe mit kleineren RGs wurde als Kontrollstichprobe verwendet, um die Radioeigenschaften, die Eigenschaften der Heimatgalaxie und die Umgebungen zwischen GRGs und kleineren RGs zu vergleichen. Die Eigenschaften der Heimatgalaxien erwiesen sich als ähnlich zwischen GRGs und RGs, beide beherbergen ein zentrales Schwarzes Loch, das radiativ ineffizient akkretiert. Darüber hinaus zeigen die stellaren Massen der Heimatgalaxien von GRG und RG Ähnlichkeiten. Interessanterweise wiesen 41% der Heimatgalaxien von GRGs eine moderate/hohe Sternentstehungsrate von > 10 M$_\odot$/yr auf, im Gegensatz zu 20% der Heimatgalaxien von RGs, die diese Schwelle überschritten. Integrierte Flussdichten und Radioluminositäten wurden auch für eine Teilmenge von RGs und GRGs durch verfügbare Bilder aus Himmelsdurchmusterungen bei 50, 150, 610 und 1400 MHz bestimmt, um integrierte Spektralindizes zu berechnen. Ich fand heraus, dass größere Quellen steilere integrierte Spektralindizes aufweisen, was darauf hindeutet, dass GRGs die späten Evolutionsstufen von RGs sind. Darüber hinaus verwendete ich für die Umgebungsanalyse einen Katalog von fotometrischen und spektroskopischen Rotverschiebungen von Galaxien aus dem Legacy Survey und nutzte die Anzahl der benachbarten Galaxien im Radius von 10 Mpc von der AGN-Heimatgalaxie als Maß für die Umgebungsdichte um RGs. Diese Analyse zeigte deutliche Dichtunterschiede auf, wobei GRGs statistisch gesehen dünnere Umgebungen im Vergleich zu ihren kleineren Pendants bevölkern. Bemerkenswert ist insbesondere die Tatsache, dass nur 3% der GRGs innerhalb eines dreidimensional-mitbewegten Abstands von 5 Mpc von einem Galaxienhaufen entfernt sind.

Die Zusammenstellung einer Liste von 447 RGs ermöglichte eine Analyse der Ausrichtung der RG-Jets im ELAIS-N1-Feld, wie sie in früheren Studien berichtet wurde. Von den für diese Analyse verwendeten RGs besitzen 95% entweder fotometrische oder spektroskopische Rotverschiebungen, was eine dreidimensionale (3D) Analyse ermöglicht. Die räumliche Verteilung der Hauptachsenpositionswinkel von RGs im ELAIS-N1-Feld wird präsentiert, begleitet von den Ergebnissen mehrerer statistischer Tests, die darauf abzielen, das Vorhandensein einer systematischen Ausrichtung festzustellen.

Die Analyse zeigt, dass die Verteilung der Positionswinkel konsistent mit einer gleichmäßigen Verteilung ist. Zwei scheinbare Spitzen um Positionswinkel von 50 und 140 Grad sind nicht signifikant, wie durch eine gründliche 3D-Analyse belegt wird, die jeglichen Hinweis auf eine intrinsische Ausrichtung entkräftet. Zusammenfassend unterstützen meine Ergebnisse keine 2D- oder 3D-Ausrichtung von RGs auf Winkelskalen unterhalb von 4 Grad.

Zusammenfassend präsentiere ich in dieser Studie eine Multi-Wellenlängen-Analyse der RGs in den LOFAR Tiefenfeldern und untersuche, wie die Umgebung sowie die Radio- und optischen Eigenschaften der RGs ihre Entwicklung beeinflussen. In naher Zukunft hat eine ähnliche Studie, erweitert auf den gesamten LOFAR Two-Metre Sky Survey, das Potenzial, die notwendige Bestätigung dieser Ergebnisse zu liefern.

Abstract

The study of radio galaxies (RGs) offers valuable insights into the complex dynamics between active galactic nuclei (AGN), host galaxies, and the surrounding medium. Among the diverse population of RGs, giant radio galaxies (GRGs) have a linear extent larger than 700 kpc and they are relatively rare compared to smaller RGs. Furthermore, the contributing factors to their exceptional size are still not very well known. In this doctoral thesis, I focus on unravelling the intricate interplay between different aspects, such as the properties of the host galaxy, the surrounding environment, the age of the radio source, and their collective role in shaping the size of GRGs. As a primary observational tool, I used the LOw-Frequency Array (LOFAR), which combines high sensitivity and angular resolution with a wide field of view and unique low-frequency capabilities.

Throughout my doctoral studies, I constructed a complete sample of GRGs through a meticulous visual inspection of the LOFAR deep fields (Boötes, ELAIS-N1, and Lockman Hole), complemented by deep optical and infrared surveys for accurate host galaxy identification. The final sample counts about 1600 RGs of which 280 are GRGs. The sample containing smaller RGs was used as a control sample to compare the radio properties, the properties of the host galaxy and the environment between GRGs and smaller RGs. Host galaxy properties were found to be similar between GRGs and RGs, both hosting a central black hole undergoing radiatively inefficient accretion. Additionally, stellar masses of GRG and RG host galaxies exhibited similarities. Intriguingly, 41% GRG host galaxies displayed a moderate/high star formation rate, $> 10 \, \mathrm{M_\odot/yr}$, in contrast to 20% of RG hosts exceeding this threshold. Integrated flux densities and radio luminosities were also determined for a subset of RGs and GRGs through available survey images at 50, 150, 610, and 1400 MHz to compute integrated spectral indices. I found that larger sources exhibit steeper integrated spectral indices, suggesting that GRGs are the late-time versions of RGs. Furthermore, the environmental analysis I implemented utilised a catalogue of photometric and spectroscopic redshifts of galaxies from the Legacy survey. I employed the number of neighbouring galaxies within a 10 Mpc radius from the host galaxy as a proxy for environmental density around RGs. This analysis exposed distinct density differences, with GRGs statistically inhabiting sparser environments compared to their smaller counterparts. Particularly noteworthy is the fact that only 3% of GRGs are located within a 3D comoving distance of 5 Mpc from a galaxy cluster.

The compilation of a list of 447 RGs enabled an analysis of the alignment of the RG jets in the ELAIS-N1 field, which was reported by previous studies. Of the RGs used for this analysis, 95% possess either photometric or spectroscopic redshifts, facilitating a three-dimensional (3D) analysis. The spatial distribution of major axis position angles of RGs in the ELAIS-N1 field is presented, accompanied by the results of multiple statistical tests aimed at discerning the presence of any systematic alignment. The analysis reveals that the distribution of position angles is consistent with being uniform. Two apparent peaks around position angles of 50 and 140 degrees are deemed spurious, as evidenced by a rigorous 3D analysis, dispelling any indication of intrinsic alignment. In conclusion, my results do not support a 2D or 3D alignment of RGs on scales of smaller than 4 deg.

In summary, in this study, I present a multi-wavelength analysis of the RGs in the LOFAR deep fields and study how the environment and the radio and optical properties of RGs affect their evolution. In the near future, a similar study extended to the full LOFAR Two-metre Sky Survey holds the

potential to provide the necessary confirmation of these results.

List of publications

This thesis is partly based on (but does not include all of) the following publications:
First author publications

- **Simonte, M.**, Andernach, H., Brüggen, M., Miley, G. K., Barthel, P., 2024. *Giant radio galaxies in the LOFAR deep fields.* Submitted to A&A.

- **Simonte, M.**, Andernach, H., Brüggen, M., Best, P. N., Osinga, E., 2023. *Revisiting the alignment of radio galaxies in the ELAIS-N1 field.* A&A 672, A178. [Simonte et al. 2023]

- **Simonte, M.**, Andernach, H., Brüggen, M., Schwarz, D. J., Prandoni, I., Willis A. G., 2022a. *Giant radio galaxies in the LOw-Frequency ARray Two-metre Sky Survey Boötes deep field.* MNRAS, 515, 2032. [Simonte et al. 2022a]

- **Simonte, M.**, Vazza, F., Brighenti, F., Brüggen, M., Jones, T. W., Angelinelli M., 2022b. *Exploring the relation between turbulent velocity and density fluctuations in the stratified intra-cluster medium.* A&A, 658, A149. [Simonte et al. 2022b]

Co-author publications

- Lovisari, L., Ettori, S., Rasia, E., Gaspari, M., Bourdin, H., Campitiello, M. G., Rossetti, M., Bartalucci, I., ..., **Simonte, M.**, et al., 2023. CHEX-MATE: Characterization of the intra-cluster medium temperature distribution. A&A, in press; arXiv:2311.02176. [Lovisari et al. 2023]

Contents

1 Introduction

"There is nothing quite as useless as a radio source". These were the words pronounced by Jim Condon in 2013. Yet, the study of radio galaxies, and active galactic nuclei (AGN) in general, is considered vitally important to model the cosmological evolution of galaxies.

It is well established that at the centre of almost all galaxies resides a supermassive black hole and its mass strongly correlates with the star's velocity dispersion. Furthermore, the global cosmic star-formation history matches fairly well the cosmic black hole accretion history, emphasising the co-evolution of the central AGN and the host galaxy. Radio galaxies host an active black hole that produces large amounts of energy in the form of radio/X-ray emitting jets. These jets inject energy into the local environment, preventing cooling and removing cold/neutral gas from the centre of the galaxy. Nevertheless, jets may also trigger star formation by compression of cold gas clouds. Hence, a full understanding of the radio galaxy evolution is mandatory to better constrain the intricate lifecycle of baryons within galaxies as shown by recent models of the cosmic galaxy evolution. In this sense, with his claim, Jim Condon underscored the necessity of a multiwavelength approach to understand the connection between supermassive black holes and their respective host galaxies as well as the role of the environment in their evolution.

The evolution of the jetted radio sources depends on several factors such as the jet power, host galaxy properties, and environment, which are often challenging to precisely constrain in individual sources. Thus, large samples of radio galaxies during different stages of their evolution are needed to refine models of the evolution of radio galaxies. Among the variety of radio galaxies, giant radio galaxies have a projected linear size ≥ 700 kpc and the reason behind their exceptional length is still puzzling. Understanding the physics behind these peculiar objects can shed light on the role of the different contributing factors (jet power, host galaxy properties, environment and multiple jet activity) in shaping the final size and morphology of radio galaxies. Since giant radio galaxies are difficult to detect and rare, probing large cosmological volumes is essential to construct large samples. The Low-Frequency Array (LOFAR) combines high sensitivity, high resolution, and a large field of view. Thus, it is perfectly suited to provide deep maps of the entire northern sky. Furthermore, its unique capabilities in the low-frequency regime (50, 150 MHz) allow the detection of the steep-spectrum emission emitted by aged electrons.

This thesis focuses on the study of giant radio galaxies from a multiwavelength point of view. My work concentrated, first, on constructing a sample of radio galaxies by matching the radio components of these objects (e.g., lobes, hotspots, and core) with the corresponding host galaxies. With this catalogue in hand, I was able to compare the radio, optical, and environmental properties of giant radio galaxies with those of a control sample made of smaller radio galaxies to identify the properties that explain the large size of giant radio galaxies.

In the following chapter, I provide an overview of our current understanding of radio galaxies from both an observational and theoretical perspective (Sect. 1.1). In Sect. 1.2, I discuss giant radio galaxies summarising key findings from the past 30 years. The radio observations I used for this project are presented in Sect. 1.3. Finally, I elaborate on the specific aims of this thesis and the individual research projects in Sect. 1.4.

1.1 Radio galaxies: a general introduction

An active galactic nucleus (AGN) is a compact region at the centre of a galaxy that is far more luminous than the combined emission of stars in the same region. Nowadays, it is widely accepted that this emission is generated by an actively accreting supermassive black hole. Some of these AGN are very luminous at radio frequencies due to the non-thermal emission produced by the relativistic electrons residing in the jets launched in the vicinity of the black hole. The interaction of these relativistic electrons with the magnetic field produces the synchrotron radiation which is observed across the whole radio spectrum from tens of MHz to hundreds of GHz. Moreover, the inverse-Compton scattering of the energetic electrons with the cosmic microwave background (CMB) photons makes the jets observable in the X-ray band as well. The acceleration of particles to relativistic energies leads to a distribution of the emitting electrons that is described by a power-law $N(E) = N_0 E^{-p}$ (Bell 1978a,b). Here, E is the energy of the electron, p is the power index, N is the number of electrons with energy E, and N_0 is the normalisation. This distribution translates into an observable radio spectrum of the form $S(\nu) \propto \nu^{-\alpha_{inj}}$, where S is the radio flux density at a specific frequency, ν, and α_{inj} is the injection spectral index, equal to $\alpha_{inj} = (p - 1)/2$, that is the index of the initial power-law injected by particle acceleration (Harwood et al. 2013, 2015). AGN showing twin jets emitting in the radio band are called jetted AGN. It is thought that we see radio galaxies with a viewing angle greater than 45 degrees, while radio quasars are thought to have a viewing angle less than 45 degrees (Urry & Padovani 1995). In this study, unless otherwise specified, I consider radio quasars within the radio galaxy classification.

The physical details of the jet production mechanism are still under discussion. The most popular jet formation mechanisms at present include the Blandford & Znajek (BZ, Blandford & Znajek 1977) and the Blandford & Payne (BP, Blandford & Payne 1982) models. The BZ model underscores the extraction of rotational energy directly from a rotating black hole with magnetic fields penetrating the event horizon. In contrast, the BP model emphasises the contribution of accretion disks and their magnetic fields to the generation and launching of jets. More recently, Meier (2001) developed a hybrid model in which the magnetic fields extract energy from both the accretion flow and the spinning hole.

Radio galaxies (RGs) can be divided into two main morphological classes according to the Fanaroff-Riley classification (Fanaroff & Riley 1974): FRI and FRII. The main morphological difference between the two classes is the brightness distribution of the radio galaxy itself. FRI RGs display higher brightness near the core, fading towards the source's edge. In contrast, FRII RGs showcase brighter lobes compared to the inner half of the source extent, culminating in bright hotspots. An example of FRI and FRII RGs is shown in Fig. 1.1. Ledlow & Owen (1996) established a strong correlation between the FRI/II dichotomy and the optical luminosity of host galaxies. Specifically, RGs above the relation $L_{radio} \propto L_{optical}^{1.8}$ are classified as FRII, while FRIs are found below this threshold. It is noteworthy that the Ledlow & Owen study, while seminal, used a somewhat heterogeneous sample, likely impacting the observed trends. Subsequent analyses by Best (2009) and Mingo et al. (2019), utilising more homogeneous samples, revealed a large overlap between the FRI and FRII populations below the observed relation. Furthermore, these studies demonstrated that low-luminosity FRII RGs often have host galaxies that are systematically fainter than those associated with high-luminosity FRIIs and FRIs matched in luminosity. This result led to the conclusion that less powerful jets in denser environments are more easily disrupted as the source grows.

Regardless of the FRI/II classification, RGs exhibit a large variety of morphologies. Here, we give a brief overview of some of the morphologies mentioned in this thesis. Double-Double RGs (DDRGs, Schoenmakers et al. 2000a) are characterised by two distinct pairs of radio lobes along the
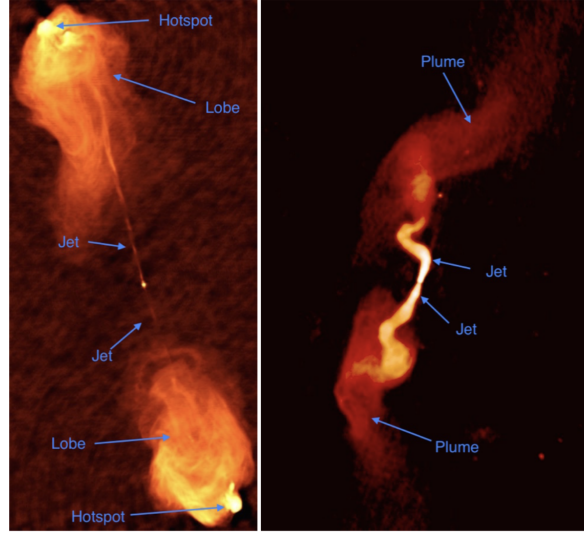
Figure 1.1: Very Large Array (VLA) radio maps of the powerful FRII radio jets in Cygnus A (left). This is a false colour representation of the grey-scale image presented in Perley et al. (1984). In the right panel is shown the FRI radio galaxy 3C31 (Laing et al. 2008). Image credit: NRAO/AUI.

same axis. The formation of each pair of lobes is associated with separate jet activities of the AGN. DDRGs provide valuable insights into different phases of AGN activity and quiescence, referred to as the duty cycle. Hybrid Morphology Radio Sources (HyMoRS, Gopal-Krishna & Wiita 2002) are radio galaxies with an FRI-type radio lobe on one side of the active nucleus and an FRII-type lobe on the opposite side. The interaction of the jets with the external environment can result in bent sources, showcasing extended and diffuse radio emission elongated along the jet direction (e.g., right panel of Fig. 1.1). According to the bending angle, they are classified as Wide-Angle Tailed (WAT, Owen & Rudnick 1976), which exhibit a larger bending angle, or Narrow-Angle Tailed (NAT, O'Dea & Owen 1985) RGs. Both these morphologies are commonly shaped by the dense intracluster medium (e.g., Burns et al. 1994). However, while WATs often originate from the main central galaxy of the galaxy cluster (Gómez et al. 1997), the host galaxies of NATs are ordinary cluster members.

1.1.1 Analytical models of radio galaxies

Analytical models of the evolution of jets and lobes are used to estimate important properties of RGs such as jet kinetic power and age, which are useful quantities to study the feedback models (Heinz et al. 2007; Gaspari et al. 2012) and the RG lifecycle (Kapinska et al. 2015). GRGs, which are the focus of this thesis, exhibit almost exclusively an FRII morphology (Dabhade et al. 2023). For this reason, FRI RGs are not discussed in this section (see Bicknell 1995, for a discussion on FRI RGs models).

Models of RGs in general consider two initial conical jets composed of accelerated relativistic particles. Early jet-lobe models are based on the work of Rees (1971), in which conical jets are pressure-balanced by the ram pressure of the ambient medium. In this model, jets are beams of low-frequency electromagnetic waves. Their radiation pressure is given by $P_{\mathrm{rad}} = Q/(\Omega R^2 c)$, where Q is jet kinetic power, ΩR^2 is the beam cross-sectional area at a given distance R from the AGN, and c is the speed of light. The interaction between the jets and the environment can lead to particle pair production. The resulting pressure can be up to double that of the radiation pressure. The exact

factor depends on the angle of the reflected particles. Therefore, the pressure generated by the jet is $P_{\text{jet}} = kQ/(\Omega R^2 c)$, where k is a dimensionless constant taking into account the pair production pressure as well as the reflection angle, and it ranges from one to two. The balance between the radiation pressure and the ram pressure from the environment, $P_{\text{ram}} = \rho v^2$, where ρ is the density of the external gas and $v = dR/dt$ is the jet velocity, results in an equation relating the jet length and source age t (Scheuer 1974). Assuming the external density is well-described by a symmetrical power-law of the form $\rho \propto r^{-\beta}$, Turner & Shabala (2023) found

$$R(t) \propto t^{2/(4-\beta)}, \tag{1.1}$$

where the constant of proportionality depends on several parameters such as the jet kinetic energy, the external density distribution and the beam cross-sectional area. The interaction between the jet and the external medium leads to an inflated lobe. By considering the work done by the jet to inflate the cavity and the kinetic power input Q integrated over the time interval of the active phase, it is possible to derive the evolution of the lobe pressure in terms of the source age (see Scheuer 1974; Turner & Shabala 2023, for details):

$$p(t) \propto t^{(4-\beta-2\alpha)/(4-\beta)}. \tag{1.2}$$

This formula is found assuming a lobe volume that expands with increasing jet length $V(R) \propto R^{\alpha}$ and a uniform distribution of the energy density and pressure within the lobe.

While this simple model is the groundwork from which all future models were built, the forward expansion of the radio source is driven by the momentum flux. Hence, it cannot be used to model the latest stages of lobe evolution in which internal pressure is the main driver of the lobe expansion. Falle (1991) developed a self-similar model relating the geometry and internal pressure of the expanding lobe to the early dynamics of the jet. Such a model served as the basis for several models including those of Kaiser & Alexander (1997), Blundell & Rawlings (2000) and Manolakou & Kirk (2002). In this model, an initially conical jet reflects a strong shock off the surrounding medium upon reaching lateral pressure equilibrium through a collimation shock (Kaye et al. 2018). This shock leads to a constant width, collimated jet (see Fig. 1.2) which terminates in a bow shock that sweeps up the ambient medium. The study by Falle assumed that the formation of lobes precedes jet collimation, suggesting that it is the pressure within the lobes, and not the ambient medium, that acts against the lateral thrust of the jet, as also shown by Alexander (2006). While the jet dynamic is dominated by the momentum flux, the expansion of the lobe is assumed to be driven by the internal pressure only. Thus, by applying the conservation of momentum across the collimation shock front, it is possible to relate the pressure of the lobe to the properties of the jet such as density, bulk velocity and opening angle. Using similar arguments, it is possible to derive an expression for the pressure acting on the contact discontinuity between the jet head and the surrounding shocked gas (see Eq. 10 and 11 in Turner & Shabala 2023). Having a significantly higher density and thus lower temperature, the shocked gas is in approximate pressure equilibrium with the proximate lobe/jet-head plasma. These relationships between the conditions in the lobe cavity, the bow shock and the ambient medium are sufficient for describing the evolution of the expanding radio source.

Using the first law of thermodynamics, which relates the jet kinetic energy input to the thermal pressure in the lobe and shell, and shocked gas volume, Falle (1991) showed that the shocked shell expands in a self-similar manner, leading to a constant scaling between the volume and cube of the jet length. In terms of the radius of the shocked gas shell along the jet axis from the active nucleus, they found
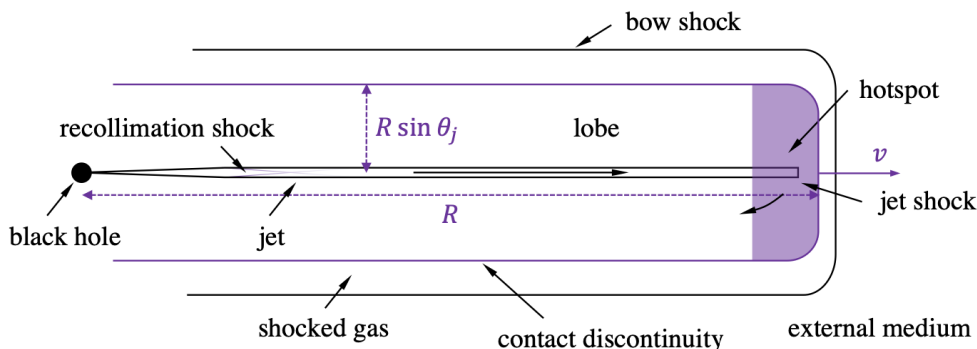
Figure 1.2: Illustration depicting the proposed dynamical model by Falle (1991). Image from Turner & Shabala (2023).

$$R(t) \propto t^{3/(5-\beta)}. \tag{1.3}$$

Future work further improved these models by solving systems of differential equations which lack an analytic solution to describe the evolutionary history of the radio source. Turner & Shabala (2015) developed a semi-analytic model, Radio AGN in Semi-analytic Environments (RAiSE). In this model, the authors considered a density profile of the surrounding medium consistent with X-ray observations of galaxy clusters and semi-analytic galaxy formation. Moreover, they modelled the morphological transition from supersonic to subsonic lobe expansion. Nevertheless, this model does not include the momentum flux of the jet plasma. Thus, it does not incorporate the jet dynamics prior to the formation of the lobe. In the 2023 version of the RAiSE model, Turner & Shabala (2023) considered the early relativistic expansion of the jet, the formation of lobes within a surrounding bow shock and the contribution of both the thermal and ram components of the jet and lobe pressure. Turner & Shabala (2015) and Turner & Shabala (2023) found that in their model the lobe expansion follows Eq. 1.3. On the other hand, including the relativistic effects in the early phase of the jet expansion, they predicted an evolutionary history with $R(t) \propto t$. Hardcastle (2018) incorporated the momentum flux of the jet plasma in the lobe-dominated expansion model of Turner & Shabala (2015). The prediction of jet and lobe evolution of this model are the same of Eq. 1.2 and Eq. 1.3.

Dynamical models make use of these (semi-)analytical models to determine the dynamical ages and jet power of observed RGs (Machalski et al. 2007b; Mahatma et al. 2020). The determination of dynamical ages relies on the X-ray observations of the external medium: powerful jets drive shocks in the ambient medium (Heinz et al. 1998; Kraft et al. 2007; Croston et al. 2009) enabling X-ray measurements to determine the physical conditions of the shocked gas (Ineson et al. 2017). Alternatively, the detection of cavities in galaxy clusters (Bîrzan et al. 2004, 2008; Cavagnolo et al. 2010) provides an opportunity to estimate the age of the lobes under the assumption of an expansion velocity close to the sound speed. Nevertheless, detecting X-ray features in the ambient medium is possible only in the dense intracluster medium and in very few massive elliptical galaxies. Moreover, these methods assume an expansion happening at a constant rate, while it is known that the expansion slows down with time. Therefore, they likely overestimate the dynamical age of RGs. Overcoming these challenges involves extending analytical models for FRII RGs. By integrating dynamical models (Falle 1991; Kaiser & Alexander 1997) with predictions for the expected radio emission from a radio source (e.g., Kaiser et al. 1997), it is possible to address these issues. The radio power at a certain frequency ν in

the analytical models is obtained by incorporating synchrotron, inverse Compton and adiabatic losses. Thus, parameters such as the jet power and the age are determined using optimization procedures for the best fit between the observed and predicted luminosity of the RG (Machalski et al. 2007b). However, a major drawback of these methods is the assumption of the density profile of the external medium.

Spectral ageing (Harwood et al. 2013, 2015) is a valid alternative to dynamical models used to determine the radiative age of relativistic electrons residing in the lobes of RGs. As the jet propagates in the environment, it drives a strong shock, accelerating particles to very high energies (Lorentz factor of $\approx 10^5$ or higher). The population of accelerated electrons will leave the acceleration region as the jet advances. At this point, the relativistic electrons experience energy losses via synchrotron radiation, inverse Compton scattering and adiabatic expansion. The energy loss time scale for the electrons is given by

$$t_{\text{sync+IC}} \propto \frac{E}{dE/dt} \propto \frac{1}{E}. \tag{1.4}$$

Hence, more energetic electrons lose their energy more rapidly than lower-energy electrons. This results in an observed radio spectrum that is a power-law at lower frequencies (≈ 100 MHz) while it curves at higher frequencies (≈ 1 GHz). The estimated age of the electrons is given by

$$t = 50.3 \frac{B^{1/2}}{B^2 + B_{\text{CMB}}^2} ((1+z)\nu_b)^{-1/2} \text{ Myr}, \tag{1.5}$$

where $B(nT)$ is the magnetic field strength in the lobes, z is the redshift of the source, and ν_b is the break frequency where the radiative losses begin to significantly affect the observed radio spectrum. B_{CMB} (nT) is the magnetic field equivalent to the CMB energy density responsible for the inverse Compton losses of the relativistic electrons.

This method carries some uncertainties. The spectral age is dependent on the magnetic field, the value of which has often been estimated assuming that the energy density of the magnetic field is in equipartition with the energy density of the electrons and protons. This assumption has been invoked in many studies (e.g., Parma et al. 1999; Shulevski et al. 2017; Brienza et al. 2020). However, if X-ray observations of the lobe inverse Compton emission are available, it is possible to determine the cosmic ray electron density and thus, the magnetic field strength from the synchrotron emission. These estimates usually yield magnetic field values that are considerably lower than what is predicted by the equipartition theory (Croston et al. 2005; Ineson et al. 2017). Another source of uncertainty is the injection spectral index. Early observations of hotspots found an injection index of about 0.5 (Meisenheimer et al. 1989; Carilli et al. 1991) which is consistent with the predictions from diffusive shock acceleration at high Mach number shocks (Longair 2011). However, more recent studies found a steeper injection index in the range 0.7-0.8 (Harwood et al. 2013, 2015, 2017).

These uncertainties manifest in the estimation of radiative age, often diverging from the dynamical age. The origin of such difference is still under discussion (Mahatma et al. 2020); re-acceleration processes happening within the lobes (Hardcastle et al. 2007), mixing of electron populations with different ages (Harwood et al. 2016, 2017; Turner et al. 2018), and assumptions on the magnetic field strength may be responsible for this tension.

1.1.2 Numerical models of radio galaxies

Analytical models, while useful for understanding the basic physics of powerful RGs, are constrained by assumptions about the symmetry and geometry of sources. On the other hand, numerical simula-

tions, while free of constraints, face the primary challenge of computing power demand, especially in high-resolution models. Therefore, simulations must make assumptions to cut down the simulation time, such as using simplified environments and non-relativistic jet speeds and have often ignored important physics such as magnetic fields, radiative losses and non-thermal particles. Due to the vastly different spatial scales needed to model radio galaxies in their entirety, from the launching of the jets to their impact on the cooling of cluster gas, simulations are forced to focus on three main areas. Large-scale cosmological simulations including AGN feedback can reproduce observed mass and luminosity functions of galaxies (Croton et al. 2005; Bower et al. 2006). Nevertheless, the jets are not directly modelled as this would be computationally infeasible. Instead, feedback is included by introducing thermal and non-thermal particles with an energy distribution dependent on values such as the black hole's mass and an observationally determined feedback efficiency (Schaye et al. 2015; Davé et al. 2019). On smaller scales, there are studies investigating the efficiency of the jet launching process as well as the energy content of the jets out to a few hundred Schwarzschild radii (Koide et al. 1999; Meier 2001; Nishikawa et al. 2005; McKinney & Blandford 2009; Tchekhovskoy et al. 2011; McKinney et al. 2012). These simulations made the simplest possible assumption of injecting material with a toroidal magnetic field into a simple uniform medium, instead of using a more realistic environment. In between, there are models that introduce an already formed and collimated jet into some form of environment (Norman et al. 1982; Basson & Alexander 2003; Krause 2005; Heinz et al. 2006; Wagner et al. 2012; Hardcastle & Krause 2014; Mukherjee et al. 2016; Yates et al. 2018; Perucho et al. 2019; Horton et al. 2020; Yates-Jones et al. 2023; Horton et al. 2023). The primary factor which shapes large-scale jet structure in these simulations is the power of the jet. Using a method based upon observations of the jet terminal hotspots Godfrey & Shabala (2013) obtained jet powers for FRIIs in the range 10^{38} to 10^{39} W, in good agreement with other work which used a variety of techniques (Gitti et al. 2012; Ghisellini et al. 2014). Numerical models found that the jet power is responsible for the FRI/FRII dichotomy (Massaglia et al. 2016; Ehlert et al. 2018) and at the intermediate power between FRI and FRII other factors such as the density ratio between the jet and the environment, Lorentz factor, and magnetic field strength determine the final morphology of the source (Mignone et al. 2010; Mukherjee et al. 2020; Massaglia et al. 2022). Moreover, Massaglia et al. (2022) noted that the timing of observations is a crucial factor, given that numerous features are subject to temporal variations.

The environment is another key factor for the jet's evolution (Kaiser & Alexander 1997; Alexander 2006). Early studies considered uniform media (Norman et al. 1982; Lind et al. 1989) which may be a reasonable assumption for the early growth of the lobes but is not over the length scales the radio lobes are observed to reach. These models were later improved considering β-profiles (Reynolds et al. 2002; Basson & Alexander 2003; Krause 2005) or an environment derived from a simulation of a dynamically active cluster (Heinz et al. 2006; Bourne & Sijacki 2017; Vazza et al. 2023; Yates-Jones et al. 2023). In Fig. 1.3, I show the synchrotron luminosity as a function of the lobe length in a set of 3D simulations from Hardcastle & Krause (2014). The authors modelled the magnetohydrodynamical evolution of powerful RGs in realistic poor cluster environments with a β-profile which is dictated by two parameters: the core radius and the slope of the density profile of the external medium, β. The core radius represents the size of the region with a nearly uniform density profile and in these simulations has a value of 20, 30 and 40 in simulation unit which roughly corresponds to a physical size of 40, 60 and 80 kpc, respectively. The slope of the density profile has values of 0.55, 0.75 and 0.90. Fig. 1.3 shows a characteristic rising and falling curve in total intensity which is followed by most sources; only the object in the very richest environment (B55-40) does not show any sign of a downturn in the radio luminosity. Sources in environments with smaller core radii and larger β have the peak of their emission at smaller linear sizes, while richer environments produce more luminous radio
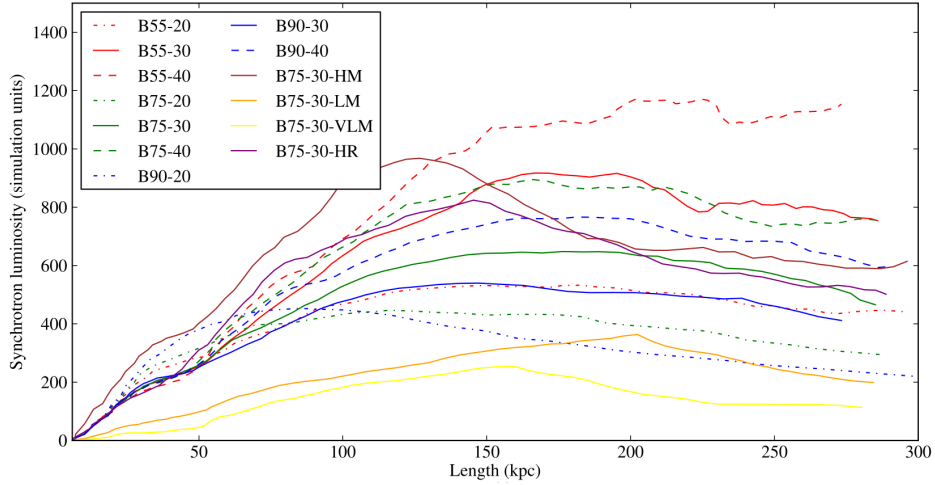
Figure 1.3: Synchrotron emission (in simulation units) as a function of the lobe length. The different colours represent different environments with varying core radii (with values of 20, 30 and 40) and slope of the external density profile (with values of 0.55, 0.75, 0.90). The code "HM", "LM" and "VLM" refers to the strength of the magnetic field: high, low and very low, respectively. The "HR" code refers to a simulation run at a higher resolution to test the convergence of the results. Image from Hardcastle & Krause (2014).

sources at all times. Moreover, O'Neill et al. (2005) found that jets advance more rapidly through stratified atmospheres than uniform environments. This suggests that the energy deposited by jets of a given length and power depends strongly on the structure of the ambient medium. Moreover, numerical models of jets propagating through inhomogeneous environments are found to create strongly asymmetric lobes (Jeyakumar et al. 2005; Krause 2005; Gaibler et al. 2009, 2011; Yates-Jones et al. 2021). Another factor that contributes to these asymmetries is the relativistic beaming of jets that are oriented predominantly towards the observer, an effect that has been observed, either as one-sided jets or non-unity jet-counterjet brightness ratios, in powerful RGs (Barthel et al. 1989; Mullin & Hardcastle 2009). A combination of relativistic beaming and environment are likely responsible for the observed asymmetries (Best et al. 1995).

Numerical modelling of radio galaxies has mostly focused on the active phase since they make up the vast majority of observed sources. Nevertheless, some studies focused on the evolution of radio galaxies once the jets are switched off, known as the remnant phase (Brüggen & Kaiser 2002; Basson & Alexander 2003; Perucho et al. 2011; English et al. 2019). The conclusions drawn from these investigations indicate that, as a consequence of perturbed cluster gas gradually returning to the original cluster potential, streams of dense gas are pushed along the jet axis behind the residual lobes. This gas displacement causes the lobes to rise out of the cluster faster than they would due to buoyancy. Consequently, this process results in larger adiabatic losses and rapid dimming.

1.1.3 The lifecycle of radio galaxies

Analytical, semi-analytical, and numerical models, when compared to radio observations of RGs, contribute significantly to our understanding of their various evolutionary phases. The transition through different stages of activity is commonly known as the lifecycle of a radio galaxy (see An & Baan 2012; Kapinska et al. 2015, for reviews on the topic) and is illustrated in Fig. 1.4. RGs start with a young phase during which the radio source is confined within the optical host galaxy and the jets have a size smaller than a few kpc. High-frequency peakers (HFPs), gigahertz peak spectrum (GPS) and compact

steep spectrum (CSS) RGs are thought to be newly born radio sources (O'Dea 1998; Orienti 2016; O'Dea & Saikia 2021). The radio spectra of HFPs, GPS, and CSS sources peak at frequencies of $\gtrsim$ 5 GHz, 1–5 GHz, and 500 MHz, respectively. Age estimation, based on both ageing and dynamical models, suggests an age range of $10^5 - 10^6$ years for these sources. Moreover, the frequency at which the emission peaks is found to be inversely proportional to the source size (O'Dea & Baum 1997; O'Dea 1998) suggesting an evolutionary sequence where HFP sources evolve into GPS sources, and subsequently into CSS sources. These findings support the idea that HFP, CSS, and GPS represent the first stages of a RG lifecycle. However, the observed overabundance of HFP, CSS, and GPS sources in comparison to the number of large-scale radio AGN (O'Dea & Baum 1997; An & Baan 2012) suggests the involvement of additional mechanisms. Morphological and spectral studies have indicated that the small size of certain sources can be attributed to the frustration scenario (Peck et al. 1999; Orienti et al. 2010). According to this hypothesis, a dense environment, coupled with the cessation of AGN activity, confines these sources to small spatial scales.

After a timespan ranging from tens to a few hundred million years, the young RG evolves into an active 'adult' phase. The jets expand into the external medium beyond the optical host galaxy, leading the source to evolve into either an FRI or FRII RG. The typical size of an evolved RG spans from tens to hundreds kpc (Parma et al. 1999; Shabala et al. 2008; Morganti et al. 2021), although some can extend to Mpc sizes and are referred to as giant radio galaxies (GRGs, Willis et al. 1974; Barthel et al. 1985; Oei et al. 2023a; Dabhade et al. 2023). During this phase, the emission from all radio components of the RG, including the core, hotspots, and lobes, is clearly detected, although not always resolved.

After the cessation of jet activity and the depletion of new relativistic electrons, the RG enters a remnant phase (Komissarov & Gubanov 1994; Parma et al. 2007; Murgia et al. 2011; Brienza et al. 2017; Mahatma et al. 2018; Jurlin et al. 2021). In this stage, the remaining relativistic electrons continue to lose energy through synchrotron emission and adiabatic expansion, causing a gradual fade in the remnant radio emission. The relatively short fading time of few Myrs (English et al. 2019) implies a small fraction of remnant RGs, estimated at up to 10% among radio-loud AGNs exhibiting restarted and remnant morphologies (Shulevski et al. 2017; Mahatma et al. 2018; Shabala et al. 2020). Observationally, these remnant sources are identified by a steep radio spectrum, a low core fraction (defined as the ratio of the core to total flux), the absence of compact sources (e.g., hotspots), and the presence of extended regions with low surface brightness (Morganti et al. 2021; Jurlin et al. 2021). After a few tens of Myr, the central AGN may undergo a renewed phase of jet activity, leading to the formation of restarted RGs (Morganti et al. 2021). These sources, characterized by very diffuse lobes typical of remnant RGs, exhibit a prominent core emission resulting from the expansion of new radio jets. However, if the fading time of the lobes is longer than the quiescent phase of the RG, or if the observations are not sensitive enough to detect the faint lobes, the restarted source may be mistakenly interpreted as a young RG.

1.1.4 Host galaxies: stellar mass, star-formation and accretion rate

The study of RGs from a multiwavelength point of view enables an understanding of the co-evolution of the optical host galaxy and the central AGN. In particular, one goal of studying the host galaxies and the environments of radio AGN is to understand how the radio activity is triggered. It has been clear since many years now (Matthews et al. 1964) that RGs are generally hosted by massive early-type galaxies and this result has been confirmed at least up to redshift z≈1 (Heeschen 1970; Ekers & Ekers 1973; Auriemma et al. 1977; Jenkins 1982; Best et al. 2005; Mauch & Sadler 2007; Smolčić et al. 2009; Sabater et al. 2019; Capetti et al. 2022). However, these results do not answer the question
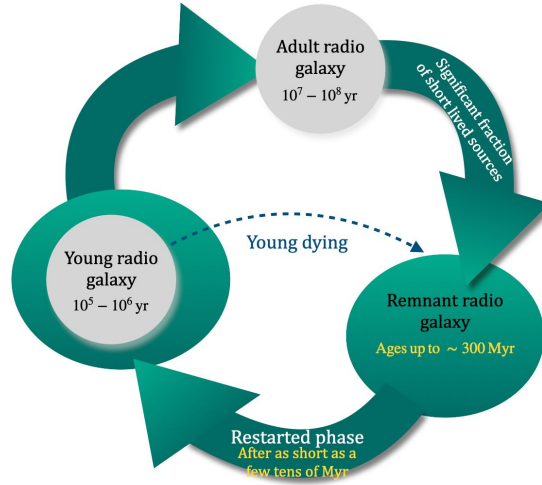
Figure 1.4: Sketch of the lifecycle of RGs. Figure adapted from Morganti et al. (2021).

of what triggers radio jets. Moreover, spiral galaxies have also been found to host extended jets (Hota et al. 2011; Bagchi et al. 2014). The fraction of host galaxies hosting a radio AGN increases with the stellar mass (Best et al. 2005; Mauch & Sadler 2007). In agreement with these results, Sabater et al. (2019) found a strong dependence of the fraction of radio-active optical galaxies on their stellar mass and radio luminosity. For luminosities at 150 MHz $L_{150} \geq 10^{21}$ W Hz^{-1} and masses larger than 10^{11} M$_\odot$, the fraction reaches a value of 100%, that is one has that all local massive galaxies are radio-active AGN, in agreement with the recent result of Capetti et al. (2022). Smolčić et al. (2009) and Williams & Röttgering (2015) looked at the evolution of the radio AGN fraction up to z=2. They showed that the fraction of optical galaxies hosting a radio AGN increases with redshift for all galaxy masses (see Fig. 1.5), with a more marked increment observed in galaxies of lower masses ($M_* \lesssim 10^{10.7}$ M$_\odot$). The authors also suggested that these findings hint at an evolution of the dominant accretion mode powering RGs.

The host galaxies of radio AGN can be divided into high-excitation radio galaxies (HERGs) and low-excitation radio galaxies (LERGs) according to the presence or absence and relative strength of emission lines in their optical spectra (Hine & Longair 1979). The black holes of HERGs (or radiatively efficient RGs, which also include quasar) have a high accretion rate and produce a luminosity which is one to ten per cent of the Eddington luminosity. The Eddington limit is the maximum luminosity that a body can isotropically radiate when there is a balance between the gravitational force acting inwards and the radiation pressure acting outwards. In the local universe, HERGs are found in smaller, lower mass, and less concentrated host galaxies compared to LERGs. Moreover, the host galaxies of HERGs exhibit higher levels of star-formation activity (Smolčić et al. 2009; Smolčić & Riechers 2011; Best & Heckman 2012). On the other hand, LERGs (or radiatively inefficient RGs) exhibit a lower accretion rate with a luminosity lower than one per cent of the Eddington limit. LERGs are also hosted by massive early-type galaxies with little star-formation activity. The difference in the accretion rate likely reflects a difference in the properties of the accretion disk around the central black hole and the source of fuel (Hardcastle et al. 2007). Radiatively efficient RGs are powered by a geometrically thin and optically thick accretion disk (Shakura & Sunyaev 1973). It is believed that the AGN activity in HERGs is triggered by an abundant supply of cold, dense gas in the galaxy's central region. However, the origin of this cold gas remains uncertain (Best & Heckman 2012). A model for
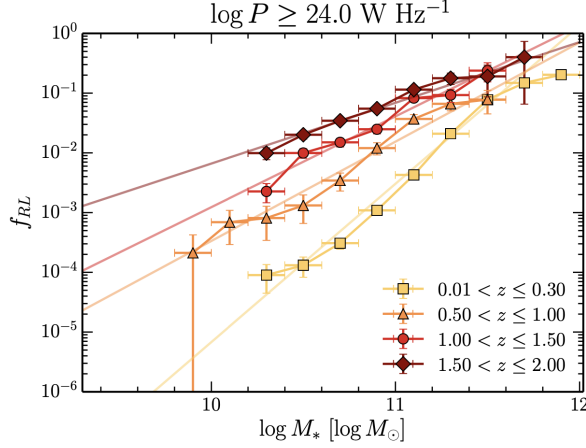
Figure 1.5: Fraction of host galaxies hosting an AGN with a radio power $L_{1.4GHz} > 10^{24}$ W Hz^{-1}. The different colours correspond to different redshift intervals. The coloured lines show the best fit in the range $10^{10} < M_*/M_\odot < 10^{11.5}$. Figure from Williams & Röttgering (2015).

radiatively inefficient RGs is the Advection-Dominated Accretion Flow (ADAF, Narayan & Yi 1994) in which the accretion disk is geometrically thick and optically thin (see Fig. 1.6). The fuel is likely hot gas and can have multiple origins. For many galaxies, the hot gas arises from recycled material from stellar mass loss. In more massive systems, such as massive elliptical galaxies and galaxies in the centre of galaxy clusters, extended hot gas halos around the central galaxy provide a more abundant gas source (see Heckman & Best 2014, for details).

It then appears that the host galaxies of HERGs and LERGs are quite different, at least up to redshift z≈0.5. However, the paradigm is less clear at higher redshifts. HERGs and LERGs show different cosmological evolution; while LERGs do not show any substantial evolution, the fraction of galaxies hosting HERGs increases with redshift (Best et al. 2014; Pracy et al. 2016; Butler et al. 2019; Best et al. 2023). Moreover, multiple studies (Fernandes et al. 2015; Williams et al. 2016; Delvecchio et al. 2017) showed that the distributions of both HERGs and LERGs host galaxies gather around 10^{11}M$_\odot$, except for a more pronounced tail visible in the distribution of HERGs at lower masses. At higher redshifts, the host galaxies of LERGs show higher star-formation rates compared to LERGs in the local universe. When interpreting these findings, it is crucial to take into account the evolution of cosmic star formation. As we approach cosmic noon, not only all galaxies become more star-forming (Madau & Dickinson 2014), but also star-formation activity gradually shifts to more massive systems (the so-called cosmic downsizing, e.g., Cowie et al. 1996).

Regardless of the type of supply that fuels that central black hole, uncertainty persists on how radio AGN are produced in the context of galaxy evolution and dynamics. A large focus in the literature is on whether major galaxy mergers might be the dominant AGN triggering mechanism through galaxy-wide, gravitationally-induced torques which drive gas towards the galactic centre (Hopkins et al. 2006). While there have been a substantial number of studies supporting the relevance of major galaxy mergers in triggering AGN (Koss et al. 2010; Ellison et al. 2011; Hong et al. 2015; Weston et al. 2017; Goulding et al. 2018; Gao et al. 2020; Breiding et al. 2023), the results are still mixed (Cisternas et al. 2011; Kocevski et al. 2012; Karouzos et al. 2014; Villforth et al. 2019; Lambrides et al. 2021). Selection bias is likely responsible for these conflicting results. There are different selection criteria for AGN, such as mid-infrared colour selection (e.g., Satyapal et al. 2014; Donley et al. 2018;
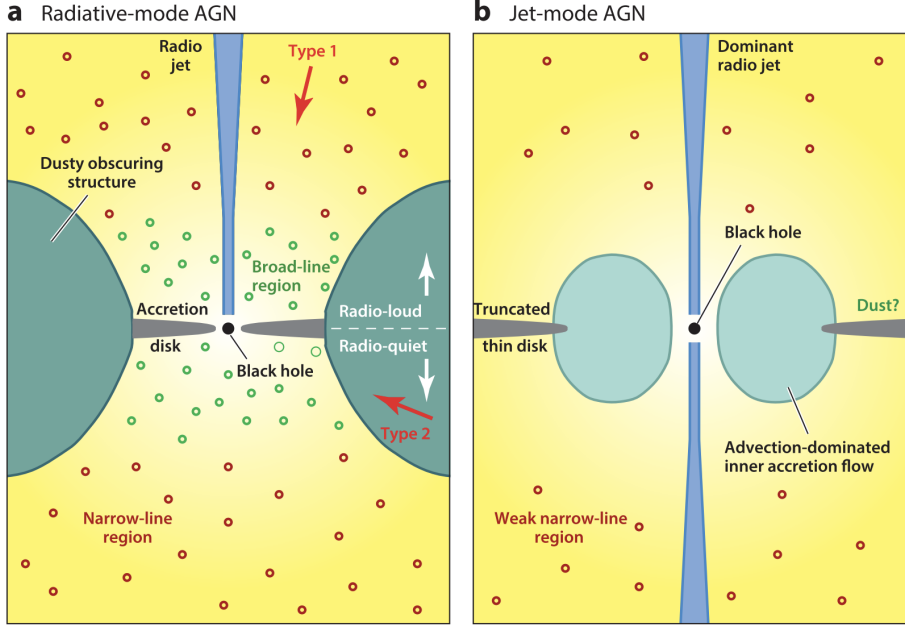
Figure 1.6: Schematics drawing of the central region of HERGs (left panel) and LERGs (right panel). Figure from Heckman & Best (2014).

Goulding et al. 2018; Ellison et al. 2019), X-ray selection (Kocevski et al. 2012; Lackner et al. 2014; Hewlett et al. 2017; Secrest et al. 2020), optical emission line ratios (the so-called BPTdiagram Baldwin et al. 1981) and radio selection (Ellison et al. 2015; Chiaberge et al. 2015; Gordon et al. 2019). AGN selected in different ways may represent different stages in the merger evolutionary scenario (Sanders et al. 1988). Moreover, the lifetime of the radio activity of $10^7 - 10^8$ yr (Parma et al. 1999; Jamrozy et al. 2004; Bird et al. 2008; Giacintucci et al. 2021) is shorter compared to that of mergers, which can last up to few billion years (Lotz et al. 2008). This difference in timescale can lead to fewer radio AGN being detected in some stages of the merger process. In addition, the time delay between merger events and the triggering of AGN activity as inflowing gas eventually falls into the vicinity of the black hole would bias towards fewer radio AGN being observed (e.g., Villforth et al. 2014; Shabala et al. 2017; Choi et al. 2023). These difficulties highlighted the need to look for alternatives to major galaxy mergers for transporting gas from kpc to sub-pc scales. These alternatives include internal "secular" processes or minor/satellite-galaxy accumulation (Hernquist & Mihos 1995; Gordon et al. 2019). Secular processes that can induce gas inflows are stellar winds (Davies et al. 2007), chaotic and cold accretion streams driven by turbulence in the host galaxy interstellar medium (Hobbs et al. 2011; Gaspari et al. 2013), gravitational disk instabilities mediated by stellar bars (Shlosman et al. 1989) and dense, inhomogeneous clumps formed through cold accretion streams from the larger-scale halo environment (Bournaud et al. 2011).

1.2 Giant radio galaxies

In 1974, Willis et al. presented the observations of the RGs 3C236 and DA240 with the Westerbork Synthesis Radio Telescope (WSRT, Hogbom & Brouw 1974) determining their linear sizes as 5.7 and 2 Mpc, respectively. Although these measurements have been revisited based on new cosmological

parameters (Planck Collaboration et al. 2016), these initial discoveries posed a significant challenge to RG evolution theory due to their exceptional sizes. Since that discovery, many GRGs have been identified (Ishwara-Chandra & Saikia 1999; Lara et al. 2001; Schoenmakers et al. 2000b; Machalski et al. 2001; Saripalli et al. 2005; Kuźmicz & Jamrozy 2012, 2021; Kuźmicz et al. 2018; Dabhade et al. 2017, 2020a,b; Brüggen et al. 2021; Andernach et al. 2021; Gürkan et al. 2022; Mahato et al. 2022; Oei et al. 2023a) using a variety of radio surveys such as the Faint Images of the Radio Sky at Twenty-cm (FIRST, Becker et al. 1995), Westerbork Northern Sky Survey (WENSS, Rengelink et al. 1997), National Radio Astronomy Observatory (NRAO) VLA Sky Survey (NVSS, Condon et al. 1998), Sydney University Molonglo Sky Survey (SUMSS, Mauch et al. 2003), the recent Rapid ASKAP Continuum Survey (RACS, McConnell et al. 2020) and the LOFAR Two-metre Sky Survey (Shimwell et al. 2019, 2022). These surveys collectively unveiled thousands of GRGs, some with exceptional sizes of 5-6 Mpc (Oei et al. 2023a; Hardcastle et al. 2023). In Fig. 1.7, I show a few examples of the largest GRGs known to date (Oei et al. 2022; Willis et al. 1974), compared in projected linear size with smaller well-known RGs (Mack et al. 1997; Perley et al. 1984).

Almost all GRG catalogues were constructed by manually analysing and inspecting survey data (see Andernach et al. 2021, for a detailed description on how to identify GRGs and respective host galaxies). Defined as radio sources with a linear size $\geq$ 700 kpc, GRGs have an angular size of at least 1.3′, adopting a flat ΛCDM cosmology with $H_0 = 70$ km s^{-1} Mpc^{-1}, $\Omega_m = 0.3$, $\Omega_\Lambda = 0.7$. Such an angular size makes GRGs relatively faint in terms of surface brightness and thus difficult to detect and recognise while inspecting the survey data. Multiple optical and infrared surveys such as the Sloan Digital Sky Survey (SDSS, York et al. 2000), the Wide-Field Infrared Survey Explorer (WISE, Wright et al. 2010) and its more recent versions of both images and catalogues AllWISE (Cutri et al. 2021), unWISE (Schlafly et al. 2019) and CWISE (Marocco et al. 2021), the Dark Energy Survey Imaging (DESI, Dey et al. 2019; Zhou et al. 2021) and Panoramic Survey Telescope and Rapid Response System (Pan-STARRS, Flewelling et al. 2020) have been crucial for identifying host galaxies. Reliable optical identifications are facilitated when radio cores are detectable; however, the task becomes more challenging in the absence of core emission.

While visual inspection remains a reliable method, the flow of new deep radio data is going to increase with more surveys (Shimwell et al. 2019, 2022; McConnell et al. 2020), especially with the Square Kilometer Array [1]. As a consequence, the manual analysis of data has become nearly unmanageable, prompting the development of novel strategies to keep up with the fast data flow. Throughout astronomy, automated techniques, including artificial neural networks (ANN), machine learning (ML), and deep learning, have proven their efficiency in dealing with large datasets. In particular, Proctor (2016) and Galvin et al. (2020) have successfully demonstrated the utility of ML algorithms in identifying and categorising GRGs. However, the detection of the radio source as well as the identification of the host galaxy is still challenging for these methods, especially for widely separated radio components without a detected radio core between them.

An alternative approach involves leveraging the expertise of trained citizens to visually inspect large datasets. Such a method was employed in various projects such the radio galaxy zoo[2] project, the RAD@home project (Hota et al. 2016), and the radio galaxy zoo: LOFAR (e.g., Hardcastle et al. 2023).

Despite these efforts in detecting and analysing a large number of GRGs, the origin and the causes for their large sizes are still not understood (see Dabhade et al. 2023, for a review). In this introduction, I summarise our current understanding of these sources based on recent results from

---

[1]https://www.skao.int/en.
[2]https://radio.galaxyzoo.org.

radio as well as multi-wavelength approaches.
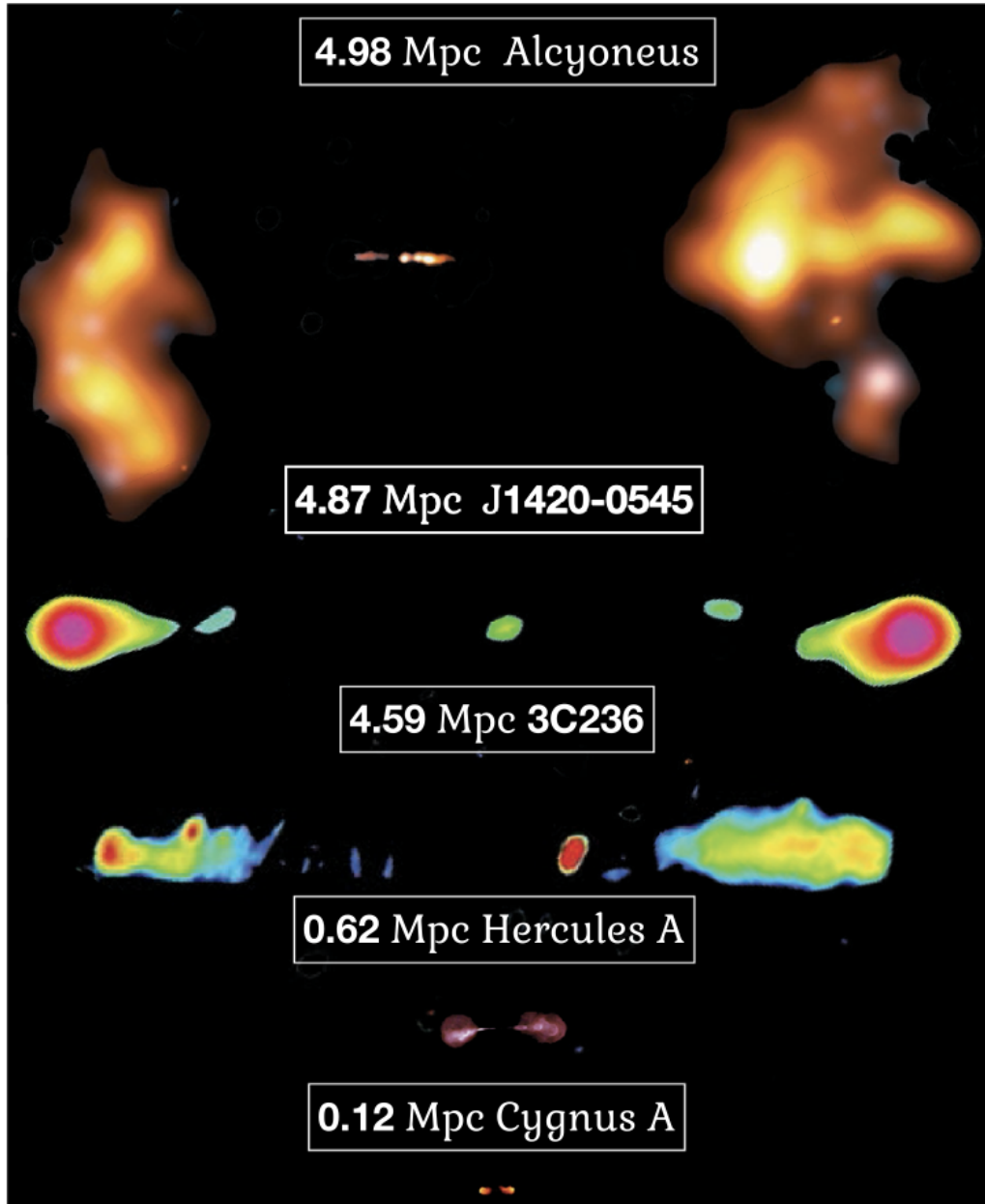
Figure 1.7: Comparison of the linear size of some of the largest GRGs with Hercules A and Cygnus A. From top to bottom: Alcyoneus with the image shown with two resolutions, 6 arcsec for the core and inner jets and 60 arcsec for the diffuse lobes (Oei et al. 2022); J1420−0545 (Machalski et al. 2008); 3C236 (Mack et al. 1997); Hercules A: (Credit: NASA, ESA, S. Baum and C. OĎea (RIT), R. Perley and W. Cotton (NRAO/AUI/NSF); Cygnus A: NRAO/AUI and Perley et al. (1984). Image from Dabhade et al. (2023).

1.2.1 Morphology of GRGs

The vast majority of GRGs exhibit an FRII morphology. In previous compilations of GRGs, the percentage of FRI sources is rather small $\approx$ 5-7% (Ishwara-Chandra & Saikia 1999; Kuźmicz et al. 2018). Furthermore, samples of GRGs extracted from LOFAR observations, which are more sensitive to faint FRI GRGs compared to previous surveys, report a percentage of FRII source larger than 90% (Dabhade et al. 2020a,b). This observed prevalence of FRII sources in GRGs may be associated with their environmental conditions. FRI sources are commonly found in galaxy clusters or groups (Croston et al. 2019) and often exhibit more dissipative jets (Barthel & Arnaud 1996). In contrast, GRGs may inhabit sparser environments (see Sect. 1.2.5), and their interaction with the surrounding medium might lead to less dissipative jets, ultimately resulting in the prevalent FRII morphology.

Subrahmanyan et al. (1996) studied a sample of 8 GRGs and found that they have less uniform and less bright bridges (i.e., the radio emission connecting the hot spots and the core of the RG) compared to their smaller counterparts (Jones & McAdam 1992). The prominence of the radio bridge is likely affected by the inverse-Compton scattering with the CMB. Ishwara-Chandra & Saikia (1999) showed that inverse-Compton losses dominate over synchrotron losses for GRGs, while it is the opposite for smaller RGs. Moreover, given the redshift scaling of the CMB energy density, $u_{CMB} \propto (1+z)^4$, the prominence of the radio bridge likely decreases with redshift (Konar et al. 2004).

Previous studies examined the symmetry parameters of GRGs (Ishwara-Chandra & Saikia 1999; Schoenmakers et al. 2000a; Lara et al. 2004; Komberg & Pashchenko 2009; Kuźmicz & Jamrozy 2012). Using a sample of 3CR and WENSS RGs, respectively, Ishwara-Chandra & Saikia (1999) and Schoenmakers et al. (2000a) found that the ratio of the lobe length in GRGs is slightly larger compared to smaller RGs. However, Lara et al. (2004), Komberg & Pashchenko (2009) and Kuźmicz & Jamrozy (2012) found no significant difference. It should be noted that this parameter depends on various properties of both the radio source itself and the external environment. Under the unification scheme, the GRGs are expected to be oriented between 45° and 90° to our line of sight. Nevertheless, GRGs can be hosted by quasars and their smaller inclination angle, coupled with the relativistic effects of time dilation and length contraction, affects the calculated ratio of lobe length. Asymmetries in the environment can also result in a shorter lobe on the side with the largest density (Pracy et al. 2016). Moreover, superluminal motions of jets would also create a more compact and brighter lobe that points to the direction of the observer (Hocuk & Barthel 2010).

1.2.2 Host galaxies and AGN properties

Like smaller RGs, GRGs are hosted by massive elliptical galaxies (Lara et al. 2001; Dabhade et al. 2017) and are predominantly LERGs (Dabhade et al. 2020b), with very few exceptions (Hota et al. 2011; Bagchi et al. 2014). Moreover, Dabhade et al. (2020b) found that the distribution of the r-band absolute magnitude for GRGs is similar to that of host galaxies of smaller RGs.

Kuźmicz et al. (2019) studied a sample of 41 GRGs and 217 RGs. They found that the host galaxies of GRGs exhibit more young ($< 10^7$) and intermediate ($9 \cdot 10^8$ yr $< t < 7.5 \cdot 10^9$ yr) stellar populations in comparison with the RG hosts. However, they did not find differences in the distribution of the stellar mass. Kuźmicz et al. (2019) suggested that these findings could be the result of a past merger activity or cold gas streams permeating through the groups of galaxies with and around GRGs, possibly triggering star formation. In support of this hypothesis, Zovaro et al. (2022) found a young stellar population ($\lesssim$ 10 Myr) in the host galaxy of the GRG 0503–286. By studying the ionised gas kinematics, they proposed that a gas inflow has triggered both the starburst and the restarted jet activity.

One of the proposed explanations for the giant sizes of the GRGs is the sustained jet activity powered by a continuous gas supply. Possible evidence of this gas may be probed via observations of neutral atomic hydrogen or HI and cold molecular gas. While the presence of HI emission has been successfully observed in numerous nearby early-type galaxies (Emonts et al. 2010), attempts to detect HI in radio-loud active galactic nuclei (RLAGN) have predominantly relied on absorption line observations. Notably, it was found that, among RGs, compact radio sources exhibit the highest detection rates (Morganti & Oosterloo 2018). Observations of HI in GRG hosts are very limited and the detection was confirmed in only very few GRGs (Pihlström et al. 2003; Gupta & Saikia 2006). HI observations of NGC315 (Morganti et al. 2009) suggested the presence of an infalling cloud into the host galaxy and some disturbed cold gas located in the centre which could be fueling the AGN. In other GRGs, the HI gas is either likely interacting with the jets (Conway & Schilizzi 2000; Schilizzi et al. 2001; O'Dea et al. 2001) or it shows a complex kinematics (Saikia et al. 2007). In a search for cold molecular gas as possible fuel, millimetre-wave observations of a small sample of three GRGs were carried out by Saripalli & Mack (2007). Using the Swedish-ESO Millimetre Telescope (SEST), they provided upper limits on the flux emitted from the molecular gas. Moreover, using results from the literature (Elfhag et al. 1996; Braine et al. 1997), Saripalli & Mack (2007) concluded that GRGs lack large ($\gtrsim 10^9$ M$_\odot$) reservoirs of molecular gas in their host galaxies. The SAGAN project (Dabhade et al. 2020b) aims to create a catalogue of all GRGs published to date including the properties of the host galaxies. As part of this project, Dabhade et al. (2020b) investigated the molecular gas content of 12 GRG hosts. They reported the detection in three of them and upper limits for the remaining sources. Nevertheless, the detection was primarily in GRG hosts exhibiting discs or spiral morphologies.

An alternative hypothesis for the large size of GRGs is that their jet expansion is driven by exceptionally powerful AGN. Thus, AGN properties, such as the black hole mass and accretion rate, in GRGs need to be compared with samples of smaller RGs. In this context, Dabhade et al. (2020b) estimated the black hole mass (M$_{BH}$) for a sample of 46 GRGs using the M$_{BH}$ - σ relation (Magorrian et al. 1998; Ferrarese et al. 2001). Here, σ represents the stellar velocity dispersion and was obtained from SDSS spectra (Ahumada et al. 2020). The authors compared the M$_{BH}$ values of GRGs with those of a sample of RGs created from the Best & Heckman (2012) catalogue and observed that both samples have similar distributions with a median value of $8.4 \cdot 10^8 M_\odot$. Kuźmicz & Jamrozy (2012) used an alternative method to estimate the black hole mass in giant radio quasars (GRQs) which involves the strength of the Hβ, MgII and CIV emission lines. They found values of M$_{BH}$ ranging from $1.6 \cdot 10^9 M_\odot$ to $2.9 \cdot 10^{10} M_\odot$ and a weak correlation between the black hole mass and the linear size of the source. However, subsequent work concluded that GRG and smaller RG hosts have no significant difference in the black hole mass distribution (Kuźmicz & Jamrozy 2021; Mahato et al. 2022). Using the estimated black hole masses, Dabhade et al. (2020b), Kuźmicz & Jamrozy (2012) and Mahato et al. (2022) estimated the Eddington luminosity of the black holes (i.e., the authors assumed that the accretion of black holes occurs at the Eddington accretion rate.). They also computed the bolometric luminosity of the central AGN using [O$_{III}$] emission line luminosity (Dabhade et al. 2020b; Mahato et al. 2022) and optical monochromatic continuum luminosity at 5100, 3000 and 1350 Å. Thus, the authors estimated the Eddington ratio (λ_{edd}) and reported significant overlap between the Eddington ratio distributions of both GRGs and RGs samples. Nevertheless, they observed that RGs exhibit higher values of λ_{edd} in comparison to GRGs; this result suggests that GRGs are evolved or aged sources with a decreasing (or already declined) accretion rate.
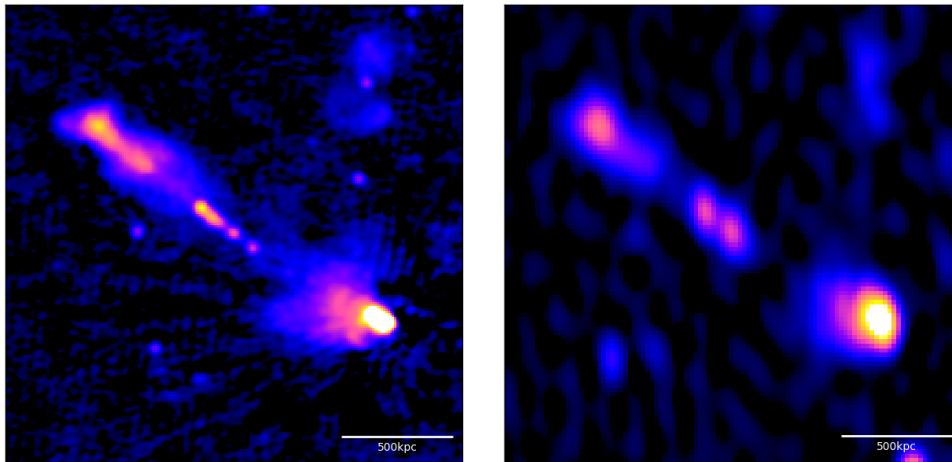
Figure 1.8: LOFAR (left) and WSRT (Kutkin et al. 2023, right) view of the GRG J1424+3436. The bar in the bottom-right corner represents a physical size of 500 kpc.

1.2.3 Age of GRGs

The impact of the powerful jets of RGs in the surrounding medium drives strong shocks that accelerate particles to relativistic energies and form hotspots. Once the shock has passed away, the relativistic electrons experience synchrotron and adiabatic losses and diffuse away from the hotpots, filling the space of the radio lobe between the core and the hotspots. Thus, these diffuse regions of the RGs are likely the locations of the oldest electrons. Under the hypothesis that GRGs are highly evolved RGs, the population of relativistic electrons in GRGs should be older than in RGs. Consequently, the radio spectrum in the inner part of the lobes of evolved RGs should exhibit a steeper spectral index. However, due to the large angular size of GRGs, their surface brightness is relatively low, posing challenges for the detection of such regions. Therefore, the total radio flux of GRGs is often dominated by those regions with newly injected or re-accelerated particles, such as the hotspots or the core, and thus a flatter spectral index, especially at high frequencies (> GHz). In Fig. 1.8, I present an example of a GRG from the dataset used in this thesis, observed by LOFAR at 150 MHz and WSRT at 1.4 GHz. J1424+3436 is likely a DDRG, with both the inner jets and outer lobes visible in both images. Notably, the diffuse emission bridging these components is primarily detected by the LOFAR observations, while the WSRT image reveals a distinct gap in radio emission between the outer and inner features of the GRG, especially along SW lobe.

Early studies of radio sources including GRGs were mostly based on GHz frequency observations (Klein et al. 1995; Parma et al. 1999; Ishwara-Chandra et al. 2001). They lacked low-frequency observations (<200 MHz) which are essential in determining the injection index and, for some cases, the break frequency (Harwood et al. 2015, 2017). Mack et al. (1998) carried out the first spectral analysis of some of the largest GRGs in a frequency range between 326 MHz and 10.6 GHz. The ages resulting from these fits align with those of smaller radio galaxies studied in previous work (Carilli et al. 1991; Klein et al. 1995). Interestingly, Parma et al. (1999), using two-frequency observations mainly at 1.4 and 5 GHz, found a positive correlation between the spectral age and the linear size of RGs. A similar relation is also reported by Jamrozy et al. (2008) for sources with a radio power larger than $10^{26.5} \mathrm{WHz}^{-1}$; however, the correlation is less clear for less powerful sources. Subsequent studies focused mainly on samples of GRGs or specific sources and extended the range of probed frequencies. Most of the sources exhibit radiative ages up to $\approx$ 80 Myr and similar to smaller RGs

(Schoenmakers et al. 2000a; Lara et al. 2000; Konar et al. 2004, 2006; Jamrozy et al. 2008; Nandi et al. 2010; Pirya et al. 2011; Tamhane et al. 2015; Harwood et al. 2017; Sebastian et al. 2018; Mhlahlo & Jamrozy 2021), with very few exceptions (Godambe et al. 2009; Ishwara-Chandra et al. 2001). A combination of sensitivity at the largest angular scales coupled with a good angular resolution of the radio interferometers at different frequencies is essential to infer the spectral properties of the GRGs. More recent studies used LOFAR to investigate the GRG properties at lower frequencies and derive spectral index maps using data from the literature such as Very Large Array (VLA), WRST, Effelsberg, and Giant Metrowave Radio Telescope (GMRT) observations (Shulevski et al. 2019; Cantwell et al. 2020; Dabhade et al. 2022; Brienza et al. 2023). These studies identified GRGs with a radiative age exceeding 100 Myr, hinting at their status as aged and evolved RGs.

Machalski et al. (2007a) developed a model to determine the ages of FRII type radio sources that, on one hand, exploits a dynamical model developed for these objects by Kaiser & Alexander (1997) and, on the other hand, uses multi-frequency radio observations not necessarily restricted to the high-resolution ones. Using this approach, Machalski et al. (2009) and Machalski (2011) estimated the dynamical ages of respectively 10 and 20 GRGs and compared them with the radiative ages of the same sources (Jamrozy et al. 2008). They found the dynamical ages of the lobes to be 1–5 times larger than the respective spectral ages, and often exceed 100 Myr. Similar kinds of discrepancies between the spectral and dynamical ages were also found by Parma et al. (1999). More recently, Marecki et al. (2021) studied the dynamics of the double-double GRG J0028+0035 exploiting a set of radio flux density measurements covering the range from 74 MHz to 14 GHz. They found that the age of the large-scale outer lobes is about 250 Myr. Moreover, Machalski et al. (2021) observed that the range of dynamical ages of the lobes of smaller RGs is 0.082–92 Myr, while for GRGs it is 38–240 Myr. Dabhade et al. (2023) used the data from Machalski et al. (2021) and reported a positive trend between the estimated dynamical age and the linear size of the RGs. This result shows that GRGs tend to be older, despite the relatively limited samples available.

An alternative approach to test whether GRGs are the result of the long-term evolution of RGs is to investigate their energy content. Traditionally, the energy of the relativistic particles filling the lobes of GRGs is estimated assuming equipartition between the particle energy density and the magnetic energy density (Subrahmanyan et al. 1996; Ishwara-Chandra & Saikia 1999; Schoenmakers et al. 2000a; Konar et al. 2004; Machalski et al. 2004). The measured minimum energy densities in the range of 4-8×10^{-13} erg cm^{-3} were found to be relatively low when compared to the RGs sample (5×10^{-12} erg cm^{-3}) of Leahy & Williams (1984). The detection of inverse-Compton X-rays from the lobes of RGs offers a method to estimate both the electron energy density and the magnetic field. The latter can be estimated by measuring the ratio of the synchrotron to X-ray flux, assuming that all X-ray emission results from inverse-Compton scattering between the relativistic electrons and the CMB (e.g., Hardcastle et al. 2003; Croston et al. 2005; Hardcastle 2013). The magnetic field in the lobe of GRGs was found to range from a fraction of μG to a few μG (Konar et al. 2009; Isobe et al. 2011b,a; Isobe & Koyama 2015; Tamhane et al. 2015; Mirakhor et al. 2021). The spectrum of the inverse-Compton radiation is strongly dependent on the properties of the energy distribution of the electrons. This includes parameters such as the power index and the minimum/maximum energy of the electrons emitting synchrotron radiation. Isobe et al. (2009, 2011b,a) and Isobe & Koyama (2015) used the Suzaku space telescope to constrain the electron and magnetic field energy density in GRGs. Dabhade et al. (2023) plotted the electron energy density as a function of the projected linear size (see their Fig. 5) using data from several papers (Subrahmanyan et al. 1996; Ishwara-Chandra & Saikia 1999; Schoenmakers et al. 2000a; Isobe & Koyama 2015) and reported a significant anti-correlation between these two variables. The presented energy densities encompass estimates derived from both the equipartition approach and inverse-Compton analysis. Such a result suggests that GRGs

experienced more adiabatic, synchrotron and inverse-Compton losses compared to smaller RGs.

1.2.4 Rejuvenated GRGs

One of the most striking examples of recurrent activity are the DDRGs and many of them are associated with GRGs (Schoenmakers et al. 2000a). Kaiser et al. (2000) proposed a model for these DDRGs in which the contamination of the cocoons of FRII sources by warm, dense clouds located in the IGM might fuel the new activity of the central AGN. Saripalli & Mack (2007) proposed a fueling mechanism for DDRGs which is driven by instabilities in the accretion process rather than a depletion of fuel followed by a recent fuel acquisition. According to this work, abundant molecular gas content (10^8–$10^9 M_\odot$) does not necessarily accompany the nuclear restarting phenomenon. Several works modelled the dynamics of the two pairs of lobes (Shulevski et al. 2012; Bruni et al. 2015; Orrù et al. 2015; Shabala et al. 2020; Bruni et al. 2020; Giacintucci et al. 2021). Brocksopp et al. (2011) modelled two DDRGs, B1450+333 and B1834+620, in terms of their dynamical evolution. In these sources, the inner lobes should reach the outer lobes in a rather short time (2-3 Myr) due to the high predicted velocity of the inner lobes (0.1-0.7c). This would in turn result in a short-lived DDRG phase compared to the total age of the source and may explain why DDRGs are rare and are typically large ($\gtrsim 100$ kpc).

Some RGs exhibit restarted jets on small scales ($\lesssim 1''$) which can not be resolved by most of the low-frequency radio interferometers. The very large baseline interferometer (VLBI) observations in the radio band enable us to achieve milli-arcsecond resolutions routinely as well as micro-arcsecond resolutions as with the Event Horizon Telescope (Event Horizon Telescope Collaboration et al. 2019). Such observations enable the study of the core and the inner part of the jets with unprecedented details (Fig. 1.9). One of the primary requirements for VLBI observations is bright nuclei with flux densities $\gtrsim 20$ mJy at GHz frequencies. Only a small fraction of GRGs (mostly powered by quasars) are bright enough to be observed with VLBI currently. Hence, only a few GRGs have been studied at VLBI resolutions to probe their core and inner jet structures (Schilizzi et al. 1988; Saripalli et al. 1997; Schilizzi et al. 2001; Barthel et al. 1989). Hocuk & Barthel (2010) combined VLBI and large-scale radio observations to study the GRG 4C34.74 which hosts one of the largest radio jets observed among RGs. The radio core of this source has been found to be variable over the years, as well as the host quasar at optical wavelengths (Hocuk & Barthel 2010). On VLBI scales, Barthel et al. (1989) and Hooimeyer et al. (1992) reported a knot proper motion of 0.29 mas year^{-1} which corresponds to a projected expansion speed of 3.9c at the redshift of the source. Another example example of GRG likely exhibiting restarted activity is NGC315 (Linfield 1981). Cotton et al. (1999) carried out VLBI observation of the core of the GRG and concluded that the core is in an active phase and exhibit some variability in the continuum radio flux. Hard X-ray observations (energies >20 keV) represent another method to find restarted RGs (Chiaraluce et al. 2020; Bassani et al. 2021). Using a sample of Hard-Xray selected GRGs, Bruni et al. (2019) found a large fraction (>60%) of young radio sources at the centre of Mpc-scale structures. The restarted activity in X-ray selected RGs is suggested from the discrepancy between the measured jet and lobes power, with respect to the one expected from core X-ray luminosity (Bruni et al. 2020). Moreover, Bruni et al. (2021) comparing X-ray selected GRGs with radio-selected GRGs from LoTSS DR1 (Shimwell et al. 2019) suggested that, on average, hard X-ray GRGs can grow to larger extents.

It is relevant to note here that only about 5% of GRGs appear to show evidence of recurrent activity in previous samples (Dabhade et al. 2020a,b). The recent development of the VLBI observations with LOFAR (Sweijen et al. 2022) will certainly help to find more GRGs or RGs harbouring unresolved inner jets and constrain the percentage of restarted sources.
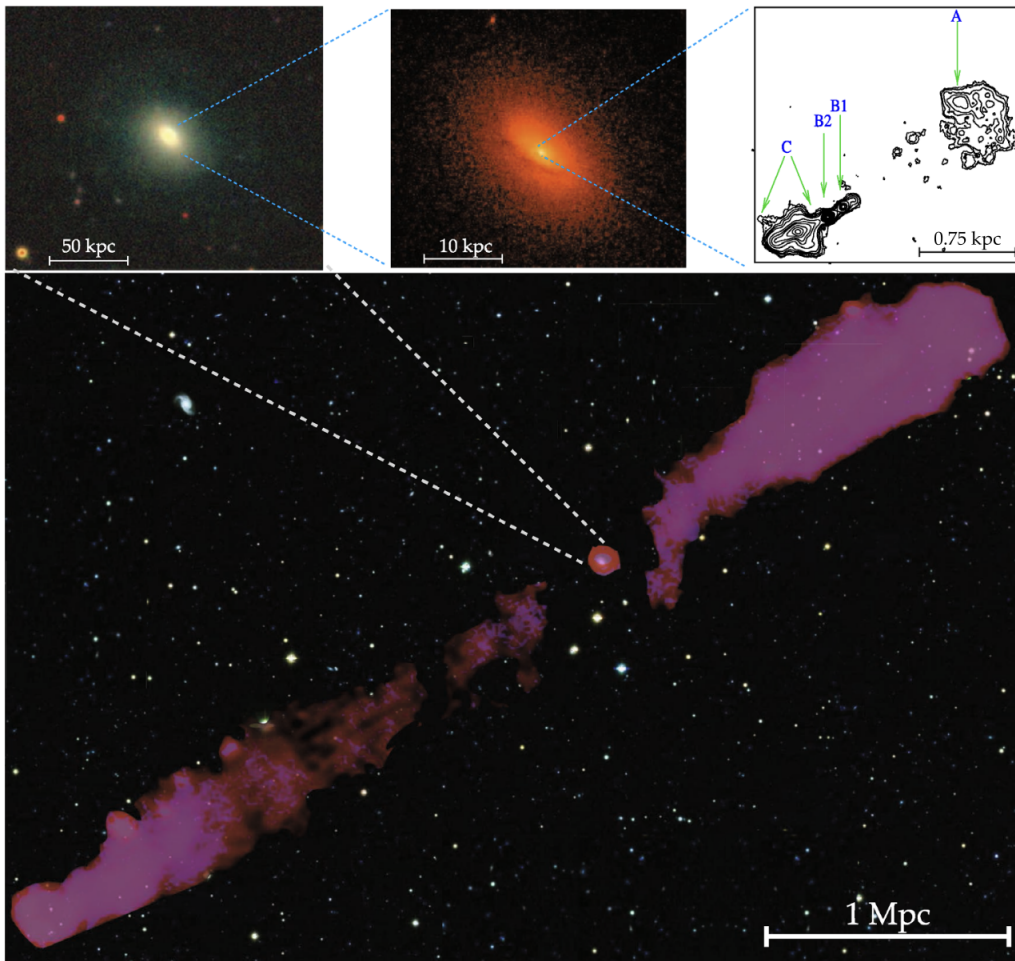
Figure 1.9: Multi-wavelength image showing the GRG 3C236 on various scales. The lower panel shows the LOFAR (144 MHz) image with a resolution of 6″ produced by Shulevski et al. (2019) overlaid on an optical colour composite image from legacy survey DR9. The upper left and central panels show the legacy survey DR9 and the high-resolution Hubble Space Telescope optical images of the host galaxy. The upper right panel shows the VLBI mas scale image of the core of the GRG (Schilizzi et al. 2001). It highlights the presence of a double structure in the core that remains unresolved by low-frequency observations with lower resolution.

1.2.5 The environment of GRGs

To have a complete understanding of GRGs and their evolution is essential to probe their environment. A small fraction of GRGs reside in known galaxy clusters (Dabhade et al. 2020a,b; Andernach et al. 2021); thus, the detection of X-ray emission from the gas halo surrounding the host galaxy is challenging. Moreover, optical spectroscopic observations of the neighboring galaxies are needed for detailed studies of the environment of GRGs. Both these observations, X-ray and optical, are rather expensive in terms of observational time, especially for large samples. Hence, such detailed studies have been restricted to a few sources (Subrahmanyan et al. 2008; Chen et al. 2011, 2012b,a; Pirya et al. 2012; Malarecki et al. 2013). Chen et al. (2011, 2012b,a) spectroscopically investigated the galaxies around the GRGs NGC 6251, NGC 315, and 4C 73.08. They found that all the GRGs reside in groups of galaxies and several components of the groups were present around the shortest and brightest lobes. The optical velocity dispersion of group members is not consistent with that expected from the correlation of the X-ray luminosity versus the velocity dispersion, suggesting that the density of the X-ray emitting gas is unusually low. They proposed that the size of the radio sources is primarily influenced by the low-density environment. Subrahmanyan et al. (2008) carried out a large optical spectroscopic survey around the asymmetric GRG 0503–286 (Saripalli et al. 1986). They discovered multiple galaxy groups at a similar redshift of the source in the direction of the shorter and brighter lobe. Pirya et al. (2012) examined the distribution of galaxies in the vicinity of 16 large radio sources, almost all of which are GRGs. They also reported that while most sources appear to occur in regions of low galaxy density, the shorter arm is brighter in most cases. This suggests that there are asymmetries in the intergalactic medium, which may not be apparent from the distribution of galaxies. Using a sample of 9076 spectroscopically identified galaxies around 16 GRGs, Malarecki et al. (2015) found that the mean galaxy number overdensity in volumes of ≈ 700 Mpc^3 near the GRG host galaxies is ≈ 70, indicating an overdense but non-virialized environment. Moreover, Malarecki et al. (2015) found that there is a clear influence of the environment. However, they found that the lobes of the bent GRGs appear to be deflected away from overdensities in the surrounding medium and the GRG lobes are perpendicular to the plane in which the neighbouring galaxies and filaments are distributed.

Extending up to Mpc sizes and considered relatively old, the lobes of GRGs are assumed to be in pressure equilibrium with the external medium. This aspect of GRGs has been used to probe the properties of the warm-hot-intergalactic medium (WHIM, Davé et al. 2001). Malarecki et al. (2013) derived the lobe energy densities of 12 GRGs from the radio observations via equipartition arguments. The inferred pressure in the lobes ranges from 1.1×10^{-15} to 2.0×10^{-14} Pa which is lower than previous measurements of the WHIM pressure inferred from X-ray observations of dense filaments (Briel & Henry 1995; Werner et al. 2008; Fraser-McKelvie et al. 2011; Dietrich et al. 2012). A comparison of these observations with cosmological simulations of Schaye et al. (2010) suggests a particle overdensity of 50–500 and a temperature of the WHIM of about $10^{6.5}$ K. It is important to highlight that the equipartition assumption is a major drawback for this kind of analysis. X-ray observations of inverse-Compton scattering represent a valid method for more accurate measurement of the pressure of the lobes. Ineson et al. (2017) investigated the relation between X-ray and equipartition lobe pressures for a representative sample of FRII radio galaxies. For almost all studied cases, the X-ray pressure is higher than the equipartition pressure by a factor of order unity. Oei et al. (2023b) used inverse-Compton X-ray observations to constrain the lobe pressure of the GRG NGC 6185 to a value around 10^{-15} Pa. A significant limitation of this approach used to infer the thermodynamical properties of the environment is the assumption of the pressure equilibrium between the lobes and the WHIM. Subrahmanyan et al. (2008) conducted a comparison of the thermodynamic properties of

the WHIM inferred from radio observations of the GRG MSH 05–22 with those derived from hydro-dynamical simulations of WHIM heating (Davé et al. 2001; Cen & Ostriker 2006). The conclusion drawn was that the IGM pressure from simulations is an order of magnitude below the expectations based on the properties of the radio source. The discordance suggests that the lobes of the GRG may be overpressured with respect to the environment as also suggested by simulations of RGs (e.g., English et al. 2019).

Polarisation studies of RGs provide valuable information on the topology of the magnetic field and can also be used to probe the environment. The coupling of relativistic electrons and an ordered magnetic field results in a synchrotron radiation that can be polarised up to 70%. However, the observed degree of polarisation could be affected by a stochastic magnetic field as well as by Faraday rotation of the polarised signal produced by thermal plasma within the source or along the line of sight (e.g., Burn 1966; Willis et al. 1974). Stuardi et al. (2020) used a sub-sample of 36 GRGs from Dabhade et al. (2020a) to study the intergalactic magnetic fields around GRGs. They used LOFAR (150 MHz) and NVSS (1400 MHz) observations and detected a larger polarisation fraction in larger GRGs. Furthermore, they infer that the GRGs are normally in a very low-density environment with thermal electron densities $< 10^{-5}$ cm^{-3} and magnetic fields of less than about 0.1 μ G.

The occurrence of GRGs within galaxy clusters challenges the conventional assumption that they exclusively inhabit sparser environments (Dabhade et al. 2020a,b). While the prevailing hypothesis suggests their presence in smaller clusters or groups with lower central gas density (Chen et al. 2011), recent investigations using LOFAR and ASKAP data by Pasini et al. (2022) and Böckmann et al. (2023) found no clear correlation between the linear size of RGs and the central density of galaxy clusters. Nevertheless, variations in density and velocity within the intracluster medium could contribute to the disturbance of plasma injected by jets, leading to the formation of Mpc-sized WAT and NAT RGs with intricate morphologies (Srivastava & Singal 2020; Lusetti et al. 2023). Consequently, the physical mechanisms dictating the shape and extent of diffuse emission in GRGs may differ for those situated in galaxy clusters.

The size of GRGs is likely influenced by factors beyond the environment alone. The kinetic power of the jets may also play a role in determining the final size of RGs, as powerful jets have the potential to create larger sources even in dense environments. There are multiple methods to estimate the radiative and kinetic power of jets and their results can differ by one or two orders of magnitude. The radiative jet power can be estimated by measuring the jet luminosity in the γ-ray band. Besides the γ-ray luminosity, this method requires the knowledge of the Doppler and Lorentz factors. These parameters can be estimated using observations of the motion and flux variations of knots in radio jets (Lister et al. 2016; Jorstad et al. 2017; Lister et al. 2019). Modelling the spectral energy distribution of the AGN makes it possible to obtain the bolometric luminosity of the source which is another proxy of the radio power of the source (Ghisellini et al. 2014). X-ray cavities are thought to provide a convenient measure of the amount of feedback power from the jets delivered to the surrounding hot gas (Bîrzan et al. 2004, 2008). Considering the work done in displacing a volume V of cluster gas and the energy of the material inside the cavity, it is possible to estimate the total cavity energy as $E_{cav} = [\gamma/(\gamma - 1)]PV$. An adiabatic index $\gamma = 4/3$ is often chosen because many cavities are filled with radio-frequency synchrotron emission from relativistic electrons, and there is little or no observable evidence for hot thermal gas inside cavities (Abdulla et al. 2019; Marchegiani 2022). Using this method, Cavagnolo et al. (2010) established a relation between the jet power and the total luminosity of the RG at 150 MHz. Furthermore, the dynamical and radiative modelling of RGs can also provide an accurate estimate of the kinetic energy of jets (e.g., Machalski et al. 2008). Nevertheless, the number of γ-ray detected GRGs is rather low (Bassani et al. 2021) and X-ray observations of the environment of GRGs can be very time-consuming. Schoenmakers et al.

(2000a) determined the jet power by dividing the total energy contents of the lobes by the age of the source. They reported a value of $\approx 10^{44}$ erg s^{-1} for seven GRGs. In the absence of the knowledge of age, internal magnetic field strength and other related parameters, Ursini et al. (2018), Dabhade et al. (2020b), Mahato et al. (2022) used the Cavagnolo et al. relation to estimate the jet power. The values of the jet power lie in the range 10^{41}–10^{45} erg s^{-1}. When compared with the jet powers of a sample of smaller RGs (Mingo et al. 2014), the GRGs are shown to carry less kinetic energy via jets. It should be noted that this method to estimate the jet power is based on the total power of the source at 150 MHz. Hence, if GRGs are evolved RGs that experienced a significant amount of synchrotron and adiabatic losses, they are inevitably less powerful than smaller and younger RGs. Hence, the jet power is likely underestimated for GRGs.

1.3 LOFAR

Several factors make the observation of GRGs at high redshift challenging. Firstly, the density of the IGM increases as $\rho_{IGM} \propto (1 + z)^3$ (Kapahi 1989), which means that, in a picture in which the environment is a contributing factor for the large size of the radio sources, it is less likely finding GRGs at high redshift. Moreover, inverse-Compton losses, due to the interaction of the relativistic electrons with CMB photons, might be a few times larger than synchrotron radiative losses in the time evolution of the lobes of giant radio sources (Machalski et al. 2001; Konar et al. 2004), especially at high redshift since the CMB energy density grows as $(1 + z)^4$. In addition, the surface brightness of a source decreases with redshift as $(1 + z)^{-4}$. In this sense, the LOFAR Two-metre Sky Survey (Shimwell et al. 2019, 2022) represents a unique opportunity to increase the statistics of GRGs at redshift $z > 1$. This survey includes high-band antenna (HBA) observations in the 120-168 MHz band across the northern sky. It provides 150 MHz images with a resolution of 6" and sensitivity of $\approx 100\,\mu$Jy/beam. As part of this survey, dedicated deeper observations have been carried out of the Boötes, the Lockman Hole (Tasse et al. 2021) and the ELAIS-N1 fields (Sabater et al. 2021). The long integration time (> 80 hours) together with the multiple baseline lengths in the array, allows these surveys to probe a combination of depth, area, resolution and sensitivity ($\approx 30\,\mu$Jy/beam) to a wide range of angular scales.

To show the capabilities of LOFAR, I traced the redshift evolution of the flux of GRGs with different radio powers. The dashed lines in Fig. 1.10 are referred to a radio power of 10^{24}, 10^{25}, 10^{26}, 10^{27}, 10^{28} W/Hz respectively from bottom to top. Coloured points represent the fluxes of the GRGs in Dabhade et al. (2020a) sample, while the colour bar shows the radio power. I included the k-correction in the estimation of the flux, using a typical spectral index for a RG of $\alpha = 0.7$. I chose a typical GRG with a longitudinal size of 1 Mpc and a vertical size of 200 kpc and estimated its area assuming an ellipsoidal shape. With such an assumption, I estimated the surface brightness, in mJy/beam, whose evolution with redshift is shown in Fig. 1.10. Different colours are related to different radio powers, while the orange horizontal line highlights the root mean square (rms) noise level of the LOFAR deep fields ($\approx 30\,\mu$Jy/beam in the inner 10 deg^2). The median radio power of Dabhade et al. (2020a) sample is about $10^{26} W/Hz$. Fig. 1.10 shows that sources with such radio power are detectable up to $z \approx 2$ with LOFAR, as well as more powerful radio sources, allowing to build a large sample of high redshift GRGs.
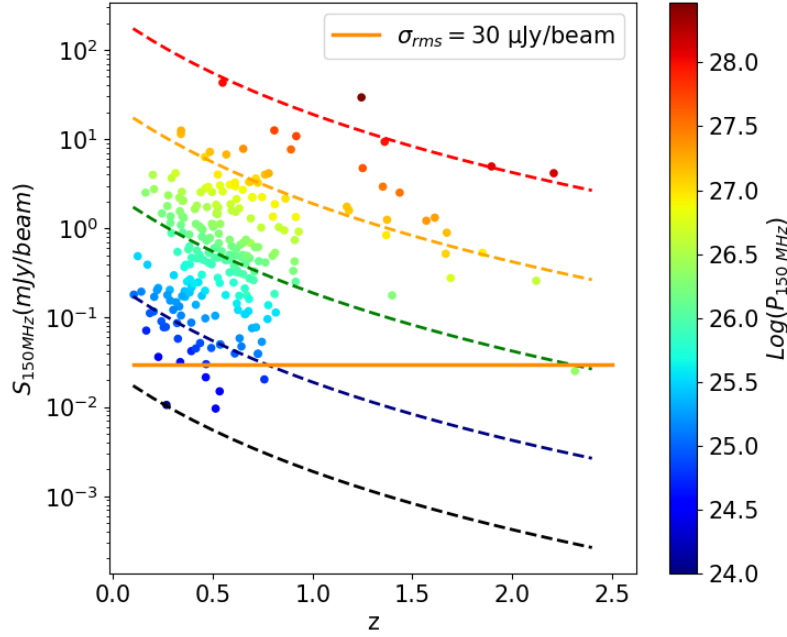
Figure 1.10: Redshift evolution of the flux (in mJy/beam) of a source with different radio powers. The dashed line traced the evolution of sources with a power of $10^{24}, 10^{25}, 10^{26}, 10^{27}, 10^{28}$ W/Hz, from bottom to top. The colorbar highlights the radio power at 150 MHz of the sources from Dabhade et al. (2020a) sample (coloured points). The horizontal orange line represents the rms noise level of the LOFAR deep fields.

1.4 Aims and outline of this thesis

During my doctoral research project, I compiled a catalogue of GRGs in the LOFAR deep fields to understand the physical origin of the radio emission up to Mpc scale of these peculiar sources. A control sample, consisting of smaller RGs, is used to compare the radio, optical and environmental properties of GRGs with those of the control sample. By investigating these factors comprehensively, this project aims to shed light on the intricate interplay between these different aspects, such as the properties of the host galaxy, the surrounding environment, and the age of the radio source, and their collective role in shaping the size of (G)RGs.

The work of my thesis project resulted in the following publications:

Publication I **Simonte, M.**, Andernach, H., Brüggen, M., Miley, G. K., Barthel, P., 2024. *Giant radio galaxies in the LOFAR deep fields.* Submitted to A&A.

Publication II **Simonte, M.**, Andernach, H., Brüggen, M., Best, P. N., Osinga, E., 2023. *Revisiting the alignment of radio galaxies in the ELAIS-N1 field.* A&A 672, A178.

Publication III **Simonte, M.**, Andernach, H., Brüggen, M., Schwarz, D. J., Prandoni, I., Willis A. G., 2022. *Giant radio galaxies in the LOw-Frequency ARray Two-metre Sky Survey Boötes deep field.* MNRAS, 515, 2032.

The content of these publications is presented in the following chapters of this thesis. The order of the chapters does not reflect the chronological order of publication.

To investigate the properties of GRGs, I studied a sample of 74 GRGs in the LOFAR Boötes deep field. Using ancillary multi-wavelength data in this field, I studied the properties of the host galaxies as

well as the environment of the GRGs. Moreover, I determined the flux densities for these GRGs from available survey images at 50 MHz, 150 MHz and 1.4 GHz to investigate the spectral properties of the sources. This work was published in article III (Simonte et al. 2022a) and is presented in Chap. 2. As a result of this work, I also published a catalogue of GRGs in this field. I am the lead author of this work and I was responsible for the manuscript and the scientific analysis. H. Andernach compiled the catalogue of GRGs in the LOFAR Boötes deep field and kindly took care of the preparation of the catalogue. The other co-authors assisted with the preparation of the manuscript and/or acted as scientific consultants.

In publication I (Simonte et al., subm.), I extended my work on the GRGs in the LOFAR Boötes deep field by adding a number of RGs and GRGs I found in the Lockman Hole and ELAIS-N1 deep fields. In this work, presented in Chap. 3, I analysed a sample of 280 GRGs and compared their properties to a control sample of about 1300 RGs I found in the LOFAR deep fields. I am the lead author of this work and I was responsible for the scientific analysis and the manuscript. The other co-authors assisted with the preparation of the manuscript and/or acted as scientific consultants.

The study of the alignment of RGs in the ELAIS-N1 field (Taylor & Jagannathan 2016) is presented in Chap. 4. I compiled a list of RGs and respective position angles and carried out a number of statistical tests to investigate their alignment over multiple scales. I am the lead author of this work and I was responsible for the scientific analysis and the manuscript. H. Andernach helped with the compilation and formatting of the resulting catalogue. The other co-authors assisted with the preparation of the manuscript and/or acted as scientific consultants.

I finally summarize my results and provide an outlook on ongoing and future projects in Chap. 5.

2 Giant radio galaxies in the LOw-Frequency ARray Two-metre Sky Survey Boötes deep field

M. Simonte, H. Andernach, M. Brüggen, D. J. Schwarz, I. Prandoni, A. G. Willis.
MNRAS, 515, 2032 (2022)

Abstract

Giant radio galaxies (GRGs) are radio galaxies that have projected linear extents of more than 700 kpc or 1 Mpc, depending on definition. We have carried out a careful visual inspection in search of GRGs of the Boötes LOFAR Deep Field (BLDF) image at 150 MHz. We identified 74 GRGs with a projected size larger than 0.7 Mpc of which 38 are larger than 1 Mpc. The resulting GRG sky density is about 2.8 (1.43) GRGs per square degree for GRGs with linear size larger than 0.7 (1) Mpc. We studied their radio properties and the accretion state of the host galaxies using deep optical and infrared survey data and determined flux densities for these GRGs from available survey images at both 54 MHz and 1.4 GHz to obtain integrated radio spectral indices. We show the location of the GRGs in the P-D diagram. The accretion mode onto the central black holes of the GRG hosts is radiatively inefficient suggesting that the central engines are not undergoing massive accretion at the time of the emission. Interestingly, 14 out of 35 GRGs for which optical spectra are available show a moderate star formation rate (10-100 $M_\odot$ yr^{-1}). Based on the number density of optical galaxies taken from the DESI DR9 photometric redshift catalogue, we found no significant differences between the environments of GRGs and other radio galaxies, at least for redshift up to $z = 0.7$.

2.1 Introduction

Giant radio galaxies (GRGs) are radio galaxies that have linear extents of more than 700 kpc or 1 Mpc, depending on definition (Willis et al. 1974; Schoenmakers et al. 2000b; Kuźmicz & Jamrozy 2012; Kuźmicz et al. 2018). The total number of GRGs known to date is relatively small, even though over the past 20 years their number has increased substantially (Ishwara-Chandra & Saikia 1999; Schoenmakers et al. 2000b; Lara et al. 2000; Machalski et al. 2001; Saripalli et al. 2005; Machalski et al. 2006; Jamrozy et al. 2008; Kuźmicz & Jamrozy 2012; Dabhade et al. 2017; Kuźmicz et al. 2018; Dabhade et al. 2020b,a,a; Kuźmicz & Jamrozy 2021; Andernach et al. 2021). Their origin and the cause for their huge sizes are still not understood.

26

In particular, it is unclear whether their environments or their host properties are responsible for the large extent of GRGs (e.g, Subrahmanyan et al. 2008; Safouris et al. 2009; Kuźmicz et al. 2019). The environment of GRGs might play a key role, affecting the accretion mode onto the central black hole and suppressing the expansion of the radio lobes in the case the GRG resides in a dense region. This would in turn lead to larger sources in more isolated galaxies (Dabhade et al. 2020b; Andernach et al. 2021). Alternatively, the large size of these galaxies might be the result of a long-term evolution of normal radio galaxies (Kaiser & Alexander 1997).

The advent of large-area radio surveys, such as the Faint Images of the Radio Sky at Twenty-cm (FIRST, Becker et al. 1995), Westerbork Northern Sky Survey (WENSS, Rengelink et al. 1997), NRAO VLA Sky Survey (NVSS, Condon et al. 1998) and the Sydney University Molonglo Sky Survey (SUMSS, Mauch et al. 2003) ushered in a new era during which systematic studies of GRGs were carried out. Early studies (Subrahmanyan et al. 1996; Saripalli et al. 1996; Mack et al. 1998) investigated the radio properties of GRGs (such as the axial ratio) finding similarities with those of smaller radio galaxies, indicative of self-similarity in the evolution of such sources (Kaiser & Alexander 1997). These authors also found that GRGs preferentially reside in low-density environments. Furthermore, Schoenmakers et al. (2000b) and Lara et al. (2000) found their radio spectra to be steep ($0.8 < \alpha < 1.2$) in the lobes of GRGs, corresponding to ages of 10 -100 Myr. More recently, Jamrozy et al. (2008), using data from the Giant Metrewave Radio Telescope (GMRT, Ananthakrishnan 1995), estimated spectral ages in the range 5 - 40 Myr, observing a steeper spectral slope at high luminosities and high redshifts. They also found steeper spectra for larger GRGs. Safouris et al. (2009) and Subrahmanyan et al. (2008) found that asymmetries in the radio morphology of GRGs may be driven by the inhomogeneities of the surrounding medium. In particular, both studies suggest that the jets of GRGs expand into regions that are relatively sparsely populated by galaxies. Machalski et al. (2008) argued that a combination of a low-density environment and jet speeds of about 0.1c - 0.2c has led to the formation of J1420-0545 which is now the second largest GRG known (Oei et al. 2022) with a linear size of 4.69 Mpc.

Subsequent work tried to model the radio data to infer the age, the spectral index and the environment of GRGs (e.g. Machalski et al. 2007b, 2009) confirming a spectral age between 10-100 Myr. In particular, Machalski (2011), using the DYNAGE algorithm (Machalski et al. 2007b), found a relation between the difference in value of the exponent describing the external gas density profile ($\rho_{IGM} \propto r^{-\beta}$) for the opposite lobes and the ratio of their volume, suggesting the non-uniformity of the environment of the GRGs.

More recent work on GRGs boosted the study providing larger samples (Dabhade et al. 2017; Kuźmicz & Jamrozy 2021; Dabhade et al. 2020b; Andernach et al. 2021), but a clear theory of the evolution of such radio sources is still missing. In those studies a few per cent of GRGs were found to reside in galaxy clusters, challenging the idea that they are typically associated with underdense environments. According to these studies, GRGs have radio powers similar to normal (i.e. smaller) radio galaxies, in agreement with the evolutionary theory (Kaiser & Alexander 1997). Altogether these analyses revealed a prevalence of FRII (Fanaroff & Riley 1974) morphology among GRGs, although other morphologies have been detected, such as double-double radio galaxies (DDRGs, Schoenmakers et al. 2000a), Hybrid Morphology Radio Sources (HyMoRS, Gopal-Krishna & Wiita 2002), which are radio galaxies with a FRI type radio lobe on one side of the active nucleus and a FR II type lobe on the opposite side, and Wide Angle Tailed radio galaxies (WAT, Owen & Rudnick 1976).

Infrared and optical surveys can be exploited to identify GRG host galaxies and investigate the galaxy distribution around them (e.g., Lan & Prochaska 2021). Among these surveys are the Panoramic Survey Telescope and Rapid Response System (Pan-STARRS; Flewelling et al. 2020), Sloan Digital Sky Survey (SDSS; York et al. 2000; Stoughton et al. 2002; Alam et al. 2015), Dark

Energy Spectroscopic Instrument survey (DESI; Dey et al. 2019; Zhou et al. 2021) and the Wide-field Infrared survey Explorer (WISE; Cutri et al. 2013; Marocco et al. 2021). A large amount of data have been used to infer information on the optical counterpart and the distribution of galaxies around GRGs (e.g., Lan & Prochaska 2021). For instance, the SAGAN project (see Dabhade et al. 2020a, for details) aims to create a catalogue of all GRGs published to date including the properties of the host galaxies.

There is ample theoretical work on the evolution of radio galaxies (e.g. Burns et al. 1991; Kaiser & Alexander 1997; Machalski et al. 2021). Recent and refined studies investigated the propagation of powerful jets and the impact with the surrounding environment (interstellar or intergalactic medium) at distances of tens to hundreds of kiloparsecs (Mignone et al. 2010; English et al. 2016; Hardcastle 2018; Perucho et al. 2021; Yates-Jones et al. 2022). However, the computational limitations make the study of the long-term simulations with an adequate resolution challenging.

The LOw-Frequency ARray (LOFAR Van Haarlem et al. 2013) with its relatively high resolution and sensitivity to very low surface brightness sources heralds a new era in the study of very large and high redshift radio galaxies. In this paper we searched for GRGs in the Boötes LOFAR Deep Field (BLDF) image at 150 MHz (Tasse et al. 2021; Kondapally et al. 2021). The resulting sample contains 74, mostly newly detected, GRGs. By cross-matching with other radio data, we obtained the radio spectral information and by cross-matching with optical and infrared data, we inferred the properties of the host galaxies as well as environments of the GRGs.

The outline of this paper is as follows: we describe the analysis of the radio data, as well as the infrared data in Sec. 2.2. In Sec. 2.3 we present the results of our analysis and compare them to previous work. Finally, we draw our conclusions in Sec. 2.4. Throughout this work we adopt a flat ΛCDM cosmology with $H_0 = 70$ km s^{-1} Mpc^{-1}, $\Omega_m = 0.3$, $\Omega_\Lambda = 0.7$ and a radio source spectral index α defined as $S_\nu \propto \nu^{-\alpha}$.

2.2 Observations and multi-frequency data

The LOFAR Two-metre Sky Survey (LoTSS; Shimwell et al. 2019, 2022,) is performed using high-band antenna (HBA) observations of the northern sky in the 120-168 MHz band and images at both 20" and 6" resolution are available. The sensitivity of the latter image is about $1\sigma = 80 \mu$Jy beam^{-1}. LoTSS provides the astrometric precision that is required for multi-wavelength cross-matching. As part of this survey, dedicated deeper observations have been carried out of the Boötes, the Lockman Hole (Tasse et al. 2021) and the ELAIS-N1 fields (Sabater et al. 2021). The long integration time (> 80 hours) combined with a sensitivity to a wide range of angular scales, makes these deep fields ideal for a search for the faintest and most distant GRGs. We have carried out a systematic search of GRGs in the Boötes LOFAR Deep Field (centered on 14h32m03.0s +34°16′33″ J2000) which covers an area of 26.5 deg^2 and with a noise level of ~30 μJy beam^{-1} in the inner 3 deg^2. A dedicated search for GRGs in the other deep fields will be part of a future study.

The inspection of LOFAR images was carried out by eye. The largest angular size (*LAS*) in arcmin, was measured on the full resolution 6" image. Kuźmicz & Jamrozy (2021) showed that an estimate based on 3-σ contours would make the source appear larger by at least one beam size for sources of FR-II type with bright compact hotspots at the outer edges of their lobes. Therefore, while for FRI we used the 3-σ contours to measure the *LAS*, for FRII type GRGs we measured the distance between the two opposite hotspots, identified on VLA Sky Survey images (VLASS, Lacy et al. 2020) if available. On the other hand, we believe that an angular size measurement based on the 3-σ contours underestimates the real size of those sources of FR I type, or those which have no

clear terminal hotspots in their lobes, some of which clearly extend beyond the 3-σ contour. For this reason, for the faintest GRGs we measure the angular size in a straight line from one end of the source to the opposite one, carefully avoiding to push our measurement in regions where the radio emission of the sources is not very clear. The same method has been used to measure the angular size of bent sources; any measure different from this would imply assumptions on the 3D structure of the source which we can only guess. We found 74 GRGs with a linear extent larger than 0.7 Mpc (which we refer to as the "Boötes LOFAR Deep Field" or BLDF-GRG sample). The only GRG reported in a GRG catalogue is J1427+3625 in Kuźmicz & Jamrozy (2021), while J1430+3519 was studied in the radio and X-ray band by Masini et al. (2021). 16 GRGs were listed in other catalogues of radio galaxies but they were published without their linear size (Williams et al. 2013; van Weeren et al. 2014; Coppejans et al. 2015; Williams et al. 2016; Mingo et al. 2022). Among our sample, 38 GRGs have a linear extent larger than 1 Mpc. The resulting sky density is about 2.8 GRGs deg^{-2} for GRGs with linear size larger than 0.7 Mpc and 1.43 deg^{-2} for those larger than 1 Mpc. This result is in agreement with recent work by Delhaize et al. (2021), who found two GRGs in the 1 square degree COSMOS field, and higher than in Brüggen et al. (2021) who found a sky density of radio galaxies with largest linear size > 0.7 Mpc of 1.7 deg^{-2} in ASKAP observation of the Abell 3395-Abell 3391. This field has similar noise level, but lower angular resolution (10") than the BLDF.

The host galaxies were identified using optical and infrared surveys: SDSS (York et al. 2000), WISE (Wright et al. 2010) and its multiple catalogues such as AllWISE (Cutri et al. 2013), unWISE (Schlafly et al. 2019) and CatWISE (Marocco et al. 2021), DESI (Dey et al. 2019; Zhou et al. 2021) and Pan-STARRS (Beck et al. 2021). Once the host galaxy has been identified we looked for available redshifts (either spectroscopic or photometric) in multiple catalogues such as El Bouchefry (2009), Chung et al. (2014), Brescia et al. (2014), Luo et al. (2015), Bilicki et al. (2016), Zou et al. (2019), Duncan et al. (2021). If various redshifts were available for a single source we computed their mean. For spectroscopic redshifts we do not report errors since they are generally more accurate (typical errors are usually around 0.00015) than the precision we can achieve on the linear sizes and luminosities given our errors in measuring angular size and total flux. The identification of the host galaxy in widely separated radio components without an obvious core emission between them is challenging. We first checked whether any of the outer components have a convincing host by itself. In such cases, they were recorded as separate extended radio galaxies. If a convincing optical galaxy between the external radio components is detected in neither optical nor infrared surveys, we discarded the source as genuine GRG. On the other hand, we take the presence of a host galaxy with AGN colour (e.g., Mateos et al. 2012; Assef et al. 2013) near the geometrical centre of the radio galaxy as a strong sign of the genuineness of the GRG, even if that host does not show a radio core. Furthermore, the presence of a radio bridge or radio emission elongated along the suspected radio axis sometimes indicates the structures to be connected. In case of uncertainties about the likely host we chose the brighter or lower redshift host. In such sources, the largest linear size (*LLS*) derived from the *LAS* and redshift should serve as a lower limit. Three GRGs, namely J1421+3521, J1423+3340 and J1434+3214C, do not have a redshift estimate in any of the mentioned catalogues and they are not detected in DESI DR9. The photometric redshift provided by the DESI DR9 photometric redshift catalogue (accessible via the NOIRlab portal[1]) for the faintest objects is around 1.3. For this reason, we assumed that the GRG hosts are located at redshift z=1.1-1.5. However, the exact value of the redshift is quite irrelevant for converting *LAS* to *LLS* since the *LAS-z* curve is practically flat in the relevant redshift range (see the *LAS-z* diagram in sect. 3.2), so it does not affect the *LLS* significantly.

We used the full resolution 6" images to measure the total radio flux at 150 MHz. We prepared

---

[1]https://astroarchive.noirlab.edu/portal/search/

cutouts of 0.5 degrees on a side, centered on the GRG host and integrated the flux of GRGs taking into account only those pixels whose intensity is larger than $3\sigma_{\rm rms}$, where $\sigma_{\rm rms}$ is the noise level in the source neighbourhood. This noise level varies with the distance from the centre of the BLDF image, but it is rather constant within each cutout. The flux error was calculated as $\sqrt{\sigma_{\rm rms}^2 + \sigma_{\rm cal}^2}$, where $\sigma_{\rm cal}$ is the uncertainty on the calibration of the flux scale which is assumed to be 10% of the total flux (Sabater et al. 2021). We measured the noise of the cutout, $\sigma_{\rm rms}$, via an iterative method. For each iteration, we calculated the rms, we removed those pixels with an intensity larger than 5 times the rms and, consequently, we re-measured the rms. The convergency criterion is dictated by the difference between two consecutive rms measurement; the threshold was set equal to 1%. Thus, we multiply the noise measurement by the square root of the area of flux integration, measured in units of beam areas. We noticed that a 3-σ clipping applied to the faintest GRGs clearly underestimates the total flux of the source as some genuine emission coming from the bridge is not included. Thus, we integrated the flux of such sources, marked by an asterisk appended to the flux measure in Table A1, considering all the pixels belonging to the region of the radio emission. Radio powers at 150 MHz for GRGs were calculated following Donoso et al. (2009):

$$P_{150} = 4\pi D_L^2 S_{150}(1 + z)^{\alpha-1}, \tag{2.1}$$

where D_L is the luminosity distance, S_{150} is the measured radio flux density at 150 MHz, $(1 + z)^{\alpha-1}$ is the standard k-correction used in radio astronomy and α is the radio spectral index for which we adopted a typical value of 0.7. The median radio power is $P_{\rm med} = 6.61 \times 10^{25}$ W Hz^{-1} and the GRGs span a wide range of redshift, up to $z \sim 2.8$, with a median redshift of $z_{\rm med} = 0.80$. Kuźmicz et al. (2018) list 10 GRGs with $10^{23} < P_{1400} < 10^{24}$ at low redshift, while Dabhade et al. (2017) and Dabhade et al. (2020b) found GRGs down to Log(P_{150}) $\sim$ 24. The median r-band magnitude of the host galaxies in our BLDF-GRG sample is 21.68, compared to 20.7 for the 181 GRGs that Andernach et al. (2021) found by inspecting the 888-MHz Rapid ASKAP Continuum Survey (RACS, McConnell et al. 2020), showing the Boötes LOFAR deep field to allow finding fainter and more distant radio galaxies. A quantitative comparison with some of the most recent and largest samples of GRGs is shown in Table 2.1. The columns are: (1) reference and survey used, (2) the observing frequency, (3) number of GRGs in the sample, (4) minimum and median flux of the sample at the observing frequency, (5) minimum and median decimal logarithm of the power of the sample at 150 MHz calculated assuming a spectral index α=0.7, (6) median of the redshift of the host galaxies. It is worthwhile to notice that the median flux of the BLDF-GRGs is the lowest among the reported samples, while the median redshift is the second largest, only slightly surpassed by Kuźmicz & Jamrozy (2021) who carried out a dedicated search for extended radio galaxies with *LLS*>1 Mpc from spectroscopic QSOs from SDSS DR14Q.

The list of our sources is provided in Table A1. A "C" appended to the GRG name indicates that it is a candidate, meaning that either the host itself, or its redshift, or its *LAS* are uncertain. Fig. A1 shows the cutouts of the BLDF image around the GRGs. The size of these cutouts is proportional to the *LAS* of the GRG and it is smaller than the size of the cutouts used for the flux integration. The cyan circle identifies the position of the galaxy host. Notes on individual GRGs are reported in the appendix.

(1)	(2)	(3)	(4)	(5)	(6)
Survey,Reference	Freq.	N of	$S_{min,med}$	$P^{150}_{min,med}$	z_{med}
	GHz	GRGs	mJy	W/Hz	
Literature[1]	0.8/1.4	349	5.20,164	23.7,26.2	0.24
NVSS[2]	1.4	25	28.0,95.0	24.7, 25.8	0.22
LOTSS[3]	0.15	239	2.00,218	24.0,26.1	0.53
NVSS[4]	1.4	161	3.00,209	24.4,25.3	0.23
NVSS,SDSS[5]	1.4	76	—,—	26.0,26.7	0.82
RACS[6]	0.888	181	5.00, 40.0	24.0,26.4	0.66
BLDF,this work	0.15	74	3.6, 29.2	24.5,25.8	0.80

Table 2.1: Comparison between our BLDF-GRG and previous samples. References: 1-Kuźmicz et al. (2018), 2-Dabhade et al. (2017), 3-Dabhade et al. (2020b), 4-Dabhade et al. (2020a), 5-Kuźmicz & Jamrozy (2021), 6-Andernach et al. (2021). References 5 and 6 are compilations of GRGs with *LLS* larger than 1 Mpc, while all the others include GRGs with *LLS* > 0.7 Mpc.

2.2.1 LoLSS and NVSS data

Data from radio surveys carried out at different frequencies allow an analysis of the spectra of the radio sources. However, the low surface brightness of GRGs makes their detection challenging, especially at higher frequencies. The only deep observation in the Boötes field at higher frequencies is presented in de Vries et al. (2002) although the image is not available. Moreover, the APERture Tile In Focus (Apertif) survey (van Cappellen et al. 2022) is not as complete as NVSS in this region. For this reason, we looked for the BLDF-GRGs in the NVSS (Condon et al. 1998) which covers the sky north of -40 deg declination at 1.4 GHz. The NVSS has an angular resolution of 45" and is very sensitive to sources with low surface brightness. The rms noise level is 0.45 mJy beam^{-1} (Stokes I). Finally, the LOFAR LBA Sky Survey (LoLLS, de Gasperin et al. 2021) covers the very low-frequency (< 100 MHz) regime. The LoLLS Boötes deep field was observed with the Low Band Antennas (LBA) at 34-75 MHz for 56 hours (Williams et al. 2021). The integration time makes this observation the first sub-mJy survey below 100 MHz, with an rms noise of 0.7 mJy beam^{-1}. The resulting image has an angular resolution of 15".

2.2.2 Infrared data

We cross-matched the GRG hosts with infrared data from the WISE survey in order to determine the accretion mode of the central engine. The Wide-field Infrared Survey (Wright et al. 2010) is an all-sky survey conducted in four spectral bands: W1 (3.4μm), W2 (4.2μm), W3(12μm), W4 (22μm) with angular resolution 6.1, 6.4, 6.5, 12", respectively. AllWISE (Cutri et al. 2013) is the resulting catalogue of the combination of WISE and NEOWISE (Mainzer et al. 2011) surveys. The AllWISE source catalogue contains accurate positions, proper motion measurements, four-band fluxes and flux variability statistics.The CatWISE2020 (CWISE) catalogue contains objects selected from WISE and NEOWISE survey data at 3.4 and 4.6 μm (W1 and W2) and it is the most extensive dataset of the full mid-infrared sky. We found that the CatWISE catalogue often (in about 25% of cases) provides multiple matches for a single position with a distance between the matches less than the angular resolution of the telescope. Moreover, often the source with the brighter magnitude appears with lower S/N ratio, opposite to expectation. Furthermore, the catalogue does not have data at 12 and 22 μm that are used in the WISE color-color diagram. Comparing the AllWISE and CatWISE magnitudes,
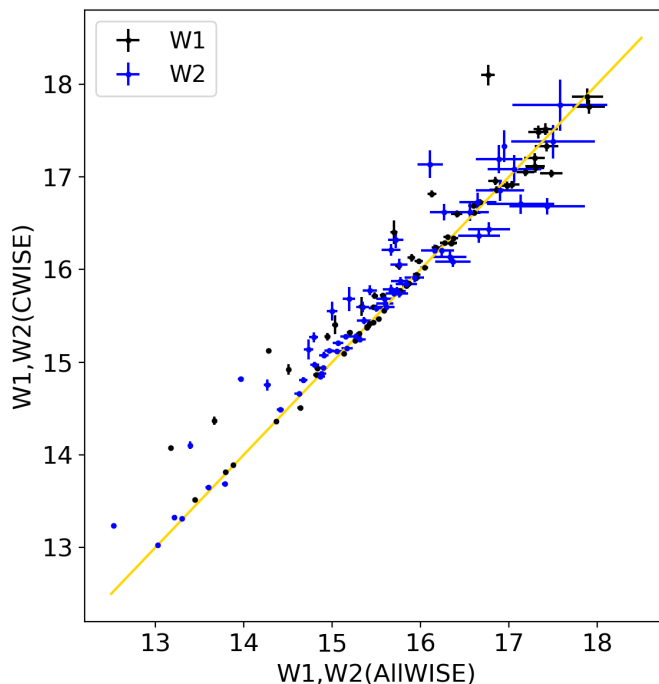
Figure 2.1: Comparison between the magnitudes in the W1 (black) and W2 (blue) bands in the AllWISE and CWISE catalogue. The yellow line marks the one-to-one relation.

we found that the W1 and W2 magnitudes in both catalogues are consistent with each other (see Fig. 2.1). We decided to use the AllWISE data for our infrared analysis. The CWISE catalogue contains fainter sources than AllWISE and eight of the GRG hosts are only detected in CWISE. Hence, we did not consider these for the infrared analysis. We noticed that two types of magnitudes are listed, namely "Wipro" and "Wimag", where i=1,2,3,4 refers to the WISE band. The former is the magnitude measured with profile-fitting photometry, while the latter is the magnitude measured in an 8.25" radius circular aperture centered on the source position (see Cutri et al. 2013, for more details) [2]. The NASA/IPAC Infrared Science Archive [3] provides the WISE magnitudes "Wipro" and the associated errors in the four bands.

2.3 Results

2.3.1 Distribution of the largest linear sizes

The distribution of the *LLS* of the (giant) radio galaxies can give clues as to whether GRGs are just extreme cases of the general population of radio galaxies (RGs), or constitute an independent class of sources.

There are several distributions that describe either the extreme values of another underlying distribution, such as the distribution of the largest size for a given sample of RGs, or distributions for random objects above a given threshold, such as the exponential, or the Pareto distribution (see e.g. Coles 2001, for more details). GRGs are part of the latter type of distributions as they are RGs whose

---

[2]https://wise2.ipac.caltech.edu/docs/release/allwise/expsup/sec2_1a.html
[3]https://wise2.ipac.caltech.edu/docs/release/allsky/

size exceeds 0.7 Mpc. As a consequence, we restrict our analysis to exponential (as a special case) and generalised Pareto (Coles 2001) distributions. The latter is commonly used to estimate the probability of exceedances over a high threshold (see Zaninetti & Ferraro 2008; Bouillot et al. 2015; Aschwanden 2015, for applications). The generalised version of such a distribution is:

$$f_P(x) = \frac{1}{\sigma} \left(1 + c\frac{x - \mu}{\sigma} \right)^{-1-\frac{1}{c}} , \qquad (2.2)$$

where c is the shape parameter. For $c > 0$ the support of the distribution is $x \geq \mu$, while for $c < 0$ it is limited to $\mu \leq x \leq \mu - \sigma/c$. The exponential distribution is a special case of the generalised Pareto distribution obtained by taking the limit $c \to 0$:

$$f_E(x) = \frac{1}{\sigma} e^{-\frac{x-\mu}{\sigma}}, \quad x \geq \mu. \qquad (2.3)$$

In Eqs. (2.2) and (2.3), μ and $\sigma > 0$ are the location (the threshold value) and scale parameters, respectively.

Recently, Oei et al. (in prep.) carried out a detailed analysis of the distribution of the *LLS* using about 500 GRGs. Assuming a Pareto distribution, the authors found a slope of -4, thus $c = 1/3$ (see Eq. 2.2). These authors mostly focused on local GRGs ($z < 0.2$) with an angular size larger than $5'$, while Andernach et al. (2021) observed a similar slope in the cumulative size distribution of a compilation of GRGs found by visual inspection of sources in the RACS survey (McConnell et al. 2020) complete down to an angular size of $\sim 2'$ and independent of redshift, which resulted in 178 new GRGs larger than 1 Mpc.

In this work, we carried out a simple statistical analysis on the *LLS* distribution of our GRGs, using the complete sample of extended RGs provided by Miraghaei & Best (2017) (MB17 hereafter). This sample provides measurements of the largest linear sizes for 1329 extended RGs (we revised the measurement of the *LAS* at 1.4 GHz of some sources and consequently re-calculated the linear size by using the listed redshifts) with hosts selected from SDSS. The flux density threshold of this sample is 40 mJy, which corresponds to roughly 200 mJy at LoTSS frequencies for $\alpha = 0.7$. The catalogue shows a lack of RGs with linear extents smaller than 50 kpc and complete catalogues for the smallest RGs are missing in literature (Capetti et al. 2017, 2020). For this reason, we did not include the RGs with *LLS* < 50 kpc in our analysis.

We used maximum likelihood estimation to fit the two distributions to the *LLS* of our GRGs and the RGs listed in MB17. The parameters of the fit are the location and scale parameters; the shape parameter, c, is considered only in the generalised Pareto distributions. In this analysis, the location parameter is the minimum size of the RGs of the two samples (50 kpc and 700 kpc for the MB17 and BLDF sample respectively). Thus, we performed a Kolmogorov-Smirnov (KS) test between our samples and randomly generated data coming from the resulting best-fit distributions for 1000 times, averaging the p-values obtained from each iteration. Such a test is commonly used to decide whether two samples derive from the same population; the closer the p-value is to 0 the more confident we are in rejecting that the samples were drawn from the exponential or Pareto distribution. The results are summarised in Table 2.2 and we show the fit in Fig. 2.2. The location and scale parameters are given in units of Mpc .

For the MB17 sample we found $c = 0.02 \pm 0.01$ when fitting the generalized Pareto distribution, which indicates that the distribution of the *LLS* is very close to exponential. The p-value resulting from the KS test between the MB17 sample and the exponential distribution is 0.52, confirming that the exponential distribution provides an acceptable description of the data. Similarly, both distributions are reasonable fits to the sample of the *LLS* of the GRGs. The rather small value of the shape

	MB17 sample	BLDF-GRG sample
Pareto	$c = 0.02 \pm 0.01$,scale= 0.14 ± 0.01	$c = 0.22 \pm 0.12$,scale= 0.52 ± 0.03
	$p = 0.47$	$p = 0.94$
Exponential	scale $= 0.14 \pm 0.01$	scale $= 0.52 \pm 0.02$
	$p = 0.52$	$p = 0.70$

Table 2.2: Results of the fit to the linear size distribution of the RGs provided from Miraghaei & Best (2017) and the BLDF-GRG sample. According to the p-value obtained by a KS-test, we cannot reject the hypothesis that exponential and Pareto distributions fit the *LLS* distribution of both RGs and GRGs.

parameter, $c = 0.22 \pm 0.12$, suggests that also the *LLS* of the GRGs follows a fairly steep Pareto distribution. It is also consistent with an exponential distribution with the same scale parameter.

However, the scale parameters of the RG and GRG samples are different. The scale parameter of the MB17 sample, which is 140 kpc, is well above the cutoff suggesting that the typical size of the extended RGs is larger than 50 kpc. On the other hand, the scale for GRGs is 0.52 Mpc which is below the cutoff, showing that GRGs are indeed larger than the intrinsic scale of the distribution. These results indicate that, even though we are not probing the same distribution for both RGs and GRGs, an exponential distribution reasonably describes the general features of both samples. The analysis also has some limitations. First of all, the two samples are selected at two different frequencies; in particular at 1.4 GHz the emission of cores is often more prominent and lobes are usually more difficult to observe. Moreover, MB17 selected only sources with a flux density larger than 40 mJy at 1.4 GHz (~ 200 mJy at 150 MHz for $\alpha = 0.7$), while there are only 9 GRGs with a correspondingly larger flux density in the BLDF sample. Furthermore, the BLDF sample is not complete in the range 0.7 Mpc $< LLS <$ 1 Mpc. These limitations might explain the difference of the inferred typical scales of the two samples.

2.3.2 Redshift evolution and P-D diagram

We show the *LAS-z* diagram for our BLDF-GRG sample in Fig. 2.3, along with some reference lines that represent the angular size of the "standard rulers" of four different sizes as function of redshift. On the upper and right sides of Fig. 2.3 we show the distributions of redshifts and *LAS*, respectively. The red histogram in the upper panel shows the distribution of the spectroscopic redshifts. It is worth emphasising that the minimum required angular size of RGs to be labeled as giant with $LLS > 0.7$ Mpc is 1.3′ and 2.0′ with $LLS > 1$ Mpc, and these minima occur near redshifts ~1.7

In Fig. 2.4 we show the radio powers of BLDF-GRGs as a function of redshift. The solid red line shows the evolution of the power of a GRG with a surface brightness equal to 30 μJy beam^{-1} which is the noise level of the BLDF in the inner 3 deg^2. We approximated the shape of GRGs by ellipses with a major and minor axis of 0.7 and 0.2 Mpc, respectively. The dashed blue line is the power of a point source with a brightness of 30 μJy beam^{-1} as function of redshift. These two lines correspond to the flux-limit of the Boötes LOFAR survey and they provide a lower limit for the observed radio power. This result suggests that the clear trend we observe, with more powerful RGs at high redshifts, is likely due to a combination of the Malmquist bias and the surface brightness dimming proportional to $(1 + z)^{-4}$ which is certainly important for extended or diffuse sources. Furthermore, inverse-Compton losses, due to interaction of the relativistic electrons with CMB photons will be larger than synchrotron radiative losses in the evolution of the lobes of giant radio sources (Machalski et al. 2001; Konar et al. 2004). Inverse-Compton losses are proportional to the initial energy of the CMB photon, leading to
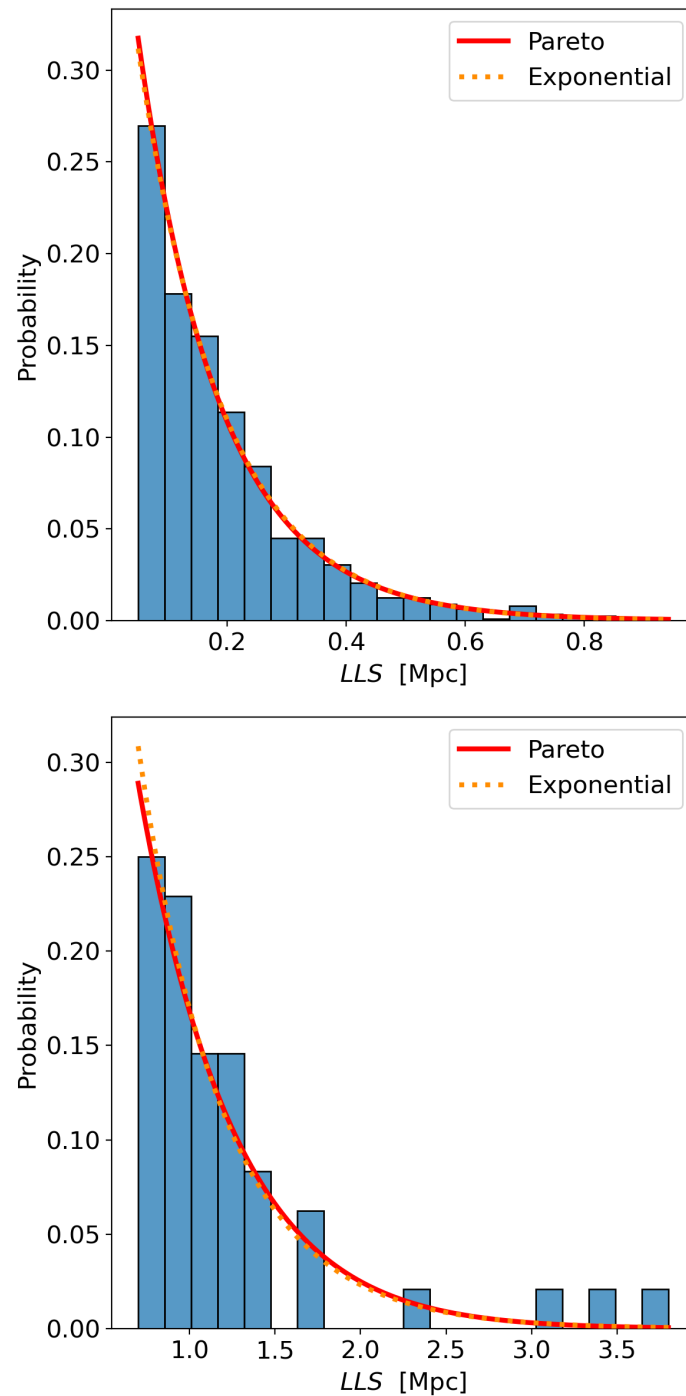
Figure 2.2: Top panel: Distribution of the largest linear sizes of a sample of RGs provided by Miraghaei & Best (2017). Lower panel: Distribution of the largest linear sizes in the BLDF-GRG sample. The solid red and dotted orange lines are the best fit of the Pareto and exponential distribution respectively. The *y*-axis represents the probability that a (G)RG has a certain *LLS*.
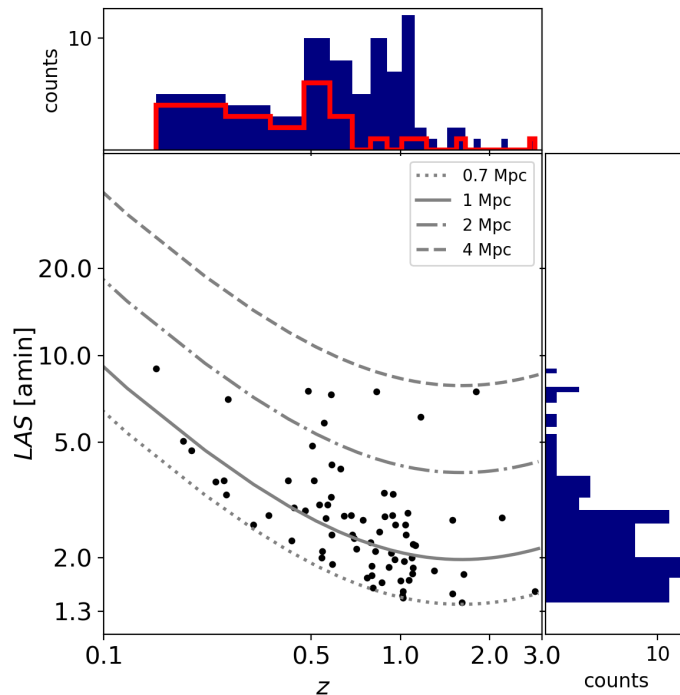
Figure 2.3: The *LAS-z* diagram in the BLDF-GRG sample along with some reference lines of four "standard rulers", whose sizes are listed in the upper-right legend. Their distributions in redshift (upper panel) and *LAS* (right panel) are also shown. The red histogram shows the spectroscopic redshifts.

larger energy losses at high redshift due to the increasing CMB energy density which is proportional to $(1 + z)^4$. Note also that in Fig. 2.4 there may be an artificial clustering at z≈1 due to photometric redshift values in DESI DR9 rarely exceeding $z \approx 1.1$.

The P-D diagram shows the relation between the radio power at a specific frequency and the linear size (Baldwin 1982). With such a diagram it is possible to trace the evolution of RGs (Ishwara-Chandra & Saikia 1999; Machalski et al. 2004). The P-D diagram of our BLDF-GRG sample along with GRGs from recent samples (Dabhade et al. 2017, 2020b,a; Kuźmicz & Jamrozy 2021; Andernach et al. 2021) is shown in Fig. 2.5. We used a standard spectral index, $\alpha = 0.7$, to compute the power at 150 MHz for those sources with a flux estimated at other frequencies. As found before (e.g., Ishwara-Chandra & Saikia 1999; Kuźmicz & Jamrozy 2012; Dabhade et al. 2020b; Kuźmicz & Jamrozy 2021), the larger RGs are less powerful. A deficit of GRGs is clearly visible in the upper-right corner, where powerful and large RGs should reside, suggesting that the luminosity of RGs decreases as they evolve to giant radio sources which is likely the latest stage of the evolution according to models (e.g., Kaiser & Alexander 1997). The electron energy losses due to adiabatic expansion and radiation over the lifetime of the lobes could cause such a deficit. Fig. 2.5 also shows a lack of GRGs with large linear sizes and small radio powers. This result might suggest that RGs have to be powerful enough in order to reach the largest sizes. However, the most extended RGs have a rather low surface brightness, thus their detection becomes more difficult with increasing size. As a matter of fact, we have been starting to observe large (> 1 Mpc) and faint ($\sim 10^{24}$W Hz^{-1}) GRGs only with the most recent observations with LOFAR and ASKAP (Andernach et al. 2021).
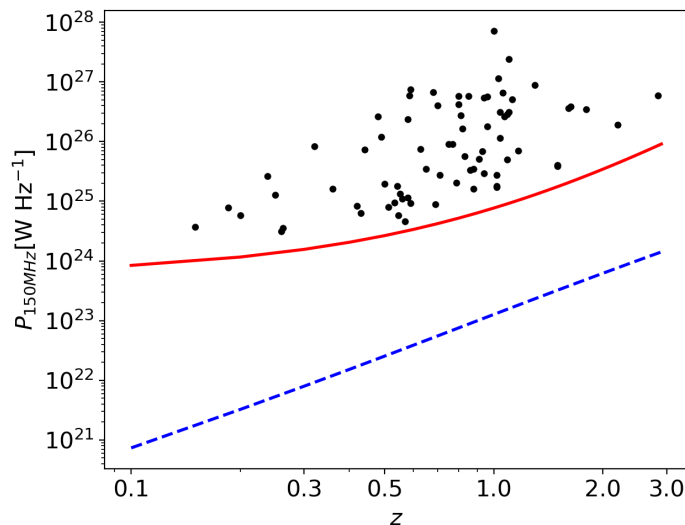
Figure 2.4: The relation between the radio power at 150 MHz, P_{150}, and the redshift, z, in the BLDF-GRG sample. The solid red line shows the power of a GRG with a surface brightness equal to the noise level of the BLDF and spectral index over its respective area of emission, at various redshifts. The dashed blue line traces the redshift evolution of the power of a point source with a flux density equal to 30 μJy beam^{-1}.

2.3.3 Spectral indices

Radiative ageing affects the radio spectra since more energetic electrons suffer higher energy losses and, consequently, have shorter lifetimes. This induces a steepening of the spectra at high frequencies ($\gtrsim$ GHz) and the spectral index can give an estimate of the age of a radio source. In order to compute the integrated spectral index (i.e., estimated from the total flux of the source) we performed the following steps: First, we convolved the higher-resolution images (LoLLS and LBDF) to the (lower) resolution of 45" of NVSS and regridded the images to a size of 0.2° centered on the sky coordinates of the source. This step is necessary because the measured flux can change with the resolution of the image. We performed sigma-clipping at a level of $3\sigma_{\rm rms}$, where $\sigma_{\rm rms}$ is the rms noise of the individual convolved image, and integrated the flux of the sources. If the source is undetected in the NVSS, we considered an upper limit for the flux of such source equal to $3\sigma_{\rm rms}$. For sources that are detected neither in NVSS nor in LoLSS we did not estimate the spectral index. We also excluded those GRGs that were blended with other sources after convolution. Once the fluxes at different frequencies are calculated, we performed a linear regression to calculate the spectral indices. In order to compute a more robust error, we carried out a simple bootstrapping to determine the errors in the fit parameters. This routine generates Gaussian-distributed random fluxes whose mean is equal to the initially estimated flux and a standard deviation that is determined from the error of this flux. Then, a fit is performed for each dataset and the final variance of the multiple fits is used as the error of the spectral index.

In Fig. 2.6 we show the relation between the spectral index and the linear size in our BLDF-GRG sample. We find spectral indices around 0.8 and no substantial spectral steepening with increasing *LLS*, mainly because the integrated flux is dominated by the regions with recently injected or re-accelerated particles (the core and hotspots). Moreover, Fig. 2.7 does not suggest a relation between the spectral index and the redshift. On the other hand, Dabhade et al. (2020a) recently found a weak correlation between the spectral index and linear size and the redshift in a larger sample of GRGs, in agreement with Blundell et al. (1999) and Jamrozy et al. (2008). Large and complete samples are
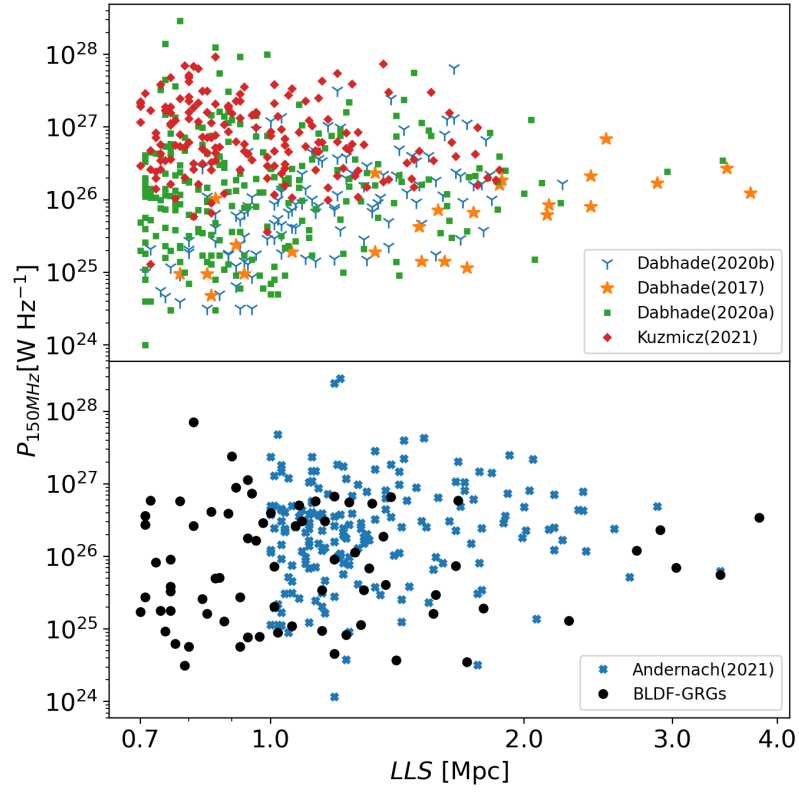
Figure 2.5: P-D diagram that shows the specific power at 1500 MHz versus the *LLS* of the BLDF-GRGs. Other GRG samples are included for comparison, such as Dabhade et al. (2017), Dabhade et al. (2020b), Kuźmicz & Jamrozy (2021), Dabhade et al. (2020a) and Andernach et al. (2021). The high sensitivity of the observations in this field enables us to detect several new GRGs at lower power ($\sim 10^{24}$W Hz^{-1}).
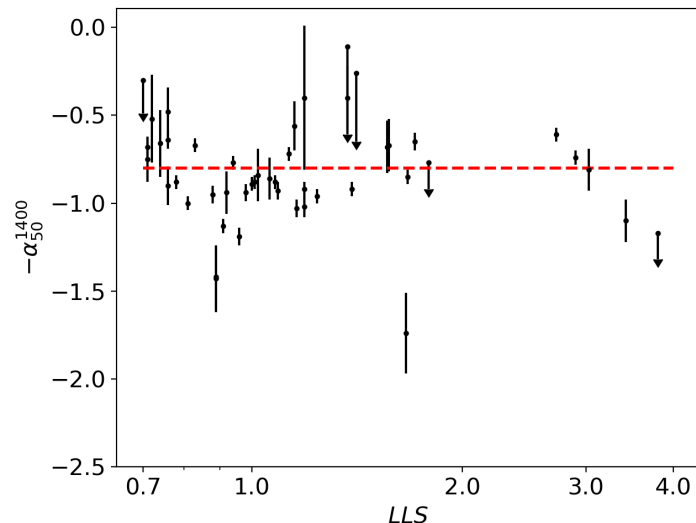
Figure 2.6: Spectral index in the range 50-1400 MHz for the BLDF-GRG sample against the linear size. The typical slope of radio spectra in such RGs is about -0.8, which is denoted by the red line. GRGs do not show a substantial steepening at the largest linear extent, mainly because we detect the regions with recently injected or re-accelerated particles (e.g., hotspots).

needed to establish whether GRGs exhibit a correlation between these properties, as well as high-resolution spectral index maps to trace a possible steepening of the spectra along the lobes. We also discuss the contribution of the core to the total flux at 150 MHz, that is the core fraction, f_c, defined as the ratio between the flux of the core and the total flux. The emission of the core of the RGs is dominated by the recent ejecta launched by the central black hole and it usually has a flatter ($\alpha < 0.5$) or inverted spectral index ($\alpha < 0$) (Konar et al. 2004, 2008). This would in turn flatten the integrated spectral index calculated from the total flux of the radio source. Thus, we calculated the flux of the core of GRGs in the BLDF image. In case of absence of core emission or indistinguishable core, we did not calculate the flux. Fig. 2.8 shows the integrated spectral index against the core fraction. For better visualisation, all spectral indices are treated as absolute measurements with a relative error, irrespective of whether they are upper limits or not. An expected trend of the spectra becoming flatter for larger values of f_c can be seen and for $f_c \approx 0.2$ the spectral index is about 0.5. This indicates a flattening of the integrated spectral index induced by the relatively large contribution of the emission of the core of some GRGs. Such a core fraction suggests that most GRGs are not entirely passive and might be in a phase of restarted activity.

2.3.4 HERG and LERG dichotomy

Based on their optical spectra, AGN can be classified as High-Excitation Radio Galaxies (HERG) and Low-Excitation Radio Galaxies (LERG). The former have an accretion rate onto the black hole between one and ten per cent of the Eddington ratio. They are hosted by bluer, star-forming galaxies and lower-mass black holes. In contrast, LERGs are likely hosted by high-mass galaxies with a central black hole that experiences accretion below one percent of the Eddington limit (Best & Heckman 2012).

The host galaxies in our BLDF-GRG sample are usually too faint to allow a SED fitting and provide a classification based on the optical spectra. Nevertheless, mid-IR data can be used to classify
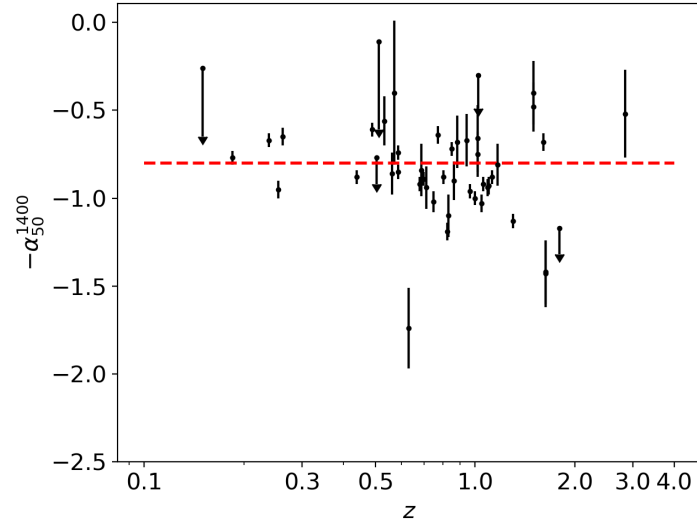
Figure 2.7: Spectral index in the range 50-1400 MHz for the BLDF-GRG sample against the redshift of the host galaxies. The spectral index does not show a clear trend with redshift.
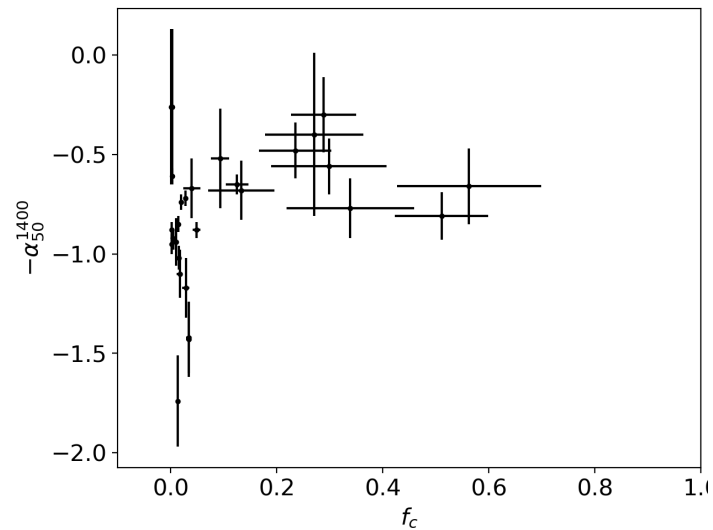
Figure 2.8: Spectral index in the range 50-1400 MHz for the BLDF-GRG sample against the core fraction f_c. Due to the increasing contribution of the core to the total emission, the radio spectra flatten in the range $0 < f_c < 0.2$, while the spectral index is constant for larger values of the core fraction.

AGN (Assef et al. 2010; Jarrett et al. 2011; Stern et al. 2012; Mateos et al. 2012; Assef et al. 2013). Gürkan et al. (2014) have shown that HERGs and LERGs have different mid-IR luminosities. The former are mostly luminous sources in the infrared band and an empirical cutoff can be drawn in the 22μm - 151 MHz luminosity plot (e.g., Fig. 2.9), with LERGs showing a mid-IR luminosity below $4 - 5 \times 10^{43}$ erg s^{-1} ($4 - 5 \times 10^{36}$ W). Moreover, while LERGs lie in the bottom-left region of the WISE colour-colour plot (which is shown in Fig. 2.10), HERGs are mostly located on the right side. The *y*-axis is the difference between the magnitude in the W1 and W2 band, while the *x*-axis shows the colour obtained from W2 and W3. Fig. 2.9 shows the relation between the radio power at 150 MHz and the infrared power at 22μ m for the BLDF GRGs. It is worth noting that most of our sources have values or upper limits for the infrared power below the orange horizontal line, indicating that in our sample the optical host galaxies are predominantly LERGs. This is also confirmed by the WISE colour-colour plots (Fig. 2.10; W2-W3 vs W1-W2). In this figure, we coloured the host galaxies according to the classification into HERGs (black) and LERGs(blue) suggested from Fig. 2.9. Even though only a few sources lie in the region delimited by W1 - W2 < 1 and W2 - W3 < 2.5 (namely the LERGS region), almost all of them are upper limits (arrows), in agreement with Fig. 2.9, and may shift into the LERG region with deeper mid-infrared observations. A source has an upper limit in the infrared power if the signal-to-noise ratio is lower than 2, either in the W3 or W4 band. The red points in both plots are either spectroscopically identified quasars or quasar candidates in our sample and lie in the upper region (W1 -W2 $\gtrsim$ 1 and W2 - W3 $\gtrsim$ 2). Our sample is drawn from the faintest sources, which poses a limitation to our analysis since most of the GRG hosts are not detected in the W4 band.

Best et al. (subm.) and Mingo et al. (2022) provide an AGN classification into HERG and LERG performed by SED fitting in the optical band. Therefore, we validated our results by crossmatching our BLDF-GRG sample with these catalogues. We found 35 matching GRGs, of which only ten are radiatively efficient AGN. Recently, Mingo et al. (2022) reported that the majority of FRII galaxies experience low accretion rates, especially for the low-power ($L_{150} < 10^{26}$ W Hz^{-1}) AGN population. Here, we confirm this result for GRGs as most of them seem to be in a radiative inefficent mode, regardless of the radio power. Based on the excitation state, it does not appear that GRGs are undergoing massive, radiatively efficient accretion at the present time. However, it is possible that the central engine has gone through a series of recurrent AGN events that have allowed the GRGs to grow to its extreme size.

During the inspection of the BLDF, we found 152 extended RGs which have a linear size in the range 10-700 kpc. We selected the RGs by angular size, trying to be reasonably complete for *LAS* $\gtrsim$ 1.3′. For this reason, only 3 of them have a linear extent smaller than 100 kpc. We compared the stellar mass and star formation rate (SFR) of GRGs and smaller radio galaxy (RG) hosts in Fig. 2.11. The total sample contains 243 sources (GRGs+RGs), 87 (35 GRGs and 52 RGs) of which have either SFRs or stellar mass values from either Best et al. (subm.) or Mingo et al. (2022). In our sample, GRG hosts have high stellar masses (> $10^{10.5} M_\odot$) and the median decimal logarithm of the stellar mass for RGs (11.24) and GRGs (11.13) is similar. Nevertheless, the distribution of GRG hosts shows an excess of stellar stellar masses lower than M$_*$ = $10^{11.5}$M$_\odot$ with respect to RG hosts. The result is in agreement with previous studies which claimed that GRGs are usually hosted by luminous elliptical galaxies dominated by the emission of evolved giant stars (Lara et al. 2001; Machalski et al. 2001; Clarke et al. 2017; Dabhade et al. 2017; Seymour et al. 2020). These are effectively dead systems in which most of the star formation and black hole growth have already come to an end, suggesting that GRGs are the last stage of the evolution of RGs. However, very rare, massive spiral galaxies that host relativistic jets and lobes that extend to Mpc scale have been found as well (e.g, Mao et al. 2015, and reference therein). Moreover, Kuźmicz et al. (2019) performed a detailed analysis of the star formation history in a sample of GRGs finding an 'intermediate' stellar population with an age
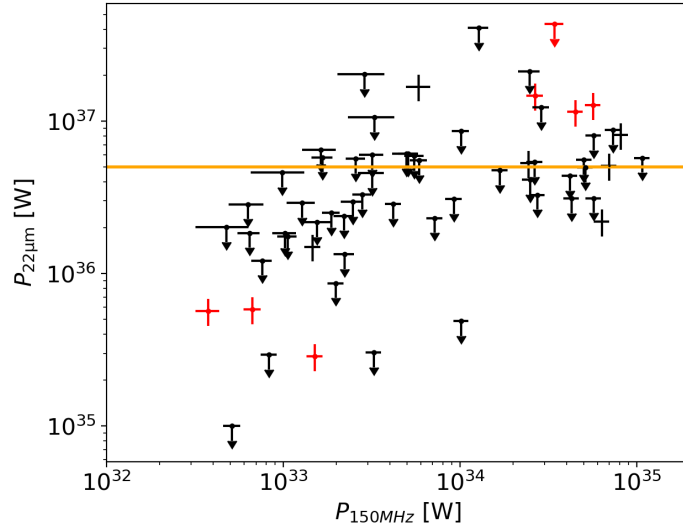
Figure 2.9: Infrared (22μm, W4) - radio (150 MHz) power plot for BLDF-GRG sample. The arrows are upper limits with a signal-to-noise ratio lower than 2 in the W4 band. The orange line is an empirical boundary between HERGs and LERGs (Gürkan et al. 2014). The plot indicates a predominance of LERGs in our sample. The red points are either spectroscopically identified quasars or candidate quasars.
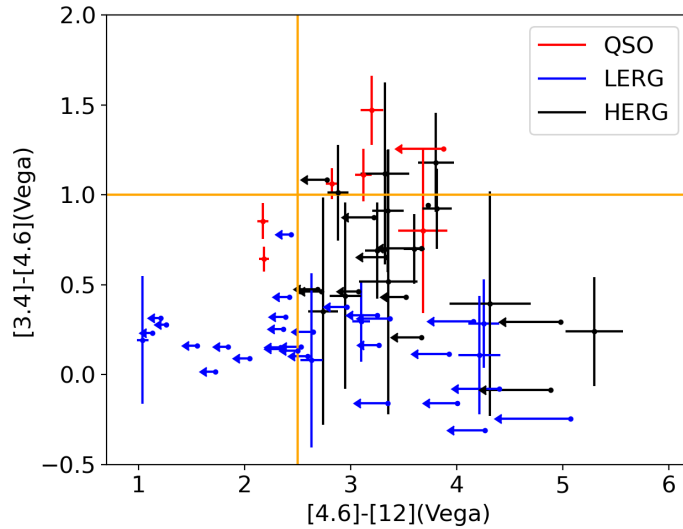
Figure 2.10: WISE colour-colour diagram in the BLDF-GRG sample. Red dots mark either spectroscopically identified quasars or candidate quasars. Almost every GRG host lies in the HERG region of the plot. However, half of them are upper limits (arrows), which means that the source has a signal-to-noise ratio smaller than 2 in the W3 band. The classification as HERGs or LERGs is based on the infrared power relation criterion (Fig. 2.9).

between $9 \cdot 10^8 - 7.5 \cdot 10^9$ yr, besides the common old stellar population residing in the host galaxies ($t > 10^{10}$ yr). Similar results have been found in the GRG ESO 422–G028 by Zovaro et al. (2022). This is indicative of star formation activity at least in some GRG hosts, as shown in the lower panel of Fig. 2.11. In fact, we see an excess of GRGs at SFR values of 10-100 $M_\odot$ yr^{-1} with respect to RGs.

2.3.5 GRG environment

Several studies have addressed the role of the environment in the evolution of RGs in the past. It is known that only a small percentage of GRGs reside in galaxy clusters or groups (e.g., Dabhade et al. 2020b; Andernach et al. 2021) and it is commonly believed that the intracluster medium can frustrate the expansion of jets and lobes in the local environment (Subrahmanyan et al. 2008; Safouris et al. 2009).

We tested the conjecture that GRGs are preferentially located in underdense environments using photometric redshifts from the DESI Legacy Imaging Survey (Dey et al. 2019), assuming that the galaxies trace the distribution of the intergalactic medium. The DESI DR9 photometric redshift catalogue includes observations from the Beijing-Arizona Sky Survey (BASS, Zou et al. 2017a), DECam Legacy Survey (DECaLS) and Mayall z-band Legacy Survey (MzLS) (Dey et al. 2019). In order to look for differences in the environments of GRGs and ordinary RGs, we performed this analysis for our BLDF-GRG sample, as well as for the sample of smaller RGs we found in the BLDF. Due to the depth limit of the DESI survey, we restricted our analysis to $z < 0.7$ yielding 35 GRGs (23 of which have linear sizes larger than 1 Mpc) and 96 RGs. To examine the source environments, we first have to create a volume-limited sample, by cutting out those galaxies with an absolute magnitude (luminosity) in the r band brighter than the absolute magnitude (luminosity) of a galaxy with an apparent magnitude equal to the flux limit, in the r band, located at the maximum redshift considered ($z = 0.7$). Such a cut limits our analysis since it is based on the most luminous galaxies which are the rarest as well. As a consequence, we might miss galaxies that are members of galaxy clusters and understimate the overdensities. We then performed a similar analysis dividing the sample into three redshift bins, $0 \leq z < 0.3, 0.3 \leq z < 0.5, 0.5 \leq z < 0.7$. This method enables us to utilise a larger number of galaxies at low redshifts and increase the robustness of the measurement of the overdensities. The results of the two analyses are similar and, due to the poor statistics of the second method, we decide to report the findings of the first method described. We counted the number of galaxies within a sphere with a radius equal to a comoving distance of 10 Mpc centred on the coordinates of the (G)RG hosts. We approximated the redshift of the source with the redshift value reported in Tab. A1, without taking into account the error. We show the distribution of GRGs (blue) and RGs (grey) with surface number density of galaxies, Σ_{gal}, within 10 Mpc in Fig. 2.12. When testing for differences in the galactic environments around GRGs and RGs, the KS test yields a p-value of 0.17. This result shows that there is no evidence that GRGs reside in environments different from other RGs, in agreement with Komberg & Pashchenko (2009) and Lan & Prochaska (2021).

Dividing the sphere of radius 10 Mpc into 15 shells with equal volumes, we compute the radial profile of the surface number density of the galaxies (Fig. 2.13). GRGs have a tendency to reside in sparser environment with respect to ordinary RGs as the latter have a larger number density of galaxies at almost every radius. However, the p-value of 0.83 of a KS test comparing GRGs with ordinary RGs suggests that this result is not statistically significant.

Our results are in agreement with Oei et al. (2022), who found the largest GRG known to date (LLS=5 Mpc, $z = 0.25$) and it has only 5 galaxies within 10 Mpc, leading to a surface number density of 0.05 Mpc^{-2}, and does not have a single galaxy within 5 Mpc. The value of the surface number density and the number of the galaxies are similar to those reported in Lan & Prochaska
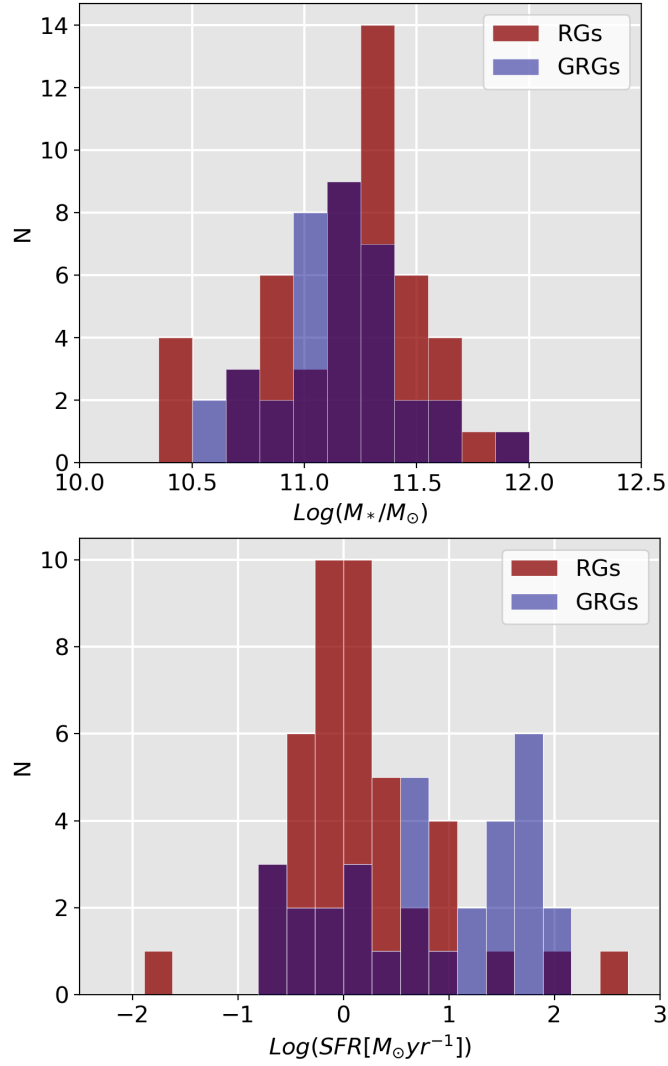
Figure 2.11: Upper panel: Distribution of the stellar mass in GRG (blue) and RG (red) hosts. The former are usually very massive galaxies ($> 10^{10.5} M_\odot$), while the latter that span the entire range from 10^{10} to $10^{12} M_\odot$. Lower panel: SFR distribution for GRGs (blue) and RGs (red). The distribution of GRGs is uniform, indicating star formation activity in at least 10 out of 23 GRG hosts.
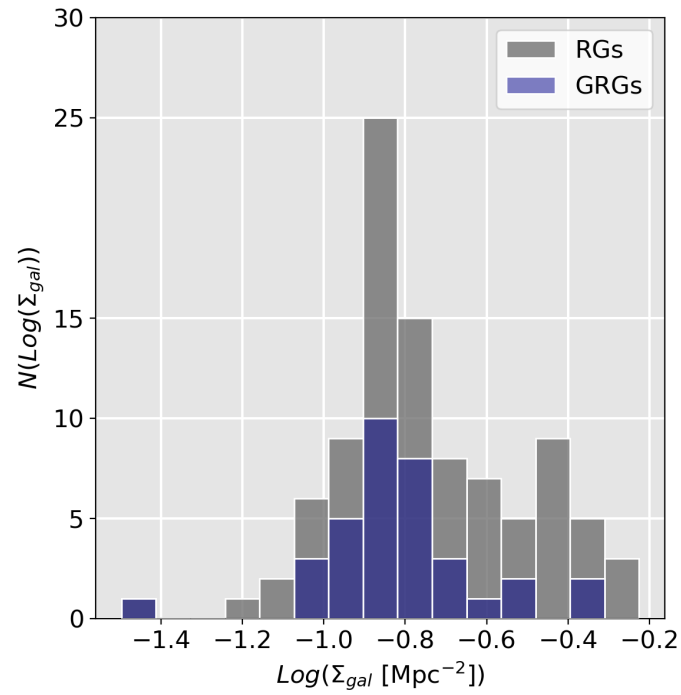
Figure 2.12: Distribution of the surface number density of galaxies within 10 Mpc of the GRGs (blue) and RGs (grey). According to the KS test, we cannot rule out the hypothesis that the samples are drawn from the same distribution at a level of significance of 90%. Nevertheless, the figure shows that GRGs have a tendency to reside in underdense environment.
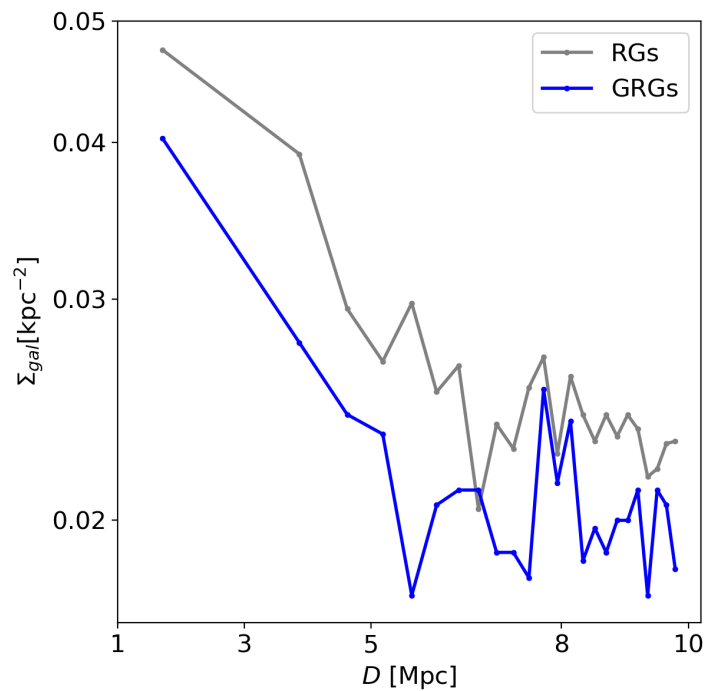
Figure 2.13: Radial distribution of the surface number density of galaxies within 10 Mpc of the GRGs (blue) and RGs (grey). The KS test suggests that the two populations inhabit similar environments.
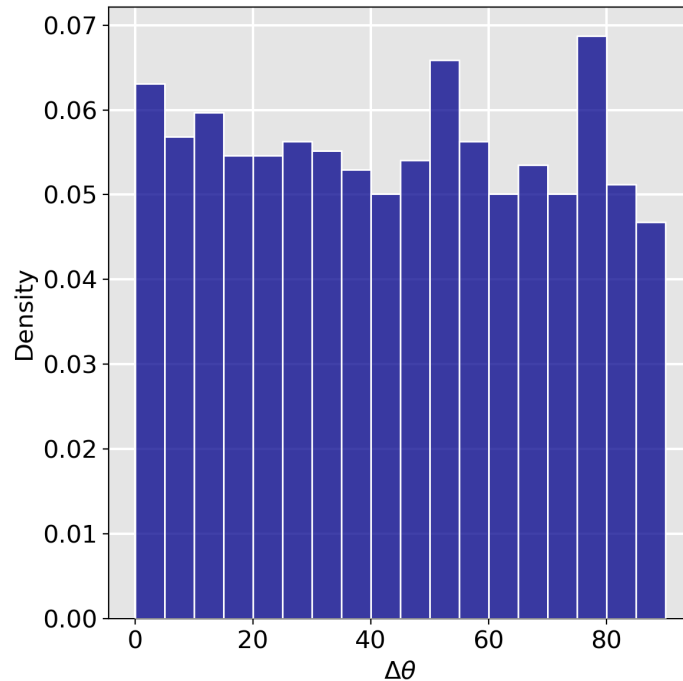
Figure 2.14: Distribution of the orientation of galaxies surrounding GRGs with respect to the direction of the expansion of jets. The distribution is consistent with being uniform.

(2021), albeit a direct comparison with their radial profile is impossible as the authors considered only the neighbouring galaxies within a sphere of radius $R = 1$ Mpc centred on the GRG hosts. Finally, we studied the location of the galaxies close to the GRGs with respect to the direction of the major axis of the source or that of the lobe expansion. With such an analysis, we tested the hypothesis whether jets expand preferentially into the direction of underdense regions. We calculated the acute angle, $\Delta\theta$, between the vector connecting the GRG host with each of the neighbouring DESI galaxies and the orientation of the source major axis, with $\Delta\theta=0$ indicating a neighbouring galaxy along the major source axis, and $\Delta\theta=90°$ a galaxy which is located perpendicular to the source major axis. The distribution of $\Delta\theta$ appears uniform (Fig. 2.14). To test this, we carried out a simple bootstrapping to generate 1000 random uniform distributions of the same size as the number of GRGs of our sample, and then performed a KS test comparing our distribution with each of these generated samples, yielding a median p-value of 0.6.

Based on a sample of 19 GRGs in the redshift range 0.05-0.15, Malarecki et al. (2015) found that GRG hosts live in overdense environments and that GRG lobes are shorter on the side that has a higher concentration of galaxies. Our analysis of the environment suggests that GRGs have a tendency to reside in underdense regions, even though a similar results is found for RGs as well. We found that the environment of GRG hosts on larger scales than 1-2 Mpc is not related to the orientation of the source major axis. As a consequence, only the inhomogeneities in the surrounding medium within ~ 1 Mpc might play a major role in the radio galaxy evolution. Previous studies have shown that asymmetries in radio morphology (e.g., length of the lobes) can be attributed to a density gradient of the external medium (Konar et al. 2008; Safouris et al. 2009; Subrahmanyan et al. 2008; Malarecki et al. 2015; Machalski 2011).

Some former studies have suggested an evolution of the linear sizes of RGs with redshift, which
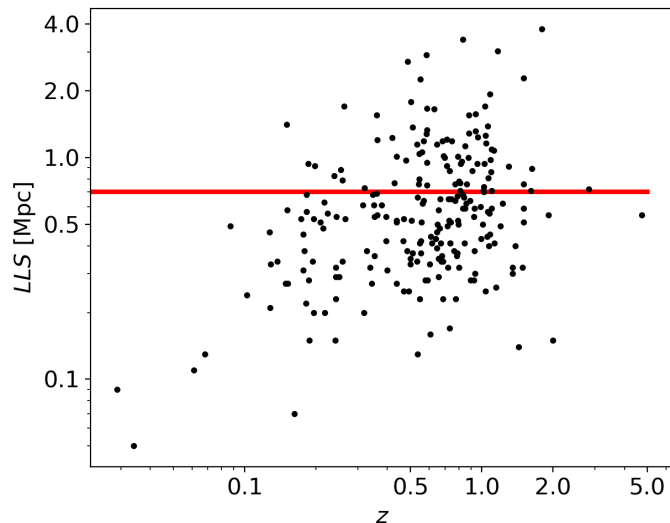
Figure 2.15: *LLS-z* scatter plot in our sample which includes both GRGs and RGs. The two variables do not show any decreasing trend up to $z = 2$. The red line marks the selected threshold of 0.7 Mpc.

might be explained by the redshift evolution of the intergalactic medium (Kapahi 1989; Machalski et al. 2007b; Onah et al. 2018). However, Brüggen et al. (2021) found no dependence of the median linear size or the median radio luminosity on the redshift and hence no evidence for cosmological evolution of the population of GRGs. In our sample, the linear sizes of RGs do not show a decrease up to $z = 2$, even though the scatter is large. At higher redshifts the sample is too small to establish a trend (Fig. 2.15). Due to the sensitivity limitations we are not able to detect extremely large sources, especially those with low radio powers at higher redshift. Moreover, $\sim 80\%$ of the BLDF-GRG have a redshift larger than 0.5, favouring the idea of GRGs being rare, so they are mainly detected at high redshift. We find that the volume number density of GRGs is $n_{grg}(z_{max} = 1.8) = 1.00 (100 \text{ Mpc})^{-3}$ (we excluded the only GRGs with $z > 2$) which is smaller than the estimate predicted by Oei et al, in prep. who used a sample of 525 GRGs at relative low redshift.

2.4 Conclusions

In this paper we carried out a detailed search for GRGs in the Boötes LOFAR deep field at 150 MHz (Tasse et al. 2021) where we identified 74 GRGs with a linear size larger than 0.7 Mpc. The highest redshift GRG in our sample is a spectroscopically confirmed quasar at $z = 2.84$.

We studied the properties of the host galaxies using deep optical and infrared survey data such as SDSS, DESI and WISE. We cross-matched our GRGs in the LOFAR LBA and NVSS images and investigated their integrated spectral index. Finally, the DESI DR9 photometric redshifts enabled us to inspect the environment in which GRGs reside. The main results can be summarised as follows:

- The GRG surface number density based on our sample is 2.8 GRGs deg^{-2}, which is higher than the estimates previously reported in the literature (e.g., Delhaize et al. 2021; Brüggen et al. 2021).

- The P-D diagram shows a lack of GRGs with large linear sizes (> 2 Mpc) and large radio powers ($P_{150} > 10^{27}$ W Hz^{-1}), suggesting an evolution of the radio luminosity of such sources.

In particular, the adiabatic expansion and radiative losses play a role. On the other hand, the high sensitivity of the Boötes LOFAR Deep Field allowed us to detect GRGs at smaller radio powers (10^{24}W Hz^{-1}) at 150 MHz (or $3 \cdot 10^{23}$W Hz^{-1} at 1.4 GHz for α=0.7).

- The integrated spectral index is independent of the linear size of the GRG. In our analysis we find spectral indices of α = 0.7-0.8. However, this result may be biased by the dominance of hotspots that usually have flatter spectra.

- Most GRG hosts are LERGs, showing that FRII radio galaxies can be produced by a (currently) low accretion rate in agreement with Mingo et al. (2022). In our sample, the optical hosts of the GRG and RG populations have a similar stellar mass distribution. In particular, both RGs and GRGs show high stellar masses ($> 10^{10.5} M_\odot$). The GRG hosts can be either quiescent galaxies with SFR $< 1 M_\odot$ yr^{-1} or galaxies with a moderate SFR around 10-100 M$_\odot$ yr^{-1}.

- Based on the number density of galaxies with DESI DR9 photometric redshifts, we found no significant differences between the environment density of GRG and RGs nor did we find the sources major axes to be oriented preferentially toward lower-density sectors.

- We tested whether the linear size of GRGs (*LLS*>0.7 Mpc) and smaller RGs (*LLS*<0.7 Mpc) have a similar distribution. We found a good agreement with the exponential and generalized Pareto distributions in both populations, even though the different scale parameters suggest that we might not probe the same distribution. The scale parameter in the BLDF-GRG sample is below the minimum size required to classify a radio galaxy as giant showing that in this work we study the extreme population of RGs.

In the future, we will expand our work to the two other LOFAR deep fields (ELAIS-N1 and Lockman Hole) and eventually LoTSS DR2 (Shimwell et al. 2022). Moreover, modelling the spectra from high-resolution images might help to reconstruct the evolution of AGN activity of GRGs as well as constrain the properties of the environment around these peculiar objects.

Acknowledgements

Data Availability

The datasets used for the analysis of this paper are publicly available at https://lofar-surveys.org/deepfields.html. Table A1 will be made available at the CDSn and through the VizieR service (https://vizier.cds.unistra.fr).

3 Giant radio galaxies in the LOFAR deep fields

M. Simonte, H. Andernach, M. Brüggen, G.K. Miley, P. Barthel.
A&A, submitted.

Abstract

Context. The reason why some radio galaxies (RGs) grow to form so-called giant radio galaxies (GRGs) with sizes > 700 kpc, is still unknown.

Aims. In this study, we compare the radio, optical and environmental properties of GRGs with those of a control sample of smaller RGs we found in the three LOw-Frequency ARray (LOFAR) deep fields.

Methods. We inspected the LOFAR deep fields and created a catalogue of 1611 extended radio galaxies (ERGs). We identified their host galaxies and classified 280 of these as GRGs. We studied their properties, such as their accretion state, stellar mass and star formation rate (SFR) using deep optical and infrared survey data. Moreover, we explored the environment in terms of the surface number density of neighbouring galaxies within these surveys. Integrated flux densities and radio luminosities were also determined for a subset of ERGs through available survey images at 50, 150, 610, and 1400 MHz to compute integrated spectral indices.

Results. We find that the properties of the GRG host galaxies are similar to those of the RGs, although the SFR shows differences between the two populations. Clearer differences emerge in the environmental densities between GRGs and RGs, using the number of neighbouring galaxies within 10 Mpc from the host galaxy as a proxy. GRGs statistically reside in a sparser environment compared to their smaller counterparts. In particular, only 3% of the GRGs reside within a 3D comoving distance of 5 Mpc from a galaxy cluster. We found that larger sources exhibit steeper integrated spectral indices, suggesting that GRGs are the late-time versions of RGs. These results suggest that, both, the environment as well as the age play a role in the origin of GRGs.

3.1 Introduction

The study of radio galaxies (RGs) can provide insights into the intricate interplay between active galactic nuclei (AGN), their host galaxies and the surrounding intergalactic medium (Magliocchetti 2022). Among the diverse population of RGs, giant radio galaxies (GRGs) have a linear extent larger than 700 kpc (Willis et al. 1974; Barthel et al. 1985; Kuźmicz et al. 2018) and they are relatively rare compared to smaller RGs (Oei et al. 2023a).

The advent of many radio surveys in the past, such as the Faint Images of the Radio Sky at Twenty-cm (FIRST, Becker et al. 1995), Westerbork Northern Sky Survey (WENSS, Rengelink et al. 1997), National Radio Astronomy Observatory (NRAO) VLA Sky Survey (NVSS, Condon et al. 1998), Sydney University Molonglo Sky Survey (SUMSS, Mauch et al. 2003) and the recent Rapid ASKAP Continuum Survey (RACS, McConnell et al. 2020) led to the discovery of about 1000 GRGs (Ishwara-Chandra & Saikia 1999; Lara et al. 2001; Schoenmakers et al. 2000b; Machalski et al. 2001; Saripalli et al. 2005; Kuźmicz & Jamrozy 2012, 2021; Kuźmicz et al. 2018; Dabhade et al. 2017, 2020a; Brüggen et al. 2021; Andernach et al. 2021; Gürkan et al. 2022; Mahato et al. 2022). Furthermore, the LOw-Frequency ARray (LOFAR, Van Haarlem et al. 2013), with its relatively high resolution and sensitivity to very low surface brightness sources, heralds a new era in the study of very large and high redshift radio galaxies. The LOFAR Two-metre Sky Survey (LoTSS Shimwell et al. 2019, 2022) has yielded the discovery of approximately 10000 GRGs (Dabhade et al. 2020b; Simonte et al. 2022a; Oei et al. 2023a, Mostert et al. subm.). Nevertheless, an explanation for the Mpc size of the GRGs is still missing.

GRGs are found preferably, but not exclusively, outside of galaxy clusters (Dabhade et al. 2020b; Andernach et al. 2021). Previous studies showed that asymmetries in the morphology of the radio lobes appear to be influenced by inhomogeneities of the surrounding medium (Subrahmanyan et al. 2008; Safouris et al. 2009; Machalski 2011). Moreover, Malarecki et al. (2015) found that their radio lobes tend to be elongated in the direction perpendicular to the plane in which galaxies and filaments are distributed. However, this result was based on a small sample of GRGs. Machalski et al. (2008); Machalski (2011) proposed that the large size of GRGs is the result of a combination of low-density environment and sustained powerful jets. More recently, Lan & Prochaska (2021), compared the statistics of the environment of small and large radio sources. They demonstrated that neither the properties nor the surface number density of surrounding galaxies can explain the presence of such large objects.

The combination of multi-frequency radio observations allows us to study the radio spectrum and thus the radiative age of the emitting electrons in RGs. Combining observations at 325 MHz, 4.8 GHz and 10.5 GHz, Schoenmakers et al. (2000a) estimated a radiative age of 10 - 100 Myr for a sample of 26 low-redshift ($z \lesssim 0.3$) GRGs. Using radio data at 325 MHz, 610 MHz and 5 GHz of a sample of 10 GRGs, Jamrozy et al. (2008) found a maximum radiative age of about 50 Myr. Furthermore, by including a sample of smaller RGs, they found a positive correlation between the age and the linear size for RGs with powers $> 10^{26.5}$ W Hz^{-1} while the relation is less clear for less powerful sources. These analyses do not take into account particle re-acceleration processes that need to take place at least in some sources, given the short radiative ages. A comparison between dynamical (Machalski et al. 2007b; Harwood et al. 2017) and radiative ages (e.g., Machalski et al. 2009; Mahatma et al. 2020) shows that radiative ages can be underestimated by a factor of at least two. Finally, Konar et al. (2004, 2008) attempted to identify steep-spectrum radio cores in GRGs which may be a sign of recurrent activity. As a matter of fact, little is known about the role of restarted jet activities in causing the size of the largest RGs (Schoenmakers et al. 2000a; Bruni et al. 2019, 2020).

The host of the RGs can be classified as High-Excitation (or radiatively efficient) Radio Galaxies (HERG) and Low-Excitation (or radiatively inefficient) Radio Galaxies (LERG) according to their optical spectra. The former have an accretion rate onto the black hole between one and ten per cent of the Eddington rate. HERGs are hosted by bluer, star-forming galaxies and lower-mass black holes. In contrast, LERGs are likely hosted by high-mass galaxies with a central black hole that experiences accretion below one per cent of the Eddington limit (Best & Heckman 2012). LERG is the dominant population, both, for GRGs and smaller RGs (Dabhade et al. 2017; Mingo et al. 2022; Simonte et al.

2022a; Best et al. 2023).

Multiple hypotheses have been put forward to explain the large sizes of GRGs. A high-density environment, such as in galaxy groups or clusters, might suppress the expansion of the radio jets and lobes leading to larger sources in more isolated galaxies. Moreover, the sustained emission of powerful jets for extended periods, i.e. $\approx 10^8$ yr (Machalski et al. 2008), or multiple jet activity of restarted sources may contribute to the growth of RGs to Mpc sizes. Finally, GRGs might be the result of the long-term evolution of radio galaxies. Thus, GRGs should consist of older electrons compared to smaller RGs. The large size of GRGs is likely influenced by a combination of factors rather than a single mechanism.

Previous studies mostly focused on the properties of GRGs alone and only very few presented a comparative analysis of the properties of GRGs and smaller RGs (e.g., Subrahmanyan et al. 1996; Lan & Prochaska 2021). In this paper, we extend our work on the GRGs in the LOFAR Boötes deep field (Simonte et al. 2022a) by adding a number of RGs and GRGs we found in the Lockman Hole and ELAIS-N1 deep fields. Using radio data for our sources at other frequencies and optical and infrared wavelengths, we compare the multi-wavelength properties of GRGs with those of the control sample of smaller RGs.

The outline of this paper is as follows: in Sec. 3.2 we explain how we built our catalogue of (G)RGs and how we carried out the analyses of the radio and optical data. In Sec. 3.3 we present the results of our analysis and compare the properties of RGs and GRGs. We draw our conclusions in Sec. 3.4. Throughout this work we adopt a flat ΛCDM cosmology with $H_0 = 70$ km s^{-1} Mpc^{-1}, $\Omega_{\mathrm{m}} = 0.3$, $\Omega_{\Lambda} = 0.7$ and a radio source spectral index α defined as $S_{\nu} \propto \nu^{-\alpha}$.

3.2 Methods

We visually inspected the images of the three LOFAR deep fields: ELAIS-N1, Boötes, which cover an area of ≈ 25 deg^2 each (Sabater et al. 2021), and Lockman Hole, which covers an area of ≈ 45 deg^2 (Tasse et al. 2021). These observations were performed using the LOFAR High-Band Antennas (HBA) which operate in the range between 120-168 MHz. With an effective observing time longer than 80 hours for each field, the observations reach a root mean square noise (rms) level at 150 MHz lower than 30 μJy beam^{-1} across the inner 10 deg^2. The sensitivity to a wide range of angular scales of such observations makes these deep fields ideal for the detection of the diffuse radio emission that characterizes GRGs.

We carried out a systematic search of extended radio galaxies (ERGs) with a largest angular size (LAS) $\gtrsim 20''$. Given the range of radio morphologies, we employed a variety of methods for estimating the LAS. In the case of bright FRII sources, we measured the LAS as the distance between the two opposite hotspots, if detected in the VLA Sky Survey (VLASS, Lacy et al. 2020), unless the LOFAR image showed evidence for emission beyond the hotspots. For FRI and more diffuse sources, we measured the LAS with a straight line between the two opposite ends of the source outlined by the 3-σ contours. This approach was also used for bent sources because, otherwise, we would have to make assumptions about the (unknown) 3D structure of the source. For the most diffuse sources, we extended the LAS measurement beyond the 3-sigma contours when we found genuine radio emission beyond those contours.
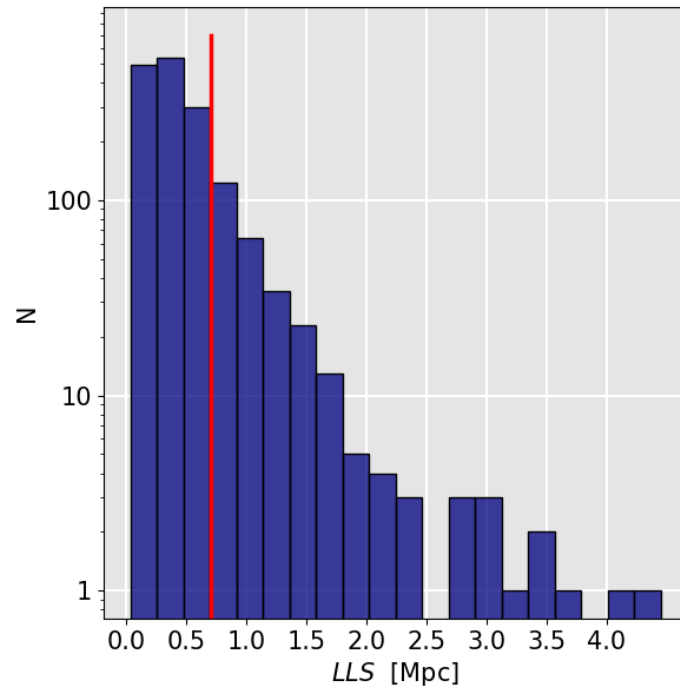
Figure 3.1: Distribution of the largest linear size in our LDF-RG sample. The red line marks the value of 0.7 Mpc.
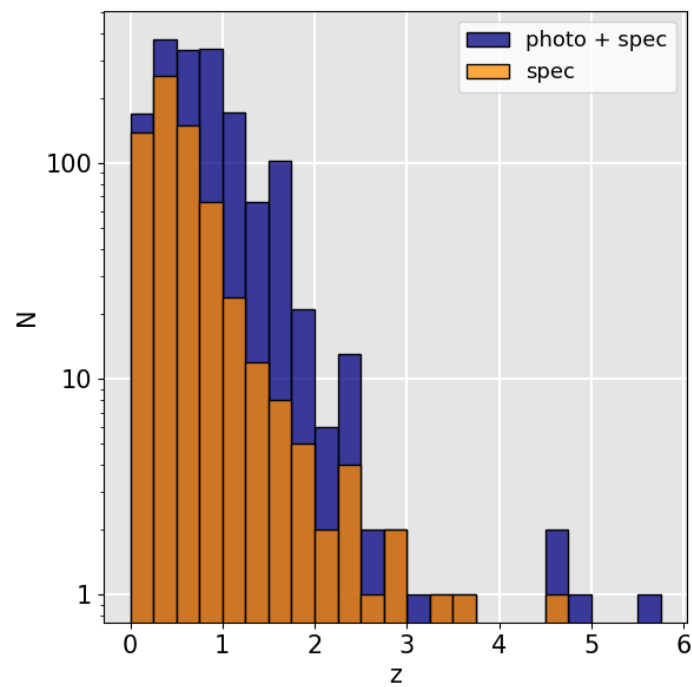
Figure 3.2: Distribution of the redshifts (spectroscopic and photometric) in our LDF-RG sample (blue histogram). The orange histogram shows the distribution of the spectroscopic redshifts.

In order to identify the host galaxies for our ERGs, we made use of a variety of multiple optical and infrared surveys: the Sloan Digital Sky Survey (SDSS, York et al. 2000), the Wide-Field Infrared Survey Explorer (WISE, Wright et al. 2010) and its more recent versions of both images and catalogues such as AllWISE (Cutri et al. 2021), unWISE (Schlafly et al. 2019) and CWISE (Marocco et al. 2021), the Dark Energy Survey Imaging (DESI, Dey et al. 2019; Zhou et al. 2021) and Panoramic Survey Telescope and Rapid Response System (Pan-STARRS, Flewelling et al. 2020). The identification of the host galaxy can be challenging for widely separated radio components without a detected radio core between them. The identification method was extensively explained in previous papers (see Andernach et al. 2021; Simonte et al. 2022a, 2023). Here, we emphasise the key concerns that may arise during this procedure.

We first check whether one of the outer radio components has a convincing host itself. In such cases, we recorded the radio source as a separate RG when larger than $\approx 20''$. For very few sources (≈ 10) we could not find an obvious host either in the optical or in the infrared surveys; thus, these sources were discarded. On the other hand, the presence of a host galaxy with AGN colours (Mateos et al. 2012; Assef et al. 2013), near the geometrical centre of the ERG, is a convincing sign of the genuineness of the ERG. In asymmetric ERGs the shorter lobe is often the brightest, perhaps caused by the denser environment encountered during the jet expansion (Pirya et al. 2012; Malarecki et al. 2015), though relativistic effects may also play a role (e.g., Marecki & Ogrodnik 2015). When faced with uncertainty, we relied on this information to locate the host galaxy closer to the brighter lobe for these sources. Moreover, the VLASS images with a resolution of $2''$ were helpful in spotting the core in a small fraction of ERGs. If neither asymmetry of the source nor the AGN colour were enough to recognise the most likely host galaxies, we chose the brighter or lower redshift host. Hence, the largest linear size (LLS) derived from the LAS and redshift should serve as a lower limit in this case.

We cross-matched the optical position of the host galaxy with various spectroscopic (Ahumada et al. 2020; DESI Collaboration et al. 2023) and photometric redshift catalogues (Rowan-Robinson et al. 2013; Brescia et al. 2014; Bilicki et al. 2016; Xu et al. 2020; Beck et al. 2021; Duncan et al. 2021; Zhou et al. 2021; Wen & Han 2021; Duncan 2022; Zhang et al. 2022; Zou et al. 2022). For the latter, we computed the average redshift and used as associated error the standard deviation of the multiple redshifts of the host galaxy reported in the different catalogues. We do not quote the errors on the spectroscopic redshifts since they are usually more accurate (typical errors are about 0.00015) than the precision we can achieve in the flux density and LAS measurements.

We found 1611 ERGs (which we refer to as LDF-RG or LDF-GRG sample) with an angular size larger than $20''$, of which 280 are classified as GRGs (i.e., with an $LLS \geq 0.7$ Mpc) and 135 have an $LLS \geq 1$ Mpc. In total, 42% of the RGs in our sample have a spectroscopic redshift, 35% when considering only GRGs. 90 host galaxies do not have a redshift estimate in any of the aforementioned catalogues. The Zhou et al. (2021) DESI DR9 photometric redshift catalogue is the deepest full-sky catalogue available (except for the inner regions of the three deep fields where a deeper catalogue from Duncan et al. 2021 exists). In Zhou et al. (2021), the faintest galaxies have a maximum photometric redshift of around 1.3. Therefore, we assumed a redshift of 1.5 for those host galaxies without redshift listed in the literature. However, the precise redshift is not essential when converting LAS to LLS since, for a given LAS, the LLS is almost constant in the redshift range from about 1.2 to 2. (see Fig. 3 in Simonte et al. 2022a). Moreover, we did not use ERGs without redshift estimates for our environmental analysis. Nevertheless, the uncertainties on the redshift estimation also affect the radio power calculation and thus the location of the ERGs in the radio power-linear size diagram (Baldwin

1982).

In Fig. 3.1 and 3.2, we show the distribution of the LLS and redshift in our LDF-RG sample. These plots encompass all ERGs, including those for which a redshift estimate is not provided in the literature; in such cases, we assigned a redshift value of 1.5.

3.2.1 Flux density and spectral index

We measured the total radio flux of the 280 GRGs using the full $6''$ resolution images of the LOFAR deep fields (Sabater et al. 2021; Tasse et al. 2021). We prepared cutouts with sizes equal to three times the angular size of the source on a side. While integrating the flux, we considered only those pixels whose intensity is larger than $3\sigma_{\rm rms}$. Here, $\sigma_{\rm rms}$ is the noise level calculated within each cutout, since the noise level varies significantly across the deep fields, and it is measured through an iterative approach. In each iteration, we calculated the root mean square (rms) value, removed pixels with intensities exceeding 5 times the rms, and subsequently recalculated the rms. The convergence criterion was defined based on the difference between two consecutive rms measurements, with a threshold set to 1%. Therefore, we scaled the noise measurement by the square root of the area of the integrated flux, measured in terms of beam areas. The final flux error was calculated as $\sqrt{\sigma_{\rm rms}^2 + \sigma_{\rm cal}^2}$, where $\sigma_{\rm cal}$ is the uncertainty on the calibration of the flux scale which is assumed to be 10% (Sabater et al. 2021; Tasse et al. 2021). The total flux of some of the largest, in terms of angular size, and faintest ERGs is underestimated with the 3-σ clipping method which misses part of the emission coming from the faintest part of the ERG (such as bridges). Thus, we integrated the flux of such sources (marked by an asterisk in Table B1) considering all the pixels belonging to the region of the radio emission.

We calculated the radio power at 150 MHz following Donoso et al. (2009):

$$P_{150} = 4\pi D_L^2 S_{150}(1 + z)^{\alpha-1}, \tag{3.1}$$

where D_L is the luminosity distance, S_{150} is the measured radio flux density at 150 MHz, $(1 + z)^{\alpha-1}$ is the standard k-correction used in radio astronomy and α is the radio spectral index for which we adopted a typical value of 0.7. This is a reasonable value considering that the radio spectrum of GRGs is often dominated by the emission from the hotspots and the core (see, Dabhade et al. 2020b, for a distribution of the integrated spectral indices in a sample of GRGs). We should also note that we found slightly steeper radio spectra in our analysis (see LLS-spectra index plots) with an integrated spectral index. Thus, some of the radio luminosities at 150 MHz can be slightly underestimated. Nevertheless, the exact value of α has a relatively small impact on the final estimate of the radio power.

In order to estimate the core fraction, we used a similar approach to calculate the flux of the GRG cores. We only used GRGs in which the core was not blended with the emission coming from the inner part of the jets. We found that 176 GRGs show a clear core emission. 33 GRGs (12% of the total sample) do not show any core emission above the $3 - \sigma$ level. For these sources, we calculated the core flux as $3\sigma_{rms}$, where σ_{rms} is the rms noise calculated in the vicinity of the source. Hence, the core fraction derived from the core flux should serve as an upper limit. The integrated radio fluxes as well as the core fractions are listed in Table B1. The full table with all the properties of the full LDF-RG sample will be made available at the CDS and through the VizieR service (Ochsenbein et al. 2000).

Furthermore, we used images at other radio frequencies to investigate the spectral properties of both

---

https://vizier.cds.unistra.fr

GRGs and smaller RGs. The LOFAR Low-Band Antenna (LBA) Sky Survey (LoLSS, e GasperinDE GASPERIN et al. 2021, 2023) is a wide-area survey at 41-66 MHz. A dedicated deep observation of the Boötes field at these frequencies has been performed at a central frequency of 50 MHz, and the resulting image has an rms noise level of 0.7 mJy beam^{-1} and a resolution of 15″ (Williams et al. 2021). Moreover, the APERture Tile In Focus array (Apertif, van Cappellen et al. 2022) survey, carried out with the Westerbork Synthesis Radio Telescope (WSRT), observed the same field at 1400 MHz (Kutkin et al. 2023). The mosaicked image has an angular resolution of 27″ × 11″ and a median background noise of 40 μJy beam^{-1}. The ELAIS-N1 field was observed with the Giant Metrewave Radio Telescope (GMRT) and imaged at 610 MHz by Garn et al. (2008). The resulting radio image has a resolution of 6″ × 5″ and a rms noise level of 40-60 μJy beam^{-1}. The Lockman hole field was observed both at 1400 MHz with Apertif (Morganti et al. 2021) and 610 MHz with GMRT (Garn et al. 2008). However, the region of overlap between the LOFAR and the Apertif image in this region of the sky is quite small and the few sources detected at multiple frequencies are too faint to obtain good-quality spectral indices.

Exploiting this multi-frequency coverage we computed the integrated spectral index (i.e., estimated from the total flux of the source) of 25 GRGs and 74 RGs between 150 and 1400 MHz, 3 GRGs and 32 RGs between 150 and 610 MHz and 24 GRGs and 21 RGs between 50 and 150 MHz. For each pair of images, we convolved the images to the angular resolution of the image with the coarsest resolution. We excluded those ERGs that were blended with other sources after the convolution. Then, we calculated the integrated flux for each source within the pair of images at two distinct frequencies. This was achieved by applying sigma-clipping at a level of $3\sigma_{rms}$, where σ_{rms} is the rms noise of the individual convolved image. Hence, we calculated the spectral index of the radio spectrum of the source using the linear least-squares method in log-space. The errors were estimated according to the Gaussian propagation of uncertainties. Note that the calculation of the integrated flux is dominated by the brightest part of the radio galaxy, such as the core and the hot spots, which host the youngest electrons and with a spectral index of about 0.4-0.7.

3.2.2 Optical analysis

Kondapally et al. (2021) and Best et al. (2023) identified the host galaxies for all the radio sources in the inner 7 deg^2 of the three LOFAR deep fields and estimated their stellar masses, star formation rates (SFRs) and accretion modes by fitting the spectral energy distribution. We cross-matched our sample of ERGs with these catalogues employing a crossmatching radius of 5″. We found 453 matches, of which 68 are GRG hosts.

3.2.3 Environmental analysis

We used the DESI DR9 photometric redshift catalogue (Zhou et al. 2021) to study the environment of the ERGs on a scale between 1 and 10 Mpc. This catalogue includes observations from the Beijing-Arizona Sky Survey (BASS, Zou et al. 2017b), DECam Legacy Survey (DECaLS) and Mayall z-band Legacy Survey (MzLS) (Dey et al. 2019) and it is the deepest large-area catalogue available. However, due to the depth limit of the DESI survey we restricted the analysis to $z \leq 0.7$. Hence, we included in our study 808 ERGs of which 122 have a linear size larger than 0.7 Mpc.

First, we created a volume-limited sample of potential neighbouring galaxies. This involves excluding galaxies with an absolute magnitude (luminosity) in the *r* band that is fainter than the absolute magnitude (luminosity) of a galaxy with an apparent magnitude equal to the flux limit in the *r* band,

observed at the maximum considered redshift ($z = 0.7$). Implementing this cut-off imposes a restriction on our analysis as it focuses on the most luminous galaxies, which are also the least common. As a consequence, we might miss faint galaxies residing in galaxy clusters and underestimate the overdensities. In this analysis, we looked at the surface number density of galaxies by calculating the number of galaxies within a sphere of radius of 10 Mpc centred on the ERG hosts. We approximated the photometric redshift of the host galaxy to the value obtained by averaging the redshifts of different catalogues as explained in Sec.3.2. We did not consider the calculated error of the photometric redshift in this analysis. Moreover, we used spectroscopic redshifts for, both, the host and neighbouring galaxies when available. We should point out that the majority of neighbouring galaxies are located at a distance larger than 1 Mpc from the ERG host. Thus, this analysis ignores the information on the environment within $\approx$ 1 Mpc which may play a crucial role in the evolution and expansion of the radio jets and lobes (Konar et al. 2008; Subrahmanyan et al. 2008; Machalski 2011; Pirya et al. 2012; Malarecki et al. 2015).

Moreover, we used multiple catalogues of galaxy clusters compiled using observations at different wavelengths (Koester et al. 2007; Yoon et al. 2008; Hao et al. 2010; Rykoff et al. 2014; Takey et al. 2014; Wen & Han 2015; Planck Collaboration et al. 2016; Clerc et al. 2016; Burenin 2017; Wen et al. 2018; Wen & Han 2018; Abdullah et al. 2020; Koulouridis et al. 2021) to study the distance of the RGs in our sample from known galaxy clusters with a spectroscopic redshift. We matched the RG hosts with the galaxy cluster having the smallest 3D comoving distance from the host. Due to the sensitivity limitations of the surveys, the detection of galaxy clusters at high redshift is challenging and not many of them are detected beyond $z \approx 0.5$ (e.g Wen & Han 2018). As a consequence, there may be undetected, high-redshift galaxy clusters closer to the ERG host than the current matched galaxy cluster. Moreover, we may miss the membership of the ERG host to a cluster at high redshift. Thus, we considered only the RGs with a galaxy cluster within a comoving distance of 50 Mpc for the analysis. This value was chosen to study the distribution of the distance of ERGs from galaxy clusters, besides their membership to a specific cluster. The final sample counts 681 RGs and 121 GRGs.

Finally, we looked for a possible cosmological evolution of the linear size of RGs (e.g., Kapahi 1989) by dividing our sample into five redshift bins of width $\Delta z = 0.3$ and calculated the median LLS in the bin. We included all the RGs with a redshift larger than 1.5 in the 1.2-1.5 redshift bin. We excluded those radio galaxies with an LLS smaller than the minimum physical size required to be resolved at any redshift. We considered an ERG as resolved when its angular size was $\geq 20''$ at any redshift. Thus, the minimum LLS required for an ERG to be resolved at any redshift is about 170 kpc.

3.3 Results and discussion

With a sample size of 1611 RGs, we looked for differences in the host galaxy properties of RGs and GRGs and compared the environments in which they reside.

3.3.1 $P - D$ diagram

We used the flux densities and radio powers of the GRGs as derived in Sec. 3.2.1 to locate our GRGs in the radio power-linear size diagram ($P - D$ diagram, Baldwin 1982). Such a plot is often used to study the evolution of radio galaxies. Every radio source has a specific evolutionary track in this diagram which depends on multiple properties such as jet power, environment and redshift (see, Ishwara-Chandra & Saikia 1999; Machalski et al. 2004; Hardcastle 2018). We show the position

of our LDF-GRGs sample in the $P - D$ diagram with the black points, along with GRGs from recent samples (Dabhade et al. 2017, 2020a,b; Kuźmicz & Jamrozy 2021; Andernach et al. 2021) in which flux densities and radio power of the listed GRGs are reported. For those GRGs with a flux estimated at other frequencies, we extrapolated the radio power at 150 MHz by using a standard spectral index, $\alpha = 0.7$. This is the typical value found in the hotspots of RGs which often dominates the radio emission of the GRGs, especially at higher frequencies (see also Sec. 3.2.1, for a discussion on the value of α).

According to the RG models, after an initial phase and once the jet activity stops, its luminosity decreases owing to synchrotron, inverse Compton and adiabatic expansion losses in the latest stages (e.g., Hardcastle 2018). Hence, if GRGs are aged RGs, it is expected that the largest RGs tend to be less powerful compared to the smaller radio sources. This effect likely drives the lack of GRGs in the upper-right corner of Fig. 3.3, where very powerful and large RGs should reside. Figs. 8 and 14 in Hardcastle (2018) show that only the most powerful ($P_{150MHz} > 10^{26}$ W Hz^{-1} and aged (> 100 Myr) RGs can grow up to Mpc sizes. Nevertheless, GRGs display a wide range of radiative ages between 10-100 Myr (Schoenmakers et al. 2000b; Lara et al. 2000; Jamrozy et al. 2008; Pinjarkar et al. 2023). Future deep radio observation at higher frequencies will certainly help to accurately estimate the age of GRGs.

On the other hand, there is a lack of very large GRGs with a small radio power as well, likely due to sensitivity limitations of the current radio facilities. The large angular size of such RGs makes their surface brightness rather low, challenging their detection in the lower power regime. As a matter of fact, we have been starting to observe large (> 1Mpc) RGs of low radio luminosity ($< 10^{25}$ W Hz^{-1}) only with the most recent and sensitive observation with LOFAR and ASKAP (Andernach et al. 2021).

3.3.2 Properties of the host galaxies

Combining our LDF-RG sample with the catalogues provided by Kondapally et al. (2021) and Best et al. (2023) for the LOFAR deep fields we compared the star formation rate (SFR), stellar mass and accretion state of the host galaxies in GRGs and RGs. The final sample for this analysis counts 385 RGs ($LLS < 0.7$ Mpc) and 68 GRGs. Fig. 3.4 shows that the distribution of the stellar mass in the host of RGs (red) and GRGs (blue) are very similar with both populations being hosted by massive early-type galaxies. The result is in line with previous work (Lara et al. 2001; Dabhade et al. 2017; Simonte et al. 2022a). However, very rare, massive spiral galaxies with radio lobes extending up to Mpc size have been found as well (Bagchi et al. 2014; Oei et al. 2023b). Moreover, previous studies (Zovaro et al. 2022; Kuźmicz et al. 2019) found a young ($< 10^7$ yr) and 'intermediate' ($\approx 10^9$ yr) stellar population, besides the population of evolved stars with an age larger than 10^{10} yr, in the host of some GRGs. These results suggest that the star formation in some GRG hosts is still ongoing and this is also shown in our Fig. 3.5. In fact, an excess of hosts with moderate and high SFR (> 10 M$_\odot$ yr^{-1}) is visible in the SFR distribution of the GRG hosts with respect to the RG distribution. The total number of RGs for which an estimate of the SFR is available is 333 of which 66 are GRGs. 41% of the latter have a SFR > 10 M$_\odot$ yr^{-1}, while only 20% of the RG hosts have a SFR above this threshold. By conducting a Kolmogorov-Smirnov (KS) test on the SFR distributions, we obtained a p-value of 0.003, providing strong evidence to reject the null hypothesis that the two samples were drawn from the same distribution. To validate this result, we performed a Mann-Whitney U test as well (Mann & Whitney 1947). This is a non-parametric test which uses the rank sums of the two samples to determine whether they come from the same distribution. The resulting p-value of 0.004 further validates the rejection of
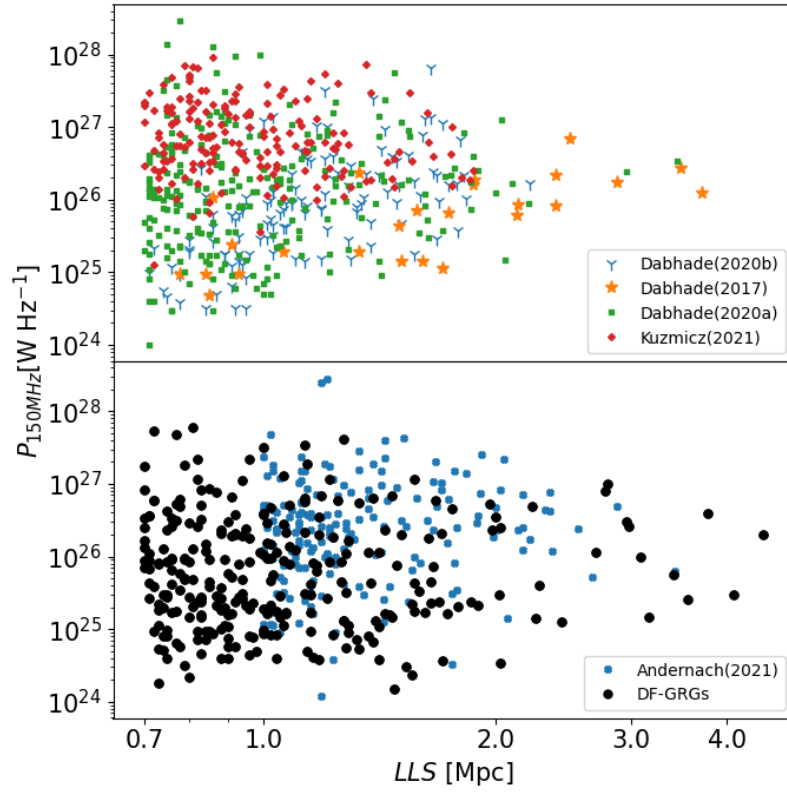
Figure 3.3: *P − D* diagram that shows the radio power at 150 MHz against the linear size (LLS) of the LDF-GRG sample. Other previous GRG samples are included in the plot for a comparison: Dabhade et al. (2017, 2020a,b); Kuźmicz & Jamrozy (2021); Andernach et al. (2021).
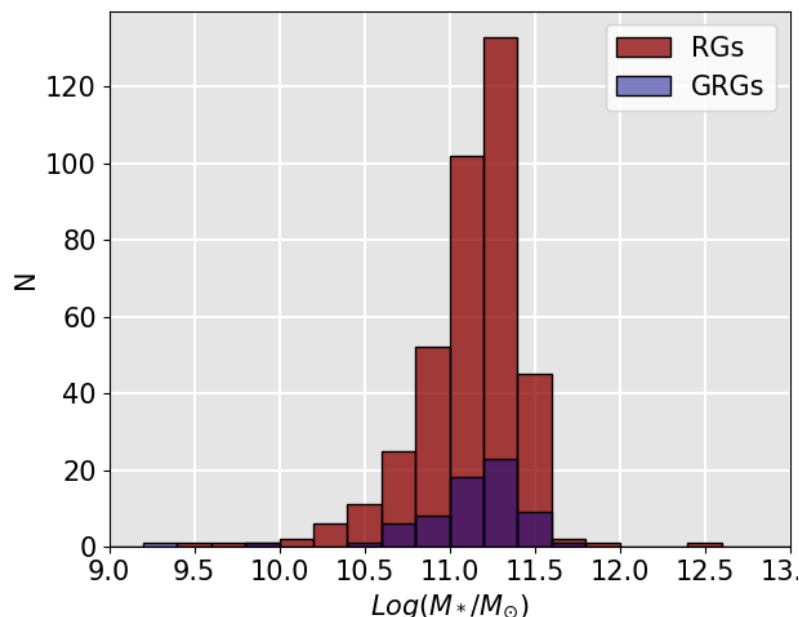
Figure 3.4: Distribution of the stellar mass of the host galaxies in RGs (red histogram) and GRGs (blue histogram).

the null hypothesis. However, the result does not hold when shifting the linear size threshold used for the definition of GRGs to lower values (e.g., 500 kpc) suggesting that larger samples are needed to provide more conclusive results. Moreover, such a different distribution may be driven by the different redshift distributions for RGs and GRGs. Previous studies have indicated an evolutionary trend in the properties of the RG hosts, revealing that the number density of LERGs exhibits a weak dependence on redshift, whereas HERGs have a higher abundance at higher redshifts (Best et al. 2014; Pracy et al. 2016; Williams et al. 2018; Butler et al. 2019; Best et al. 2023). Moreover, a large population of star-forming LERGs has been found at higher redshift (Delvecchio et al. 2017; Kondapally et al. 2022). Nevertheless, we checked that the two redshift distributions for GRG and RG hosts that have a SFR estimate in the literature are similar by performing a KS test which exhibits a p-value = 0.22. Overall, the result suggests that the GRG host galaxies tend to show slightly more star formation. Such events may fuel the central black hole and eventually trigger new jet activity (Gürkan et al. 2015; Kozieł-Wierzbowska et al. 2017; Shabala et al. 2017; Toba et al. 2019), although we did not find any correlation between the core fraction and the SFR or radio power and SFR of the host galaxy. It is crucial to account for inherent time delays between star-forming processes and AGN activity. While the star formation observed in a galaxy is contemporaneous with our observations, AGN radio activity likely occurred $10^7 - 10^8$ years ago. Therefore, establishing a direct link between the radio emission of RGs and the current SFR of their host galaxies is non-trivial, especially considering the uncertainty of whether the present star-forming activity is a result of the same processes that might have triggered AGN activity in the past.

Furthermore, we looked at the accretion status, that is radiatively efficient (HERG) or inefficient (LERG), of the host galaxies. We find that the percentage of HERGs in GRGs and RGs is slightly different: 22% and 13%, respectively. Nevertheless, in both samples, LERGs are the dominant population.

In Fig. 3.6, we show the SFR-radio power (P_{150MHz}) diagram for our LDF-GRG sample. The GRGs
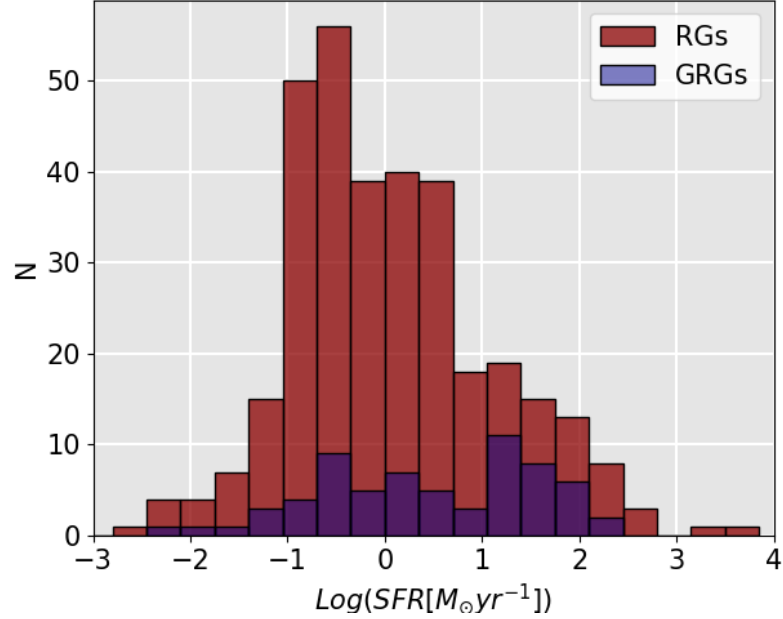
Figure 3.5: Distribution of the star formation rate of the host galaxies in RGs (red histogram) and GRGs (blue histogram).

are colour-coded according to their accretion status: blue for radiatively efficient and orange for radiatively inefficient GRGs. As expected, LERGs have lower SFR ($<$ few $M_\odot$ yr^{-1}) compared to HERGs. However, there is a population of LERGs with moderate or high SFR as well. The threshold value of 10^{26} W Hz^{-1} is represented by the red line. Despite acknowledging the limitation imposed by the small sample size, we notice that RGs with a radiatively efficient accretion have also high radio luminosities ($> 10^{26}$ W Hz^{-1}), while they are rare at lower luminosities. The results are in agreement with Mingo et al. (2022), who used a sample of 286 RGs in the LOFAR deep fields, showing that this dichotomy encompasses ERGs of any size, including GRGs. It is worth noticing that the apparent relation between the SFR and radio power is not real. As mentioned before, we expect an evolution of the SFR of the host galaxies with cosmic epoch, with a peak of the SFR around z=2 (Madau & Dickinson 2014). Furthermore, in brightness-limited surveys such as the LOFAR deep fields, more luminous sources can be observed at a greater redshift. We calculated the partial correlation coefficient (Baba et al. 2004) which measures the strength of the correlation between two variables while controlling for the effect of one or more other variables (which is the redshift in our case). The resulting coefficient of R=0.11 suggests that the correlation between the SFR and the radio power is very mild.

3.3.3 Environment

We tested the conjecture that GRGs reside in rather sparse environments following the method described in Sec. 3.2.3. In Fig. 3.7 we show the distribution of the surface number density of galaxies, Σ_{gal}, within 10 Mpc. In order to increase the sample of the largest RGs and the significance of our results, we relaxed the definition of GRGs by considering a threshold of 500 kpc rather than the usual 700 kpc. Our sample of 808 RGs used for this analysis consists of 256 RGs with an LLS $>$ 500 kpc with redshift up to $z = 0.7$. The distribution shows that only the smaller RGs reside in the densest environment while only very few GRGs have a number of neighbouring galaxies larger than ≈ 200
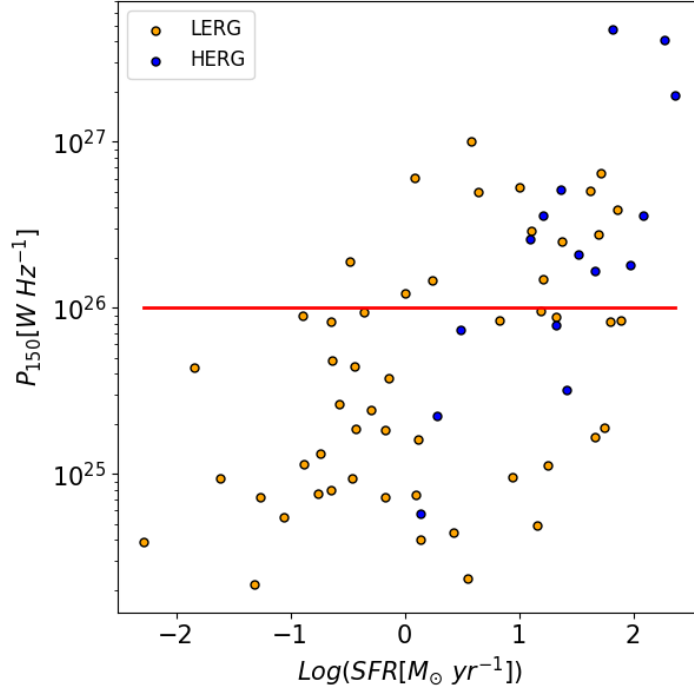
Figure 3.6: $SFR - P_{150\text{MHz}}$ diagram for LDF-GRG sample. The orange points are radio galaxy hosts classified as LERGs, while the blue points are HERGs. The red line represents the traditional boundary used to distinguish between FRI and FRII (Fanaroff & Riley 1974; Ledlow & Owen 1996).

$(\text{Log}(\Sigma_{\text{gal}}) \gtrsim -0.2)$.

We performed a KS test to compare the distribution of the two which resulted in a p-value of 0.002. Thus, we can reject the hypothesis that the two distributions come from the same distribution with a confidence level >99%. The Mann-Whitney U test returns a similar result with a p-value ¡ 0.001. The result of the KS test does not hold when keeping a threshold of 500 kpc for the smaller galaxies while using the widely accepted definition of GRGs (700 kpc). However, this discrepancy is likely a consequence of the reduced sample size (122 GRGs with a linear size larger than 700 kpc) resulting from the more stringent threshold. Furthermore, the Mann-Whitney U test, with a p-value of 0.014, continues to support a difference in the distribution even with these new thresholds.

Whenever available, we employed spectroscopic redshifts for both the neighbouring and host galaxies to calculate the comoving distances in our analysis. However, the majority of redshift used in this analysis are photometric. The average error of the latter is 0.09 for the host galaxies and 0.14 for the neighbouring galaxies with a slight tendency to increase with the redshift estimate. To validate our results we performed the same analysis considering only the RGs whose hosts have a spectroscopic redshift (i.e. the uncertainties on the linear size are only due to the uncertainties on the LAS), up to $z = 0.7$, while all the neighbouring galaxies were retained, without consideration for the type of redshift. The employed sample counts 228 RGs (LLS<500 kpc) and 72 GRGs (LLS>500) kpc with spectroscopic redshifts. We obtained a p-value of 0.08 and 0.06 for the KS and the Mann-Whitney U test respectively. Moreover, we performed such an analysis by using the Early Data Release of the Dark Energy Spectroscopic Instrument (DESI Collaboration et al. 2023), referred to as DESI EDR in what follows, which provides a catalogue of spectroscopic redshifts obtained with the DESI survey. Thus, we only used spectroscopic redshifts for both the sample of RGs and the sample of neighbouring

galaxies used to calculate the galaxy density within 10 Mpc. In this catalogue, there is no dedicated column for the magnitude of the astrophysical object. Thus, we did not apply any cut in magnitude. DESI EDR does not cover the Lockman Hole, which limits the number of RGs and neighbouring galaxies we can use in the analysis. The retrieved p-values are larger than 0.10. However, the distribution still shows that only RGs reside in environments with a $\text{Log}(\Sigma_{\text{gal}}) \gtrsim -0.2$.

Oei et al. (2022), using data from the SDSS DR7 (Abazajian et al. 2009), found that "Alcyoneus", the largest GRG published yet, has only 5 neighbouring galaxies with similar r-band magnitude to its host within 10 Mpc. This result positions Alcyoneus on the far left end of the distribution shown in Fig. 3.7. Komberg & Pashchenko (2009), using SDSS data, demonstrated that GRGs with redshifts up to 0.1 can be found in various environments, ranging from small groups to rich clusters, although they tend to predominately inhabit sparsely populated environments, in agreement with our study. Moreover, in their study, Lan & Prochaska (2021) reported no difference in the environment within a 1 Mpc radius from the host when comparing a sample of GRGs to smaller RGs. It is worth noting that, although our sample of GRGs is of a similar size, our study focused on the galaxies within 10 Mpc, but is less reliable on scales smaller than 1 Mpc as our algorithm likely misses faint satellites around the main galaxies.

Moreover, we show the distribution of the minimum comoving distance (D) of ERG hosts from known clusters with spectroscopic redshift in Fig. 3.8. While for RGs smaller than 700 kpc the number of host galaxies per bin remains almost constant in the range of 0-25 Mpc, the GRG distribution shows a drop in the number of host galaxies per bin in the range 0-15 Mpc with respect to the range 15-30 Mpc. In particular, the GRG hosts within 15 Mpc are almost half of the GRGs with the nearest galaxy cluster in the range 15-30 Mpc. Thus, the result indicates that GRGs tend to avoid the densest environments such as galaxy groups and clusters. Nevertheless, the KS test and Mann-Whitney U test reveal that the differences in the two distributions are not very significant, showing p-values between 0.02 to 0.15, dependent on the specific test and size threshold employed for defining GRGs. The presence of 7 GRGs in our sample in galaxy clusters challenges the idea that GRGs reside only in sparse environments. A hypothesis is that they reside only in small clusters or groups with a lower central density of the gas. However, using LOFAR and ASKAP data, Pasini et al. (2022) and Böckmann et al. (2023) did not find any relation between the linear size of RGs and the central density of galaxy clusters detected within the eROSITA survey (Merloni et al. 2012; Predehl et al. 2021; Liu et al. 2022) suggesting that radio power is more prominent than ambient density in determining the size of the radio galaxy in clusters. However, as emphasised by Fig. 3.3, a relation between the size and the radio power in our sample is not obvious. Nevertheless, variations of density and velocity in the intracluster medium may account for the stirring of the plasma injected by the jets and lead to Mpc size Wide-Angles Tail (WAT) and Narrow-Angled Tail (NAT) RGs with complex morphologies (Srivastava & Singal 2020, Lusetti et al. subm.). Thus, the physical mechanisms responsible for the shape and extent of the diffuse emission of GRGs may be different for those residing in galaxy clusters.

3.3.4 Cosmological size evolution of RGs

Former studies have suggested an evolution of the linear sizes of RGs with redshift, which might be explained by the redshift evolution of the intergalactic medium (Kapahi 1989; Machalski et al. 2007b; Onah et al. 2018). We found that binning the ERGs in redshift bins of width $\Delta z = 0.3$ (see Sec. 3.3.3), the median LLS in each bin does not show evolution with redshift. Furthermore, we computed the KS and Mann-Whitney U tests to compare the LLS distribution in different bins of Δz. We found no evidence that they are drawn from different populations and hence no evidence for cosmological size evolution of GRGs. These results are in agreement with Brüggen et al. (2021) who found no
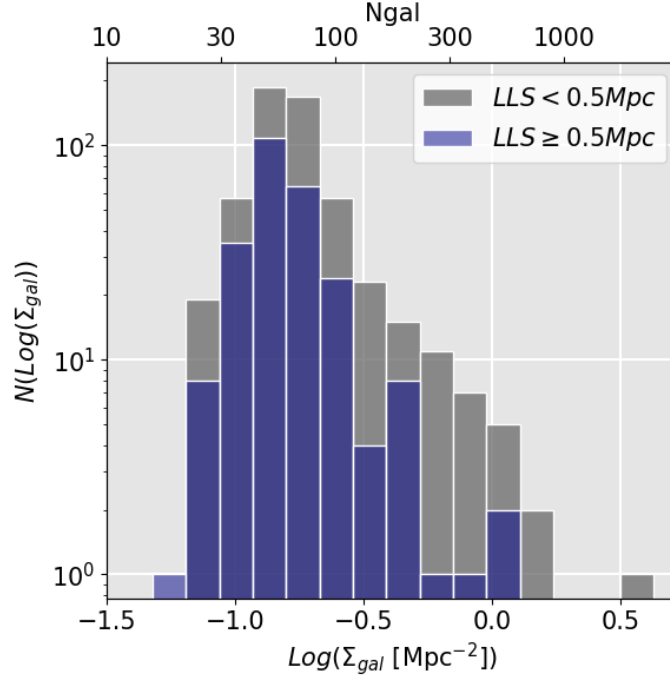
Figure 3.7: Distribution of the galaxy surface density, within 10 Mpc, around the hosts of RGs smaller (grey) and larger (blue) than 500 kpc. The labels on the top x-axis have the same meaning as those on the lower one, only converted to the number of galaxies within a sphere of 10 Mpc.

dependence of the median linear size or the median radio luminosity on the redshift and hence no evidence for cosmological evolution of the population of GRGs.

3.3.5 Spectral analysis

According to the hypothesis that GRGs represent a later stage in the evolution of RGs, we expect GRGs to exhibit steeper spectral indices, indicative of the presence of older electrons compared to smaller RGs. We calculated spectral indices for three frequency ranges: 50-150 MHz (LBA, HBA), 150-610 MHz (HBA, GMRT), and 150-1400 MHz (HBA, Apertif). We aimed to identify differences between GRGs and smaller RGs that may indicate the presence of older electrons in the larger RGs. Fig. 3.9 shows the relation between the linear size of RGs and the integrated spectral index for each frequency pair. The colorbar indicates the redshift of the relevant source and we applied a redshift limit of z=1.5 in the plots to enhance clarity and visualization. Consequently, the redshift of the sources with the highest values in these plots is equal to or greater than 1.5. However, it is worth noting that a few sources are located at higher redshifts and 13 (G)RGs used in this analysis have a spectroscopic redshift greater or equal to one. When using a combination of Apertif and LOFAR images (lower panel), the two variables show a correlation suggesting that the largest RGs exhibit steeper integrated spectra. We assessed the degree of correlation by calculating the weighted Pearson's correlation coefficient, R. The correlation coefficient ranges between -1 and 1. These limits represent a perfect (anti)correlation, while a value of 0 implies that the variables are uncorrelated. We calculated the weights as the inverse of the squared error of the spectral index. We retrieved R=0.36 corresponding to a p-value < 0.001. Such a result indicates that the largest RGs contain the most aged electrons,
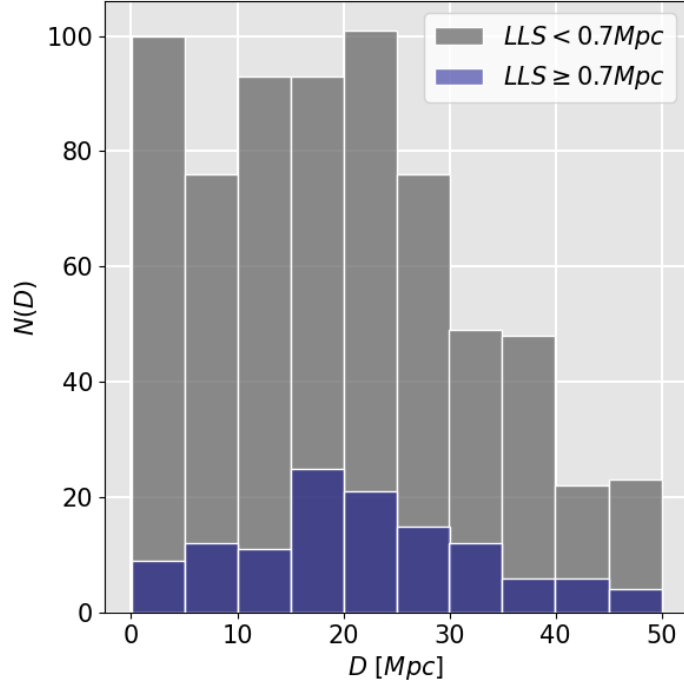
Figure 3.8: Distribution of the minimum distance of ERG hosts from known galaxy clusters. The blue and grey histograms show the distribution for GRGs ($LLS \geq 700$ kpc) and RGs ($LLS \leq 700$ kpc), respectively.

pointing to a scenario in which GRGs are in the latest stage of the evolutionary track. It is worth noticing that this correlation is less evident when exclusively considering GRGs (LLS $\gtrsim$ 700kpc), also because of the smaller number of objects in this range. The result may suggest that factors beyond the age of GRGs contribute to the final size of GRGs. The obtained spectral indices between 150 and 1400 MHz are similar to those reported by Dabhade et al. (2020b) who combined LOFAR DR1 and NVSS data. Moreover, previous work suggested a correlation between the size and the radiative age of the RGs (Parma et al. 1999; Murgia et al. 1999; Jamrozy et al. 2008). Our results support this correlation although we did not directly compute the age of the sources. We also observed a trend involving the spectral index and redshift. It is known that the largest RGs are rarer compared to their smaller counterparts (e.g., Oei et al. 2023a; Simonte et al. 2022a); thus, larger cosmological volumes are needed to sample large RGs. Consequently, the correlation between spectral index and redshift is primarily driven by the relationship between linear size and redshift that may appear in an incomplete sample, rather than an independent trend, in our case. Nevertheless, high-redshift RGs have been found originally by their steep spectral index and small angular size (Tielens et al. 1979; Blumenthal & Miley 1979) and the correlation between the spectral index and redshift is still under discussion (e.g. Miley & De Breuck 2008).

The correlation is not significant when using images at 50 MHz (R=0.27,p-value=0.07) and 610 MHz (R=0.03, p-value=0.87). However, the lack of correlation might be due to the smaller sample size employed for the analysis.

Using the KS and Mann-Withney U tests, we also analysed the distribution of the integrated spectral index of GRGs and smaller RGs. These tests reject the null hypothesis that the two distributions are drawn from the same population with a confidence level greater or equal to 97% only when employing a combination of LOFAR HBA-LBA and HBA-Apertif data and not using HBA-GMRT data. The
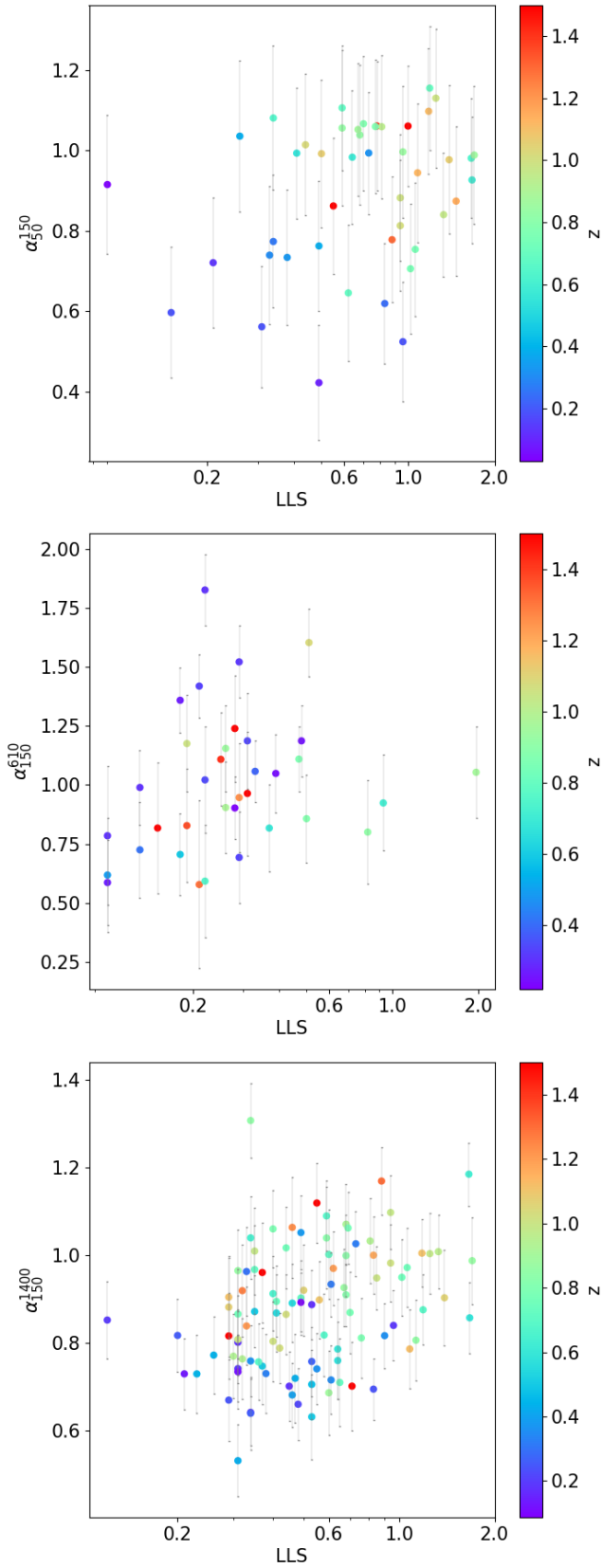
Figure 3.9: Relation between the integrated spectral index, calculated in the range 50-150 MHz (upper panel), 150-610 MHz (middle panel) and 150-1400 MHz (lower panel), and the largest linear size of RGs. The colorbar highlights the redshift of the sources, while the errorbars represent the error on the spectral index.

outcomes may indicate that GRGs and their smaller counterparts have a distinct integrated spectral index distribution, even if the results are not conclusive.

3.4 Conclusions

Even though the number of GRGs has significantly increased in the past few years (Oei et al. 2023a, Mostert et al. subm.), the origin and the causes for their large sizes are still not understood. Previous studies mostly focused only on the physics of GRGs themselves without looking for differences between the properties of the largest and smallest ERGs. Here, we visually inspected the three LOFAR deep fields and compiled a catalogue of 1600 ERGs, of which 280 are classified as GRGs. We measured the integrated radio fluxes of the GRGs and located them in the radio power-size (P-D) diagram. The result highlights the ability of LOFAR to detect faint radio emissions from extended RGs. In particular, we reported a few GRGs with a LLS > 1 Mpc and a radio power smaller than 10^{25} W Hz^{-1} that were not detected in previous radio surveys. The lack of very powerful (> 10^{27} W Hz^{-1}) and large (LLS > 2Mpc) GRGs indicates that the largest GRGs are likely in their latest stage of evolution. Moreover, we used optical catalogues to perform a comprehensive analysis to study the properties of the host galaxies and the environment of GRGs and smaller RGs. To quantify the environmental density, we calculated the galaxy surface density within 10 Mpc from the host galaxy using DESI catalogues (Zhou et al. 2021; DESI Collaboration et al. 2023). We found that the distribution of the galaxy surface density for RGs larger and smaller than 500 kpc is significantly different (p-value=0.002), showing that GRGs statistically reside in sparser environments compared to their smaller counterparts. The result holds when performing the same analysis considering only the ERG hosts with a spectroscopic redshift while retaining all the neighbouring optical galaxies, regardless of their type of redshift. This result does not imply that the environment solely dictates the size of the GRGs. Rather, it indicates that, statistically, within our sample, larger RGs tend to reside in sparser environments compared to their smaller counterparts. Restricting the analysis to only those RGs and neighbouring galaxies for which a spectroscopic redshift is reported in the literature, the KS test returns a p-value= 0.16. However, the sample size, in this case, is three times smaller and much larger samples with spectroscopic redshift available are needed to firmly conclude that GRGs reside in less densely populated environments. The full LoTSS and DESI survey, when finished, hold the potential to provide the necessary confirmation of these results.

The host galaxies of RGs and GRGs share similar properties. Both populations are hosted by massive early-type galaxies with similar stellar masses and accretion mode (predominantly LERG). Nevertheless, the distribution of the SFR in GRG hosts shows an excess of host galaxies with a SFR > 10 M$_\odot$yr^{-1} compared to the hosts of smaller RGs. If star formation triggers the central AGN as well, the results might suggest that these GRGs experience or will experience multiple periods of active jets.

Moreover, we looked at the radio spectra of some of the sources in the LDF-RG sample to find differences in the spectral properties of GRGs and smaller RGs. We calculated the integrated spectral index between multiple pairs of frequencies (50-150 MHz, 150-610 MHz, 150-1400 MHz) and found a positive correlation between the linear size of the ERGs and the steepness of their radio spectrum when using a combination of LOFAR HBA (150 MHz) and Apertif (1400 MHz) observations. On the other hand, the correlation is less evident when considering other frequencies. This result supports the idea that the largest ERGs are also evolved RGs hosting more aged electrons compared to their smaller counterparts. In summary, our results suggest that both age and the surrounding environment may play a significant role in the evolution and size of GRGs. In contrast, the properties of the host

galaxies may have a relatively lesser impact, although we observed differences in the distribution of the SFR within the host galaxies of GRGs compared to smaller RGs.

3.5 acknowledgements

4 Revisiting the alignment of radio galaxies in the ELAIS-N1 field

M. Simonte, H. Andernach, M. Brüggen, D. J. Schwarz, P. N. Best E. Osinga.
A&A, 672, A178 (2023)

Abstract

Aims. Previous studies reported an alignment of the major axes of radio galaxies on various angular scales. Here, we study the alignment of radio galaxies in the ELAIS-N1 Low Frequency ARray (LOFAR) deep field, which covers an area of 25 deg^2.

Methods. The low noise level of about 20 μJy/beam of the LOFAR deep field observations at 150 MHz enabled the identification of 447 extended ($> 30''$) radio galaxies for which we measured the position angle of the major axis. We find that 95% of these sources have either photometric or spectroscopic redshifts, which we then used for a three-dimensional (3D) analysis.

Results. We show the distribution of the position angles of radio galaxies in the ELAIS-N1 field and the results of multiple statistical tests carried out to decipher whether the radio galaxies are randomly oriented. We find that the distribution of position angles is consistent with being uniform. Two peaks around position angles of 50 and 140 deg are spurious and are not caused by an alignment, as shown by a 3D analysis. In conclusion, our results do not support a 2D or 3D alignment of radio galaxies on scales of smaller than ~ 4 deg.

4.1 Introduction

The cosmological principle is an assumption in modern cosmology that states that the Universe is (statistically) isotropic and homogeneous on suitably large scales ($\gtrsim 100$ Mpc). Multiple observations have been carried out in order to investigate the degree of anisotropy in the cosmic microwave background (Bennett et al. 1996; Hansen et al. 2004; Planck Collaboration et al. 2016, 2020) confirming the principle of homogeneity and isotropy of the Universe. However, several authors have reported an intriguing alignment of the linear polarisation of quasars (Stockman et al. 1979; Hutsemekers 1998; Hutsemékers & Lamy 2001; Jain et al. 2004; Cabanac et al. 2005; Pelgrims & Cudell 2014; Slagter & Miedema 2021; Friday et al. 2022). Interestingly, they found an alignment mainly occurring in groups of 10-30 objects and potentially on gigaparsec (Gpc) scales.

Some other studies focused on the alignment of radio galaxy jets (e.g., Sanders 1984; Kapahi et al. 1985; West 1991; Joshi et al. 2007; Tiwari & Jain 2013), and some of their findings support a possible

departure from the cosmological principle. Taylor & Jagannathan (2016) studied the spatial distributions of the major-axis position angle of radio galaxies in the ELAIS-N1 Giant Metrewave Radio Telescope (GMRT, Ananthakrishnan 1995) deep field. These authors claimed the existence of a 2D alignment around $PA \sim 140°$ over an area of ~ 1.7 deg^2. However, without redshift information for the host galaxies, they were not able to perform a 3D analysis. The first attempts to detect an alignment on larger scales were made by Contigiani et al. (2017) and Panwar et al. (2020) who used catalogue data from the Faint Images of the Radio Sky at Twenty-centimetres (FIRST, Becker et al. 1995; Helfand et al. 2015) and the TIFR GMRT Sky Survey (TGSS, Intema et al. 2017). Contigiani et al. (2017) and Panwar et al. (2020) detected a signal over a scale of smaller than 2°, but did not find strong evidence for a 3D alignment. For the first time, Blinov et al. (2020) explored the alignment of parsec-scale jets, finding that their radio sources do not show any global alignment. However, Mandarakas et al. (2021), with a similar but larger sample, detected a strong signal of an alignment of parsec-scale jets in multiple regions of the sky. Nevertheless, the redshift distribution of their sources spans a wide range, $0 < z \lesssim 1.5$ Most recently, Osinga et al. (2020) searched for alignment using 7555 extended sources from the first data release of the Low Frequency ARray Two metre Sky Survey (LoTSS, Shimwell et al. 2019). However, despite their use of host redshifts, Osinga et al. (2020) were only able to detect a 2D alignment of the position angles of the radio galaxies over a scale of 5° and were unable to exclude the possibility that the signal arises from systematic effects.

Although multiple studies have now presented evidence for a 2D or 3D alignment, an explanation for such a phenomenon is lacking. West (1991), Hutsemékers et al. (2014) and Pelgrims & Hutsemékers (2016) found an alignment between the radio and optical emissions from active galactic nuclei (AGN) and the surrounding large-scale structure. Moreover, Malarecki et al. (2013, 2015) showed that giant radio galaxies (Willis et al. 1974) have a tendency to grow in a direction perpendicular to the major axes of galaxy overdensities. However, the connection between the orientation of radio galaxy jets and the large-scale structure is unclear.

In this paper, we revisit the alignment of the jets of radio galaxies in the ELAIS-N1 field. We make use of photometric redshifts of the host galaxies to perform a 3D analysis.

The layout of this paper is as follows: In Sect. 4.2 we explain how we built our catalogue of extended radio galaxies (ERGs) and how we measured their orientation. In Sect. 4.3 we present the results of our 2D and 3D analyses. In Sect. 4.4, we discuss our results in the context of theoretical and observational work on the orientation of radio galaxies and provide a summary.

Throughout this work we adopt a flat ΛCDM cosmology with $H_0 = 70$ km s^{-1} Mpc^{-1}, $\Omega_{\rm m} = 0.3$, and $\Omega_{\Lambda} = 0.7$.

4.2 Methods

We inspected the ELAIS-N1 LOw-Frequency ARray (LOFAR, Van Haarlem et al. 2013) deep field (Sabater et al. 2021). With an effective observing time of 163.7 h, it reaches a root mean square noise level at 150 MHz lower than 30 μJy beam^{-1} across the inner 10 deg^2 and below 20 μJy beam^{-1} in the very centre. The ELAIS-N1 LOFAR Deep Field (ELDF) is centred on 16h11m00s+55°00′00″(J2000) and covers an area of about 25 deg^2. The 6" resolution of the radio image ensures a robust classification of the sources and, most importantly, the identification of the hosts and radio features such as jets and hotspots.

4.2.1 The sample of extended radio galaxies

We searched for all the ERGs with a largest angular size (LAS) of greater than $\sim$ 30" within an area of $\sim$ 25 deg^2. We measured the LAS as the distance between the opposite ends of the ERGs. However, this method can overestimate the size of the Fanaroff-Riley type II (FRII, Fanaroff & Riley 1974) as mentioned by Kuźmicz & Jamrozy (2021). For ERGs of this kind, we therefore measured the LAS as the distance between the two hotspots, whenever identified on the VLA Sky Survey images (Lacy et al. 2020). The radio position angles (RPAs) were manually measured (using Aladin[*], Bonnarel et al. 2000) in the range of [0,180) degrees as the angle between the major axis and the local meridian of the sources from N through E. For straight (or only slightly bent) FRI and FRII ERGs, the RPA is either that of the inner jets (FR I) or that of the direction connecting the two hotspots (FR II). In the case of bent sources (e.g., wide-angle-tailed RGs), measuring the RPA is less trivial. For such cases, we measured the RPA in the vicinity of the core where the jets are not usually bent yet and flagged them as uncertain measurements. We carefully avoided measuring the RPA of overlapping sources unless the morphology of the ERGs was very clear.

A large number of optical and infrared surveys, such as the Wide-Field Infrared Survey Explorer (WISE, Cutri & et al. 2012; Cutri et al. 2013; Schlafly et al. 2019; Marocco et al. 2021), the Sloan Digital Sky Survey (SDSS, York et al. 2000), the Legacy survey (Dey et al. 2019), and the Panoramic Survey Telescope and Rapid Response System (Pan-STARRS, Flewelling et al. 2020) enabled us to identify the host galaxies (see Kondapally et al. 2021; Andernach et al. 2021; Simonte et al. 2022a, for further details of the host identification and radio-source classification). We looked for available spectroscopic (Ahumada et al. 2020) and photometric (Rowan-Robinson et al. 2013; Bilicki et al. 2014, 2016; Beck et al. 2016, 2021; Zhou et al. 2021; Duncan et al. 2021; Wen & Han 2021; Duncan 2022) redshifts in multiple catalogues. If multiple photometric redshifts were available for a single source, we computed their mean and error by taking the standard deviation of the various redshifts. For spectroscopic redshifts, we do not report errors because they are generally more accurate (typical errors are usually around 0.00015) than the precision we can achieve on the linear size given our errors in measuring the angular size. There is no available redshift estimate for 15 host galaxies; these sources are either optically very faint or are only detected with infrared. The deepest full-sky catalogue is the Zhou et al. (2021) DESI DR9 photometric redshift catalogue (a deeper catalogue from Duncan et al. (2021) exists over the inner 7deg^2 of the ELAIS-N1 field). In Zhou et al. (2021), the faintest galaxies have a maximum redshift of around 1.3. We therefore assumed a redshift in the range of 1.1-1.5 for those host galaxies without redshift listed in the literature. This assumption will not affect our analysis as we used only those sources with a redshift reported in the literature for the 3D analysis.

We find 447 ERGs for which we provide a redshift, LAS, largest linear size (LLS), and RPA. We show some of our ERGs in Table C1 and the full list will be made available at the CDS and through the VizieR service[†] (Ochsenbein et al. 2000). To test the alignment in the region inspected by Taylor & Jagannathan (2016), we located all the sources that these authors used in their analysis (their Fig. 2) and measured their RPAs. Some of these RGs have an angular size of smaller than 30″. The resolution of 6" of the LOFAR images does not enable reliable measurement of the RPA of the smallest sources and we flagged these measurements as uncertain. We had to discard 9 RGs used by Taylor & Jagannathan (2016) as 8 of them are separate sources and one is a spiral galaxy (see Appendix C). However, we were able to identify a further 24 ERGs using the LOFAR data within the sky area studied by these latter authors and added these to our sample. Table 4.1 compares our sample with previous lists of RGs used for the RPA analysis. In this work, we analysed a field that is approximately ten times

---

[*]https://aladin.cds.unistra.fr
[†]https://vizier.cds.unistra.fr

(1)	(2)	(3)	(4)	(5)
Survey	Freq.	RMS	N of	RGs density
	GHz	mJy/b	RGs	deg^{-2}
Taylor[1]	0.61	0.01	65	38.2
FIRST[2]	1.4	0.15	30059	4.3
FIRST[3]	1.4	0.15	18775	1.9
LoTSS[4]	0.15	0.07	7555	17.8
ELDF[5]	0.15	0.03	447	17.9
ELDF-C[6]	0.15	0.02	78	45.9

Table 4.1: Comparison between our catalogue and previous samples. References: 1-Taylor & Jagannathan (2016), 2-Contigiani et al. (2017), 3-Panwar et al. (2020), 4-Osinga et al. (2020), 5,6-this work: ELDF-C refers to the central region of the ELDF ($241.5° < RA < 243.75°, 53.9° < DEC < 55.2°$).

larger than that of Taylor & Jagannathan (2016), but much smaller than those used by Contigiani et al. (2017), Panwar et al. (2020), and Osinga et al. (2020). Nevertheless, our sample has the largest RG sky density in the central region ($241.5° < RA < 243.75°, 53.9° < DEC < 55.2°$), which is reported in the last row of Table 4.1, while the second-to-last row shows the RG sky density considering the full ELDF.

4.2.2 Statistical tests

We performed multiple tests to assess the (non-)uniformity of the RPA distribution. Different methods have been used in past analyses to study the distribution of the orientation of RGs. We use five different tests for (non-)uniformity of angles:

1. The Kolmogorov-Smirnov (KS) test compares the underlying distribution of the sample of the RPA against a given distribution, which in our case is a uniform distribution. The null hypothesis is that the two distributions are identical and the closer the p-value is to zero the more confident we are in rejecting the null hypothesis. A common threshold used to reject the null hypothesis of the two distributions being drawn from the same population is a p-value p<0.05, which means that there is only a 5% chance that the two samples are in fact drawn from the same population.

2. Pearson's χ^2 test for uniformity tests the null hypothesis that the frequency distribution of certain events observed in a sample is consistent with a particular theoretical distribution (in our case a uniform one). As with the KS test, the smaller the p-value the more likely it is that the two distributions are different. This test is performed with binned data, and in our case we used 18 bins of 10° in width.

3. Our set of RPAs belongs to the category of circular data (Fisher 1993), which are fundamentally different from linear data due to their periodic nature. The Rayleigh test (Mardia & Jupp 2000) assesses the uniformity of circular data. To this end, this test compares the test statistic of the unit vector resulting from the sum of all the vectors pointing towards the different angles of the sample, with the same statistics estimated from a uniformly distributed sample. The null hypothesis of such test is that the data are uniformly distributed over the circle. The test statistic is the mean resultant length of the unit vector and is defined as

$$\bar{R} = \frac{1}{n}\left[\left(\sum_{i=1}^{n}\cos\theta_i\right)^2 + \left(\sum_{i=1}^{n}\sin\theta_i\right)^2\right]^{1/2}, \tag{4.1}$$

where n is the size of the sample and the angles θ_i are the RPAs multiplied by two (because these are orientations (axial vectors) in the range [0°, 180°) while the Rayleigh test is performed on the range [0°, 360°)). $\bar{R}$ can range from 0 to 1. This statistic is zero for a uniform distribution, and therefore it is reasonable to reject uniformity when R is large. It is worth mentioning that this test is not sensitive to non-uniform distributions that have $\bar{R} = 0$. An example is a bimodal distribution with two peaks that are 180° apart as every vector pointing towards a certain direction is cancelled by a vector pointing along the opposite direction. This issue can mildly affect our analysis because the major peaks in our distributions of the RPAs are 180° apart once the RPAs are multiplied by two (see Sect. 4.3 below).

4. The semi-variance (Cressie 1993) is a statistical tool used in spatial analysis to measure the dispersion of a certain variable on different scales. It is defined as follows:

$$\gamma(d) = \frac{1}{2m(d)} \sum_{i=1}^{m(d)} [s(x_i) - s(x_i + d)]^2 , \tag{4.2}$$

where $m(d)$ is the number of pairs separated by a (angular) distance in the range $[d, d + \delta d]$ (we used $\delta d = 0.2°$) and s is the variable measured at the vector location x_i and in our case is the RPA of the ERGs. The semi-variance is constant over all angular scales when the distribution of the variable s is uniform. A value for the semi-variance of smaller than what is predicted by a uniform distribution at a certain scale indicates an alignment of the ERGs. On the other hand, a larger semi-variance suggests a larger dispersion than expected from a random distribution, indicating that no alignment is present on that scale. We performed a simple Monte-Carlo simulation to infer the value of the semi-variance of randomly distributed ERGs on different angular scales. We generated 447 (which is the size of our sample) random angles uniformly distributed in the range $[0, 180)$, which have the same spatial distribution as the ERGs in our sample and we computed the semi-variance on different angular scales. We repeated the operation 10000 times and then averaged the semi-variance values on the different scales. We folded the data in circularity to take into account the periodicity of the RPAs. On every scale, we obtained a constant semi-variance of 0.82, which is consistent with the result from Taylor & Jagannathan (2016). The error on the semi-variance, σ_{SM} was estimated by calculating the standard deviation of the 10000 values on each angular scale.

5. Finally, we probed the alignment of the ERGs at different angular scales using the dispersion measure analysis (Jain et al. 2004). The dispersion measure is defined as the inner product between a certain position angle θ and the RPAs, θ_k, of the n closest sources to a certain i-th ERG (including the source itself) and it is an indication of the alignment of the ERGs. Following Jain et al. (2004), Contigiani et al. (2017), and Osinga et al. (2020), it can be shown that the maximum dispersion measure around the source i is

$$D_{i,n}|_{\max} = \frac{1}{n} \left[\left(\sum_{k=1}^{n} \cos(\theta_k) \right)^2 + \left(\sum_{k=1}^{n} \sin(\theta_k) \right)^2 \right]^{1/2} . \tag{4.3}$$

The closer $D_{i,n}|_{\max}$ is to 1, the more aligned the n galaxies are. The statistic, S_n used to test the (non-)uniformity of the distribution of the RPAs is the average of the $D_{i,n}|_{\max}$ calculated for each source of the sample. This statistic computed from our dataset is compared to the same statistics coming from Monte-Carlo-simulated samples, $S_{n,\mathrm{MC}}$. To compute $S_{n,\mathrm{MC}}$ we generated 447 randomly oriented ERGs with the same spatial distribution as our sources and followed the formalism described in Jain et al. (2004), Contigiani et al. (2017) and Osinga et al. (2020). We repeated the calculation of $S_{n,\mathrm{MC}}$ 10000 times and estimated the average, $\langle S_{n,\mathrm{MC}} \rangle$, and the error, $\sigma_{n,\mathrm{MC}}$, as the standard deviation of 10000 generated statistics. The significance level for rejecting the null hypothesis that a sample of
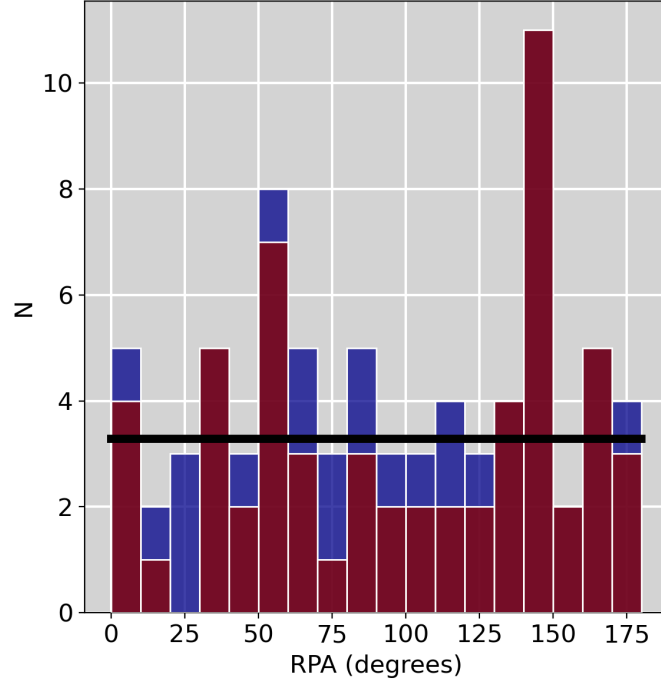
Figure 4.1: Distribution of the RPAs of the 78 ERGs (blue histogram) that we found in the inner region of the ELDF and of the 59 certain sources (red histogram). The black line shows the expected number of objects per bin for a uniform distribution of 78 ERGs.

ERGs is randomly oriented is found through a one-tailed significance test, expressed as:

$$SL = 1 - \Phi\left(\frac{S_{n} - \langle S_{n,MC} \rangle}{\sigma_{n,MC}}\right), \tag{4.4}$$

where Φ is the cumulative normal distribution function. The closer the significance level is to zero the more confident we are in rejecting the hypothesis of uniformity. As the number of nearest neighbours can be translated to an angular scale extending to the *n*-th nearest neighbour, we can probe multiple angular scales by varying *n*. To do so, we calculated the maximum angular distance between the relevant ERG and the n-th closest neighbour and took the median value among the 447 sources. The same analysis can be implemented considering the 3D position of the ERGs to test whether a 3D alignment is present between sources that are physically close to each other. We approximated the redshift of the source with the average redshift estimated for each ERG without taking into account the error and we did not include those sources without a redshift value reported in the literature. The uncertainties of some redshift estimations could mildly affect the analysis: in fact, while ERGs with $z < 1$ have a redshift error of about 0.05, for more distant sources, which represent 30% of our sample, the error increases to 0.2. We then converted the redshift to comoving distance and measured the 3D comoving distance between all the ERGs in our sample.

Moreover, Jain et al. (2004) verified that the variance of the statistic S_n is inversely proportional to the size of the sample which means that, compared to Contigiani et al. (2017) and Osinga et al. (2020), who used much larger samples, we are more affected by the shot noise.
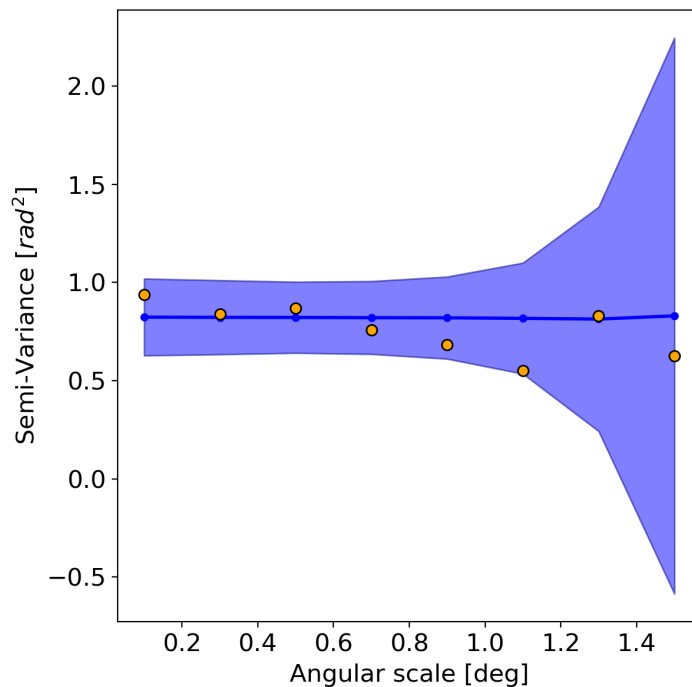
Figure 4.2: Estimate of the semi-variance on different angular scales in the inner region of the ELAIS-N1 field. The blue line and points are the semi-variance values obtained for randomly generated position angles with the same spatial distribution of the 78 ERGs. The shadowed region represents the $2\sigma_{SM}$ values. The orange points are estimated from our dataset.

4.3 Results

In this section, we present the distribution of the RPAs in the ELAIS-N1 field. We initially focus on the inner region studied by Taylor & Jagannathan (2016) and then expand the analysis to the entire ELDF.

4.3.1 Alignment in the central part of ELAIS-N1

Here, we look at the distribution of the RPAs in the inner ~ 1.7 deg^2 of the ELAIS-N1 field ($241.5 < RA < 243.75, 53.9 < DEC < 55.2$), where Taylor & Jagannathan (2016) found a statistically significant alignment of radio galaxies. We recall that 9 of the radio sources they used in their analysis are not genuine radio galaxies and we were able to add a further 24 ERGs using LOFAR data. Thus, the sample for such an analysis consists of 78 ERGs, of which 19 are flagged as uncertain RPA measurements. We show the distribution of the RPAs in the inner region of the ELAIS-N1 field in Fig. 4.1. The blue histogram shows the distribution of the total sample of RPAs in this region, while the red histogram shows the same but with the uncertain measurements excluded. The figure clearly shows a peak at RPAs around $140°$, which is in agreement with Taylor & Jagannathan (2016). We then carried out the statistical tests explained in Sect. 4.2.2 and found a p-value of 0.66 and 0.31 for the KS test and the χ^2 test, respectively. The latter test is valid for large samples and it is customary to recommend in applications of the test that the smallest expected number should be 5 in any one bin (Cochran 1952). We performed the test using 13 bins, each with a width of $15°$, which lead to an expected value of about 6.5 elements per bin. The resulting p-value is 0.23 in this case. Concerning the Rayleigh test,
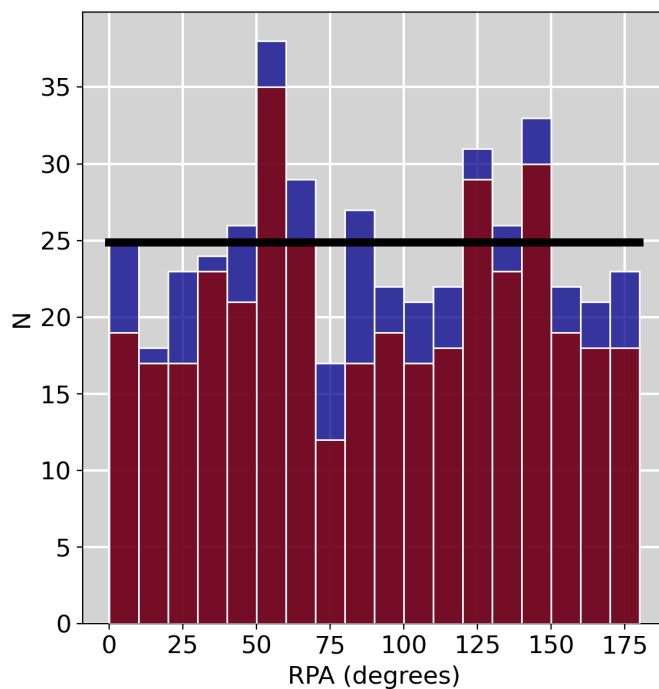
Figure 4.3: Distribution of the RPAs of the 447 ERGs we find in the ELDF (red histograms) and of the 377 certain sources (red histogram). The black line shows the expected number of objects per bin for a uniform distribution considering the total sample.

we find a mean resultant length of $\bar{R} = 0.009$ which results in a p-value=0.96. Therefore, even though the distribution shows a clear peak, we cannot reject the hypothesis of uniformity of the RPAs in this region. Moreover, the analysis involving the semi-variance (Fig. 4.2) shows that there is no correlation between the RPAs of the ERGs located at different positions on the sky at any angular scale. In Fig. 4.2, the blue line and points are the values estimated using randomly generated data that have the same spatial distribution as the 78 ERGs in the inner region of the ELAIS-N1 field, while the orange points are the result of the analysis performed on our dataset.

We did not perform an analysis based on the dispersion measure (i.e. method 5 listed in Sect. 4.2.2) because of the smaller number of ERGs when restricting the study to the inner region of the field. With a sample of only 78 objects, we are certainly dominated by the shot noise (Jain et al. 2004), which would cancel out any signal unless the alignment is very strong, which does not seem to be the case here.

We performed the statistical tests on the sample of 59 ERGs for which we could measure a reliable RPA as well. We obtained p-values of 0.10, 0.01 and 0.46 for the KS, χ^2, and Rayleigh test, respectively. The result of the χ^2 test holds when considering bins with a width of 15°. Nevertheless, this is the only test that suggests an alignment of the ERGs in the inner region; we reiterate that the semi-variance test applied to this smaller sample cannot reject the hypothesis of a uniform distribution.

The sensitivity of the LOFAR ($20\,\mu Jy$/beam) and GMRT ($10\,\mu Jy$/beam) ELAIS-N1 deep field observations are quite similar, but the four-times-lower frequency of LOFAR makes an RG with a typical spectral index of -0.8 about three times brighter at 144 MHz compared to 610 MHz. Moreover, the availability of deeper infrared source catalogues, such as CatWISE (Marocco et al. 2021) and unWISE (Schlafly et al. 2019), enables the identification of more distant galaxies, which may emit in the radio
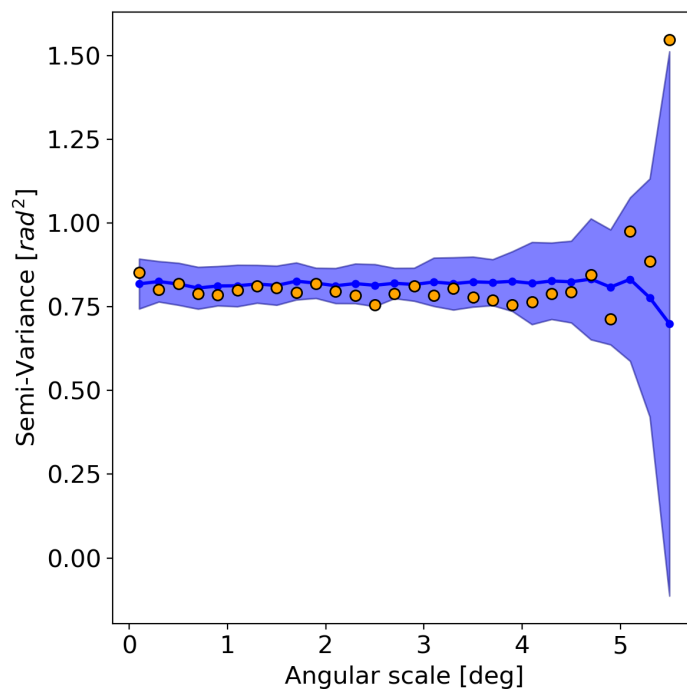
Figure 4.4: Estimate of the semi-variance on different angular scales. The blue line and points highlight the constant value of the semi-variance for randomly generated position angles with the same spatial distribution of the 447 ERGs in our sample. The shadowed region represents the $2\sigma_{SM}$ values. The orange points are the semi-variance values of our sample.

band as point-like sources. Such contamination, if superimposed on the emission of an ERG, may slightly change the morphology of the latter and lead to an erroneous RPA measurement.

In order to attempt to reproduce the Taylor & Jagannathan (2016) results, we extracted the positions, sizes and RPAs of the RGs from their Fig. 2 as follows: the end points of all vectors were digitised with the g3data software, and saved as RA, DEC in degrees. We then reviewed the RPA measurements and were able to closely match the histogram shown in their Fig. 3. We ran our first four statistical tests on the recovered data, but found that none of them is able to reject the hypothesis of uniformity. In particular, for the Rayleigh test, we obtained a mean resultant length of 0.09 from our analysis of these data, which is highly discrepant with the value of 0.68 derived by Taylor & Jagannathan (2016) that led them to claim a non-uniformity of RPAs. The origin of this difference is uncertain, although we note that if we do not multiply the RPAs by a factor of two (a step that is required, because the test assesses uniformity over a circle and the RPAs are distributed over [0, 180)), we obtain an erroneous mean resultant length of 0.64, which is much closer to the value quoted by Taylor & Jagannathan (2016).

4.3.2 Alignment in the entire ELAIS-N1 field

We show the distribution of the RPAs of the radio galaxies in the ELDF in Fig. 4.3. The blue histogram represents the total sample, while the red histogram shows the distribution for the 377 certain sources, that is, those ERGs that do not show a complex morphology and for which we were able to accurately measure the RPA. The black line denotes the expected number of objects per bin if the distribution were uniform. We subsequently performed the same statistical tests considering the total
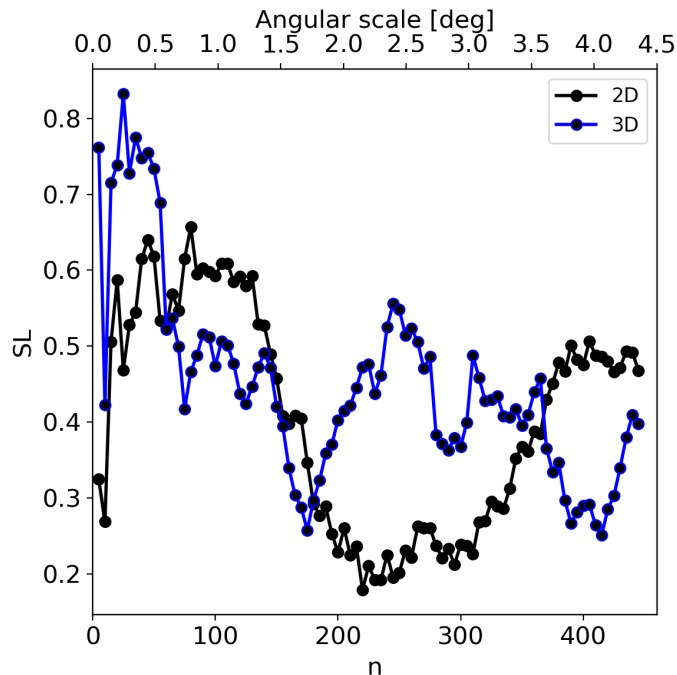
Figure 4.5: Significance level of the dispersion measure test (SL) as a function of the nearest neighbours (n, lower abscissa) and angular scale in degrees (upper abscissa). The black line shows the results of the 2D analysis while the 3D analysis is shown with the blue line. Such a large SL (>> 0.03) shows that no alignment is present in the ELAIS-N1 field at any scale in our analysis.

sample. The results, with p-values equal to 0.71, 0.33, and 0.88 for the KS test, χ^2 test, and Rayleigh test, respectively, suggest that the uniformity holds when including the entire field as well. These results are also confirmed by the analysis of the semi-variance. We measured the semi-variance in our sample, shown by the orange points in Fig. 4.4. The blue line and points are the semi-variance values estimated from randomly generated data and the shadowed region represents the $2\sigma_{SM}$ values. The larger uncertainties on the largest scale are due to poor statistics, because not many pairs are separated by such large distances. Overall, there is no clear evidence for a convincing signal in favour of an alignment as the orange points are always consistent with 0.82 within the error.

Finally, we show the results of the 2D (black line) and 3D (blue line) dispersion measure tests in Fig. 4.5. The significance level, SL, is plotted as a function of the number of nearest neighbours, n, and angular scale in degrees. Following previous studies (e.g. Contigiani et al. 2017), a commonly used criterion for the presence of an alignment signal is SL <0.03 (log(SL) < −1.5). As mentioned in Sect. 4.2.2, our analysis is more affected by the shot noise because of the comparatively small size of our sample. However, a minimum significance level of about 0.2 in Fig. 4.5 suggests there is no evident signal, either in the 2D or in the 3D analysis, at any scale.
These results also hold when considering only the ERGs with reliable RPA measurement.
Even though the tests suggest that radio galaxies are randomly oriented, two conspicuous peaks are visible on an RPA range: one between $50° − 60°$ and another between $140° − 150°$ (the latter was seen by Taylor & Jagannathan 2016 as well). The Poisson distribution gives the probability of a given number of observations occurring in a fixed interval of PAs, where the rate of occurrence of these
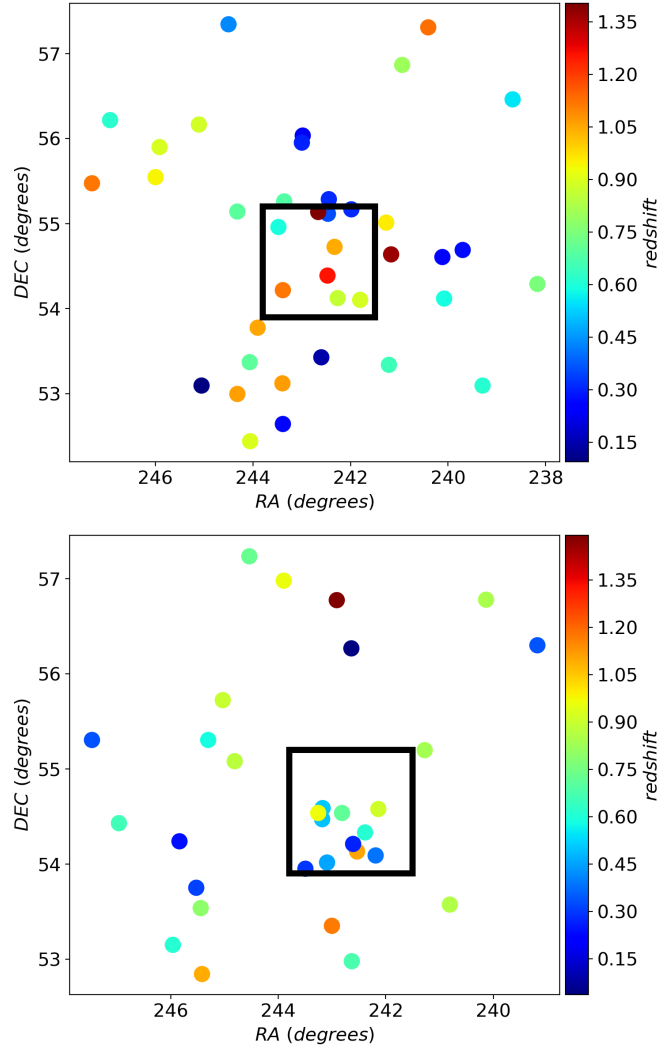
Figure 4.6: Spatial distribution of 39 ERGs with RPA between 50° and 60° (upper panel) and 31 ERGs with RPA in the range 140° − 150°. The colour bar shows the redshifts of the ERGs. The analysis was restricted to $z \le 1.5$. The black box represents the field of Taylor & Jagannathan (2016).

observations is constant and known. This rate is obtained from the uniform distribution. Therefore, using such a distribution, we find that the two peaks are $\sim 2.5\sigma$ (for RPAs between 50° and 60°) and $\sim 1.5\sigma$ (for RPA between 140° and 150°) above the average. Fig. 4.6 shows the spatial and redshift distributions of the ERGs with an orientation of between 50° and 60° (upper panel) and between 140° and 150° (lower panel). We selected the ERGs up to redshift 1.5 because the majority of ERGs at larger redshifts either do not have a redshift estimate in the literature or have very large errors. The black rectangles highlight the region inspected by Taylor & Jagannathan (2016). In both cases, there is no 3D alignment of ERGs as the redshifts span the range of $0.1 \lesssim z \lesssim 1.5$.

4.4 Discussion and summary

The tidal torque theory predicts that the angular momentum of the dark matter proto-halos is acquired during their formation which occurs along the entire evolution of the large-scale structure of the Universe (Peebles 1969; Doroshkevich 1970; White 1984; Porciani et al. 2002; Schäfer 2009). As a result, an alignment between optical galaxies and the large-scale structure (e.g. filaments and sheets) is expected (Hu et al. 2006; Joachimi et al. 2015; Kirk et al. 2015). In a first attempt to study this alignment, Hawley & Peebles (1975) found a small departure from isotropy in the distribution of the orientation angle, which is measured as the angle between the major axis of the galaxy and the local meridian. Lee (2004) argued that the observed large-scale coherence in the orientation of nearby spiral galaxies found by Navarro et al. (2004) can be fully explained by the tidal torque theory. Others have tried to look at a possible alignment of galaxies and most authors found that the minor axes of early-type galaxies are preferentially oriented perpendicular to the host filament (Tempel et al. 2013; Tempel & Libeskind 2013; Hirv et al. 2017), while late-type galaxies have spin axes parallel to the closest filament (Tempel et al. 2013; Tempel & Libeskind 2013; Hirv et al. 2017; Blue Bird et al. 2020; Kraljic et al. 2021; Tudorache et al. 2022). However, some conflicting results have been found (Jones et al. 2010; Zhang et al. 2015; Pahwa et al. 2016; Krolewski et al. 2019). Recently, Rodriguez et al. (2022), using the IllustrisTNG simulations (Nelson et al. 2019), found an alignment with the large-scale structure of red galaxies in the centres of galaxy clusters and groups. These authors then speculated that this anisotropy in the orientation of the central galaxies is the consequence of a concatenation of alignments. Starting from the alignment between the central galaxy and the host cluster (Yuan & Wen 2022), eventually, the host halo aligns with the structures surrounding it.

Some work found that there is a mild preference for radio jets to align with the minor axis of the galaxy host (Kotanyi & Ekers 1979; Battye & Browne 2009; Kamali et al. 2019; Vazquez Najar & Andernach 2019). Assuming that the alignment between radio jets and optical galaxies is real, one could in principle look at the alignment between the radio galaxies and the large-scale structure (e.g. West 1991). Nevertheless, some opposing results regarding the orientations of radio jets have been found (Schmitt et al. 2002; Verdoes Kleijn & de Zeeuw 2005; Hopkins et al. 2012), casting doubts on this assumption.

In the present work, we revisited the alignment of radio jets in the ELAIS-N1 field. We inspected the LOFAR ELAIS-N1 deep field in which we identified the host galaxies of 447 ERGs whose radio emission extends over at least $\sim 0.5'$. We measured the RPA of the major radio axis (assuming it to be a tracer of the underlying radio jet direction) and studied its distribution using a number of statistical tests, none of which is able to reject the null hypothesis of uniform orientations. Similar results are obtained when restricting the analysis to the region inspected by Taylor & Jagannathan (2016). Only when restricting the sample to the 59 ERGs with a reliable RPA measurement in the inner region does the χ^2 test return a p-value=0.01 (i.e. it suggests there is a 1% chance that the result is a statistical fluctuation). However, none of the other statistical tests on this sample are able to reject the hypothesis of uniformity of the RPA distribution. We recovered the data used by Taylor & Jagannathan (2016) in their analysis and show that, even with such sample, we cannot obtain the same results. Furthermore, we find that the redshifts of ERGs with orientations near the two peaks (around 50° and 140°) span a wide range, namely $0.1 \lesssim z \lesssim 1.5$, strongly arguing against the idea of a 3D alignment of radio galaxies. Other reports of a 3D alignment (e.g. Contigiani et al. 2017; Panwar et al. 2020) have not been statistically significant. However, several studies reported a 2D alignment (Contigiani et al. 2017; Panwar et al. 2020; Mandarakas et al. 2021) over angular scales similar to those that we studied. The maximum angular scale we were able to explore is $\sim 4°$ (see Fig. 4.4), which is the scale over which Osinga et al. (2020) found a 2D alignment. The combination of the two results might suggest that the

2D alignment of radio galaxies may exist on scales larger than those probed by our analysis.

Acknowledgements

5 Conclusion and Outlook

Despite the extensive literature on various properties of GRGs, the underlying reason for their exceptional size remains enigmatic. Previous work predominantly delved into the properties of GRGs alone, with only a handful providing a comparative analysis between GRGs and smaller RGs. In this thesis, I presented a relatively novel approach by incorporating a sample of smaller RGs and conducting a comprehensive comparison of their properties with those of GRGs across multiple wavelengths.

After introducing the basic astrophysical and observational concepts of this thesis in Chap. 1, I presented the properties of 74 GRGs in the LOFAR Boötes deep field in Chap. 2. This section explores the spectral properties of GRGs through radio observations at 150 MHz and 1.4 GHz, revealing that nearly all GRGs exhibit an integrated spectral index of 0.8, regardless of the linear size of the GRG. Furthermore, I discussed that GRGs are unlikely to be fueled by exceptionally powerful Active Galactic Nuclei (AGN), given that they host a black hole undergoing radiatively inefficient accretion. Additionally, in this preliminary investigation, I did not find any significant environmental differences when comparing the GRG sample with a small sample of approximately 200 RGs.

In Chap. 3, I extended this analysis to the three LOFAR deep fields (Boötes, ELAIS-N1, Lockman Hole). Here, I report the detection of 280 GRGs, most of which are new. Noteworthy some of these GRGs have a projected linear size larger than 1 Mpc and a radio power smaller than 10^{25} W Hz^{-1} —too faint to have been detected in previous radio surveys. By providing a catalogue of about 1300 smaller RGs, I systematically tested the impact of the environment, host galaxy properties, and RG age on the final size and morphology of RGs. Utilising a proxy for environmental density based on the number of neighbouring galaxies within a 10 Mpc radius from the host galaxy, I found that GRGs statistically reside in sparser environments compared to their smaller counterparts. While my results do not imply that the environment solely dictates the GRG size, they suggest a statistical tendency for larger RGs to inhabit sparser environments. Deep optical and infrared data further reveal that the properties of GRG and RG host galaxies are quite similar. Both populations are predominantly hosted by massive early-type galaxies and the central black hole is undergoing radiatively inefficient accretion. My calculations of the integrated spectral indices between various frequency pairs affirm a positive correlation between the RG size and the steepness of their radio spectrum. This correlation supports the hypothesis that larger RGs are in a more advanced evolutionary state, hosting more aged electrons compared to their smaller counterparts. In summary, my findings propose that both age and the surrounding environment may significantly influence the evolution and size of GRGs. In contrast, host galaxy properties might have a relatively lesser impact, although differences in the distribution of SFR within host galaxies of GRGs compared to smaller RGs were observed.

Several authors reported an intriguing alignment of the jets of RGs across multiple scales. In Chap. 4, I reviewed the alignment of RGs in the ELAIS-N1 field. Utilising spectroscopic and photometric redshifts for the analysed radio sources, I conducted a meticulous 3D analysis to investigate the alignment of jets among physically proximate RGs. The results revealed a uniform orientation of the major axis position angle of RGs in the ELAIS-N1 field. Despite the presence of peaks around 50° and 140° in the distribution of the position angle, the broad range of redshifts (ranging from 0.1 to 1.5) observed among RGs with orientations near these peaks strongly argues against the hypothesis of a 3D alignment of radio galaxies.

5.1 Future projects

The LOFAR observations have proven to be a powerful tool for detecting a large number of GRGs. While serving as a valuable starting point, these low-frequency observations need to be complemented with studies at higher frequencies to thoroughly investigate the spectral properties of these radio sources. The LOFAR deep fields are observed for a long integration time (> 80 hours) leading to a sensitivity of about 30 μJy/beam. Achieving a comparable sensitivity at higher frequencies (e.g., 1.4 GHz) would necessitate time-consuming observations. Consequently, only a limited number of GRGs have been studied using a combination of LOFAR and high-frequency observations.

To address this gap, I will focus on some of the brightest GRGs in the LOFAR deep fields to study their spectral properties. The first project consists of 16 hours observation of the GRG J1424+3436, a DDRG of 1.7 Mpc in the Boötes deep field (see Fig. 1.8) obtained at the GMRT (with me as the P.I.). With this project, I aim to produce a highly resolved (6″ resolution) spectral index map between 150 and 650 MHz of the source. Furthermore, combining these observations with LBA (50 MHz) and Apertif (1.4 GHz) data, I aim to address the following questions: *Are GRGs the long-term evolutionary products of smaller RGs? What is the duty cycle in J1424+3436 and does it have an impact on the size of the source? Is the NE lobe of J1424+3436 able to re-accelerate particles?* This study of the GRG J1424+3436 will not only provide valuable insights into the specific source but will also contribute to the general knowledge of RGs evolution. The results obtained from this study will be essential for testing and refining existing models, improving our understanding of the lifecycle of relativistic electrons in extreme environments such as the jets, lobes and hotspots of RGs. Moreover, this study will serve as a pilot study for future deep observations of some of the GRGs in the LOFAR deep fields.

6 Acknowledgments

The three years of my PhD in Hamburg have been the best years of my life. Here, I had the chance of doing the best job in the world, exploring different cultures and creating and building new friendships that I hope will last forever. For these amazing years, I would like to express my gratitude to the following people:

My parents, whose unwavering trust and support have been my guiding light throughout my academic journey. I am profoundly grateful for their encouragement, understanding, and for allowing me the freedom to pursue my passions without pressure.

I would like to thank my supervisor, *Marcus Brüggen*, for his support during my PhD. I feel privileged to have had him as both a supervisor and a friend. I deeply admire his exceptional ability to build a positive relationship with his students, as well as his dedication to the continued growth and success of the Hamburg Observatory.

Next, I want to thank my second supervisor, *Heinz Andernach*. I deeply appreciate his passion for radio galaxies and I will be always grateful for his invaluable guidance throughout my PhD journey.

I extend my gratitude to *Jochen Liske, Stephan Rosswog and Jan-Torge Schindler* for being part of the examination commission of my doctoral defense.

I want to thank all the people I had the pleasure of meeting at the observatory, and in particular, to *Thomas, Gabriella, Antonio, Raghav, Deepali, Lovorka, Simone and Thorben*, for their companionship and for making my time at the observatory and in Hamburg so enjoyable.

A special thank to *Kathrin* and *Henrik* who showed me the authentic ~~techno~~ German culture and shared unforgettable nights with me.

Outside of academia, I want to express my gratitude to my group of international friends, including *Ankit, Seba, Adri, Stratos, Hadaba and Sasha*. My fondness for Hamburg is greatly influenced by the strong bonds I have formed with these guys. Within this group, a special acknowledgment is reserved for *Giulia*. Over the past 8 years, we have shared both joys and sorrows, and I feel privileged to have experienced these moments with such an enjoyable and talented researcher.

A big thank you goes to all my long-distance friends in Italy: *Tuk, Gabri, Gianfranco, Mini, Nico, Elle, Canzi, Pic, Toni, Armish*. I appreciate their constant support and the resilience of our relationships despite the distance.

Lastly, I want to express my immense gratitude to my *gigia*. I admire her patience and unwavering support throughout my PhD journey. Her steadfast presence has been a source of strength and inspiration. I hope to have been a supporter to her as much as she has been to me.

7 Bibliography

Abazajian, K. N., Adelman-McCarthy, J. K., Agüeros, M. A., et al. 2009, ApJ Suppl., 182, 543

Abdulla, Z., Carlstrom, J. E., Mantz, A. B., et al. 2019, ApJ, 871, 195

Abdullah, M. H., Wilson, G., Klypin, A., et al. 2020, ApJ Suppl., 246, 2

Ahumada, R., Allende Prieto, C., Almeida, A., et al. 2020, ApJ Suppl., 249, 3

Alam, S., Albareti, F. D., Allende Prieto, C., et al. 2015, ApJ Suppl., 219, 12

Alberts, S., Pope, A., Brodwin, M., et al. 2016, ApJ, 825, 72

Alexander, P. 2006, MNRAS, 368, 1404

An, T. & Baan, W. A. 2012, ApJ, 760, 77

Ananthakrishnan, S. 1995, Journal of Astrophysics and Astronomy Supplement, 16, 427

Andernach, H., Jiménez-Andrade, E. F., & Willis, A. G. 2021, Galaxies, 9, 99

Aschwanden, M. J. 2015, ApJ, 814, 19

Assef, R. J., Kochanek, C. S., Brodwin, M., et al. 2010, ApJ, 713, 970

Assef, R. J., Stern, D., Kochanek, C. S., et al. 2013, ApJ, 772, 26

Astropy Collaboration, Robitaille, T. P., Tollerud, E. J., et al. 2013, A&A, 558, A33

Auriemma, C., Perola, G. C., Ekers, R. D., et al. 1977, A&A, 57, 41

Baba, K., Shibata, R., & Sibuya, M. 2004, Australian & New Zealand Journal of Statistics, 46, 657

Bagchi, J., Vivek, M., Vikram, V., et al. 2014, ApJ, 788, 174

Baldwin, J. A., Phillips, M. M., & Terlevich, R. 1981, PASP, 93, 5

Baldwin, J. E. 1982, Symposium - International Astronomical Union, 97, 21–24

Barthel, P. D. & Arnaud, K. A. 1996, MNRAS, 283, L45

Barthel, P. D., Hooimeyer, J. R., Schilizzi, R. T., Miley, G. K., & Preuss, E. 1989, ApJ, 336, 601

Barthel, P. D., Schilizzi, R. T., Miley, G. K., Jagers, W. J., & Strom, R. G. 1985, A&A, 148, 243

Bassani, L., Ursini, F., Malizia, A., et al. 2021, MNRAS, 500, 3111

Basson, J. F. & Alexander, P. 2003, MNRAS, 339, 353

7 Bibliography

Battye, R. A. & Browne, I. W. A. 2009, MNRAS, 399, 1888

Beck, R., Dobos, L., Budavári, T., Szalay, A. S., & Csabai, I. 2016, MNRAS, 460, 1371

Beck, R., Szapudi, I., Flewelling, H., et al. 2021, MNRAS, 500, 1633

Becker, R. H., White, R. L., & Helfand, D. J. 1995, ApJ, 450, 559

Bell, A. R. 1978a, MNRAS, 182, 147

Bell, A. R. 1978b, MNRAS, 182, 443

Bennett, C. L., Banday, A. J., Gorski, K. M., et al. 1996, ApJ Let., 464, L1

Best, P. N. 2009, Astronomische Nachrichten, 330, 184

Best, P. N., Bailer, D. M., Longair, M. S., & Riley, J. M. 1995, MNRAS, 275, 1171

Best, P. N. & Heckman, T. M. 2012, MNRAS, 421, 1569

Best, P. N., Kauffmann, G., Heckman, T. M., et al. 2005, MNRAS, 362, 25

Best, P. N., Ker, L. M., Simpson, C., Rigby, E. E., & Sabater, J. 2014, MNRAS, 445, 955

Best, P. N., Kondapally, R., Williams, W. L., et al. 2023, MNRAS, 523, 1729

Bicknell, G. V. 1995, ApJ Suppl., 101, 29

Bilicki, M., Jarrett, T. H., Peacock, J. A., Cluver, M. E., & Steward, L. 2014, ApJ Suppl., 210, 9

Bilicki, M., Peacock, J. A., Jarrett, T. H., et al. 2016, ApJ Suppl., 225, 5

Bird, J., Martini, P., & Kaiser, C. 2008, ApJ, 676, 147

Bîrzan, L., McNamara, B. R., Nulsen, P. E. J., Carilli, C. L., & Wise, M. W. 2008, ApJ, 686, 859

Bîrzan, L., Rafferty, D. A., McNamara, B. R., Wise, M. W., & Nulsen, P. E. J. 2004, ApJ, 607, 800

Blandford, R. D. & Payne, D. G. 1982, MNRAS, 199, 883

Blandford, R. D. & Znajek, R. L. 1977, MNRAS, 179, 433

Blinov, D., Casadio, C., Mandarakas, N., & Angelakis, E. 2020, A&A, 635, A102

Blue Bird, J., Davis, J., Luber, N., et al. 2020, MNRAS, 492, 153

Blumenthal, G. & Miley, G. 1979, A&A, 80, 13

Blundell, K. M. & Rawlings, S. 2000, AJ, 119, 1111

Blundell, K. M., Rawlings, S., & Willott, C. J. 1999, AJ, 117, 677

Böckmann, K., Brüggen, M., Koribalski, B., et al. 2023, A&A, 677, A188

Bonnarel, F., Fernique, P., Bienaymé, O., et al. 2000, A&A Suppl. Ser., 143, 33

Bouillot, V. R., Alimi, J.-M., Corasaniti, P.-S., & Rasera, Y. 2015, MNRAS, 450, 145

Bournaud, F., Dekel, A., Teyssier, R., et al. 2011, ApJ Let., 741, L33

Bourne, M. A. & Sijacki, D. 2017, MNRAS, 472, 4707

Bower, R. G., Benson, A. J., Malbon, R., et al. 2006, MNRAS, 370, 645

Braine, J., Guelin, M., Dumke, M., et al. 1997, A&A, 326, 963

Brand, K., Brown, M. J. I., Dey, A., et al. 2006, ApJ, 641, 140

Breiding, P., Chiaberge, M., Lambrides, E., et al. 2023, arXiv e-prints, arXiv:2305.11804

Brescia, M., Cavuoti, S., Longo, G., & De Stefano, V. 2014, A&A, 568, A126

Briel, U. G. & Henry, J. P. 1995, A&A, 302, L9

Brienza, M., Gilli, R., Prandoni, I., et al. 2023, A&A, 672, A179

Brienza, M., Godfrey, L., Morganti, R., et al. 2017, A&A, 606, A98

Brienza, M., Morganti, R., Harwood, J., et al. 2020, A&A, 638, A29

Brocksopp, C., Kaiser, C. R., Schoenmakers, A. P., & de Bruyn, A. G. 2011, MNRAS, 410, 484

Brüggen, M. & Kaiser, C. R. 2002, Nature, 418, 301

Brüggen, M., Reiprich, T. H., Bulbul, E., et al. 2021, A&A, 647, A3

Bruni, G., Brienza, M., Panessa, F., et al. 2021, MNRAS, 503, 4681

Bruni, G., Mack, K. H., Montenegro-Montes, F. M., Brienza, M., & González-Serrano, J. I. 2015, A&A, 582, A9

Bruni, G., Panessa, F., Bassani, L., et al. 2019, ApJ, 875, 88

Bruni, G., Panessa, F., Bassani, L., et al. 2020, MNRAS, 494, 902

Burenin, R. A. 2017, Astronomy Letters, 43, 507

Burn, B. J. 1966, MNRAS, 133, 67

Burns, J. O., Norman, M. L., & Clarke, D. A. 1991, Science, 253, 522

Burns, J. O., Rhee, G., Roettiger, K., et al. 1994, in Astronomical Society of the Pacific Conference Series, Vol. 54, The Physics of Active Galaxies, ed. G. V. Bicknell, M. A. Dopita, & P. J. Quinn, 325

Butler, A., Huynh, M., Kapińska, A., et al. 2019, A&A, 625, A111

Cabanac, R. A., Hutsemékers, D., Sluse, D., & Lamy, H. 2005, in Astronomical Society of the Pacific Conference Series, Vol. 343, Astronomical Polarimetry: Current Status and Future Directions, ed. A. Adamson, C. Aspin, C. Davis, & T. Fujiyoshi, 498

Cantwell, T. M., Bray, J. D., Croston, J. H., et al. 2020, MNRAS, 495, 143

Capetti, A., Brienza, M., Baldi, R. D., et al. 2020, A&A, 642, A107

Capetti, A., Brienza, M., Balmaverde, B., et al. 2022, A&A, 660, A93

Capetti, A., Massaro, F., & Baldi, R. D. 2017, A&A, 598, A49

Carilli, C. L., Perley, R. A., Dreher, J. W., & Leahy, J. P. 1991, ApJ, 383, 554

Cavagnolo, K. W., McNamara, B. R., Nulsen, P. E. J., et al. 2010, ApJ, 720, 1066

Cen, R. & Ostriker, J. P. 2006, ApJ, 650, 560

Chen, R., Peng, B., Strom, R. G., & Wei, J. 2011, MNRAS, 412, 2433

Chen, R., Peng, B., Strom, R. G., & Wei, J. 2012a, MNRAS, 420, 2715

Chen, R., Peng, B., Strom, R. G., & Wei, J. 2012b, MNRAS, 422, 3004

Chiaberge, M., Gilli, R., Lotz, J. M., & Norman, C. 2015, ApJ, 806, 147

Chiaraluce, E., Panessa, F., Bruni, G., et al. 2020, MNRAS, 495, 3943

Choi, E., Somerville, R. S., Ostriker, J. P., Hirschmann, M., & Naab, T. 2023, arXiv e-prints, arXiv:2312.08449

Chung, S. M., Kochanek, C. S., Assef, R., et al. 2014, ApJ, 790, 54

Cisternas, M., Jahnke, K., Inskip, K. J., et al. 2011, ApJ, 726, 57

Clarke, A. O., Heald, G., Jarrett, T., et al. 2017, A&A, 601, A25

Clerc, N., Merloni, A., Zhang, Y. Y., et al. 2016, MNRAS, 463, 4490

Cochran, W. G. 1952, The Annals of Mathematical Statistics, 23, 315

Coles, S. 2001, An Introduction to Statistical Modeling of Extreme Values (Springer London)

Condon, J. J., Cotton, W. D., Greisen, E. W., et al. 1998, AJ, 115, 1693

Contigiani, O., de Gasperin, F., Miley, G. K., et al. 2017, MNRAS, 472, 636

Conway, J. E. & Schilizzi, R. T. 2000, in EVN Symposium 2000, Proceedings of the 5th european VLBI Network Symposium, ed. J. E. Conway, A. G. Polatidis, R. S. Booth, & Y. M. Pihlström, 123

Coppejans, R., Cseh, D., Williams, W. L., van Velzen, S., & Falcke, H. 2015, MNRAS, 450, 1477

Cotton, W. D., Feretti, L., Giovannini, G., Lara, L., & Venturi, T. 1999, ApJ, 519, 108

Cotton, W. D., Thorat, K., Condon, J. J., et al. 2020, MNRAS, 495, 1271

Cowie, L. L., Songaila, A., Hu, E. M., & Cohen, J. G. 1996, AJ, 112, 839

Cressie, N. A. C. 1993, Statistics for Spatial Data, (John Wiley & Sons)

Croston, J. H., Hardcastle, M. J., Harris, D. E., et al. 2005, ApJ, 626, 733

Croston, J. H., Hardcastle, M. J., Mingo, B., et al. 2019, A&A, 622, A10

Croston, J. H., Kraft, R. P., Hardcastle, M. J., et al. 2009, MNRAS, 395, 1999

Croton, D. J., Farrar, G. R., Norberg, P., et al. 2005, MNRAS, 356, 1155

Cutri, R. M. & et al. 2012, VizieR Online Data Catalog, II/311

Cutri, R. M., Wright, E. L., Conrow, T., et al. 2013, Explanatory Supplement to the AllWISE Data Release Products, Explanatory Supplement to the AllWISE Data Release Products, by R. M. Cutri et al.

Cutri, R. M., Wright, E. L., Conrow, T., et al. 2021, VizieR Online Data Catalog, II/328

Dabhade, P., Gaikwad, M., Bagchi, J., et al. 2017, MNRAS, 469, 2886

Dabhade, P., Mahato, M., Bagchi, J., et al. 2020a, A&A, 642, A153

Dabhade, P., Röttgering, H. J. A., Bagchi, J., et al. 2020b, A&A, 635, A5

Dabhade, P., Saikia, D. J., & Mahato, M. 2023, Journal of Astrophysics and Astronomy, 44, 13

Dabhade, P., Shimwell, T. W., Bagchi, J., et al. 2022, A&A, 668, A64

D'Abrusco, R., Álvarez Crespo, N., Massaro, F., et al. 2019, ApJ Suppl., 242, 4

Davé, R., Anglés-Alcázar, D., Narayanan, D., et al. 2019, MNRAS, 486, 2827

Davé, R., Cen, R., Ostriker, J. P., et al. 2001, ApJ, 552, 473

Davies, R. I., Müller Sánchez, F., Genzel, R., et al. 2007, ApJ, 671, 1388

de Gasperin, F., Edler, H. W., Williams, W. L., et al. 2023, A&A, 673, A165

de Gasperin, F., Williams, W. L., Best, P., et al. 2021, A&A, 648, A104

Delhaize, J., Heywood, I., Prescott, M., et al. 2021, MNRAS, 501, 3833

Delvecchio, I., Smolčić, V., Zamorani, G., et al. 2017, A&A, 602, A3

DESI Collaboration, Adame, A. G., Aguilar, J., et al. 2023, arXiv e-prints, arXiv:2306.06308

de Vries, W. H., Morganti, R., Röttgering, H. J. A., et al. 2002, AJ, 123, 1784

Dey, A., Schlegel, D. J., Lang, D., et al. 2019, AJ, 157, 168

Dietrich, J. P., Werner, N., Clowe, D., et al. 2012, Nature, 487, 202

Donley, J. L., Kartaltepe, J., Kocevski, D., et al. 2018, ApJ, 853, 63

Donoso, E., Best, P. N., & Kauffmann, G. 2009, MNRAS, 392, 617

Doroshkevich, A. G. 1970, Astrophysics, 6, 320

Duncan, K. J. 2022, MNRAS, 512, 3662

Duncan, K. J., Kondapally, R., Brown, M. J. I., et al. 2021, A&A, 648, A4

7 *Bibliography*

Ehlert, K., Weinberger, R., Pfrommer, C., Pakmor, R., & Springel, V. 2018, MNRAS, 481, 2878

Ekers, R. D. & Ekers, J. A. 1973, A&A, 24, 247

El Bouchefry, K. 2009, MNRAS, 396, 2011

Elfhag, T., Booth, R. S., Hoeglund, B., Johansson, L. E. B., & Sandqvist, A. 1996, A&A Suppl. Ser., 115, 439

Ellison, S. L., Patton, D. R., & Hickox, R. C. 2015, MNRAS, 451, L35

Ellison, S. L., Patton, D. R., Mendel, J. T., & Scudder, J. M. 2011, MNRAS, 418, 2043

Ellison, S. L., Viswanathan, A., Patton, D. R., et al. 2019, MNRAS, 487, 2491

Emonts, B. H. C., Morganti, R., Struve, C., et al. 2010, MNRAS, 406, 987

English, W., Hardcastle, M. J., & Krause, M. G. H. 2016, MNRAS, 461, 2025

English, W., Hardcastle, M. J., & Krause, M. G. H. 2019, MNRAS, 490, 5807

Event Horizon Telescope Collaboration, Akiyama, K., Alberdi, A., et al. 2019, ApJ Let., 875, L1

Falle, S. A. E. G. 1991, MNRAS, 250, 581

Fanaroff, B. L. & Riley, J. M. 1974, MNRAS, 167, 31P

Fernandes, C. A. C., Jarvis, M. J., Martínez-Sansigre, A., et al. 2015, MNRAS, 447, 1184

Ferrarese, L., Pogge, R. W., Peterson, B. M., et al. 2001, ApJ Let., 555, L79

Fisher, N. I. 1993, Statistical Analysis of Circular Data (Cambridge University Press)

Flewelling, H. A., Magnier, E. A., Chambers, K. C., et al. 2020, ApJ Suppl., 251, 7

Fraser-McKelvie, A., Pimbblet, K. A., & Lazendic, J. S. 2011, MNRAS, 415, 1961

Friday, T., Clowes, R. G., & Williger, G. M. 2022, MNRAS, 511, 4159

Gaibler, V., Khochfar, S., & Krause, M. 2011, MNRAS, 411, 155

Gaibler, V., Krause, M., & Camenzind, M. 2009, MNRAS, 400, 1785

Galvin, T. J., Huynh, M. T., Norris, R. P., et al. 2020, MNRAS, 497, 2730

Gao, F., Wang, L., Pearson, W. J., et al. 2020, A&A, 637, A94

Garn, T., Green, D. A., Riley, J. M., & Alexander, P. 2008, MNRAS, 383, 75

Gaspari, M., Brighenti, F., & Temi, P. 2012, MNRAS, 424, 190

Gaspari, M., Ruszkowski, M., & Oh, S. P. 2013, MNRAS, 432, 3401

Ghisellini, G., Tavecchio, F., Maraschi, L., Celotti, A., & Sbarrato, T. 2014, Nature, 515, 376

Giacintucci, S., Clarke, T., Kassim, N. E., Peters, W., & Polisensky, E. 2021, Galaxies, 9, 108

Gitti, M., Brighenti, F., & McNamara, B. R. 2012, Advances in Astronomy, 2012, 950641

Godambe, S., Konar, C., Saikia, D. J., & Wiita, P. J. 2009, MNRAS, 396, 860

Godfrey, L. E. H. & Shabala, S. S. 2013, ApJ, 767, 12

Gómez, P. L., Pinkney, J., Burns, J. O., et al. 1997, ApJ, 474, 580

Gopal-Krishna & Wiita, P. J. 2002, NARev, 46, 357

Gordon, Y. A., Pimbblet, K. A., Kaviraj, S., et al. 2019, ApJ, 878, 88

Goulding, A. D., Greene, J. E., Bezanson, R., et al. 2018, PASJ, 70, S37

Gupta, N. & Saikia, D. J. 2006, MNRAS, 370, 738

Gürkan, G., Hardcastle, M. J., & Jarvis, M. J. 2014, MNRAS, 438, 1149

Gürkan, G., Hardcastle, M. J., Jarvis, M. J., et al. 2015, MNRAS, 452, 3776

Gürkan, G., Prandoni, I., O'Brien, A., et al. 2022, MNRAS, 512, 6104

Hansen, F. K., Banday, A. J., & Górski, K. M. 2004, MNRAS, 354, 641

Hao, J., McKay, T. A., Koester, B. P., et al. 2010, ApJ Suppl., 191, 254

Hardcastle, M. J. 2013, MNRAS, 433, 3364

Hardcastle, M. J. 2018, MNRAS, 475, 2768

Hardcastle, M. J., Evans, D. A., & Croston, J. H. 2007, MNRAS, 376, 1849

Hardcastle, M. J., Horton, M. A., Williams, W. L., et al. 2023, A&A, 678, A151

Hardcastle, M. J. & Krause, M. G. H. 2014, MNRAS, 443, 1482

Hardcastle, M. J., Worrall, D. M., Kraft, R. P., et al. 2003, ApJ, 593, 169

Harwood, J. J., Croston, J. H., Intema, H. T., et al. 2016, MNRAS, 458, 4443

Harwood, J. J., Hardcastle, M. J., & Croston, J. H. 2015, MNRAS, 454, 3403

Harwood, J. J., Hardcastle, M. J., Croston, J. H., & Goodger, J. L. 2013, MNRAS, 435, 3353

Harwood, J. J., Hardcastle, M. J., Morganti, R., et al. 2017, MNRAS, 469, 639

Hawley, D. L. & Peebles, P. J. E. 1975, AJ, 80, 477

Heckman, T. M. & Best, P. N. 2014, Ann. Rev. A&A, 52, 589

Heeschen, D. S. 1970, AJ, 75, 523

Heinz, S., Brüggen, M., Young, A., & Levesque, E. 2006, MNRAS, 373, L65

Heinz, S., Merloni, A., & Schwab, J. 2007, ApJ Let., 658, L9

Heinz, S., Reynolds, C. S., & Begelman, M. C. 1998, ApJ, 501, 126

Helfand, D. J., White, R. L., & Becker, R. H. 2015, ApJ, 801, 26

Hernquist, L. & Mihos, J. C. 1995, ApJ, 448, 41

Hewlett, T., Villforth, C., Wild, V., et al. 2017, MNRAS, 470, 755

Hine, R. G. & Longair, M. S. 1979, MNRAS, 188, 111

Hirv, A., Pelt, J., Saar, E., et al. 2017, A&A, 599, A31

Hobbs, A., Nayakshin, S., Power, C., & King, A. 2011, MNRAS, 413, 2633

Hocuk, S. & Barthel, P. D. 2010, A&A, 523, A9

Hogbom, J. A. & Brouw, W. N. 1974, A&A, 33, 289

Hong, J., Im, M., Kim, M., & Ho, L. C. 2015, ApJ, 804, 34

Hooimeyer, J. R. A., Schilizzi, R. T., Miley, G. K., & Barthel, P. D. 1992, A&A, 261, 25

Hopkins, P. F., Hernquist, L., Cox, T. J., et al. 2006, ApJ Suppl., 163, 1

Hopkins, P. F., Hernquist, L., Hayward, C. C., & Narayanan, D. 2012, MNRAS, 425, 1121

Horton, M. A., Krause, M. G. H., & Hardcastle, M. J. 2020, MNRAS, 499, 5765

Horton, M. A., Krause, M. G. H., & Hardcastle, M. J. 2023, MNRAS, 521, 2593

Hota, A., Konar, C., Stalin, C. S., et al. 2016, Journal of Astrophysics and Astronomy, 37, 41

Hota, A., Sirothia, S. K., Ohyama, Y., et al. 2011, MNRAS, 417, L36

Hu, F. X., Wu, G. X., Song, G. X., Yuan, Q. R., & Okamura, S. 2006, APSS, 302, 43

Huchra, J. P., Macri, L. M., Masters, K. L., et al. 2012, ApJ Suppl., 199, 26

Hutsemekers, D. 1998, A&A, 332, 410

Hutsemékers, D., Braibant, L., Pelgrims, V., & Sluse, D. 2014, A&A, 572, A18

Hutsemékers, D. & Lamy, H. 2001, A&A, 367, 381

Ineson, J., Croston, J. H., Hardcastle, M. J., & Mingo, B. 2017, MNRAS, 467, 1586

Intema, H. T., Jagannathan, P., Mooley, K. P., & Frail, D. A. 2017, A&A, 598, A78

Ishwara-Chandra, C. H. & Saikia, D. J. 1999, MNRAS, 309, 100

Ishwara-Chandra, C. H., Saikia, D. J., McCarthy, P. J., & van Breugel, W. J. M. 2001, MNRAS, 323, 460

Isobe, N. & Koyama, S. 2015, PASJ, 67, 77

Isobe, N., Seta, H., Gandhi, P., & Tashiro, M. S. 2011a, ApJ, 727, 82

Isobe, N., Seta, H., & Tashiro, M. S. 2011b, PASJ, 63, S947

Isobe, N., Tashiro, M. S., Gandhi, P., et al. 2009, ApJ, 706, 454

Jain, P., Narain, G., & Sarala, S. 2004, MNRAS, 347, 394

Jamrozy, M., Klein, U., Mack, K. H., Gregorini, L., & Parma, P. 2004, A&A, 427, 79

Jamrozy, M., Konar, C., Machalski, J., & Saikia, D. J. 2008, MNRAS, 385, 1286

Jarrett, T. H., Cohen, M., Masci, F., et al. 2011, ApJ, 735, 112

Jenkins, C. R. 1982, MNRAS, 200, 705

Jeyakumar, S., Wiita, P. J., Saikia, D. J., & Hooda, J. S. 2005, A&A, 432, 823

Joachimi, B., Cacciato, M., Kitching, T. D., et al. 2015, SSR, 193, 1

Jones, B. J. T., van de Weygaert, R., & Aragón-Calvo, M. A. 2010, MNRAS, 408, 897

Jones, P. A. & McAdam, W. B. 1992, ApJ Suppl., 80, 137

Jorstad, S. G., Marscher, A. P., Morozova, D. A., et al. 2017, ApJ, 846, 98

Joshi, S. A., Battye, R. A., Browne, I. W. A., et al. 2007, MNRAS, 380, 162

Jurlin, N., Brienza, M., Morganti, R., et al. 2021, A&A, 653, A110

Kaiser, C. R. & Alexander, P. 1997, MNRAS, 286, 215

Kaiser, C. R., Dennett-Thorpe, J., & Alexander, P. 1997, MNRAS, 292, 723

Kaiser, C. R., Schoenmakers, A. P., & Röttgering, H. J. A. 2000, MNRAS, 315, 381

Kamali, F., Henkel, C., Koyama, S., et al. 2019, A&A, 624, A42

Kapahi, V. K. 1989, AJ, 97, 1

Kapahi, V. K., Subrahmanyan, R., & Singal, A. K. 1985, Nature, 313, 463

Kapinska, A. D., Hardcastle, M., Jackson, C., et al. 2015, in Advancing Astrophysics with the Square Kilometre Array (AASKA14), 173

Karouzos, M., Jarvis, M. J., & Bonfield, D. 2014, MNRAS, 439, 861

Kaye, C. D., Cawthorne, T. V., & Hughes, P. A. 2018, Galaxies, 6, 53

Kirk, D., Brown, M. L., Hoekstra, H., et al. 2015, SSR, 193, 139

Klein, U., Mack, K. H., Gregorini, L., & Parma, P. 1995, A&A, 303, 427

Kocevski, D. D., Faber, S. M., Mozena, M., et al. 2012, ApJ, 744, 148

Kochanek, C. S., Eisenstein, D. J., Cool, R. J., et al. 2012, ApJ Suppl., 200, 8

Koester, B. P., McKay, T. A., Annis, J., et al. 2007, ApJ, 660, 239

Koide, S., Shibata, K., & Kudoh, T. 1999, ApJ, 522, 727

7 Bibliography

Komberg, B. V. & Pashchenko, I. N. 2009, Astronomy Reports, 53, 1086

Komissarov, S. S. & Gubanov, A. G. 1994, A&A, 285, 27

Konar, C., Hardcastle, M. J., Croston, J. H., & Saikia, D. J. 2009, MNRAS, 400, 480

Konar, C., Jamrozy, M., Saikia, D. J., & Machalski, J. 2008, MNRAS, 383, 525

Konar, C., Saikia, D. J., Ishwara-Chandra, C. H., & Kulkarni, V. K. 2004, MNRAS, 355, 845

Konar, C., Saikia, D. J., Jamrozy, M., & Machalski, J. 2006, MNRAS, 372, 693

Kondapally, R., Best, P. N., Cochrane, R. K., et al. 2022, MNRAS, 513, 3742

Kondapally, R., Best, P. N., Hardcastle, M. J., et al. 2021, A&A, 648, A3

Koss, M., Mushotzky, R., Veilleux, S., & Winter, L. 2010, ApJ Let., 716, L125

Kostrzewa-Rutkowska, Z., Jonker, P. G., Hodgkin, S. T., et al. 2018, MNRAS, 481, 307

Kotanyi, C. G. & Ekers, R. D. 1979, A&A, 73, L1

Koulouridis, E., Clerc, N., Sadibekova, T., et al. 2021, A&A, 652, A12

Kozieł-Wierzbowska, D., Vale Asari, N., Stasińska, G., et al. 2017, ApJ, 846, 42

Kraft, R. P., Nulsen, P. E. J., Birkinshaw, M., et al. 2007, ApJ, 665, 1129

Kraljic, K., Duckworth, C., Tojeiro, R., et al. 2021, MNRAS, 504, 4626

Krause, M. 2005, A&A, 431, 45

Krolewski, A., Ho, S., Chen, Y.-C., et al. 2019, ApJ, 876, 52

Kutkin, A. M., Oosterloo, T. A., Morganti, R., et al. 2023, arXiv e-prints, arXiv:2306.03710

Kuźmicz, A., Czerny, B., & Wildy, C. 2019, A&A, 624, A91

Kuźmicz, A. & Jamrozy, M. 2012, MNRAS, 426, 851

Kuźmicz, A. & Jamrozy, M. 2021, ApJ Suppl., 253, 25

Kuźmicz, A., Jamrozy, M., Bronarska, K., Janda-Boczar, K., & Saikia, D. J. 2018, ApJ Suppl., 238, 9

Lackner, C. N., Silverman, J. D., Salvato, M., et al. 2014, AJ, 148, 137

Lacy, M., Baum, S. A., Chandler, C. J., et al. 2020, PASP, 132, 035001

Laing, R. A., Bridle, A. H., Parma, P., et al. 2008, MNRAS, 386, 657

Lambrides, E. L., Chiaberge, M., Heckman, T., et al. 2021, ApJ, 919, 129

Lan, T.-W. & Prochaska, J. X. 2021, MNRAS, 502, 5104

Lang, D. 2014, AJ, 147, 108

Lara, L., Giovannini, G., Cotton, W. D., et al. 2004, A&A, 421, 899

Lara, L., Mack, K. H., Lacy, M., et al. 2000, A&A, 356, 63

Lara, L., Márquez, I., Cotton, W. D., et al. 2001, A&A, 378, 826

Leahy, J. P. & Williams, A. G. 1984, MNRAS, 210, 929

Ledlow, M. J. & Owen, F. N. 1996, AJ, 112, 9

Lee, J. 2004, ApJ Let., 614, L1

Lind, K. R., Payne, D. G., Meier, D. L., & Blandford, R. D. 1989, ApJ, 344, 89

Linfield, R. 1981, ApJ, 244, 436

Lister, M. L., Aller, M. F., Aller, H. D., et al. 2016, AJ, 152, 12

Lister, M. L., Homan, D. C., Hovatta, T., et al. 2019, ApJ, 874, 43

Liu, A., Bulbul, E., Ghirardini, V., et al. 2022, A&A, 661, A2

Longair, M. S. 2011, High Energy Astrophysics

Lotz, J. M., Jonsson, P., Cox, T. J., & Primack, J. R. 2008, MNRAS, 391, 1137

Lovisari, L., Ettori, S., Rasia, E., et al. 2023, arXiv e-prints, arXiv:2311.02176

Luo, A. L., Zhao, Y.-H., Zhao, G., et al. 2015, Research in Astronomy and Astrophysics, 15, 1095

Lusetti, G., de Gasperin, F., Cuciti, V., et al. 2023, MNRAS[eprint[arXiv]2401.04710]

Machalski, J. 2011, MNRAS, 413, 2429

Machalski, J., Chyzy, K. T., & Jamrozy, M. 2004, actaa, 54, 391

Machalski, J., Chyży, K. T., Stawarz, Ł., & Kozieł, D. 2007a, A&A, 462, 43

Machalski, J., Jamrozy, M., & Saikia, D. J. 2009, MNRAS, 395, 812

Machalski, J., Jamrozy, M., & Zola, S. 2001, A&A, 371, 445

Machalski, J., Jamrozy, M., Zola, S., & Koziel, D. 2006, A&A, 454, 85

Machalski, J., Kozieł-Wierzbowska, D., & Goyal, A. 2021, ApJ Suppl., 255, 22

Machalski, J., Kozieł-Wierzbowska, D., & Jamrozy, M. 2007b, actaa, 57, 227

Machalski, J., Kozieł-Wierzbowska, D., Jamrozy, M., & Saikia, D. J. 2008, ApJ, 679, 149

Mack, K. H., Klein, U., O'Dea, C. P., & Willis, A. G. 1997, A&A Suppl. Ser., 123, 423

Mack, K. H., Klein, U., O'Dea, C. P., Willis, A. G., & Saripalli, L. 1998, A&A, 329, 431

Madau, P. & Dickinson, M. 2014, Ann. Rev. A&A, 52, 415

Magliocchetti, M. 2022, A&A Rev., 30, 6

Magorrian, J., Tremaine, S., Richstone, D., et al. 1998, AJ, 115, 2285

Mahatma, V. H., Hardcastle, M. J., Croston, J. H., et al. 2020, MNRAS, 491, 5015

Mahatma, V. H., Hardcastle, M. J., Williams, W. L., et al. 2018, MNRAS, 475, 4557

Mahato, M., Dabhade, P., Saikia, D. J., et al. 2022, A&A, 660, A59

Mainzer, A., Grav, T., Bauer, J., et al. 2011, ApJ, 743, 156

Malarecki, J. M., Jones, D. H., Saripalli, L., Staveley-Smith, L., & Subrahmanyan, R. 2015, MNRAS, 449, 955

Malarecki, J. M., Staveley-Smith, L., Saripalli, L., et al. 2013, MNRAS, 432, 200

Mandarakas, N., Blinov, D., Casadio, C., et al. 2021, A&A, 653, A123

Mann, H. B. & Whitney, D. R. 1947, The Annals of Mathematical Statistics, 18, 50

Manolakou, K. & Kirk, J. G. 2002, A&A, 391, 127

Mao, M. Y., Owen, F., Duffin, R., et al. 2015, MNRAS, 446, 4176

Marchegiani, P. 2022, in European Physical Journal Web of Conferences, Vol. 257, mm Universe @ NIKA2 - Observing the mm Universe with the NIKA2 Camera, 00030

Mardia, K. V. & Jupp, P. E. 2000, Directional Statistics, (John Wiley & Sons)

Marecki, A., Jamrozy, M., Machalski, J., & Pajdosz-Śmierciak, U. 2021, MNRAS, 501, 853

Marecki, A. & Ogrodnik, M. 2015, in Galaxies in 3D across the Universe, ed. B. L. Ziegler, F. Combes, H. Dannerbauer, & M. Verdugo, Vol. 309, 326–327

Marocco, F., Eisenhardt, P. R. M., Fowler, J. W., et al. 2021, ApJ Suppl., 253, 8

Masini, A., Celotti, A., Grandi, P., Moravec, E., & Williams, W. L. 2021, A&A, 650, A51

Masini, A., Hickox, R. C., Carroll, C. M., et al. 2020, ApJ Suppl., 251, 2

Massaglia, S., Bodo, G., Rossi, P., Capetti, A., & Mignone, A. 2022, A&A, 659, A139

Massaglia, S., Bodo, G., Rossi, P., Capetti, S., & Mignone, A. 2016, A&A, 596, A12

Mateos, S., Alonso-Herrero, A., Carrera, F. J., et al. 2012, MNRAS, 426, 3271

Matthews, T. A., Morgan, W. W., & Schmidt, M. 1964, ApJ, 140, 35

Mauch, T., Murphy, T., Buttery, H. J., et al. 2003, MNRAS, 342, 1117

Mauch, T. & Sadler, E. M. 2007, MNRAS, 375, 931

McConnell, D., Hale, C. L., Lenc, E., et al. 2020, PASA, 37, e048

McKinney, J. C. & Blandford, R. D. 2009, MNRAS, 394, L126

McKinney, J. C., Tchekhovskoy, A., & Blandford, R. D. 2012, MNRAS, 423, 3083

Meier, D. L. 2001, ApJ Let., 548, L9

Meisenheimer, K., Roser, H. J., Hiltner, P. R., et al. 1989, A&A, 219, 63

Merloni, A., Predehl, P., Becker, W., et al. 2012, arXiv e-prints, arXiv:1209.3114

Mhlahlo, N. & Jamrozy, M. 2021, MNRAS, 508, 2910

Mignone, A., Rossi, P., Bodo, G., Ferrari, A., & Massaglia, S. 2010, MNRAS, 402, 7

Miley, G. & De Breuck, C. 2008, A&A Rev., 15, 67

Mingo, B., Croston, J. H., Best, P. N., et al. 2022, MNRAS, 511, 3250

Mingo, B., Croston, J. H., Hardcastle, M. J., et al. 2019, MNRAS, 488, 2701

Mingo, B., Hardcastle, M. J., Croston, J. H., et al. 2014, MNRAS, 440, 269

Miraghaei, H. & Best, P. N. 2017, MNRAS, 466, 4346

Mirakhor, M. S., Walker, S. A., Bagchi, J., et al. 2021, MNRAS, 500, 2503

Morabito, L. K., Williams, W. L., Duncan, K. J., et al. 2017, MNRAS, 469, 1883

Morganti, R., Jurlin, N., Oosterloo, T., et al. 2021, Galaxies, 9, 88

Morganti, R. & Oosterloo, T. 2018, A&A Rev., 26, 4

Morganti, R., Peck, A. B., Oosterloo, T. A., et al. 2009, A&A, 505, 559

Mukherjee, D., Bicknell, G. V., Sutherland, R., & Wagner, A. 2016, MNRAS, 461, 967

Mukherjee, D., Bodo, G., Mignone, A., Rossi, P., & Vaidya, B. 2020, MNRAS, 499, 681

Mullin, L. M. & Hardcastle, M. J. 2009, MNRAS, 398, 1989

Murgia, M., Fanti, C., Fanti, R., et al. 1999, A&A, 345, 769

Murgia, M., Parma, P., Mack, K. H., et al. 2011, A&A, 526, A148

Nandi, S., Pirya, A., Pal, S., et al. 2010, MNRAS, 404, 433

Narayan, R. & Yi, I. 1994, ApJ Let., 428, L13

Navarro, J. F., Abadi, M. G., & Steinmetz, M. 2004, ApJ Let., 613, L41

Nelson, D., Springel, V., Pillepich, A., et al. 2019, Computational Astrophysics and Cosmology, 6, 2

Nishikawa, K. I., Richardson, G., Koide, S., et al. 2005, ApJ, 625, 60

Norman, M. L., Winkler, K. H. A., Smarr, L., & Smith, M. D. 1982, A&A, 113, 285

Ochsenbein, F., Bauer, P., & Marcout, J. 2000, A&A Suppl. Ser., 143, 23

O'Dea, C. P. 1998, PASP, 110, 493

O'Dea, C. P. & Baum, S. A. 1997, AJ, 113, 148

O'Dea, C. P., Koekemoer, A. M., Baum, S. A., et al. 2001, AJ, 121, 1915

7 Bibliography

O'Dea, C. P. & Owen, F. N. 1985, AJ, 90, 954

O'Dea, C. P. & Saikia, D. J. 2021, A&A Rev., 29, 3

Oei, M. S. S. L., van Weeren, R. J., Gast, A. R. D. J. G. I. B., et al. 2023a, A&A, 672, A163

Oei, M. S. S. L., van Weeren, R. J., Hardcastle, M. J., et al. 2022, A&A, 660, A2

Oei, M. S. S. L., van Weeren, R. J., Hardcastle, M. J., et al. 2023b, MNRAS, 518, 240

Onah, C. I., Ubachukwu, A. A., Odo, F. C., & Onuchukwu, C. C. 2018, rmxaa, 54, 271

O'Neill, S. M., Tregillis, I. L., Jones, T. W., & Ryu, D. 2005, ApJ, 633, 717

Orienti, M. 2016, Astronomische Nachrichten, 337, 9

Orienti, M., Murgia, M., & Dallacasa, D. 2010, MNRAS, 402, 1892

Orrù, E., van Velzen, S., Pizzo, R. F., et al. 2015, A&A, 584, A112

Osinga, E., Miley, G. K., van Weeren, R. J., et al. 2020, A&A, 642, A70

Owen, F. N. & Rudnick, L. 1976, ApJ Let., 205, L1

Pahwa, I., Libeskind, N. I., Tempel, E., et al. 2016, MNRAS, 457, 695

Panwar, M., Prabhakar, Sandhu, P. K., Wadadekar, Y., & Jain, P. 2020, MNRAS, 499, 1226

Parma, P., Murgia, M., de Ruiter, H. R., et al. 2007, A&A, 470, 875

Parma, P., Murgia, M., Morganti, R., et al. 1999, A&A, 344, 7

Pasini, T., Brüggen, M., Hoang, D. N., et al. 2022, A&A, 661, A13

Peck, A. B., Taylor, G. B., & Conway, J. E. 1999, ApJ, 521, 103

Peebles, P. J. E. 1969, ApJ, 155, 393

Pelgrims, V. & Cudell, J. R. 2014, MNRAS, 442, 1239

Pelgrims, V. & Hutsemékers, D. 2016, A&A, 590, A53

Perley, R. A., Dreher, J. W., & Cowan, J. J. 1984, ApJ Let., 285, L35

Perucho, M., Martí, J.-M., & Quilis, V. 2019, MNRAS, 482, 3718

Perucho, M., Martí, J.-M., & Quilis, V. 2021, MNRAS[eprint[arXiv]2112.02978]

Perucho, M., Quilis, V., & Martí, J.-M. 2011, ApJ, 743, 42

Pihlström, Y. M., Conway, J. E., & Vermeulen, R. C. 2003, A&A, 404, 871

Pinjarkar, S., Hardcastle, M. J., Harwood, J. J., et al. 2023, MNRAS, 523, 620

Pirya, A., Nandi, S., Saikia, D. J., Konar, C., & Singh, M. 2011, Journal of Astrophysics and Astronomy, 32, 471

Pirya, A., Saikia, D. J., Singh, M., & Chandola, H. C. 2012, MNRAS, 426, 758

Planck Collaboration, Ade, P. A. R., Aghanim, N., et al. 2016, A&A, 594, A16

Planck Collaboration, Akrami, Y., Ashdown, M., et al. 2020, A&A, 641, A7

Porciani, C., Dekel, A., & Hoffman, Y. 2002, MNRAS, 332, 339

Pracy, M. B., Ching, J. H. Y., Sadler, E. M., et al. 2016, MNRAS, 460, 2

Predehl, P., Andritschke, R., Arefiev, V., et al. 2021, A&A, 647, A1

Proctor, D. D. 2016, ApJ Suppl., 224, 18

Rees, M. J. 1971, Nature, 229, 312

Rengelink, R. B., Tang, Y., de Bruyn, A. G., et al. 1997, A&A Suppl. Ser., 124, 259

Reynolds, C. S., Heinz, S., & Begelman, M. C. 2002, MNRAS, 332, 271

Robitaille, T. & Bressert, E. 2012, APLpy: Astronomical Plotting Library in Python, Astrophysics Source Code Library, record ascl:1208.017

Rodriguez, F., Merchán, M., Artale, M. C., & Andrews, M. 2022, arXiv e-prints, arXiv:2212.09781

Rowan-Robinson, M., Gonzalez-Solares, E., Vaccari, M., & Marchetti, L. 2013, MNRAS, 428, 1958

Rykoff, E. S., Rozo, E., Busha, M. T., et al. 2014, ApJ, 785, 104

Sabater, J., Best, P. N., Hardcastle, M. J., et al. 2019, A&A, 622, A17

Sabater, J., Best, P. N., Tasse, C., et al. 2021, A&A, 648, A2

Safouris, V., Subrahmanyan, R., Bicknell, G. V., & Saripalli, L. 2009, MNRAS, 393, 2

Saikia, D. J., Gupta, N., & Konar, C. 2007, MNRAS, 375, L31

Sanders, D. B., Soifer, B. T., Elias, J. H., et al. 1988, ApJ, 325, 74

Sanders, R. H. 1984, Nature, 309, 35

Saripalli, L., Gopal-Krishna, Reich, W., & Kuehr, H. 1986, A&A, 170, 20

Saripalli, L., Hunstead, R. W., Subrahmanyan, R., & Boyce, E. 2005, AJ, 130, 896

Saripalli, L. & Mack, K. H. 2007, MNRAS, 376, 1385

Saripalli, L., Mack, K. H., Klein, U., Strom, R., & Singal, A. K. 1996, A&A, 306, 708

Saripalli, L., Patnaik, A. R., Porcas, R. W., & Graham, D. A. 1997, A&A, 328, 78

Satyapal, S., Ellison, S. L., McAlpine, W., et al. 2014, MNRAS, 441, 1297

Schäfer, B. M. 2009, International Journal of Modern Physics D, 18, 173

Schaye, J., Crain, R. A., Bower, R. G., et al. 2015, MNRAS, 446, 521

Schaye, J., Dalla Vecchia, C., Booth, C. M., et al. 2010, MNRAS, 402, 1536

Scheuer, P. A. G. 1974, MNRAS, 166, 513

Schilizzi, R. T., Skillman, E. D., Miley, G. K., et al. 1988, in The Impact of VLBI on Astrophysics and Geophysics, ed. M. J. Reid & J. M. Moran, Vol. 129, 127

Schilizzi, R. T., Tian, W. W., Conway, J. E., et al. 2001, A&A, 368, 398

Schlafly, E. F., Meisner, A. M., & Green, G. M. 2019, ApJ Suppl., 240, 30

Schmitt, H. R., Pringle, J. E., Clarke, C. J., & Kinney, A. L. 2002, ApJ, 575, 150

Schoenmakers, A. P., de Bruyn, A. G., Röttgering, H. J. A., van der Laan, H., & Kaiser, C. R. 2000a, MNRAS, 315, 371

Schoenmakers, A. P., Mack, K. H., de Bruyn, A. G., et al. 2000b, A&A Suppl. Ser., 146, 293

Sebastian, B., Ishwara-Chandra, C. H., Joshi, R., & Wadadekar, Y. 2018, MNRAS, 473, 4926

Secrest, N. J., Ellison, S. L., Satyapal, S., & Blecha, L. 2020, MNRAS, 499, 2380

Seymour, N., Huynh, M., Shabala, S. S., et al. 2020, PASA, 37, e013

Shabala, S. S., Ash, S., Alexander, P., & Riley, J. M. 2008, MNRAS, 388, 625

Shabala, S. S., Deller, A., Kaviraj, S., et al. 2017, MNRAS, 464, 4706

Shabala, S. S., Jurlin, N., Morganti, R., et al. 2020, MNRAS, 496, 1706

Shakura, N. I. & Sunyaev, R. A. 1973, A&A, 24, 337

Shimwell, T. W., Hardcastle, M. J., Tasse, C., et al. 2022, A&A, 659, A1

Shimwell, T. W., Tasse, C., Hardcastle, M. J., et al. 2019, A&A, 622, A1

Shlosman, I., Frank, J., & Begelman, M. C. 1989, Nature, 338, 45

Shulevski, A., Barthel, P. D., Morganti, R., et al. 2019, A&A, 628, A69

Shulevski, A., Morganti, R., Harwood, J. J., et al. 2017, A&A, 600, A65

Shulevski, A., Morganti, R., Oosterloo, T., & Struve, C. 2012, A&A, 545, A91

Simonte, M., Andernach, H., Brüggen, M., Best, P. N., & Osinga, E. 2023, A&A, 672, A178

Simonte, M., Andernach, H., Brüggen, M., et al. 2022a, MNRAS, 515, 2032

Simonte, M., Vazza, F., Brighenti, F., et al. 2022b, A&A, 658, A149

Slagter, R. J. & Miedema, P. G. 2021, MNRAS, 501, 3054

Smolčić, V. & Riechers, D. A. 2011, ApJ, 730, 64

Smolčić, V., Zamorani, G., Schinnerer, E., et al. 2009, ApJ, 696, 24

Srivastava, S. & Singal, A. K. 2020, MNRAS, 493, 3811

Stern, D., Assef, R. J., Benford, D. J., et al. 2012, ApJ, 753, 30

Stockman, H. S., Angel, J. R. P., & Miley, G. K. 1979, ApJ Let., 227, L55

Stoughton, C., Lupton, R. H., Bernardi, M., et al. 2002, AJ, 123, 485

Stuardi, C., O'Sullivan, S. P., Bonafede, A., et al. 2020, A&A, 638, A48

Subrahmanyan, R., Saripalli, L., & Hunstead, R. W. 1996, MNRAS, 279, 257

Subrahmanyan, R., Saripalli, L., Safouris, V., & Hunstead, R. W. 2008, ApJ, 677, 63

Sweijen, F., van Weeren, R. J., Röttgering, H. J. A., et al. 2022, Nature Astronomy, 6, 350

Takey, A., Schwope, A., & Lamer, G. 2014, A&A, 564, A54

Tamhane, P., Wadadekar, Y., Basu, A., et al. 2015, MNRAS, 453, 2438

Tasse, C., Shimwell, T., Hardcastle, M. J., et al. 2021, A&A, 648, A1

Taylor, A. R. & Jagannathan, P. 2016, MNRAS, 459, L36

Tchekhovskoy, A., Narayan, R., & McKinney, J. C. 2011, MNRAS, 418, L79

Tempel, E. & Libeskind, N. I. 2013, ApJ Let., 775, L42

Tempel, E., Stoica, R. S., & Saar, E. 2013, MNRAS, 428, 1827

Tielens, A. G. G. M., Miley, G. K., & Willis, A. G. 1979, A&A Suppl. Ser., 35, 153

Tiwari, P. & Jain, P. 2013, International Journal of Modern Physics D, 22, 1350089

Toba, Y., Yamashita, T., Nagao, T., et al. 2019, ApJ Suppl., 243, 15

Tudorache, M. N., Jarvis, M. J., Heywood, I., et al. 2022, MNRAS, 513, 2168

Turner, R. J., Rogers, J. G., Shabala, S. S., & Krause, M. G. H. 2018, MNRAS, 473, 4179

Turner, R. J. & Shabala, S. S. 2015, ApJ, 806, 59

Turner, R. J. & Shabala, S. S. 2023, Galaxies, 11, 87

Urry, C. M. & Padovani, P. 1995, PASP, 107, 803

Ursini, F., Bassani, L., Panessa, F., et al. 2018, MNRAS, 481, 4250

van Cappellen, W. A., Oosterloo, T. A., Verheijen, M. A. W., et al. 2022, A&A, 658, A146

van der Walt, S., Colbert, S. C., & Varoquaux, G. 2011, Computing in Science and Engineering, 13, 22

Van Haarlem, M. P., Wise, M. W., Gunst, A. W., et al. 2013, A&A, 556, A2

van Weeren, R. J., Williams, W. L., Tasse, C., et al. 2014, ApJ, 793, 82

Vazquez Najar, L. A. & Andernach, H. 2019, arXiv e-prints, arXiv:1908.09989

Vazza, F., Wittor, D., Di Federico, L., et al. 2023, A&A, 669, A50

Verdoes Kleijn, G. A. & de Zeeuw, P. T. 2005, A&A, 435, 43

Villforth, C., Hamann, F., Rosario, D. J., et al. 2014, MNRAS, 439, 3342

Villforth, C., Herbst, H., Hamann, F., et al. 2019, MNRAS, 483, 2441

Wagner, A. Y., Bicknell, G. V., & Umemura, M. 2012, ApJ, 757, 136

Wen, Z. L. & Han, J. L. 2015, ApJ, 807, 178

Wen, Z. L. & Han, J. L. 2018, MNRAS, 481, 4158

Wen, Z. L. & Han, J. L. 2021, MNRAS, 500, 1003

Wen, Z. L., Han, J. L., & Liu, F. S. 2012, ApJ Suppl., 199, 34

Wen, Z. L., Han, J. L., & Yang, F. 2018, MNRAS, 475, 343

Werner, N., Finoguenov, A., Kaastra, J. S., et al. 2008, A&A, 482, L29

West, M. J. 1991, ApJ, 379, 19

Weston, M. E., McIntosh, D. H., Brodwin, M., et al. 2017, MNRAS, 464, 3882

White, S. D. M. 1984, ApJ, 286, 38

Williams, W. L., Calistro Rivera, G., Best, P. N., et al. 2018, MNRAS, 475, 3429

Williams, W. L., de Gasperin, F., Hardcastle, M. J. H., et al. 2021, A&A, 655, A40

Williams, W. L., Intema, H. T., & Röttgering, H. J. A. 2013, A&A, 549, A55

Williams, W. L. & Röttgering, H. J. A. 2015, MNRAS, 450, 1538

Williams, W. L., van Weeren, R. J., Röttgering, H. J. A., et al. 2016, MNRAS, 460, 2385

Willis, A. G., Strom, R. G., & Wilson, A. S. 1974, Nature, 250, 625

Wright, E. L., Eisenhardt, P. R. M., Mainzer, A. K., et al. 2010, AJ, 140, 1868

Xu, H., Dai, Y. S., Huang, J.-S., et al. 2020, ApJ, 905, 103

Yates, P. M., Shabala, S. S., & Krause, M. G. H. 2018, MNRAS, 480, 5286

Yates-Jones, P. M., Shabala, S. S., & Krause, M. G. H. 2021, MNRAS, 508, 5239

Yates-Jones, P. M., Shabala, S. S., Power, C., et al. 2023, PASA, 40, e014

Yates-Jones, P. M., Turner, R. J., Shabala, S. S., & Krause, M. G. H. 2022, MNRAS, 511, 5225

Yoon, J. H., Schawinski, K., Sheen, Y.-K., Ree, C. H., & Yi, S. K. 2008, ApJ Suppl., 176, 414

York, D. G., Adelman, J., Anderson, John E., J., et al. 2000, AJ, 120, 1579

Yuan, Z. S. & Wen, Z. L. 2022, MNRAS, 516, 3159

Zaninetti, L. & Ferraro, M. 2008, Central European Journal of Physics, 6, 1

Zhang, P., D'Amico, G., Senatore, L., Zhao, C., & Cai, Y. 2022, JCAP, 2022, 036

Zhang, Y., Yang, X., Wang, H., et al. 2015, ApJ, 798, 17

Zhou, R., Newman, J. A., Mao, Y.-Y., et al. 2021, MNRAS, 501, 3309

Zou, H., Sui, J., Xue, S., et al. 2022, Research in Astronomy and Astrophysics, 22, 065001

Zou, H., Zhang, T., Zhou, Z., et al. 2017a, AJ, 153, 276

Zou, H., Zhou, X., Fan, X., et al. 2017b, PASP, 129, 064101

Zou, H., Zhou, X., Fan, X., et al. 2019, ApJ Suppl., 245, 4

Zovaro, H. R. M., Riseley, C. J., Taylor, P., et al. 2022, MNRAS, 509, 4997

A Notes on individual sources in the Boötes field

J1419+3337 has two elongated straight and symmetric relic-type lobes. The compact source NE of the N end of the N lobe is DESI J214.7968+33.6483, r=14.18, and unrelated to the GRG.

J1421+3431 has a radio core slightly extended towards two faint, diffuse outer lobes.

J1421+3521 is a rather symmetric classical FR II source along PA $\sim$ 100°. The E lobe lies at the S end of an unrelated remnant-type radio galaxy hosted by 2MASX J14220065+3523086 with $LAS\sim$ 3.3′, with its N lobe outside of our cutout.

J1422+3320 is a very straight FR II type source with relatively narrow lobes showing emission decreasing in surface brightness from the hotspots right to the host galaxy. Also displayed in Williams et al. (2016).

J1422+3255 No radio core is detected, and the source may also be hosted by DESI J215.6873+32.9360, r=24.69, with $z_{ph} = 1.020$, although this would not alter its LLS.

J1423+3600 is a restarted or double-double radio galaxy with an inner double of $\sim$24″ size and both inner and outer double having stronger N lobes.

J1423+3403 shows some evidence for being restarted with two faint inner lobes $\sim$24″ apart and outer lobes being of remnant type. About 32″ NNE of the host a compact radio source (SDSS J142337.34+340330.2 at z_{ph} $\sim$0.42) is superposed on the NNE lobe.

J1423+3302: The BLDF image is slightly affected by sidelobes, but both VLASS epoch 1 and 2 images confirm this is a restarted source, with an inner double of $\sim$27″. The ENE outer lobe is resolved out in VLASS while the WSW outer lobe shows two hotspots, though the W hotspot may be hosted by DESI J215.8935+33.0419, r=23.79, at a similar redshift as the host.

J1423+3529 has the second-largest linear size (3.4 Mpc) in our sample. It is a restarted source with an inner asymmetric double of $LAS\sim$1.6′. The 6″ BLDF image shows rather disrupted, and generally straight outer lobes, but the LoTSS-DR2 low-resolution image leaves no doubt that the source is a physical entity. Only the host is detected as a faint point source in VLASS.

J1423+3340 is a symmetric and straight FR II source with a core slightly brighter than the lobes in BLDF. The host is only detected in CWISE, thus we estimate a redshift of at least $\sim$1.5.

J1423+3605 is a WAT-type source with radio tails due SSE and W in a poor cluster or group. An apparent loop of radio emission in BLDF W of the host is caused by extended radio emission of a pair of galaxies at the same redshift and $\sim$11″ SW of the host.

J1424+3609 is a very large and straight FR II source with clear diffuse emission trailing back from the outer extremities of the NNE and SSW lobes towards the host. Only the NNE lobe shows a hotspot in VLASS while the end of SSW lobe is diffuse and of very low surface brightness in VLASS. A compact radio source $\sim$20″ SSW of the host has no optical or IR counterpart and is likely a knot of the SSW jet. The source was first noticed by us in Williams et al. (2016).

J1424+3436 is likely a restarted radio galaxy with inner lobes of size $\sim$50″ but no clear hotspots in VLASS. Beyond the NE inner lobe a collimated radio feature connects with the diffuse outer NE lobe, while beyond the SW inner lobe the radio emission connecting with the SW lobe seems bifurcated. The outer lobes show distinct radio morphologies with only the SW one showing two hotspots

in VLASS. First seen by us in the 62-MHz cutouts by van Weeren et al. (2014), albeit with much lower sensitivity than BLDF.

J1425+3633 is a regular, straight, but slighty asymmetric FR II with outer lobes highly dilute in VLASS and no hotspots.

J1425+3506 is an FR II source with faint, dilute lobes. The host could also be DESI J216.2998+35.1115, r=25.00, with z_{ph}=0.971,1.308,1.56 from Zhou et al. (2021), Duncan et al. (2021), Chung et al. (2014) in which case its *LLS* would be ∼1.1 Mpc.

J1425+3557 is a core-dominated source with very dilute remnant-type lobes extending due E and W. An extended brightening ∼30″ from the host due W has no optical or IR counterpart and may qualify it as a hybrid-morphology source (HyMORS).

J1426+3407C is a candidate FR II source since the SSE lobe has SDSS J142625.73+340657.8 as a possible host, and the NNW lobe features SDSS J142622.04+340902.0 at its S end.

J1426+3320 is an FR II source where both lobes bend from the E-W direction towards S, giving it a C shape. It is completely resolved out in VLASS with no hotspots.

J1426+3236 is a regular, straight and symmetric FR II source completely resolved out in VLASS, suggesting that the hotspots have already disappeared. Also listed in Mingo et al. (2022).

J1426+3222 is an FR II source with diffuse lobes towards E and W, already shown with a lower-sensitivity image by Williams et al. (2016). From the inner parts of each lobe faint radio plumes stretch out due N.

J1427+3625 is an asymmetric, slightly bent FR II source extending along PA∼48°, with the NE lobe featuring a curved ridge of emission stretching from the hotspot first due SE and then SW towards the host. The SW lobe only shows a short trail from the end of the lobes towards the host. This is the only source in our sample that has been reported before as a giant radio quasar by Kuźmicz & Jamrozy (2021).

J1427+3312: Its host was detected in X-rays (CXOXB J142718.3+331205) by Brand et al. (2006). The radio emission features a strong, short NW lobe and a much longer and lower surface brightness SE lobe whose exact length is somewhat uncertain, making it a hybrid morphology source.

J1427+3328C: the source with the largest angular size in our sample with very inflated and low surface brightness lobes, with the E lobe slightly flattened with major axis along PA∼70° and the W lobe closer to the host and extended in the N-S direction, almost perpendicular to the major axis of the source. Several compact sources are superimposed on the lobes and it is difficult to state a precise total flux. There is no radio emission detected at the location of our proposed host 2MASX J14273770+3328081. However, it is the brightest galaxy in both the optical and MIR (un-WISE) in the entire region of the radio emission. Also, its angular and linear sizes may be larger in more sensitive future radio images. No radio emission detected at the location of our proposed host 2MASX J14273770+3328081. However, it is the brightest galaxy in both the optical and mid-infrared (unWISE) in the entire region of the radio emission. There is in fact a second-brightest galaxy in this region 46″ SSW of 2MASX J14273770+3328081, SDSS J142736.24+332726.0, r=18.03, z_{sp}=0.231 (Kochanek et al., 2012), which does coincide with a radio source of 150-MHz flux of 0.37-mJy in the LoTSS Bootes Deep Field. which is also closer to lying mid-way between the flux-weighted centers of each lobe. If this were the true host, its *LLS* would be 2.0 Mpc.

J1427+3255C is a straight, symmetric classical FR II source along PA∼135°. The SE lobe shows a diffuse radio tail (or plume) due N from the termination point, while the NW lobe is fainter and more compact in the BLDF image. We consider it a candidate GRG, although neither lobe has a suitable optical or IR counterpart.

J1428+3432 is a remnant-type FR II radio galaxy with a clear core but very diffuse, non-collinear lobes due NE and S.

J1428+3631 is a classical FR II source already shown by Williams et al. (2016) with lobe emission almost all the way from the hotspots (clearly seen in VLASS) and the radio core (faint, but detected in VLASS). There is another, smaller and unrelated FR II source ~1.6′ SW of the host.

J1428+3446 is a core-dominated FR II type source with rather straight and very low surface brightness lobes along PA~150°. Background sources are superposed due W of the S lobe, as well as to the SW and NE of the N lobe.

J1428+3525 is a remnant-type radio galaxy with a clear core, a shorter and stronger W lobe, and a longer and fainter E lobe. Both lobes are of very low surface brightness and are aligned with the host, suggesting that a few starlike optical objects in these lobes are superposed accidentally.

J1429+3326: the source features an unusual emission spur or plume emanating from the SW lobe, close to the host, in the NW direction and perpendicular to the main source axis, also seen in Fig. A1 of Williams et al. (2016) but too faint to be seen in the 62-MHz image by van Weeren et al. (2014). The source is completely resolved out in VLASS. Such features have been seen in both lobes of X-shaped sources like in PKS 2014−55 Cotton et al. (2020) but in J1429+3326 we see it only in one lobe.

J1429+3355 is a straight and slightly asymmetric FR II radio galaxy with the shorter NW lobe being strong and featuring a hotspot in VLASS, while the SE lobe is fainter in BLDF and undetected in VLASS suggesting the absence of a hotspot. This source was first noticed by us in a 325-MHz VLA image kindly supplied by R. Coppejans (Coppejans et al. 2015), but is also displayed in Williams et al. (2016).

J1429+3356 is a core-dominated FR II source with a collimated (jet?) feature half-way from the core to the NW lobe. This feature is very faint in VLASS which also detects the end of the NW lobe as a diffuse feature (no hotspot), while the SE lobe is completely undetected. The BLDF image shows some background sources ~30″ SW of the SE lobe and ~30″ N of the end of the NW lobe. This source was first noticed by us in a 325-MHz VLA image kindly supplied by R. Coppejans (Coppejans et al. 2015).

J1429+3717 is a remnant-type radio galaxy which shows a clear core, a short E lobe and a much larger SW lobe which has an unrelated strong FR II source superposed. The latter does not permit us to measure a reliable size for the diffuse source which is completely resolved out in VLASS.

J1429+3230C: this source, supposedly a large FR II with major axis along PA~165°, is somewhat speculative, since the faint S lobe has optical and IR objects superposed. However, the N lobe is elongated along the source major axis and does not feature suitable optical or IR counterparts. The suggestion of a ~2.2′ wide double source straddling the host along PA~100° is due to two sources aligned with the host but with clear counterparts.

J1430+3519 is a symmetric and straight FR II radio galaxy with strong, but very diffuse remnant-type lobes. Unusual features are two compact sources, one at the SW edge of the SE lobe and another close to the middle of the NW lobe, neither one having an obvious optical or IR counterpart. This source has the steepest radio spectrum in our sample and was first seen by us in Williams et al. (2016).

J1430+3322C: this faint source features an inner FR I-type structure of ~32″ E-W extent, with the core faintly detected in VLASS, including a slight E-W extent. The stronger W lobe is closer to the host than the more detached E lobe located ~1.8′ from the host. The source may well extend further into a WAT-type source in future, more sensitive images.

J1431+3345 is probably a good example of an FR I source with continuous jets from the host towards both lobes which seem to end in a strong bend, perhaps seen in project in the SW lobe. Due to the presence of these outer lobes we classify it as an FR I/II. While the jets appear rather straight for the first arcmin from the host, their PA differs by about 7°. The host is the brightest cluster galaxy in cluster WHL J143103.5+334542 (Wen et al. 2012). This source was first noticed by us in a 325-MHz

VLA image kindly supplied by R. Coppejans (Coppejans et al. 2015), but is also seen in Williams et al. (2016).

J1431+3535C is a relatively straight FR II source with lobes of different morphology. Both lobes have optical/IR objects superposed, but in our opinion these are less likely to explain the radio structure. There is a circularly extended source immediately NW of the host, perpendicular to the major source axis, which has no optical/IR counterpart. The strong extended radio source ~1′ W of the N end of the source is the bright foreground starburst galaxy MCG +06-32-056 with a dust lane. The r=18.1 mag low surface brightness galaxy is superposed on the SW lobe, but its blue color and low z_{phot} suggest it is a starforming galaxy in the foreground.

J1431+3440 is a straight and symmetric FR II source with diffuse lobes, each of them showing plumes due W. The source is difficult to recognize due to various compact sources due W and NW of the host.

J1431+3427 is a straight and symmetric FR II source with a faint radio core. This source was first noticed by us in a 325-MHz VLA image kindly supplied by R. Coppejans (Coppejans et al. 2015), but is also displayed in Williams et al. (2016).

J1432+3411 is a symmetric, though slightly bent FR II source with no detected hotspots in VLASS. The BLDF image suggests the jets feeding the lobes to have a difference in PA of ~7°. This source was first noticed by us in a 325-MHz VLA image kindly supplied by R. Coppejans (Coppejans et al. 2015), but is also displayed in Williams et al. (2016).

J1432+3328 is a rather asymmetric, though straight, FR II with an armlength (or lobelength) ratio of 2.8. The source is listed in Mingo et al. (2022).

J1432+3545 is a very extended WAT-type source hosted by the brightest galaxy of cluster WHL J143233.9+354540 (aka GMBCG J218.14135+35.76114 and MaxBCG J218.14136+35.76113). The angular size we list may well be exceeded by future more sensitive observations.

J1432+3220 is a symmetric FR II source with faint hotspots and a faint core detected in VLASS. This source was first noticed by us in a 325-MHz VLA image kindly supplied by R. Coppejans (Coppejans et al. 2015) and is also seen in Williams et al. (2016).

J1432+3154C is a rather faint FR II source with diffuse lobes and a core symmetrically placed between these lobes. We consider it a candidate because each lobe has optical/IR objects which may explain the lobes as separate sources. No part of the source is detected in VLASS.

J1432+3647 is an FR II source with detached, diffuse, low surface brightness lobes bent at an angle of ~25° with respect to the host. The NE lobe appears bifurcated. Only the radio nucleus is detected in VLASS.

J1433+3220 is a possible restarted FR II source with an inner double of ~38″ along PA~104°, very close to the PA connecting the diffuse, low surface brightness outer lobes. Since these lobes are large, some optical/IR objects are seen superposed, but they are unlikely to explain each lobe as a separate source. The host itself is undetected in both BLDF and VLASS, which does not detect any part of the source.

J1433+3328 is a core-dominated straight FR II source oriented E-W and hosted by a QSO at z_{sp}=1.609. While the W lobe has a typical FR II morphology being brightest at the end in BLDF with a barely detected hotspot in VLASS, the E lobe is brightest about half way down the lobe, and is undetected in VLASS. It is thus a possible hybrid-morphology source.

J1433+3450 is a classical, slightly bent FR II source with a faint core detected in both BLDF and VLASS. While our proposed host coincides with that radio core, it differs from that proposed by Morabito et al. (2017) which is off the main radio ridge. The hotspots are strong in VLASS, albeit with much shorter trails towards the host than those in BLDF. This source was first noticed by us in van Weeren et al. (2014) and is also seen in Williams et al. (2016). This is the source with the highest

radio luminosity in our sample.

J1433+3145C is a low surface brightness diffuse radio galaxy without a clear radio core. The LoTSS DR2 low-resolution image suggests a WAT-type source whose host may also be located further South, e.g. SDSS J143320.32+314544.0 with z_{ph} ~0.4 which would make its *LLS* about 0.77 Mpc, but still large enough to be a GRG. The strongest compact 150-MHz source at the S end of the emission region, ILT J143320.57+314529.1 of ~1 mJy, does not have any optical/IR counterpart.

J1434+3428 is a complex, slightly bent FR II source with several radio knots along the E lobe. Both lobes feature hotspots in BLDF which are also faintly detected in VLASS, but which are located due N of the symmetry axis of the lobes. The host of this source is still unclear. We have chosen the brighter one, but ~19″ E of it there is WISEA J143430.65+342757.0 with more typical AGN colors, undetected in the optical in DESI DR9, but found to be a member of cluster ISCS J1434.5+3427 with z_{sp}=1.240 from Alberts et al. (2016), also detected as X-ray source 2CXO J143430.6+342757, and as FIRST J143430.6+342757 in the radio. Adopting the latter host this source would be only slightly larger and more radio luminous, as well as a candidate restarted source. The source was first noticed by us in a 325-MHz VLA image kindly supplied by R. Coppejans (Coppejans et al. 2015).

J1434+3214C has a clearly detected inner source of ~1.0′ extent that is accompanied by fainter lobes more or less symmetrically placed on the E and W side of the latter, making it more of an FR I rather than FR II type source. The source fades away below noise at *LAS*~3.7′ but may continue further in more sensitive images.

J1434+3648 is an almost straight FR II source with low-surface brightness or remnant-type lobes along PA~140°. Some optical/IR objects in the area of the lobes seem unlikely to explain them individually, so we consider the source as genuine.

J1434+3328C is a very large diffuse source of oval shape with major axis near PA~160° with a low surface brightness extension from the end of the N lobe towards SW. The N lobe is much brighter and of FR II type, while the S lobe is fainter and of FR I type, thus it is a candidate hybrid morphology source. The innermost source shows a compact radio knot ~6″S of the host, also seen in VLASS and Coppejans et al. (2015). An additional diffuse source is seen ~16″ from the host with no optical/IR counterpart. The host itself is a broadline QSO at z_{sp}=0.19756 (from SDSS) and is apparently located in a compact triple of galaxies. However, while the 2nd-brightest member of that triple, SDSS J143444.88+332817.3 ~6″WSW of the host has a z_{ph} compatible with the host, the 3rd-brightest member (SDSS J143445.33+332823.5) ~3″N of the host is a galaxy at z_{sp}=0.24565, so apparently in the background. The host was also detected in X-rays as 1RXS J143445.8+332814 and more recently with Chandra (Masini et al. 2020) and Kostrzewa-Rutkowska et al. (2018) report the host to have featured a Gaia transient. The host had been proposed as a blazar candidate by D'Abrusco et al. (2019). It is thus possible that the source is oriented at a large angle with respect to the plane of the sky and is intrinsically much larger. The peak of the emission of the N lobe in the full-res. Deep Field coincides with SDSS J143442.62+333015.8 with z_{phot} indistinguishable from the QSO host's z_{spec}, so that galaxy could be the host of a WAT-like source that constitutes most of the NNW lobe including the circular wings running to SSE and SSW, making the inner source only about 3.4′ (LLS = 0.67 Mpc), and N WAT-type source would have 3′ or LLS=0.59 Mpc.

J1435+3404 is a rather faint Z-shaped source with a clear radio nucleus and evidence for precessing jets or lobes starting in the E-W direction and gradually turning S in the E lobe and N in the W lobe.

J1435+3547: the BLDF image shows this to be a straight and symmetric restarted FR II radio galaxy with inner lobes of *LAS*~32″. Except for very faint hotspots it is not detected in VLASS, suggesting both inner and outer lobes having aged substantially, which is consistent with the fact that it is the source with the second-steepest radio spectrum in our sample.

J1436+3416 is a straight, restarted FR II with asymmetric inner lobes of LAS~1.1′. The inner lobes have well-detected hotspots in VLASS but no detection of the host. The hotspot of the inner NE lobe is displaced significantly from the galaxy SDSS J143654.42+341726.9 near the middle of that lobe and we regard this galaxy as accidentally superposed. The outer lobes are undetected in VLASS. Our proposed host is undetected in WISEA, and closer to the centre between the inner hotspots there is WISEA J143653.20+341657.1 with AGN-like WISE colours and undetected in DESI DR9, but listed with z_{ph}=1.54 in Duncan et al. (2021), which would imply an LLS of ~1.88 Mpc. Some 52″ NW of the host the very bright foreground galaxy MCG +06-32-076 appears as a strong radio source.

J1437+3650 is a slightly asymmetric remnant-type FR II source with low surface brightness lobes along PA~140°. Part of the farther SE lobe may be caused by emission from superposed objects.

J1437+3233 is a WAT-type source with indications of the far WSW lobe showing a bend of ~150°, perhaps due to projection. The host is too faint to recognize any cluster around it on optical images, but the unWISE image (Lang 2014) suggests a concentration of objects around the source.

J1438+3445C is a slightly bent FR II source with very detached lobes. Only the stronger SE lobe, which has no optical/IR counterpart, shows a faint indication of a hotspot in VLASS.

J1438+3526 is a straight, core-dominated FR II source with a stronger NE lobe terminating in what appears as a hotspot, which is undetected in VLASS. The SW lobe is of very low surface brightness and suggests a bend due SE near its end.

J1438+3355: this is the third-largest source in angular size but the one of largest linear size (3.8 Mpc) in our sample. The outer lobes are very detached from the host, but both show the characteristic (though short) trail of radio emission from the far end of the lobes towards the host. The lobe length ratio is only 1.4 (NE/SW lobe) and both lobes are aligned with the host to within 1.5°. The source has a radio luminosity in the upper quartile and a rather steep spectrum ($\alpha > 1.17$).

J1438+3539 is a rather asymmetric source with the southern more compact lobe reaching twice as far from the host than the northern, more diffuse lobe. A faint hotspot is seen in the S lobe in VLASS, separated from two WISE objects E of it. This, together with the fact that the S lobe has a faint, low surface brightness spur due NE, suggests that this is in fact the S lobe of a large source. Also, the lobe orientations with respect to the host are aligned to within 2°.

J1439+3251C: this candidate radio galaxy features two symmetric, low surface brightness lobes along PA~54°, and we include in its size a compact source at the end of the NE lobe which we interpret as a hotspot since it does not show any optical/IR counterpart.This hotspot is the only part of the source detected in VLASS. We chose the host as it features an apparent radio core in BLDF, while a similarly bright galaxy due E (SDSS J143903.20+325135.9) does not.

J1439+3254 is a straight, symmetric FR II source of high radio luminosity. VLASS shows diffuse lobes with indications of two hotspots in the stronger N lobe and a very faint one in the S lobe. This source was first noticed by us in a 325-MHz VLA image kindly supplied by R. Coppejans (Coppejans et al. 2015).

J1439+3221C is a core-dominated remnant-type source of intermediate FR type. The N lobe shows some wiggling before it reaches its maximum brightness at its end, though a hotspot is not detected in VLASS. The S lobe shows continuous very low surface brightness emission in the low-resolution LoTSS DR2 image before it seems to fade away below noise ~2.5′ S of the host, but may in fact continue for another 1.3′ due S.

J1440+3211 is one of the angularly largest sources in our sample, this is an FR II source with very detached lobes, both of them showing radio trails from their end towards the host, which both lobes being oriented parallel to within less than 1°. The host is barely detected in BLDF, and undetected in VLASS. The N lobe shows a prominent hotspot in VLASS while in the S lobe none is detected.

J1440+3348: this source is similar to the protypical FR I sources with precessing jets (like 3C 31

or 3C 449), though the jets are below the detection limit of VLASS.

J1442+3457 is a rather straight FR II type source with a very detached NW lobe and a more diffuse SE lobe, both of low surface brightness. The more compact source ~30″ N of the N lobe has a separate host and is thus unrelated.

J1442+3605: this FR II type source has one of the highest radio luminosities in our sample and VLASS resolved the lobes into broad, almost circular emission regions of almost constant surface brightness, albeit with hotspots embedded in them. These hotspots are not located at the outer edges of the lobes, such that the distance between them is 1.5′ compared to 1.84′ for the total projected size of the source.

J1442+3243 is a straight, asymmetric FR II type source with strong lobes in VLASS showing constant surface brightness over an oval region in which a hotspot (or at least a "spine") is embedded. The exact size of this source is difficult to measure on its E side where it overlaps with the NE lobe of J1442+3242. This source was first noticed by us in a GMRT 150-MHz image by Williams et al. (2013).

J1442+3242: the host of this FR II source is only ~18″ SE of the E hotspot of J1442+3243, thus its diffuse NNE lobe overlaps with the E lobe of J1442+3243. Only the stronger SSW lobe shows a well-detected hotspot in VLASS surrounded by a faint envelope of diffuse emission. Future, improved VLASS images may confirm a possible *LAS* of up to 2.0′.

J1444+3445C is one of the sources with the lowest radio luminosity in our sample. It has an FR I type inner region with two very low surface brightness lobes due W and ESE with a bending angle of ~25° between them. Some optical/IR objects are superposed on the outer lobes which we consider unlikely to account for the lobes, which are entirely undetected in VLASS.

J1444+3348: this source has an uncertain radio morphology and features a faint (if any) radio core, a strong but diffuse W lobe close to the host and a longer, more collimated E lobe which bends due N close to its end.

J1444+3444 is a rather straight FR II source oriented along PA~157° and is difficult to recognize due to a compact source superposed ~18″ WNW of the host. It features a continuous SSE lobe of moderate surface brightness that curves due W before its end, and a more detached and patchy NNW lobe. No part of this source (except the superposed one) is detected in VLASS.

Table A1: Col. (1), name of the giant radio galaxy. The superscript refers to the reference of the catalogue that reported the source: 1-Coppejans et al. (2015), 2-Williams et al. (2016), 3-van Weeren et al. (2014), 4-Kuźmicz & Jamrozy (2021), 5-Williams et al. (2013), 6-Mingo et al. (2022), 7-Masini et al. (2021). Col. (2) and Col. (3), right ascension and declination (J2000) of the host galaxy in degrees. Col. (4), largest angular size. Col. (5), classification of GRGs according to the Fanaroff–Riley classification. Col. (6), redshift of the host galaxy. Col. (7), redshift error when available. Errors of the spectroscopic redshifts are not reported since they are generally more accurate than the precision we can achieve on the linear sizes and luminosities. Col. (8), type of the redshift: p for photometric, s for spectroscopic and e if estimated. Col. (9), references for the redshift. These are either spectroscopic measurements, such as 3-SDSS(Beck et al. 2016), 8-LAMOST(Luo et al. 2015), 9-Huchra et al. (2012), 10-Kochanek et al. (2012), or photometric estimates: 1-DESI (Zou et al. 2019; Zhou et al. 2021), 2-Duncan et al. (2021), 4-Pan-STARRS (Beck et al. 2021), 5-Chung et al. (2014), 6-Bilicki et al. (2016), 7-Brescia et al. (2014). Col. (10), name of the host galaxy. Col. (11) type of host galaxy: galaxy (G) or QSO (Q) or candidate quasars (Qc). Col. (12), largest linear size. Col. (13), magnitude of the host galaxy in the r-band if available from the DESI DR9 photometric catalogue; the label W1 and W2 indicates that the magnitude is taken from either WISEA or CWISE catalogue. Col. (14), total flux at 150 MHz from the full resolution 6″ image. Col. (15) total flux 1σ error from the 6″ image. An asterisk is appended to the flux estimate of the source if the flux integration is computed by considering all the pixels belonging to the region of the radio emission. Col. (16), log10 of power at 150 MHz. Col. (17) spectral index α measured by using NVSS (1.4GHz), LOFAR HBA (150MHz) and LOFAR LBA (50MHz) data. Col. (17), spectral index error.

(1) Name LBDF-GRG	(2) RA_J °	(3) Dec_J °	(4) LAS (′)	(5) FR type	(6) z	(7) Δz	(8) ztype	(9) ref	(10) Hostname	(11) type	(12) LLS (Mpc)	(13) mag (mag)	(14) S_{150} (mJy)	(15) σ_S	(16) $\log_{10} P_{150}$ (W/Hz)	(17) α	(18) $\Delta\alpha$
J419+3337	214.8027	33.6328	1.8	II	1.09	0.16	p	1,4	DESI J214.8027+33.6329	?	0.9	23.41 r	9.6	1.4	25.7		
J421+3431	215.4634	34.5289	1.5	II	1.02	0.25	p	1	DESI J215.4634+34.5289	G	0.7	24.59 r	4.1	0.8	25.2	0.66	0.19
J421+3521	215.4909	35.3570	2.2	II	1.1		e		CWISE J142157.80+352125.3	?	1.1	17.31 W2	58.6	5.9	26.5	0.93	0.05
J422+3320	215.6373	33.3354	2.8	II	0.94	0.11	p	1,4	DESI J215.6373+33.3353	G	1.3	23.83 r	145	15	26.7		
J422+3255	215.6913	32.9322	1.7	II	1.07	0.23	p	1	DESI J215.6913+32.9322	G	0.8	24.17 r	53.8	5.5	26.4		
J423+3600	215.7846	36.0052	2.0	II	1.09	0.21	p	1	DESI J215.7846+36.0053	G	1.0	24.16 r	55.6	5.7	26.5	0.94	0.05
J423+3403	215.9003	34.0506	2.7	I/II	0.561		s	3	SDSS J142336.06+340302.1	G	1.1	20.17 r	9.9	1.4	25.0	0.86	0.12
J423+3302	215.9105	33.0484	1.9	II	1.03	0.19	p	1,4	DESI J215.9106+33.0483	G	0.9	23.82 r	258	26	27.1		
J423+3529	215.9201	35.4888	7.5	II	0.83	0.05	p	1,3,4	SDSS J142340.83+352919.7	G	3.4	21.91 r	20.4	3.0	25.7	1.10	0.12
J423+3340	215.9259	33.6693	1.5	II	1.5		e	-	CWISE J142342.22+334009.6	?	0.8	18.05 W1	3.6	0.9	25.6	0.48	0.14
J423+3605	215.9486	36.0946	2.8	I	0.36	0.02	p	1,3,6	SDSS J142347.66+360540.5	G	0.8	18.73 r	40.7	4.2	25.2		
J424+3609[2]	216.0397	36.1547	7.3	II	0.58	0.07	p	1,3,4	SDSS J142409.52+360917.0	G	2.9	20.89 r	191	19.3	26.4	0.74	0.04
J424+3436[2,3]	216.1358	34.6127	4.2	I/II	0.586		s	3	SDSS J142432.58+343645.8	G	1.7	20.14 r	486	49	26.8	0.85	0.04
J425+3633	216.2942	36.5612	2.3	II	0.70	0.08	p	1,3,4,7	SDSS J142510.60+363340.3	G	1.0	21.13 r	217	22	26.6	0.89	0.04
J425+3506[6]	216.2995	35.1045	2.1	II	0.71	0.05	p	1,2,3,4	SDSS J142511.88+350616.1	G	0.9	22.09 r	14.3	1.7	25.4	0.94	0.12
J425+3557	216.3287	35.9574	3.7	II	0.419		s	3	SDSS 142518.87+355726.7	G	1.2	18.54 r	14.6	1.7	24.9		
J426+3407C	216.6021	34.1285	2.7	II	0.75	0.14	p	1,2,3,4	SDSS J142624.49+340742.6	G	1.2	21.96 r	42.8	4.5	26.0	1.02	0.06
J426+3320[6]	216.6026	33.3373	2.1	II	0.82	0.15	p	1,2	DESI J216.6026+33.3373	G	1.0	23.66 r	62.2	6.3	26.2	1.19	0.05
J426+3236[6]	216.6109	32.6024	2.0	II	0.96	0.11	p	1,2	DESI J216.6109+32.6024	G	0.9	24.05 r	46.8	4.8	26.2		
J426+3222[2]	216.7126	32.3717	2.8	II	0.68	0.12	p	1,2,3,4,5	SDSS J142651.02+322218.0	G	1.2	21.36 r	386	39	26.8	0.92	0.04
J427+3625[4]	216.8259	36.4170	2.4	II	0.851		s	3	SDSS J142718.21+362501.1	G	1.1	18.02 r	200	20	26.8	0.72	0.04
J427+3312	216.8265	33.2016	2.1	I/II	0.93	0.28	p	1,2,4,11	DESI J216.8265+33.2016	Q	1.3	22.89 r	18.3	1.9	25.8	1.12	0.11
J427+3328C	216.9070	33.4688	9.0	II	0.150		s	3,10	2MASX J14273770+3328081	G	1.4	16.66 r	64.7*	7.2	24.6	>−0.26	
J427+3255C	216.9363	32.9289	2.7	II	2.18	1.65	p	2	SSTSL2 J142744.69+325543.9	G	1.4	16.49 W2	7.5*	1.0	26.3	>0.30	
J428+3432	217.0151	34.5361	1.4	II	1.02	0.11	p	1,2,4	SDSS J142803.63+343210.0	G	0.7	23.24 r	3.9	0.7	25.2		
J428+3631[2]	217.0284	36.5249	2.4	II	0.59	0.19	p	1,3,7	SDSS J142806.81+363129.5	G	0.9	21.60 r	602	60	26.9		
J428+3446	217.0977	34.7752	1.9	II	0.588		s	11	SDSS J142823.44+344630.6	G	0.7	20.67 r	7.5	1.0	25.0		
J428+3525	217.1499	35.4271	2.8	II	0.88	0.23	p	1,2,4,5	DESI J217.1498+35.4271	G	1.3	23.16 r	10.9	1.4	25.5		
J429+3326[2,3]	217.2997	33.4437	2.6	II	0.320		s	8	SDSS J142911.92+332637.5	G	0.7	18.83 r	270	27	25.9		
J429+3355[1,2]	217.3171	33.9270	2.8	II	1.059		s	3	SDSS J142916.10+335537.4	G	1.4	23.03 r	137	14	26.8	0.92	0.04
J429+3356[1,2,4]	217.4277	33.9486	2.2	II	1.124		s	3	SDSS J142942.63+335654.8	Q	1.1	18.97 r	92.9	9.3	26.7	0.88	0.04
J429+3717	217.4724	37.2914	2.8	II	0.65	0.06	p	1,3	SDSS J142953.37+371728.9	G	1.1	21.95 r	22.6	2.4	25.5		

111

J1429+3230C	217.4756	32.5127	6.1	I/II	1.17	0.26	p	1,2,3,4	SDSS J142954.06+323045.8	Qc	3.0	22.67 r	11.6	1.6	25.8	0.81	0.12
J1430+3519[2,7]	217.5410	35.3329	4.0	II	0.629		s	3	SDSS J143009.83+351958.2	G	1.7	20.76 r	52.0	5.3	25.9	1.74	0.23
J1430+3322C	217.6154	33.3804	3.7	I	0.512		s	3	SDSS J143027.69+332249.4	G	1.4	19.52 r	14.6	1.5	25.1	>0.11	
J1431+3345[1,2,5]	217.7644	33.7616	3.6	I/II	0.238		s	3	2MASX J14310340+3345414	G	0.8	16.77 r	166	17	25.4	0.67	0.04
J1431+3535C	217.8483	35.5976	2.6	II	1.04	0.18	p	1,2,4	DESI J217.8484+35.5975	G	1.3	23.01 r	24.0*	2.7	26.0		
J1431+3440	217.8485	34.6681	2.2	II	0.79	0.09	p	1,2,3,4	SDSS J143123.56+344005.0	G	1.0	21.68 r	8.2	0.9	25.3	0.88	0.04
J1431+3427[1,2]	217.8639	34.4506	3.0	II	0.44	0.15	p	1,3	SDSS J143127.33+342702.3	G	1.0	20.82 r	116	11	25.9	1.03	0.05
J1432+3411[1,2]	218.0479	34.1926	2.4	II	1.04	0.15	p	1,2,3,4,5	SDSS J143211.50+341133.2	G	1.2	22.68 r	65.7	6.6	26.5	1.13	0.04
J1432+3328[6]	218.1046	33.4770	1.8	I	1.30	0.04	p	1,2,4,5	DESI J143223.46+332852.5	Qc	0.9	21.84 r	114	11	26.9	0.77	0.04
J1432+3545[2]	218.1413	35.7612	5.0	II	0.185		s	3	2MASX J14323389+3545397	G	0.9	16.71 r	84.0	8.5	24.9		
J1432+3220[1,2]	218.1777	32.3459	1.6	II	0.81	0.08	p	1,2,4	SDSS J143242.64+322045.4	G	0.7	22.30 r	107	11	26.4	0.68	0.15
J1432+3154C	218.2283	31.9030	3.3	II	0.88	0.15	p	1	DESI J218.2283+31.9030	G	1.6	23.15 r	5.2	1.7	25.2	0.52	0.25
J1432+3647	218.2430	36.7894	1.5	II	2.836		s	3	SDSS J143258.30+364721.7	Q	0.7	22.20 r	13.1	1.6	26.8		
J1433+3220	218.2569	32.3435	5.9	II	0.552		s	3	SDSS J143301.66+322036.7	Q	2.3	20.40 r	12.3	2.5	25.12	0.68	0.05
J1433+3328	218.3156	33.4830	1.4	I/II	1.609		s	8	SDSS J143315.74+332858.6	Q	0.7	22.76 r	28.4	2.9	26.6	1.00	0.04
J1433+3450[2,3]	218.3258	34.4485	1.7	II	1.00	0.14	p	1,2,4,5	DESI J218.3257+34.8485	G	0.8	22.79 r	1628	163	27.8	0.84	0.15
J1433+3145C	218.3367	31.7665	2.4	II	0.69	0.06	p	1,3,4	SDSS J143320.81+314559.2	G	1.0	22.13 r	5.1	1.4	24.9	0.96	0.04
J1434+3428[1,2]	218.6212	34.4668	2.6	II	0.96	0.04	p	1,2,3,4	SDSS J143429.09+342800.4	G	1.2	22.71 r	145	14	26.7	0.40	0.18
J1434+3214C	218.6639	32.2407	2.7	I	1.5		e	–	CWISE J143439.34+321426.6	?	1.4	17.83 W2	3.7	1.2	25.6		
J1434+3648	218.6889	36.8099	2.3	I	0.429		s	3	SDSS J143445.33+364835.5	G	0.8	19.27 r	10.6	1.4	24.8		
J1434+3328C	218.6890	33.4724	4.7	II	0.198		s	3	2MASX J143444537+3328211	Q	0.9	16.72 r	54.8	5.7	24.8		
J1435+3404	218.8812	34.0780	2.1	II	0.546		s	3	SDSS J143531.49+340440.9	G	0.8	21.82 r	5.6*	0.8	24.8		
J1435+3547	218.9370	35.7978	1.7	II	1.63	0.27	p	1,2,3,4	SDSS J143544.87+354752.2	G	0.9	22.72 r	30.1	3.1	26.6	1.43	0.19
J1436+3416	219.2216	34.2807	3.7	II	0.25	0.15	p	1,2,3,4	SDSS J143653.19+341650.5	G	0.9	21.67 r	69.8	7.1	25.1	0.95	0.05
J1437+3650	219.3635	36.8387	3.3	II	0.94	0.09	p	1,3,4	SDSS J143727.24+365019.3	G	1.6	23.31 r	8.0	1.6	25.5	0.67	0.15
J1437+3233	219.4135	32.5566	1.5	I	1.02	0.21	p	1,3,4	SDSS J143739.23+323323.8	G	0.7	23.46 r	6.3	0.8	25.4	0.75	0.13
J1438+3445C	219.5403	34.7591	3.2	II	0.58	0.05	p	1,2,3,4,7	SDSS J143809.66+344532.8	G	1.3	21.11 r	9.5	1.5	25.1		
J1438+3526	219.5529	35.4368	1.6	II	0.86	0.08	p	1,3	SDSS J143812.69+352612.6	G	0.8	22.32 r	11.0	1.2	25.5	0.90	0.11
J1438+3355	219.5877	33.9290	7.5	II	1.80	0.17	p	2,5	SDSS J143821.02+335544.4	Qc	3.8	15.77 W2	21.5	2.7	26.5	>1.17	
J1438+3539	219.6260	35.6545	7.1	II	0.262		s	3,10	SDSS J143830.23+353916.1	Q	1.7	18.36 r	17.9	2.3	24.5	0.65	0.05
J1439+3251C	219.7544	32.8586	3.0	II	0.57	0.11	p	1,3,4,6,9	SDSS J143901.04+325131.0	G	1.2	21.41 r	4.0	1.2	24.7	0.40	0.41
J1439+3254[1,2]	219.8133	32.9137	1.7	II	0.80	0.04	p	1,3,4	SDSS J143915.18+325449.4	G	0.8	21.35 r	228	23	26.8	0.88	0.04
J1439+3221C	219.9937	32.3575	4.9	II	0.50	0.02	p	1,3,4	SDSS J143958.48+322126.9	G	1.8	20.54 r	23.2*	3.1	25.3	>0.77	
J1440+3211	220.0520	32.1865	7.5	II	0.49	0.12	p	1,3,4	SDSS J144012.47+321111.3	G	2.7	20.48 r	149	15	26.1	0.61	0.15
J1440+3348	220.1655	33.8009	2.0	I/II	0.542		s	3	SDSS J144039.70+334803.2	G	0.8	20.43 r	17.4	1.9	25.2		
J1442+3457	220.5530	34.9617	3.0	II	0.532		s	3	SDSS J144212.71+345742.2	G	1.1	20.17 r	9.7*	1.2	25.0	0.56	0.14
J1442+3605	220.6305	36.0897	1.8	?	1.10	0.15	p	1	DESI J220.6304+36.0893	G	0.9	23.17 r	457	46	27.4		
J1442+3243[5]	220.6456	32.7242	2.9	II	0.48	0.20	p	1,3,7	SDSS J144234.93+324326.9	Qc	1.1	19.02 r	344	34	26.4		
J1442+3242	220.6844	32.7163	1.9	II	0.80	0.05	p	1,3	SDSS J144244.26+324258.6	G	0.8	22.30 r	166	17	26.6		
J1444+3445C	221.0615	34.7596	3.3	?	0.259		s	3	SDSS J144414.75+344534.5	G	0.8	17.69 r	16.5*	1.9	24.5	0.64	0.05
J1444+3348	221.1075	33.8054	1.8	II	0.91	0.07	p	1,3,4	SDSS J144425.80+334819.3	G	0.9	22.69 r	15.0	2.2	25.7		
J1444+3444	221.1722	34.7425	1.7	II	0.77	0.03	p	1,3,4	SDSS J144441.33+344433.0	G	0.8	21.71 r	39.6	4.3	26.0		
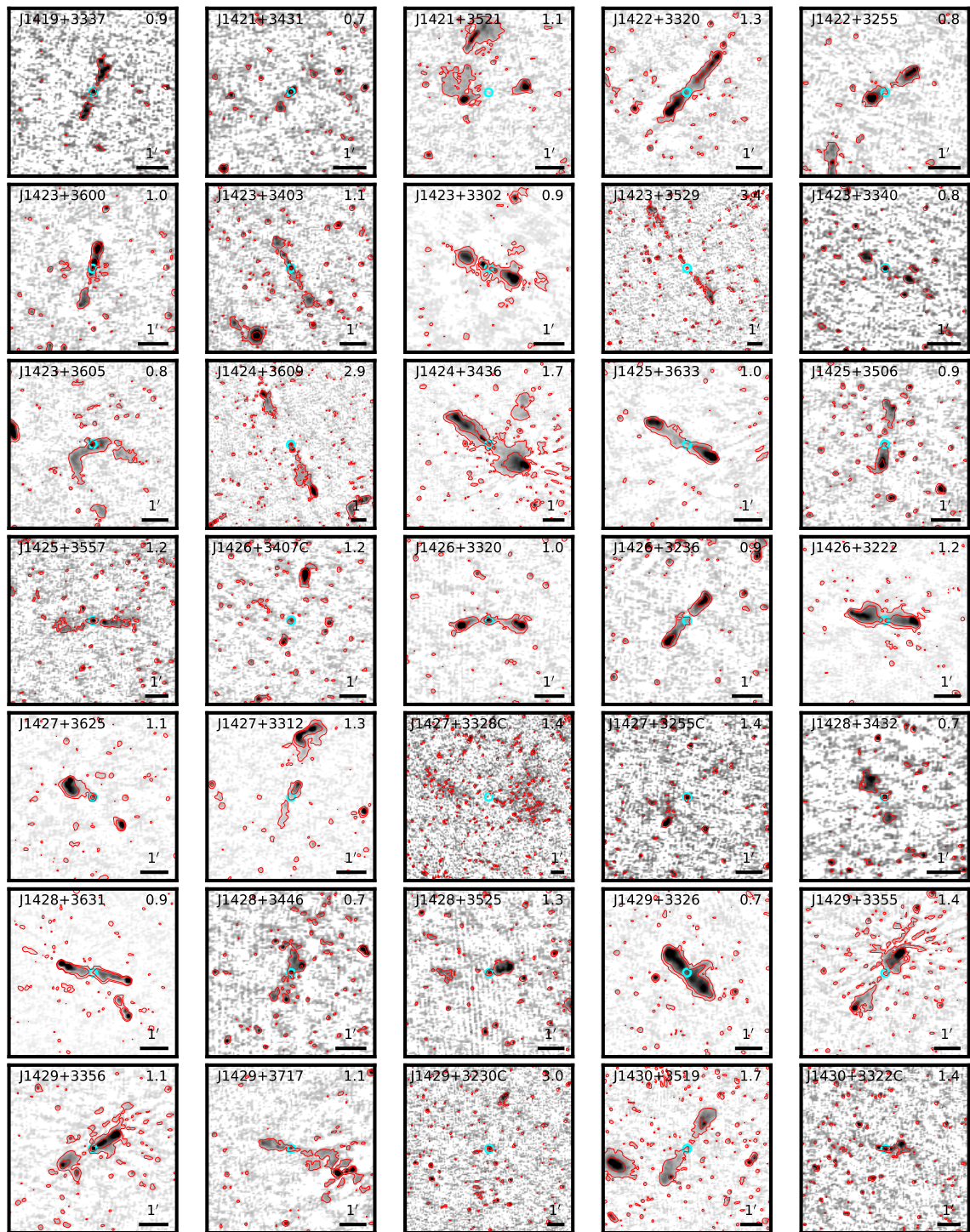
Figure A1: Cutouts of the BLDF image around our GRGs at 150 MHz with 3 and 24-σ_{rms} red contours superimposed. The resolution of the images is 6". The cyan circle identifies the position of the host galaxy. The bar in the bottom-right corner represents an angular size of 1′, while the name and the largest linear size (in Mpc) of the GRGs are reported in the top-left and top-right corners, respectively.
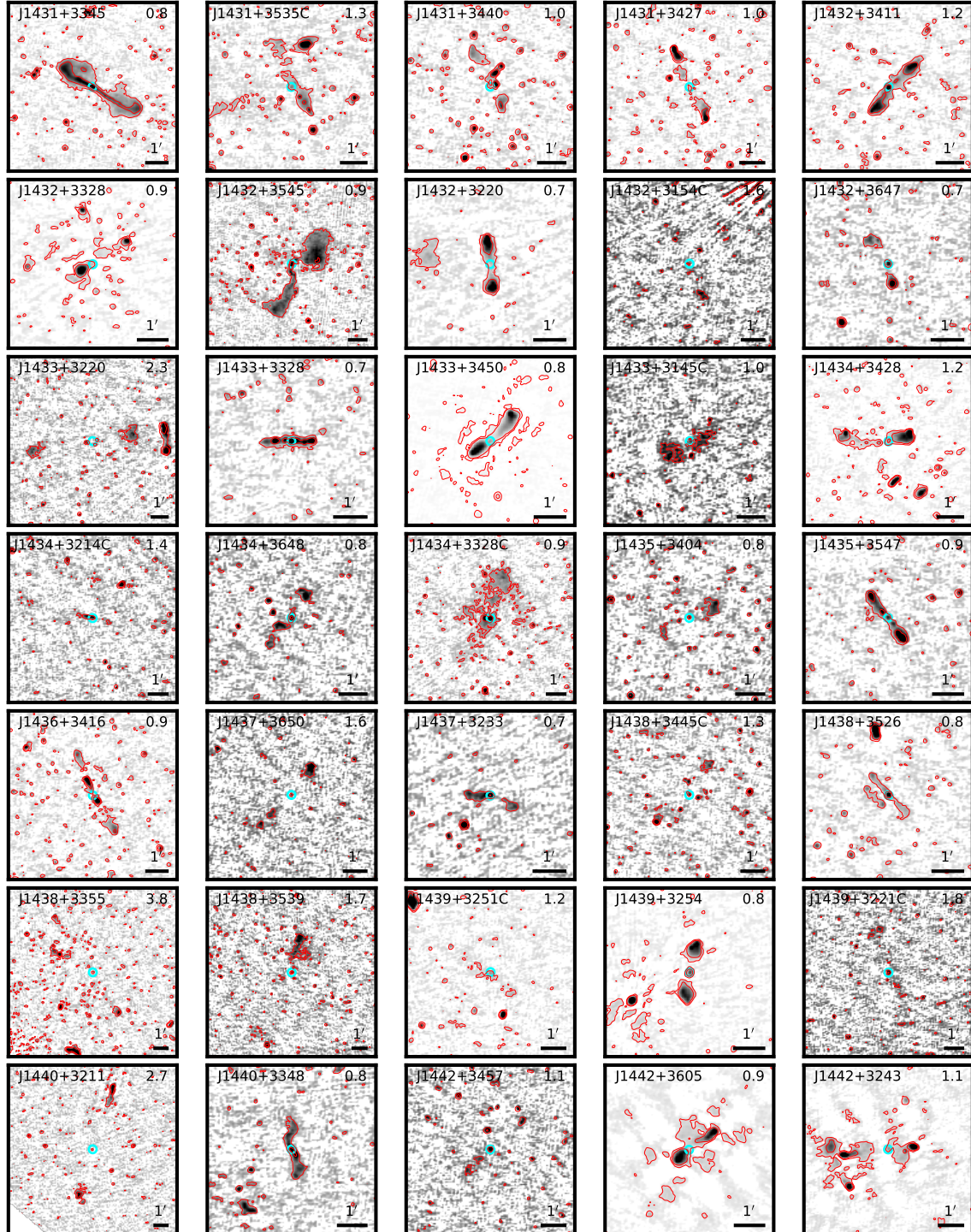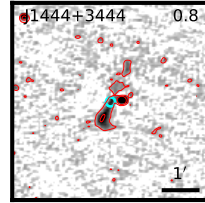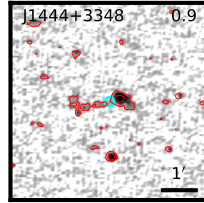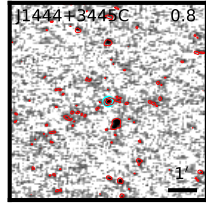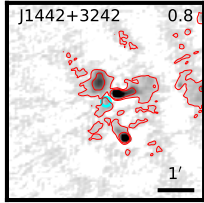
B Table and images of the LDF-GRG sample

In this section, we report the list of GRGs in our sample in Table B1 and their cutouts in Fig. B1. Col. (1), name of the giant radio galaxy. A "C" appended to the ERG name indicates that it is a candidate, meaning that either the host itself, its redshift, or its LAS are uncertain. An "a" or "b" is appended when multiple RGs have the same name in the full catalogue of ERGs in the LOFAR deep fields. Col. (2) and Col. (3), right ascension and declination (J2000) of the host galaxy in degrees. Col. (4), largest angular size. Col. (5), classification of GRGs according to the Fanaroff–Riley classification. Col. (6), redshift of the host galaxy. Col. (7), redshift error. Errors of the spectroscopic redshifts are not reported since they are generally more accurate than the precision we can achieve on the linear sizes and luminosities. Col. (8), type of the redshift: p for photometric, s for spectroscopic and e if estimated. Col. (9), references for the redshift. These are either spectroscopic measurements, such as 1-SDSS(Ahumada et al. 2020) and 13-DESI EDR(DESI Collaboration et al. 2023), or photometric estimates: 2-Pan-STARRS (Beck et al. 2021), 3-Zou et al. (2022), 4-(Rowan-Robinson et al. 2013), 5-Xu et al. (2020), 6-Bilicki et al. (2016), 7-Wen & Han (2021), 8-Brescia et al. (2014), 9-Duncan et al. (2021), 10-Zhou et al. (2021), 11-Duncan (2022), 12-Zhang et al. (2022). Col. (10), largest linear size. Col. (11), name of the host galaxy. Col. (12) type of host galaxy: galaxy (G) or spectroscopically confirmed QSO (Q) or candidate quasars (Qc) defined according to the WISE colours(Mateos et al. 2012). Col. (13), magnitude of the host galaxy in the r-band if available from the DESI DR9 photometric catalogue (r) or SDSSDR12 (r'); the label W1 and W2 indicates that the magnitude is taken from either WISEA (Cutri & et al. 2012; Cutri et al. 2013) or CWISE (Marocco et al. 2021) catalogues. Col. (14), total flux at 150 MHz from the full resolution 6″ image. An asterisk is appended to the flux estimate of the source if the flux integration is computed by considering all the pixels belonging to the region of the radio emission. Col. (15) total flux 1σ error from the 6″ image. Col. (16), log10 of power at 150 MHz. Col. (17) core fraction. Upper limits are identified by the symbol < in front of the estimate.

The table containing all the 1611 ERGs will be uploaded in electric form at the CDS and through the VizieR service (https://vizier.cds.unistra.fr). Besides the columns shown in Table B1, the following additional columns will be available:

- aptspidx: integrated spectral index calculated between 150 and 1400 MHz.

- aptspidx-err: 1sigma error of the integrated spectral index calculated between 150 and 1400 MHz.

- lbaspidx: integrated spectral index calculated between 50 and 150 MHz.

- lbaspidx-err: 1sigma error of the integrated spectral index calculated between 50 and 150 MHz.

- gmrtspidx: integrated spectral index calculated between 150 and 610 MHz.

- gmrtspidx-err: 1sigma error of the integrated spectral index calculated between 150 and 610 MHz.

Table B1: List of GRGs in the LDF-GRG sample.

(1) Name LDF-GRG	(2) RA$_J$ °	(3) Dec$_J$ °	(4) LAS (')	(5) FR type	(6) z	(7) Δz	(8) ztype	(9) ref	(10) LLS (Mpc)	(11) Hostname	(12) type	(13) mag (mag)	(14) S$_{150}$ (mJy)	(15) σ$_S$	(16) log$_{10}$ P$_{150}$ (W/Hz)	(17) f$_c$
J1018+5906	154.5062	59.1148	1.38	FRII	1.5		e		0.70	CWISE J101801.48+590653.2	G	17.08W1	77.9	8.1	26.92	
J1018+5643	154.6400	56.7303	2.03	FRII	0.580		s	1	0.80	SDSS J101833.61+563809.2	G	20.62r'	22.7	4.2	25.43	
J1018+5638	154.7024	56.6359	2.34	FRII	0.51	0.02	p	1,10,11	0.87	SDSS J101848.57+563950.4	G	19.98r'	31.8	5.1	25.45	<0.04
J1020+5639	155.1020	56.6640	3.80	FRII	0.51	0.04	p	1,10,11	1.40	SDSS J102024.47+563950.4	G	21.66r'	14.8	4.9	25.12	0.04
J1020+5606	155.1284	56.1079	2.94	FRII	0.480		s	1	1.05	SDSS J102030.82+560628.5	G	19.82r'	18.9	6.3	25.16	0.14
J1020+5718	155.1868	57.3128	2.17	FRII	0.66	0.06	p	1,10,11	0.91	SDSS J102044.83+571845.9	G	21.57r'	122.	12	26.29	0.01
J1021+5848C	155.2915	58.8088	3.34	FRII	0.29	0.01	p	1,10,11	0.88	SDSS J102109.97+584831.6	G	18.41r'	40.9	5.5	25.00	0.02
J1022+5631b	155.6563	56.5182	1.46	FRII	0.97	0.07	p	10,11	0.70	DESI J155.6563+56.5182	G	22.56r	85.6	8.9	26.53	
J1022+5737C	155.7466	57.6265	2.49	FRII	1.09	0.05	p	10,11	1.22	DESI J155.7466+57.6265	G	23.39r	16.6	2.2	25.93	0.05
J1024+5647	156.2275	56.7900	2.48	FRII	0.428		s	1	0.83	SDSS J102454.59+564723.9	G	18.88r'	46.0	5.1	25.44	0.16
J1025+5612C	156.4566	56.2011	5.83	FRII	1.5		e	1	2.96	CWISE J102549.58+561203.9	Qc	16.56W1	28.4	4.1	26.49	<0.01
J1026+5701C	156.5039	57.0203	3.51	FRII	0.91	0.14	p	2,10,11	1.65	DESI J156.5039+57.0203	G	23.23r	13.2*	4.4	25.65	0.04
J1026+5800	156.6870	58.0113	1.74	FRI	0.68	0.04	p	1,2,3,8,10,11	0.74	SDSS J102644.87+580040.6	G	22.33r'	17.5	2.0	25.48	0.43
J1026+5904	156.7260	59.0753	2.16	FRII	0.74	0.07	p	1,2,3,8,10,11	0.95	SDSS J102654.23+590431.0	G	21.94r'	10.0	1.4	25.32	0.22
J1027+6049	156.7658	60.8230	3.11	FRII	0.87	0.24	p	10,11	1.44	DESI J156.7658+60.8230	G	22.75r	76.6	8.2	26.37	<0.01
J1027+5748	156.8247	57.8160	1.84	FRII	0.62	0.08	p	1,2,3,8,10,11	0.75	SDSS J102717.92+574857.7	G	21.33r'	60.1	6.0	25.92	<0.01
J1027+5855	156.8817	58.9234	2.90	FRII	0.468		s	1	1.02	SDSS J102731.60+585524.2	G	19.65r'	64.5	6.6	25.67	0.01
J1027+6027	156.9818	60.4532	3.47	FRII	0.67	0.11	p	10	1.46	DESI J156.9818+60.4532	G	21.79r	9.28	3.09	25.19	0.12
J1030+5827	157.5394	58.4509	1.41	FRII	1.15	0.20	p	9,10,11	0.70	DESI J157.5394+58.4509	G	25.10r	28.3	2.9	26.22	0.01
J1031+5806	157.9823	58.1165	8.00	FRI	0.092		s	1	0.82	SDSS J103155.76+580659.5	G	15.43r'	352.	35	24.86	
J1032+5644	158.2454	56.7481	46.0	FRII	0.045		s	1	2.44	SDSS J103258.88+564453.2	G	13.43r'	2.65e3	260	25.09	
J1034+6005	158.5988	60.0886	4.90	FRII	0.228		s	1	1.07	SDSS J103423.72+600519.1	G	17.18r	112.	11	25.21	
J1034+5620	158.7472	56.3426	3.61	FRII	1.07	0.16	p	9,10,11	1.76	DESI J158.7472+56.3426	G	26.98r	93.4	9.4	26.66	0.01
J1035+5647	158.8953	56.7945	2.05	FRII	0.834		s	1	0.94	SDSS J103534.87+564740.3	G	21.59r'	9.67	1.12	25.43	0.41
J1035+5752	158.9253	57.8674	3.53	FRII	0.520		s	1	1.32	SDSS J103542.08+575202.5	G	21.24r'	7.83	0.89	24.86	0.04
J1035+5426	158.9861	54.4368	3.39	FRII	0.351		s	1	1.01	SDSS J103556.67+542612.5	G	18.88r'	415.	42	26.20	0.01
J1036+5540	159.0155	55.5690	1.67	FRII	0.81	0.07	p	1,2,3,10,11	0.76	SDSS J103603.71+554008.2	G	22.81r'	35.4	3.7	25.96	
J1036+5643	159.0880	56.7230	2.00	FRII	0.68	0.10	p	1,2,3,8,9,10,11	0.85	SDSS J103621.12+564322.7	G	21.17r'	494.	49	26.93	
J1036+6126	159.2191	61.4459	1.51	FRII	1.32	0.13	p	10,11	0.76	DESI J159.2191+61.4459	Qc	20.87r	41.6	4.4	26.52	
J1037+5717	159.3775	57.2981	2.13	FRI/II	1.01	0.07	p	2,9,10,11	1.02	DESI J159.3775+57.2981	G	23.02r	33.8	3.4	26.17	0.73
J1038+6011	159.5220	60.1977	1.80	FRII	0.67	0.03	p	1,2,3,8,10,11	0.76	SDSS J103805.27+601151.7	G	21.38r'	159.	16	26.42	0.01
J1038+5652	159.5530	56.8746	8.48	FRI	0.171		s	1	1.48	SDSS J103812.74+565228.6	G	16.88r'	19.7	2.4	24.18	0.46
J1038+5635	159.6714	56.5954	1.55	FRII	0.82	0.14	p	1,2,3,9,10,11	0.70	SDSS J103841.13+563543.5	G	23.84r'	26.5	2.9	25.85	0.06
J1040+5611	160.2045	56.1993	2.17	FRII	0.420		s	1	0.72	SDSS J104048.37+561157.3	G	19.53r'	16.2	1.8	24.96	0.03
J1040+6135	160.2458	61.5938	2.00	FRII	1.01	0.13	p	10,11	0.96	DESI J160.2458+61.5938	G	23.77r	500.	50	27.33	<0.01
J1040+5420	160.2479	54.3483	4.00	FRI/II	0.47	0.04	p	1,10,11	1.41	SDSS J104059.48+542053.7	G	20.94r'	14.5	4.8	25.03	0.19
J1041+5807	160.3026	58.1319	3.07	FRII	0.65		s	1	0.84	SDSS J104112.61+580754.8	G	18.32r'	32.9	3.3	24.97	0.01
J1041+5529	160.4357	55.4985	1.87	FRII	0.65	0.19	p	1,2,3,8,10,11	0.77	SDSS J104144.57+552954.4	G	20.88r'	198.	20	26.49	0.04
J1042+5920	160.5330	59.3384	2.76	FRII	0.510		s	1	1.02	SDSS J104207.91+592018.2	G	19.47r'	106.	11	25.97	<0.02
J1042+6140	160.5707	61.6826	3.17	FRII	0.91	0.01	p	10,11	1.49	DESI J160.5707+61.6826	G	22.62r	22.7	5.1	25.89	
J1042+5427	160.5797	54.4568	2.98	FRI/II	0.29	0.01	p	1,10,11	0.78	SDSS J104219.12+542724.3	G	18.84r'	22.9	7.6	24.75	0.01
J1042+6104	160.5827	61.0727	3.09	FRII	0.513		s	1	1.15	SDSS J104219.85+610421.6	G	20.23r'	45.9	4.9	25.62	0.01
J1042+5450	160.5842	54.8432	5.59	FRII	1.18	0.10	p	10,11	2.78	DESI J160.5842+54.8432	G	23.69r	128.	13	26.90	0.01
J1042+5512	160.6425	55.2046	2.71	FRII	0.93	0.12	p	10,11	1.28	DESI J160.6425+55.2046	G	23.76r	30.9	3.5	26.04	<0.01

Name	R.A.	Dec.		Morph.	z	Δz		bands	ratio	Host		mag				
J1043+5520	160.8133	55.3391	3.65	FRI/II	0.322		s	1	1.02	SDSS J104315.18+552020.7	G	18.56r*	27.3	3.1	24.93	0.19
J1043+5653C	160.8456	56.8888	4.37	FRII	0.182		s	1	0.80	SDSS J104322.93+565319.7	G	16.71r*	24.3*	8.1	24.33	0.13
J1043+5813	160.9679	58.2242	4.01	FRI	0.390		s	1	1.27	SDSS J104352.28+581327.0	G	19.02r*	27.6	2.8	25.12	0.38
J1044+5620	161.0561	56.3474	2.77	FRII	0.64	0.06	p	1,2,3,8,9,10,11	1.15	SDSS J104413.46+562050.6	G	21.45r*	11.2	1.2	25.23	0.02
J1044+6037	161.0759	60.6172	1.90	FRII	1.054		s	1	0.92	SDSS J104418.20+603701.8	Q	19.00r*	43.8	4.4	26.32	0.48
J1044+5628	161.1580	56.4779	2.72	FRII	0.88	0.06	p	2,9,10,11	1.26	DESI J1161.1580+56.4779	G	23.10r	14.2	1.5	25.65	0.10
J1045+5936	161.2578	59.6004	2.20	FRII	1.02	0.10	p	2,3,4,9,10,11	1.06	DESI J1161.2578+59.6004	G	22.93r	62.9	6.3	26.44	
J1045+5455	161.3271	54.9307	1.65	FRII	1.5		e		0.84	CWISE J104518.50+545550.7	G	17.25W1	10.9	1.6	26.07	0.12
J1045+5631	161.3333	56.5302	3.42	FRII	0.28	0.24	p	1,3,6,8,9,10,11	0.88	SDSS J104519.99+563148.7	G	18.00r*	17.1	1.8	24.59	0.08
J1045+6003	161.4584	60.0639	1.80	FRII	1.5		e		0.91	CWISE J104550.02+600350.2	Qc	18.16W1	60.4	6.1	26.81	0.01
J1046+5738	161.5175	57.6384	1.53	FRII	1.353		s	1	0.77	SDSS J104604.20+573818.4	G	19.77r*	561.	56	27.68	
J1046+5905	161.5996	59.0895	1.38	FRII	1.61	0.02	p	4,9	0.70	CWISE J104623.90+590522.1	G	17.66W1	138.	14	27.24	
J1046+5620	161.6935	56.3485	2.96	FRI	0.359		s	1	0.89	SDSS J104646.43+562054.4	G	18.52r*	28.5	2.9	25.05	0.32
J1046+5636	161.7479	56.6124	1.94	FRII	0.527		s	1,2,3,8,9,10,11	0.73	SDSS J104659.49+563644.5	G	20.27r*	19.4	2.0	25.27	0.03
J1047+5645	161.7920	56.7575	2.29	FRII	0.48	0.05	p	9	0.82	SDSS J104710.07+564526.9	G	21.03r*	12.0*	1.6	24.97	<0.01
J1047+5629	161.8187	56.4965	1.57	FRII	1.68	0.40	p	1,2,3,6,8,10,11	0.80	CWISE J104716.48+562947.6	Qc	17.14W1	20.7	2.1	26.46	0.09
J1047+5549	161.8926	55.8324	3.09	FRII	0.53	0.07	p	2,4,9,10,11	1.17	SDSS J104734.23+554956.5	G	20.97r*	78.0	7.8	25.88	0.01
J1047+5908	161.9126	59.1336	1.93	FRII	1.19	0.35	p	4,9	0.96	DESI J1161.9126+59.1336	Qc	24.70r	13.2	1.3	25.92	0.14
J1048+5906	162.0265	59.1072	1.64	FRII	1.79	0.02	p	2,9,10,11	0.83	CWISE J104806.44+590625.6	Qc	18.30W1	31.4	3.2	26.70	0.01
J1048+5623	162.0543	56.3994	2.14	FRII	0.98	0.08	p	2,4,9,10,11	1.02	DESI J1162.0543+56.3994	G	23.57r	5.22	0.64	25.32	
J1049+5908	162.2692	59.1413	1.67	FRII	1.36	1.63	p		0.84	DESI J1162.2692+59.1413	G	22.47r	17.2	1.8	26.17	
J1049+5513	162.2803	55.2208	12.0	FRI	0.126		s	1,2,3,4,8,9,10,11	1.62	SDSS J104907.26+551314.9	G	15.45r*	430.	43	25.24	0.21
J1049+5745	162.3245	57.7583	1.97	FRI/II	0.77	0.07	p	1	0.88	SDSS J104917.89+574530.0	G	22.56r*	7.93*	1.13	25.26	<0.01
J1049+5847	162.3319	58.7838	3.21	FRII	2.368		p	1,2,3,8,10,11	1.57	SDSS J104919.65+584701.6	Q	20.90r*	38.8	3.9	27.07	<0.02
J1049+6041C	162.4281	60.6846	3.15	FRII	0.38	0.05	p	1	0.98	SDSS J104942.75+604104.5	G	20.64r*	10.8	2.9	24.69	0.31
J1050+5940	162.5549	59.6750	4.82	FRI/II	0.463	0.05	s	1	1.69	SDSS J105013.18+594029.9	G	19.10r*	34.0	3.4	25.38	0.11
J1050+5934	162.5826	59.5679	2.02	FRII	1.29		s	9,10,11	1.01	DESI J1162.5826+59.5679	Qc	23.75r	12.5	1.3	25.98	<0.02
J1050+5404	162.6434	54.0669	2.94	FRII	0.89	0.24	p	1,10,11	1.37	SDSS J105034.40+540401.0	G	22.93r*	35.0	6.1	26.05	0.64
J1051+5641	162.7935	56.6966	2.85	FRI	0.353	0.10	p	1	0.85	SDSS J105110.43+564147.6	G	18.36r*	24.6	2.5	24.97	0.47
J1051+6002	162.8838	60.0395	3.95	FRII	0.462		s	10,11	1.39	SDSS J105132.12+600222.3	G	19.57r*	9.42*	3.14	24.82	
J1052+5503	163.0059	55.0564	1.73	FRII	0.93	0.19	s	1,3,4,8,9,10,11	0.82	DESI J1163.0059+55.0564	G	23.58r	330.	33	27.07	
J1052+5850	163.0915	58.8477	2.00	FRII	1.27	0.55	p	1,2,3,6,8,9,10,11	1.00	SDSS J105221.96+585051.6	G	22.42r*	53.6	5.4	26.60	0.71
J1052+5636a	163.1275	56.6028	4.14	FRII	1.02	2.19	p		2.00	SDSS J105230.60+563610.1	G	19.26r*	79.2	8.0	26.54	
J1052+5456C	163.1966	54.9435	9.59	cpx	0.88	0.01	p	1	4.45	SDSS J105247.19+545636.5	G	22.65r*	63.2	9.6	26.30	<0.01
J1053+5953	163.3050	59.8884	3.91	FRI	0.675	0.06	p	1,2,3,4,9,10,11	1.65	SDSS J105313.20+595305.4	G	20.63r*	13.3	1.6	25.35	0.13
J1053+5745	163.3595	57.7621	1.72	FRII	0.86	0.09	p	1,2,3,8,9,10,11	0.79	SDSS J105326.29+574543.7	Q	23.81r*	31.1	3.1	25.97	<0.01
J1053+5613	163.3766	56.2275	1.97	FRII	0.80	0.05	p	10,11	0.89	SDSS J105330.37+561338.9	Q	22.42r*	7.94	1.06	25.30	0.27
J1054+6102	163.5318	61.0489	2.30	FRII	0.92	0.08	p	1,2,3,9,10,11	1.08	DESI J1163.5318+61.0489	G	22.73r	22.2	2.6	25.89	0.03
J1054+5952	163.5753	59.8722	1.93	FRII	0.90	0.05	p	9,10,11	0.90	SDSS J105418.07+595219.7	G	22.41r*	17.7	1.8	25.77	0.12
J1054+5714	163.5876	57.2404	3.04	FRII	0.65		p	1	1.27	DESI J1163.5876+57.2404	G	20.04r*	8.32	0.95	25.11	0.06
J1054+5909	163.6488	59.1503	1.99	FRII	0.886		s	9	0.93	SDSS J105435.71+590900.9	G	20.84r*	8.73	0.91	25.44	0.45
J1056+5622	164.0811	56.3781	3.96	FRII	1.25	1.31	p	1	1.98	CWISE J105619.46+562241.3	G	17.48W1	33.2	3.4	26.37	0.15
J1057+5548	164.3113	55.8156	1.82	FRII	1.399		s	9	0.92	SDSS J105714.72+554856.0	G	19.88r*	41.0	4.2	26.58	0.18
J1057+5357	164.4528	59.1473	9.50	FRII	0.130		s	1	1.53	SDSS J105748.68+590850.3	G	16.12r*	70.2	17.7	24.48	<0.01
J1057+5908	164.4611	59.1499	10.9	FRII	0.52	0.91	p	1,2,3,6,8,9,10,11	4.08	SDSS J105750.67+590859.7	G	18.54r*	32.2*	10.7	25.47	<0.01
J1058+5954	164.6175	59.9086	1.54	FRII	0.86	0.05	p	2,9,10,11	0.71	DESI J1164.6175+59.9086	G	23.53r	36.5	3.7	26.04	<0.01
J1058+6008	164.6319	60.1444	10.4	FRII	0.196		s		2.03	SDSS J105831.65+600839.7	G	16.93r*	32.9	3.6	24.53	0.20
J1058+5648	164.7028	56.8002	1.51	FRII	2.692		s		0.72	SDSS J105848.67+564800.7	Q	19.40r*	134.	13	27.73	0.03

J1058+5643	164.7126	56.7190	9.78	FRII	0.139		s	1	1.44	SDSS J105851.01+564308.5	G	16.78r’	335.	34	25.22	
J1059+5552	164.7528	55.8731	2.38	FRII	0.370		s	1	0.73	SDSS J105900.67+555223.0	G	18.71r’	12.7	1.5	24.73	0.06
J1059+5610	164.8044	56.1685	1.68	FRII	0.73	0.05	p	1,3,8,9,10,11	0.73	SDSS J105913.05+561006.4	G	22.54r’	5.50*	1.83	25.05	0.14
J1059+5942	164.8183	59.7069	1.62	FRII	1.04	0.07	p	10,11	0.79	DESI J164.8183+59.7069	G	26.24r	20.5	2.1	25.98	0.04
J1059+5709	164.9745	57.1543	1.79	FRII	1.73	1.75	p	2,4,9,10,11	0.91	DESI J164.9745+57.1543	G	23.50r	3.46	0.74	25.71	<0.04
J1059+5446C	164.9933	54.7810	2.01	FRII	0.83	0.02	p	10,11	0.92	DESI J164.9933+54.7810	G	22.51r	72.6	7.7	26.30	<0.01
J1100+5617	165.0581	56.2868	1.61	FRII	1.08	0.14	p	2,9,10,11	0.79	DESI J165.0581+56.2868	Qc	23.29r	363.	36	27.26	
J1100+6034C	165.1238	60.5752	1.73	FRII	0.94	0.03	p	10,11	0.82	DESI J165.1238+60.5752	G	23.28r	6.47	1.07	25.37	0.20
J1101+5723	165.3363	57.3885	3.80	FRII	0.630		s	1	1.56	SDSS J110120.72+572318.4	G	21.34r’	15.4	2.0	25.35	0.03
J1101+6019C	165.3597	60.3265	3.21	FRII	0.49	0.02	p	1,10,11	1.16	SDSS J110126.33+601935.4	G	20.27r’	5.00	1.15	24.61	0.17
J1101+5917	165.4281	59.2993	1.76	FRII	0.84	0.04	p	2,3,9,10,11	0.81	DESI J165.4281+59.2993	G	22.62r	16.9	1.8	25.68	<0.01
J1101+5652C	165.4322	56.8745	2.44	FRII	0.44	0.03	p	1,3,8,9,10,11	0.83	SDSS J110143.72+565228.2	G	20.86r’	24.8	2.5	25.19	<0.01
J1101+5725	165.4471	57.4248	2.75	FRII	0.465		s	1	0.97	SDSS J110147.31+572529.2	G	19.23r’	10.6	1.4	24.88	0.51
J1102+5924	165.5391	59.4128	2.78	FRII	1.18	0.17	p	10,11	1.38	DESI J165.5391+59.4128	Qc	23.12r	6.93	0.99	25.63	0.04
J1102+5829	165.5490	58.4835	1.92	FRII	0.81	0.18	p	1,2,3,8,9,10,11,12	0.87	SDSS J110211.75+582900.5	G	22.27r’	296.	30	26.89	
J1102+6022	165.7487	60.3731	2.74	FRII	0.399		s	1	0.88	SDSS J110259.68+602223.3	G	19.40r’	51.9	5.4	25.42	0.26
J1103+5737	165.8157	57.6318	2.64	FRII	0.79	0.09	p	1,2,3,8,9,10,11	1.18	SDSS J110315.76+573754.6	G	21.91r’	81.1	8.1	26.30	0.51
J1103+6040	165.8859	60.6726	1.88	FRII	1.00	0.01	p	10,11	0.90	DESI J165.8859+60.6726	G	23.66r	72.4	7.3	26.49	<0.01
J1104+6007C	166.0846	60.1202	9.39	FRII	0.43	0.03	p	1,10,11	3.17	SDSS J110420.29+600712.7	G	20.48r’	24.5*	8.2	25.17	0.02
J1105+5441	166.2967	54.6906	2.92	FRII	0.48	0.23	p	10	1.05	DESI J166.2967+54.6906	G	13.81r	37.4	12.5	25.46	<0.03
J1105+5857	166.3800	58.9531	2.48	FRII	0.71	0.05	p	1,10,11	1.07	SDSS J110531.19+585711.2	G	21.69r’	111.	11	26.33	0.01
J1106+5955	166.5635	59.9264	1.77	FRII	0.79	0.10	p	1,10,11	0.79	SDSS J110615.24+595534.9	G	21.78r’	20.3	2.2	25.70	0.01
J1106+5736	166.5696	57.6080	2.19	FRII	0.84	0.05	p	10,11	1.00	DESI J166.5696+57.6080	G	22.57r	38.1	3.9	26.03	0.07
J1106+6102	166.5747	61.0436	1.41	FRII	1.5		e		0.72	CWISE J110617.92+610237.0	Qc	18.21W1	55.2	5.8	26.77	<0.01
J1106+5714	166.6756	57.2338	1.69	FRII	1.01	0.06	p	10,11	0.81	DESI J166.6756+57.2338	G	22.72r	29.1	3.0	26.10	0.37
J1107+5840	166.8004	58.6683	1.51	FRII	1.07	0.01	p	10,11	0.74	DESI J166.8004+58.6683	G	24.04r	25.4	2.6	26.10	
J1107+5733	166.9855	57.5643	1.43	FRII	1.5		e		0.73	CWISE J110756.51+573351.6	Qc	18.08W1	2.02	0.62	25.34	
J1108+5736C	167.0599	57.6057	2.43	FRII	1.5		e		1.23	CWISE J110814.37+573620.7	Qc	16.80W1	17.3	1.9	26.27	0.66
J1108+5952	167.0956	59.8756	2.22	FRII	1.08	0.05	p	10,11	1.08	DESI J167.0956+59.8756	G	23.29r	27.0	3.1	26.13	<0.01
J1109+5532	167.3545	55.5468	5.92	FRII	0.40	0.07	p	1,10,11	1.90	SDSS J110925.07+553248.6	G	20.47r’	41.1	5.9	25.32	<0.02
J1111+5646	167.9117	56.7692	1.51	FRII	1.02	0.12	p	10,11	0.73	DESI J167.9117+56.7692	G	24.92r	17.6	2.2	25.89	
J1112+5704a	168.0620	57.0742	4.65	FRII	0.73	0.99	p	1,10,11	2.02	SDSS J111214.87+570427.0	G	24.80r’	14.7	3.6	25.48	0.10
J1113+5643	168.2530	56.7255	1.63	FRII	0.98	0.31	p	10	0.78	DESI J168.2530+56.7255	G	22.86r	121.	12	26.69	
J1113+5529	168.4498	55.4977	1.43	FRII	1.12	0.04	p	10,11	0.70	DESI J168.4498+55.4977	G	24.01r	24.1	6.3	26.12	
J1115+5712	168.8391	57.2011	2.37	FRII	0.98	0.08	p	10,11	1.13	DESI J168.8391+57.2011	G	22.37r	53.5	6.3	26.33	
J1117+5810	169.4950	58.1739	1.66	FRII	0.90	0.09	p	1,10,11	0.78	SDSS J111758.79+581025.9	G	22.68r’	10.5	2.9	25.54	0.15
J1118+6039C	169.7098	60.6598	1.83	FRII	0.57	0.03	p	1,10,11	0.71	SDSS J111850.35+603935.4	G	21.26r’	77.3	11.6	25.95	0.03
J1419+3337	214.8027	33.6328	1.76	FRII	1.00	0.08	p	2,10,11	0.85	DESI J214.8027+33.6329	G	23.44r	9.17	1.43	25.59	0.14
J1420+3413C	215.0086	34.2249	3.94	FRI/II	0.94	0.14	p	2,10,11	1.86	DESI J215.0088+34.2248	G	23.14r	6.55*	1.39	25.38	0.11
J1421+3512	215.4100	35.2049	11.6	FRII	0.05	0.11	p	1,2,3,6,8,10,11	0.73	SDSS J142138.40+351217.5	G	21.11r’	312.	32	24.26	
J1421+3431	215.4634	34.5289	1.53	FRII	1.06	0.06	p	10,11	0.74	DESI J215.4634+34.5289	G	24.63r	4.07*	0.85	25.29	0.58
J1421+3521	215.4909	35.3570	2.22	FRII	1.5		e		1.13	CWISE J142157.80+352125.3	G	17.89W1	58.9	5.9	26.80	<0.01
J1422+3320	215.6373	33.3354	2.80	FRII	0.96	0.02	p	2,10,11	1.33	WISEA J142232.95+332007.4	G	23.86r	145.	15	26.75	
J1422+3255	215.6913	32.9322	1.67	FRII	1.17	0.14	p	10,11	0.83	WISEA J142245.90+325555.7	G	16.16W2	53.5	5.5	26.51	
J1423+3600	215.7846	36.0052	2.00	FRII	1.22	0.18	p	10,11	1.00	DESI J215.7846+36.0053	G	24.19r	55.4	5.7	26.57	
J1423+3403	215.9003	34.0506	2.74	FRI/II	0.561		s	1	1.06	SDSS J142336.06+340302.1	G	20.70r’	10.2	1.4	25.05	
J1423+3302	215.9105	33.0484	1.94	FRII	1.01	0.03	p	2,10,11	0.94	WISEA J142338.50+330254.2	G	16.28W1	253.	25	27.04	
J1423+3529	215.9201	35.4888	7.49	FRII	0.82	0.04	p	1,2,3,10,11	3.41	SDSS J142340.83+352919.7	G	21.94r	20.7	3.0	25.74	0.02

Name	RA	Dec	size	FR	$S_{1.5}$	err	t	comp	ratio	Host	cl	mag	f1	f2	M	err
J1423+3340	215.9259	33.6693	1.50	FRII	0.36	0.01	e		0.76	CWISE J142342.22+334009.6	Qc	18.05W1	3.86	0.84	25.62	0.22
J1423+3605	215.9486	36.0946	3.00	FRI	0.62	0.11	p	1,2,3,6,8,10,11	0.90	SDSS J142347.66+360540.5	G	19.05r'	39.4	4.1	25.20	0.02
J1424+3609	216.0397	36.1547	7.33	FRII	2.98		p	1,2,3,8,10,11,12	2.98	SDSS J142409.52+360917.0	G	21.34r'	190.	19	26.42	0.01
J1424+3436	216.1358	34.6127	4.20	FRI/II	0.586	0.09	p	1	1.67	SDSS J142432.58+343645.8	G	20.23r'	484.	48	26.77	0.01
J1425+3633	216.2942	36.5612	2.33	FRII	0.75		p	1,2,3,8,10,11	1.02	SDSS J142510.60+363340.3	G	20.75r'	214.	22	26.67	0.01
J1425+3506	216.2995	35.1045	2.14	FRII	0.745		s		0.94	SDSS J142511.88+350616.1	G	22.51r	14.4	1.8	25.49	0.01
J1425+3557	216.3287	35.9574	3.70	FRII	0.419	0.33	s	1	1.23	SDSS J142518.87+355726.7	G	18.79r'	15.0	1.8	24.93	0.47
J1425+3235Ca	216.4137	32.5876	2.80	FRII	0.71	0.08	p	1,2,3,8,9,10,11	1.21	SDSS J142539.29+323515.2	G	22.13r	13.8*	2.1	25.42	0.01
J1426+3407	216.6021	34.1285	2.70	FRII	0.71	0.12	p	1,2,3,8,9,10,11	1.16	SDSS J142624.49+340742.6	G	22.17r'	43.0	4.5	25.91	0.01
J1426+3320	216.6026	33.3373	2.10	FRII	0.85	0.07	p	9,10,11	0.96	DESI J1216.6026+33.3373	G	23.66r	62.0	6.3	26.25	0.02
J1426+3236	216.6109	32.6024	1.97	FRII	0.99	0.07	p	9,10,11	0.94	DESI J1216.6109+32.6024	G	24.07r	46.0	4.8	26.28	0.12
J1426+3222	216.7126	32.3717	2.80	FRII	0.69		p	1,2,3,8,9,10,11	1.19	SDSS J142651.02+322218.0	G	21.23r'	386.	39	26.84	
J1427+3625	216.8259	36.4170	2.45	FRII	0.851	0.11	s	1	1.13	SDSS J142718.21+362501.1	Q	18.48r'	199.	20	26.76	0.03
J1427+3311C	216.8322	33.1945	2.07	FRII	0.82		p	1,2,3,9,10,11	0.94	SDSS J142719.72+331140.0	G	22.90r'	18.1	2.0	25.68	
J1427+3328	216.9070	33.4688	9.00	FRII	0.150	0.27	s	1	1.41	SDSS J142737.66+332807.5	G	16.89r'	64.7*	7.2	24.58	<0.01
J1428+3631	217.0284	36.5249	2.40	FRII	0.75		p	1,3,8,10,11,12	1.06	SDSS J142806.81+363139.5	G	21.78r'	602.	60	27.11	
J1428+3446	217.0977	34.7752	1.90	FRII	0.588	0.12	p	1	0.75	SDSS J142823.44+344630.6	G	20.86r'	7.73	0.99	24.98	0.14
J1428+3525	217.1499	35.4271	2.77	FRII	0.87		p	2,9,10,11	1.28	DESI J1217.1498+35.4271	G	23.19r	10.5	1.4	25.51	0.18
J1429+3326	217.2997	33.4437	2.60	FRII	0.320		s	1	0.73	SDSS J142911.92+332637.5	G	19.11r'	269.	27	25.92	
J1429+3355	217.3171	33.9270	2.85	FRII	1.059		s		1.39	SDSS J142916.10+335537.4	G	23.57r'	134.	14	26.81	0.01
J1429+3356	217.4277	33.9486	2.20	FRII	1.124		s	1	1.08	SDSS J142942.63+335654.8	G	18.70r'	92.7	9.3	26.71	0.06
J1429+3717	217.4724	37.2914	2.78	FRII	0.65	0.02	p	1,10,11	1.15	SDSS J142953.37+371728.9	G	21.97r	19.0	2.2	25.47	0.12
J1429+3230C	217.4753	32.5127	6.12	FRI/II	1.35	0.34	p	1,2,3,9,10,11,12	3.09	SDSS J142954.06+323045.8	Qc	22.68r	11.5	1.6	25.99	0.52
J1430+3519	217.5410	35.3329	4.05	FRII	0.629		p	1	1.66	SDSS J143009.83+351958.2	G	20.88r'	51.3	5.2	25.87	0.01
J1430+3322	217.6154	33.3804	3.70	FRI	0.512		s		1.37	SDSS J143027.69+332249.4	G	20.22r'	8.98	0.98	24.90	0.63
J1431+3345	217.7644	33.7616	3.65	FRI/II	0.238		s	1	0.83	SDSS J143103.46+334541.6	Q	17.02r'	166.	17	25.42	0.10
J1431+3535C	217.8484	35.5975	2.60	FRII	1.04	0.17	p	2,9,10,11	1.26	DESI J1217.8484+35.5975	G	23.01r	18.1	2.0	25.92	0.04
J1431+3440	217.8485	34.6681	2.25	FRII	0.77	0.26	p	1,2,3,8,9,10,11	1.00	SDSS J143123.56+344005.0	G	21.71r	8.17	0.91	25.27	0.03
J1431+3427	217.8639	34.4506	2.98	FRII	1.15	1.24	p	1,3,8,9,10,11	1.47	SDSS J143127.33+342702.3	G	21.10r'	116.	12	26.83	0.01
J1432+3411	218.0479	34.1926	2.40	FRII	1.113		s	1	1.18	SDSS J143211.50+341133.2	G	22.54r'	65.7	6.6	26.55	
J1432+3437C	218.0606	34.6279	3.97	FRII	0.34	0.03	p	1,2,3,6,8,9,10,11	1.14	SDSS J143214.54+343740.4	G	19.92r'	13.8*	2.0	24.69	0.07
J1432+3407C	218.0653	34.1233	3.23	FRII	0.64	0.13	p	1,3,8,9,10,11	1.33	SDSS J143215.65+340723.8	G	21.27r	3.50*	1.42	24.72	0.01
J1432+3545	218.1413	35.7611	5.05	FRI	0.189		p		0.96	SDSS J143233.92+354540.1	G	17.18r'	84.8	8.6	24.91	0.10
J1432+3220	218.1777	32.3459	1.57	FRII	0.78		p	1,2,3,9,10,11	0.70	SDSS J143242.64+322045.4	G	22.32r'	106.	11	26.40	
J1432+3154C	218.2283	31.9030	3.35	FRII	0.91		p	10,11	1.57	DESI J1218.2283+31.9030	Q	23.17r	5.19*	1.73	25.25	0.09
J1432+3647	218.2430	36.7894	1.53	FRII	2.836		s	1	0.72	SDSS J143258.30+364721.7	Q	21.91r'	13.1	1.6	26.77	0.74
J1432+3551C	218.2471	35.5181	5.16	FRII	0.360		s	1	1.56	SDSS J143259.29+353105.2	G	19.61r'	5.81	0.67	24.37	0.67
J1433+3220	218.2569	32.3435	5.86	FRII	0.552		s	1	2.26	SDSS J143301.66+322036.7	G	20.67r'	13.3	2.5	25.15	<0.02
J1433+3328	218.3156	33.4830	1.40	FRI/II	1.609		s		0.71	SDSS J143315.74+332858.6	Qc	22.78r	28.4	2.9	26.56	0.30
J1433+3131	218.3172	31.5240	2.16	FRII	2.947		s	1	1.00	SDSS J143316.11+313126.3	Q	17.24r'	64.8	6.7	27.50	
J1433+3450	218.3271	34.8474	1.70	FRII	0.94	0.31	p	1,2,9,10,11,12	0.81	SDSS J143318.51+345050.7	Q	22.90r'	1.62e3	160	27.77	
J1433+3145C	218.3367	31.7665	2.40	FRII	0.65	0.02	p	1,2,3,8,10	1.00	SDSS J143320.81+314559.2	Q	21.73r'	6.25	1.39	24.99	<0.01
J1433+3546C	218.3497	35.7704	1.54	FRII	1.42		e	9	0.78	CWISE J143323.94+354613.5	Qc	17.07W1	63.8	6.4	26.78	0.14
J1433+3351C	218.4967	33.8657	3.53	FRII	1.099		s	1	1.73	SDSS J143359.19+335156.5	G	22.77r'	3.15*	1.05	25.22	0.52
J1434+3545	218.5083	35.7585	2.71	FRII	0.544		p	1,2,3,8,10,11	1.04	SDSS J143402.00+354530.7	G	20.07r'	3.88*	1.29	24.60	0.79
J1434+3222	218.5752	32.3688	1.71	FRI	0.73	0.07	p		0.75	SDSS J143418.05+322207.8	G	21.95r'	4.00	0.65	24.91	0.01
J1434+3428	218.6212	34.4668	2.60	FRII	0.986		s	1	1.25	SDSS J143429.09+342800.4	G	23.05r'	144.	14	26.77	

Name	RA (°)	Dec (°)	θ	Type	z	Δz	m	Refs	α	Counterpart	Cl	mag	S	ΔS	logL	q
J1434+3214C	218.6639	32.2407	4.50	FRII	1.5		e		2.28	CWISE J143439.34+321426.6	G	17.83W1	3.76	1.15	25.61	0.39
J1434+3648	218.6889	36.8099	2.29	FRI	0.429		s		0.77	SDSS J143445.33+364835.5	G	19.60r*	10.7	1.4	24.80	0.28
J1434+3328	218.6890	33.4724	4.70	?	0.198		s		0.92	SDSS J143445.35+332820.5	Q	17.48r*	54.4	5.7	24.76	0.51
J1434+3507C	218.6928	35.1229	2.15	FRII	0.87			1	0.99	SDSS J143446.27+350722.5	Q	21.97r	37.7*	3.7	26.06	
J1434+3555	218.7331	35.9244	2.90	cpx	0.422	0.05	p	1,2,3,9,10,11	0.97	SDSS J143455.93+355527.7	G	19.48r	40.4	4.1	25.37	0.02
J1435+3404	218.8812	34.0780	0.60	FRII		0.01	p	1	0.84	SDSS J143531.49+340440.9	G	22.44r*	5.60*	0.8	24.86	0.03
J1435+3547	218.9370	35.7978	2.10	FRII	1.30	0.77	p	1,2,3,9,10,11	0.88	SDSS J143544.87+354752.2	Q	22.75r	30.1	3.1	26.37	<0.01
J1436+3416	219.2216	34.2807	1.75	FRII	0.86	1.14	p	1,2,3,8,9,10,11	1.70	SDSS J143653.19+341650.1	Qc	21.77r*	69.7	7.1	26.32	<0.01
J1436+3404	219.2498	34.0803	1.30	FRII	0.55	0.04	p	1,2,9,10,11	1.29	SDSS J143659.95+340449.1	G	21.23r*	8.59*	1.35	24.96	
J1437+3650	219.3635	36.8387	3.69	FRII	0.55	0.06	p	1,2,10,11	1.59	SDSS J143727.24+365019.3	G	23.33r	7.59	1.64	25.52	0.21
J1437+3233	219.4135	32.5566	3.31	FRI	0.99	0.14	p	1,2,10,11	0.71	SDSS J143739.23+323223.8	G	23.49r	6.38	0.78	25.42	0.05
J1437+3554	219.4518	35.9086	3.36	FRII	1.01	0.01	p	1,2,3,6,8,9,10,11	0.83	SDSS J143748.43+355430.9	G	19.27r*	36.2	3.7	25.16	0.05
J1438+3445C	219.5403	34.7591	0.55	FRI	0.59	0.07	p	1,2,3,8,9,10,11	1.29	SDSS J143809.66+344532.8	G	21.46r*	8.99	1.44	25.05	0.03
J1438+3526	219.5529	35.4368	1.01	FRII	0.36		p	1,10,11	0.75	SDSS J143812.69+352612.6	G	22.34r*	10.4	1.2	25.44	0.66
J1438+3259	219.5568	32.9952	0.99	FRI/II	0.82	0.05	p	1,2,3,8,10,11	0.80	SDSS J143813.63+325942.5	G	21.50r*	7.43*	0.97	25.17	0.35
J1438+3355	219.5877	33.9290	1.48	FRI/II	0.72	0.16	p	9	3.78	WISEA J143821.02+335544.4	Qc	15.77W2	20.7	2.8	26.59	0.12
J1438+3539	219.6260	35.6545	2.75	FRII	0.262		p	1	1.71	SDSS J143830.23+353916.1	Q	18.41r*	18.8	2.4	24.57	0.30
J1439+3251	219.7544	32.8586	3.24	FRI	0.55	0.12	p	1,2,3,8,10,11	1.18	SDSS J143901.04+325131.0	Qc	18.20r*	3.59	1.13	24.58	0.01
J1439+3600C	219.7837	36.0130	0.36	FRI			s	1	0.74	SDSS J143908.07+360046.8	G	21.49r*	26.1*	2.8	24.71	0.03
J1439+3254	219.8133	32.9137	0.59	FRII		0.18	p	1,2,3,8,10,11	0.77	SDSS J143915.18+325449.4	Qc	21.56r*	227.	23	26.73	0.05
J1439+3406	219.9393	34.1159		FRII		0.04	p	1,2,3,8,10,11	0.86	SDSS J143945.43+340657.1	G	23.2r*	4.55	0.84	24.94	0.53
J1439+3221IC	219.9937	32.3575		FRII		0.01	p	1,2,3,8,10,11	1.79	SDSS J143958.48+322126.9	G	20.88r*	3.1	3.1	25.31	0.10
J1440+3211	220.0520	32.1865		FRII		0.05	p	1,10,11	2.70	SDSS J144012.47+321111.3	G	20.47r*	149.	15	26.06	0.01
J1440+3348	220.1655	33.8009		FRI			s	1	0.76	SDSS J144039.70+334803.2	G	20.74r*	16.8	1.9	25.23	0.09
J1442+3457	220.5530	34.9617		FRII			s	1	1.15	SDSS J144212.71+345742.2	Qc	20.32r*	9.70*	1.2	24.98	0.09
J1442+3243b	220.6456	32.7242		FRII			p	1,10,11	1.01	SDSS J144234.93+324326.9	Qc	19.61r*	342.	34	26.46	0.01
J1442+3242	220.6844	32.7163		FRII		0.06	p	1,10,11	0.75	SDSS J144244.26+324258.6	G	22.46r*	159.	16	26.63	0.01
J1443+3523	220.9604	35.3979		FRII		0.02	p	1,2,3,8,10,11	0.75	SDSS J144350.50+352352.4	G	20.39r*	28.4	3.1	25.48	
J1444+3445	221.0615	33.8054		FRII			p	1,2,3,10,11	0.79	SDSS J144414.75+344534.5	G	17.82r*	16.5*	1.9	24.50	0.34
J1444+3348	221.1075	34.7596		cpx		0.05	p	1,2,3,10,11	0.85	SDSS J144425.80+334819.3	G	22.7r*	15.0	2.2	25.65	
J1444+3444	221.1722	34.7425		FRII		0.03	s	1	0.76	SDSS J144441.33+344433.0	G	21.74r*	39.1	4.3	25.98	
J1554+5334	238.6527	53.5750		FRII			s	1	1.13	SDSS J155436.64+533430.0	G	21.61r*	13.9	2.0	25.49	0.13
J1557+5409	239.3297	54.1571		FRII		0.32	p	10,11	0.85	DESI J1239.3297+54.1571	G	22.50r	35.1	3.5	25.96	0.30
J1600+5251	240.1162	52.8522		FRII		0.05	p	1,2,3,8,10,11	0.91	SDSS J160027.88+525107.7	Qc	21.33r*	9.41*	1.07	25.21	0.22
J1602+5531	240.5787	55.5252		FRII		0.04	p	1,2,3,4,8,9,10,11	0.72	SDSS J160218.88+553130.8	G	22.22r*	24.0	2.4	25.59	
J1602+5254	240.6407	52.9086		FRII			e	1	0.82	DESI J1240.6407+52.9086	G	22.50r	202.	20	27.34	
J1603+5336	240.7585	53.6139		FRII		0.05	p	2,3,6,8,10,11	0.74	DESI J1240.7593+53.6111	G	21.17W1	14.1	1.5	24.90	<0.01
J1603+5429	240.8672	54.4995		FRII		0.22	p	13	1.97	CWISE J160328.14+542957.4	?	17.17W1	140.	14	26.73	0.01
J1604+5546a	241.0201	55.7792		FRII	1.15		p	7,9,10	1.10	DESI J1241.0201+55.7792	G	23.01r	20.9	2.2	26.09	0.03
J1604+5546b	241.2171	55.7671		FRII	0.828		s	1	1.01	SDSS J160452.09+554601.6	G	22.10r*	5.95	0.64	25.21	0.82
J1604+5320	241.2175	53.3400		FRII	0.649		s	1	1.04	SDSS J160452.20+532024.1	G	21.14r*	3.62	0.6	24.92	0.04
J1605+5524C	241.4599	55.4134		FRII	0.77	0.11	p	1,2,3,4,7,8,9,10,11	0.87	SDSS J160550.36+552448.3	Qc	21.51r*	13.8	1.5	25.33	0.04
J1606+5223	241.5984	52.3911		FRII	1.5		e		0.71	CWISE J160623.61+522328.0	Qc	17.85W1	6.22	0.76	25.83	0.46
J1606+5631	241.7322	56.5239		FRII	0.338		s	1	0.90	SDSS J160655.74+563126.1	G	18.86r*	11.2	1.2	24.59	0.26
J1607+5447	241.8385	54.7991		FRII	1.18	0.20	p	7,9,10,11	1.64	DESI J1241.8385+54.7991	G	23.39r	29.1	2.9	25.26	<0.01
J1608+5249	242.0448	52.8301		FRII	0.89	0.12	s	2,3,10,11	1.03	DESI J1242.0448+52.8301	G	22.45r*	17.5	1.8	25.75	0.04
J1608+5434	242.1406	54.5813		FRII	0.909		s	1	0.82	SDSS J160833.75+543452.7	G	22.76r	75.9	7.6	26.41	0.10

| Name	RA	Dec		FR				refs		Host	class	mag				
J1608+5415	242.1548	54.2579	2.69	FRII	1.00	0.30	p	4,7,9,10,11	1.29	DESI J242.1548+54.2579	Qc	22.93r	39.6	4.0	26.22	0.03
J1608+5454	242.1882	54.9019	1.69	FRII	0.906		s	13	0.79	DESI J242.1882+54.9019	G	22.77r	14.3	1.4	25.68	
J1608+5611	242.2175	56.1865	2.53	FRII	1.320		s	1	1.27	SDSS J160852.19+561111.5	Qc	20.70r	511.	51	27.61	0.06
J1609+5354	242.3049	53.9082	2.37	FRII	0.993		s	1	1.14	SDSS J160913.18+535429.6	Qc	18.05r	458.	46	27.28	
J1609+5525	242.3863	55.4284	2.64	FRII	0.360		s		0.80	SDSS J160932.70+552542.0	Qc	20.37r	215.	22	25.94	
J1610+5221	242.6030	52.3500	1.70	FRII	1.08	0.10	p	10,11	0.83	DESI J242.6030+52.3501	G	24.47r	5.25	0.78	25.42	0.27
J1610+5508	242.6620	55.1376	1.74	FRII	1.40	0.17	p	7,9	0.88	CWISE J161038.87+550815.2	G	17.65W1	22.7	2.3	26.32	0.07
J1610+5614C	242.6627	56.2491	4.33	FRII	0.231		s	1	0.96	SDSS J161039.04+561456.7	G	17.37r	30.0	3.0	24.65	0.03
J1611+5432	242.8208	54.5402	2.15	FRII	0.714		p		0.93	SDSS J161116.99+543224.7	G	21.22r	40.7	4.1	25.90	0.01
J1613+5303	243.2820	53.0558	1.94	FRI/II	0.70	0.04	p	1,2,3,8,10,11	0.83	SDSS J161307.67+530320.9	G	21.87r	13.0	1.4	25.38	0.08
J1613+5608	243.2976	56.1347	1.60	FRI/II	0.90	0.11	p	2,7,9,10,11	0.75	DESI J243.2976+56.1347	G	23.37r	69.7	7.0	26.36	
J1613+5741	243.3723	57.6853	2.09	FRII	0.52	0.02	p	1,10,11	0.78	SDSS J161329.35+574107.2	G	20.21r	63.7	6.5	25.77	0.07
J1613+5413	243.3927	54.2180	5.54	FRII	1.269		s	13	2.80	CWISE J161334.24+541304.3	G	16.81W1	136.	14	27.00	0.01
J1613+5238	243.3932	52.6476	3.89	FRI	0.267		s		0.96	SDSS J161334.37+523851.2	G	17.66r	93.3	9.4	25.28	0.03
J1613+5412	243.4010	54.2163	4.40	FRII	1.41	0.21	p	7,9	2.23	CWISE J161336.25+541258.4	G	16.57W1	53.1	5.3	26.70	0.14
J1613+5615	243.4693	56.2666	8.61	FRII	0.180		s	1	1.57	SDSS J161352.64+561559.9	G	17.03r	506.	51	25.64	0.03
J1614+5550C	243.5125	55.8459	2.15	FRII	1.05	0.38	p	2,3,10,11	1.04	DESI J243.5125+55.8459	G	21.66r	3.75	0.53	25.25	0.04
J1614+5541	243.5498	55.6923	5.43	FRI	0.251		s	1	1.28	SDSS J161411.94+554132.4	G	17.37r	30.8	3.6	24.74	0.36
J1614+5542	243.6534	55.7064	1.50	FRII	0.901		s	1	0.70	SDSS J161436.82+554222.9	G	21.77r	26.5	2.7	25.94	0.01
J1615+5721	243.9071	57.3625	1.60	FRII	0.78	0.05	p	1,3,10,11	0.71	SDSS J161537.70+572145.1	G	22.72r	18.3	1.9	25.64	0.05
J1615+5328	243.9492	53.4746	2.88	FRII	0.391		s	1	0.92	SDSS J161547.80+532828.5	G	18.78r	50.1	5.0	25.38	0.18
J1615+5332	243.9870	53.5353	2.20	FRII	0.992		s	1	1.06	SDSS J161556.88+533207.0	G	23.12r	21.2	2.2	25.94	0.26
J1616+5257b	244.0563	52.9556	2.98	FRII	1.5		e		1.51	DESI J244.0562+52.9553	G	21.39r	18.6	1.9	26.30	
J1616+5621	244.0640	56.3664	2.07	FRII	0.83	0.07	p	1,2,3,7,9,10,11	0.95	SDSS J161615.35+562159.0	G	21.93r	86.6	8.7	26.38	0.14
J1616+5322	244.0681	53.3734	1.91	FRI/II	0.61	0.78	p	1,2,3,6,8,9,10,11	0.77	SDSS J161616.35+532224.1	G	19.18r	13.1	1.5	25.24	0.13
J1616+5639	244.1048	56.6548	1.64	FRII	1.49	0.87	p	2,9,10,11	0.83	DESI J244.1048+56.6548	Qc	23.22r	77.5	7.8	26.91	0.41
J1616+5455	244.2323	54.9295	2.56	FRII	0.47	0.28	p	1,2,3,4,6,7,8,9,10,11,12	0.290	SDSS J161655.74+545546.1	G	21.29r	10.1	1.1	24.87	0.01
J1617+5354	244.4234	53.9015	3.10	FRI/II	0.400		s		1.00	SDSS J161741.60+535405.3	G	19.42r	17.1	1.8	24.94	
J1618+5720b	244.5118	57.3451	2.36	FRII	0.47	0.06	p	1,2,3,8,10,11	0.83	SDSS J161802.83+572042.5	G	21.00r	6.22	1.12	24.66	
J1618+5517	244.6088	55.2892	1.93	FRII	0.82	0.26	p	1,2,7,8,9,10	0.88	SDSS J161826.10+551721.3	G	21.36r	14.0	1.5	25.57	0.03
J1620+5700	245.2490	57.0080	1.40	FRII	1.5		e		0.71	DESI J245.2490+57.0080	Qc	23.91r	34.3	3.4	26.57	0.01
J1621+5518	245.3107	55.3048	2.25	FRII	0.58	0.02	p	1,2,3,7,8,9,10,11	0.89	SDSS J162114.54+551817.4	Qc	21.89r	75.2	7.5	25.95	
J1621+5259	245.4690	52.9930	1.80	FRII	0.67	0.52	p	1,10	0.76	SDSS J162152.55+525938.3	G	19.28r	39.7	4.0	25.82	
J1621+5647	245.4692	56.7887	2.27	FRII	0.41	0.03	p	1,2,3,6,8,10,11	0.75	SDSS J162152.60+564719.4	G	19.88r	7.34*	0.86	24.60	
J1623+5543	245.8046	55.7235	2.52	FRI/II	0.477		s	1	0.90	SDSS J162313.09+554324.6	G	19.65r	7.55	0.84	24.76	0.49
J1623+5320	245.9110	53.3365	3.30	FRII	0.385		p	1	1.04	SDSS J162338.64+532011.3	G	18.57r	241.	24	26.05	
J1623+5532	245.9951	55.5481	4.29	FRII	0.944		s		2.03	SDSS J162358.82+553253.3	G	22.91r	67.4	6.8	26.40	0.18
J1625+5556	246.3362	55.9453	4.40	FRII	0.40	0.03	p	2,3,8,10,11	1.41	DESI J246.3362+55.9453	G	20.11r	222.	22	26.05	
J1625+5508	246.4221	55.1433	2.25	FRII	1.28	1.49	p	1,2,3,8,9,10,11	1.13	SDSS J162541.29+550835.8	G	21.18r	454.	45	27.53	0.03
J1626+5434	246.7358	54.5726	9.82	FRII	0.489		s	1	3.55	SDSS J162656.58+543421.3	G	20.98r	32.0	3.9	25.41	0.03
J1626+5636	246.7365	56.6055	3.50	FRII	0.664		s		1.47	SDSS J162656.75+563619.8	G	21.24r	9.11*	1.09	25.17	0.10
J1627+5419	246.9674	54.3202	4.22	FRII	0.315		s		1.17	SDSS J162752.18+541912.5	G	17.46r	216.	22	25.81	0.21
J1628+5438	247.0154	54.6457	2.42	FRII	1.363		p		1.22	SDSS J162803.70+543844.6	Qc	20.44r	132.	13	27.06	0.02
J1628+5351	247.0156	53.8558	2.28	FRII	0.92	0.05	p	2,10,11	1.07	DESI J247.0156+53.8558	Qc	21.52r	4.94	0.63	25.24	
J1628+5601	247.1210	56.0299	2.45	FRII	0.50	0.04	p	1,10,11	0.90	SDSS J162829.04+560147.6	G	21.35r	12.7	1.5	25.03	
J1630+5421	247.5102	54.3595	3.10	FRII	0.289		s	1	0.81	SDSS J163002.45+542134.3	G	18.15r	84.7	8.6	25.32	<0.01
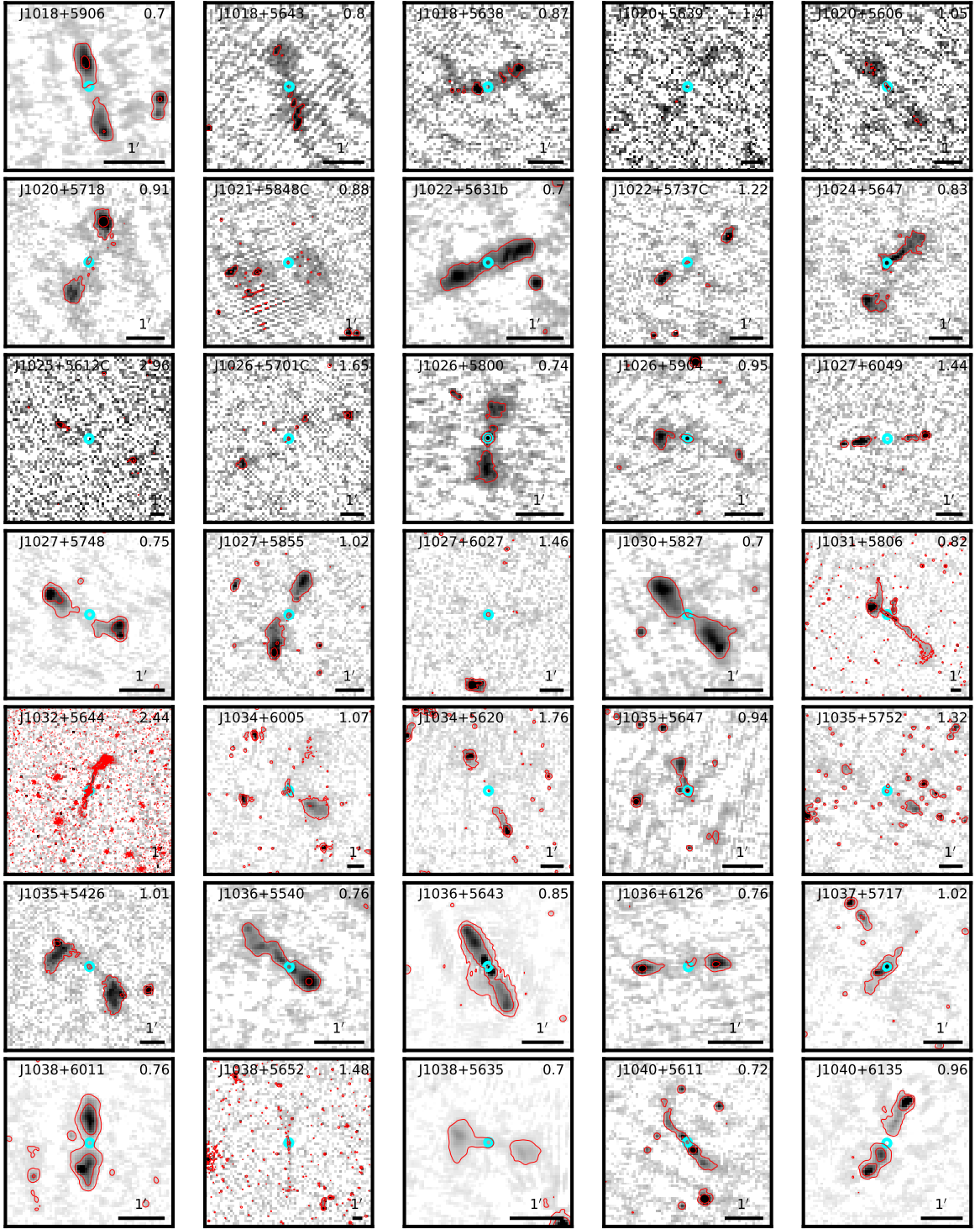
Figure B1: Cutouts of the LOFAR deep fields image around our GRGs at 150 MHz with 3 and 24-σ_{rms} red contours superimposed. The resolution of the images is $6''$. The cyan circle identifies the position of the host galaxy. The bar in the bottom-right corner represents an angular size of $1'$, while the name and the largest linear size (in Mpc) of the GRGs are reported in the top-left and top-right corners, respectively.

J1050+5934 1.01 J1050+5404 1.37 J1051+5641 0.85 J1051+6002 1.39 J1052+5503 0.82

J1052+5850 1.0 J1052+5636a 2.0 J1052+5454C 4.45 J1053+5953 1.05 J1053+5745 0.79

J1053+5613 0.89 J1054+6102 1.08 J1054+5952 0.9 J1054+5714 1.27 J1054+5909 0.93

J1056+5622 1.98 J1057+5548 0.92 J1057+5357 2.73 J1057+5908 4.08 J1058+5954 0.71

J1058+6008 2.03 J1058+5648 0.72 J1058+5643 1.44 J1059+5552 0.73 J1059+5610 0.73

J1059+5942 0.79 J1059+5709 0.91 J1059+5446C 0.92 J1100+5617 0.79 J1100+6034C 0.82

J1101+5723 1.56 J1101+6019C 1.16 J1101+5917 0.81 J1101+5652C 0.83 J1101+5725 0.97
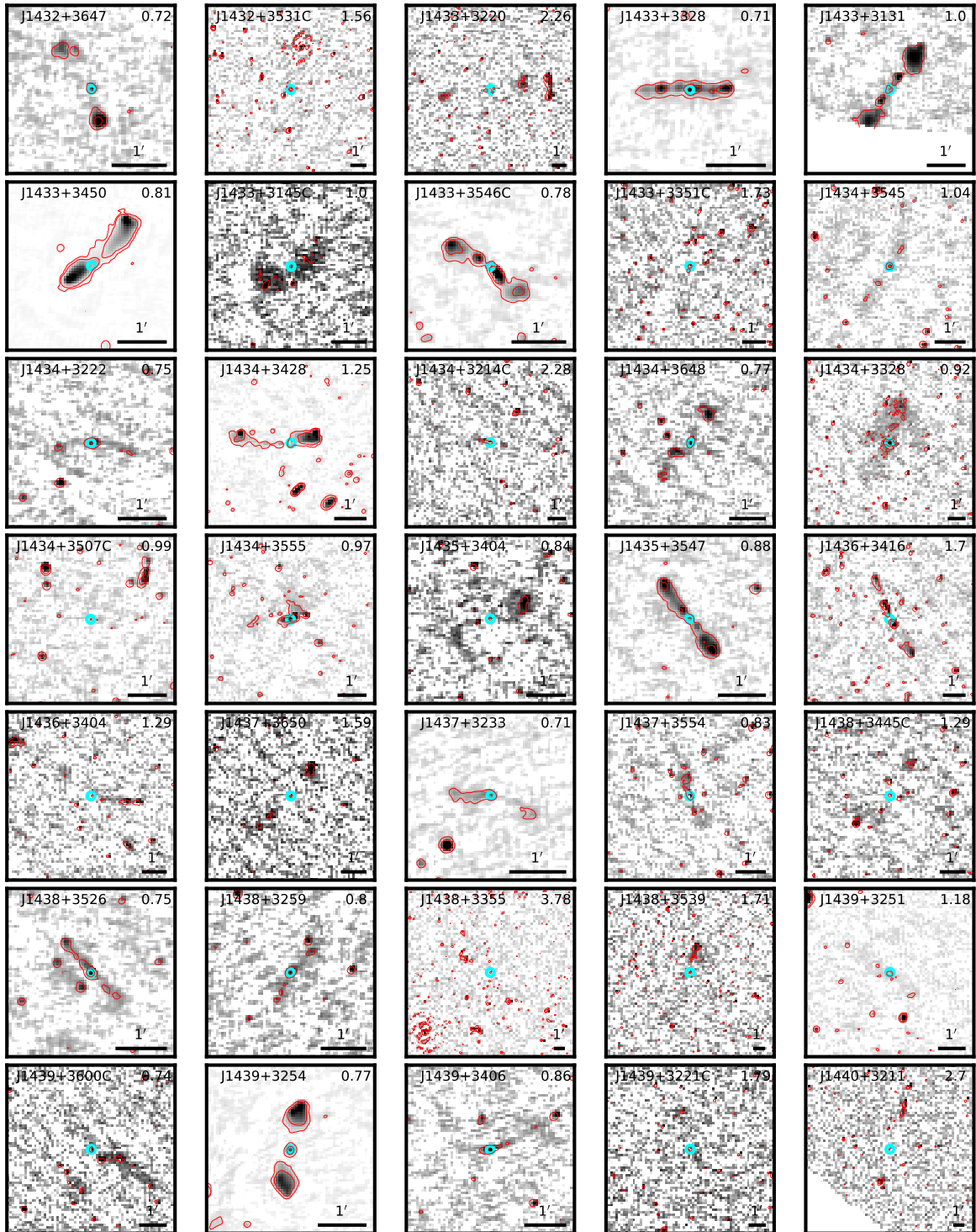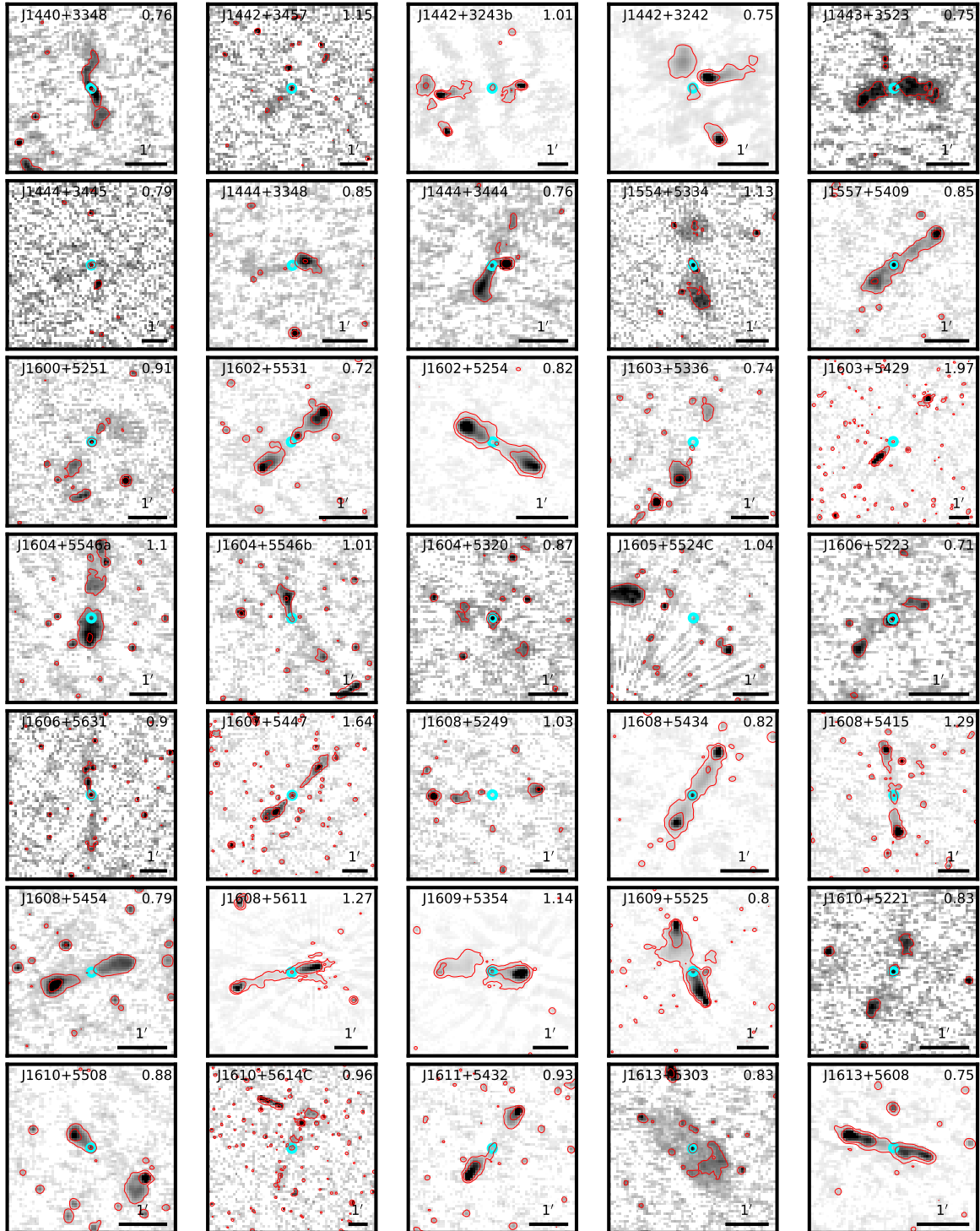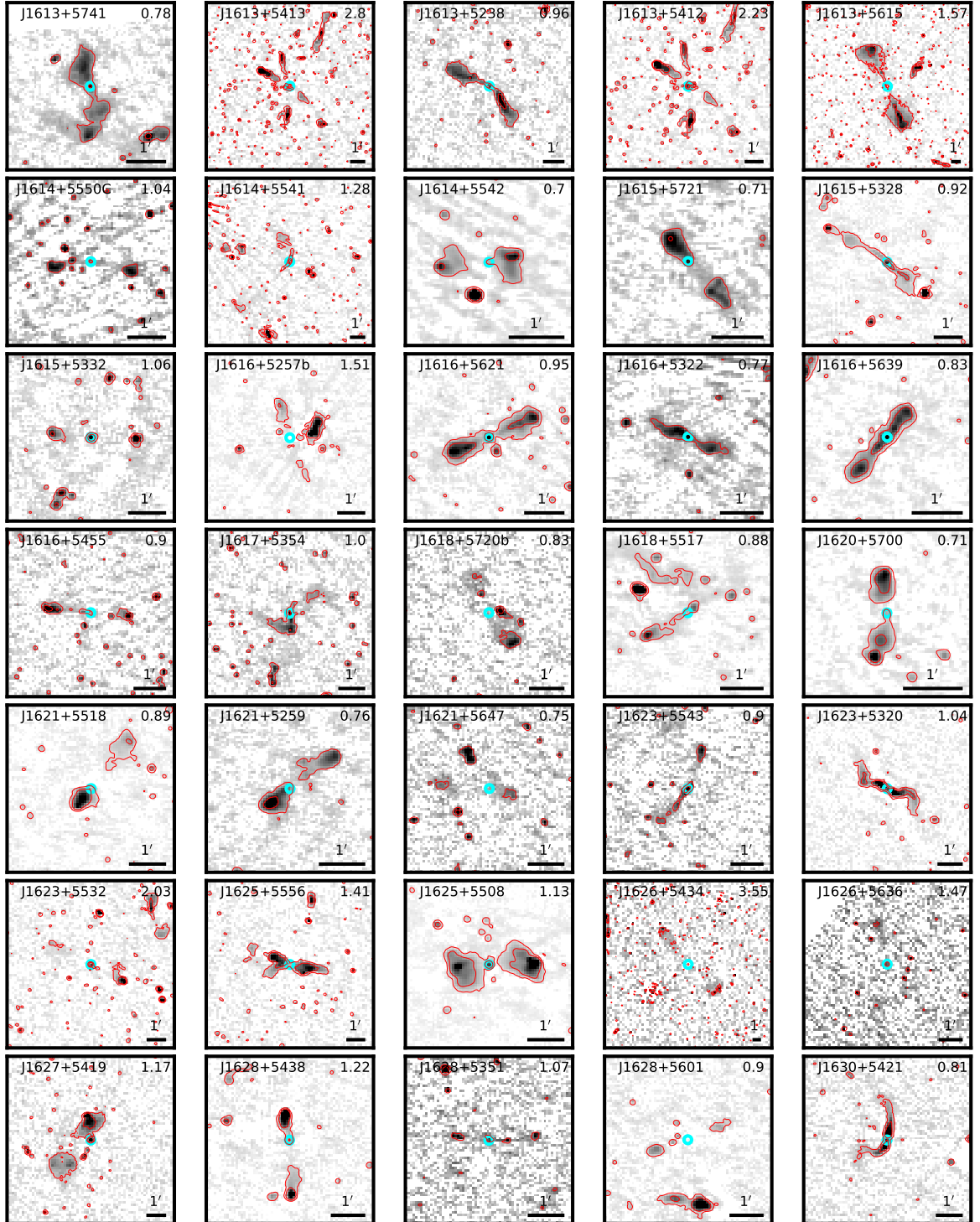
C Notes on discarded sources in the ELAIS-N1 field

J1609+5452 ($RA = 242.4899, DEC = 54.8794$). The radio emission coming from the two hotspots of this FRII candidate is the result of two separate point-like radio sources, hosted by SDSS J160958.85+545249.4 and CWISE J160956.26+545243.4.

J1609+5500 ($RA = 242.4858, DEC = 55.0000$) is actually two separate sources. The source to the NE is likely an RG itself (which we did not include in our sample) with an uncertain host galaxy. We propose CWISE J160959.21+550019.8 as the host candidate, even though the radio morphology makes this claim uncertain. On the other hand, the SW source is a clear wide-angle tailed (WAT) RG with host galaxy SDSS J160952.46+545937.9.

J1610+5416 ($RA = 242.5074, DEC = 54.2767$) might be a genuine RG with host SDSS J161002.72+541640.0. However, the radio morphology is very unclear and we consider the RPA measurement of this source to be very uncertain. Therefore, following the criteria applied during our inspection, we discarded this source.

J1610+5506 ($RA = 242.5574, DEC = 55.1125$) is a candidate RG whose radio emission is the result of at least two separate sources, hosted by SDSS J161013.41+550649.9 and SDSS J161014.30+550638.3.

J1612+5358 ($RA = 243.1542, DEC = 53.9686$) is the spiral galaxy SDSS J161236.98+535807.2. Thus, the RPA of the radio source is just the major axis of the galaxy and not that of any jets.

J1613+5411 ($RA = 243.3983, DEC = 54.1908$) is likely the combination of two different radio emissions. Part of the emission comes from the radio lobe of J1613+5412 an ERG (with host CWISE J161336.25+541258.4) that is included in our sample and whose RPA measurement is reliable. Moreover, there might be a contribution coming from the host galaxy SDSS J161334.98+541112.0 for which a reliable RPA measurement is not possible.

J1613+5414a ($RA = 243.4417, DEC = 54.2347$) is the NE lobe of another ERG (host galaxy CWISE J161334.24+541304.3) that we have in our sample and was used for the analysis. Again, there might be a contribution from another point-like source with host galaxy SDSS J161347.93+541405.6.

J1613+5414b ($RA = 243.3708, DEC = 54.2489$) is likely the result of the emission of two separate sources: DESI J243.3650+54.2490 and CWISE J161329.52+541454.7.

J1613+5415 ($RA = 243.4104, DEC = 54.2514$) is the N lobe of J1613+5412.

Table C1: First 50 rows of the ERGs catalogue used for our analysis.

(1) Name	(2) RA_J °	(3) Dec_J °	(4) *LAS* (')	(5) RPA °	(6) FR type	(7) z	(8) Δz	(9) ztype	(10) Hostname	(11) type	(12) mag (mag)	(13) *LLS* (Mpc)
J1552+5540	238.1360	55.6731	0.50	10	II	1.50		e	CWISE J155232.64+554023.1	Qc	18.60W1	0.25
J1552+5417	238.1721	54.2920	0.68	50	II	0.74	0.06	p	SDSS J155241.30+541731.3	G	21.25r'	0.30
J1553+5454	238.2511	54.8994	1.23	30	II	0.97	0.23	p	DESI J238.2511+54.8994	Qc	23.67r	0.59
J1553+5516	238.3149	55.2773	0.45	155	II	0.88	0.04	p	DESI J238.3149+55.2773	G	23.11r	0.21
J1554+5506C	238.5454	55.1050	1.31	67	II	0.720		s	SDSS J155410.89+550617.9	G	22.11r'	0.57
J1554+5438	238.5471	54.6374	0.93	44	I/II	0.925		s	SDSS J155411.32+543814.8	G	21.09r'	0.44
J1554+5334	238.6527	53.5750	2.55	25	II	0.761		s	SDSS J155436.64+533430.0	G	21.61r'	1.13
J1554+5344	238.6665	53.7407	1.08	84	II	0.74	0.04	p	SDSS J155439.96+534426.5	G	22.07r'	0.47
J1554+5628	238.6835	56.4664	0.72	55	II	0.554		s	SDSS J155444.03+562758.9	G	20.85r'	0.28
J1556+5539	239.0106	55.6599	2.25	87	II	0.31	0.04	p	SDSS J155602.54+553935.6	G	18.80r'	0.62
J1556+5348	239.0622	53.8046	0.58	10	II	0.98	0.11	p	DESI J239.0622+53.8046	G	23.12r	0.28
J1556+5559	239.0914	55.9918	0.55	73	II	0.97	0.14	p	SDSS J155621.93+555930.5	G	22.55r'	0.26
J1556+5627	239.1139	56.4524	0.63	33	II	0.75	0.02	p	SDSS J155627.34+562708.8	G	21.04r'	0.28
J1556+5538	239.1143	55.6493	0.48	179	II	0.91	0.08	p	SDSS J155627.42+553857.4	G	22.67r'	0.22
J1556+5342	239.1211	53.7064	0.60	24	II	0.71	0.03	p	SDSS J155629.05+534222.9	G	22.63r'	0.26
J1556+5430	239.1267	54.5048	0.72	177	II	1.12	0.01	p	DESI J239.1267+54.5048	G	23.28r	0.35
J1556+5353	239.1312	53.9000	0.78	77	II	0.87	0.12	p	DESI J239.1312+53.9000	G	23.31r	0.36
J1556+5314	239.1368	53.2427	2.63	156	II	0.241		s	SDSS J155632.82+531433.7	G	17.71r'	0.60
J1556+5618	239.1805	56.2996	1.38	148	II	0.340		s	SDSS J155643.33+561758.7	G	18.21r'	0.40
J1556+5407	239.1856	54.1247	1.05	152	II	0.499		s	SDSS J155644.54+540728.8	G	20.10r'	0.38
J1556+5558	239.1902	55.9771	0.50	178	II	0.83	0.22	p	DESI J239.1902+55.9771	G	23.18r	0.23
J1556+5422	239.2119	54.3713	1.12	40	II	1.50		e	CWISE J155650.86+542216.8	Qc	17.01W1	0.57
J1556+5647	239.2142	56.7877	0.67	30	II	0.91	0.08	p	DESI J239.2142+56.7877	G	22.58r	0.31
J1557+5446	239.2544	54.7722	0.70	122	I	0.73	0.07	p	DESI J239.2544+54.7722	G	22.27r	0.30
J1557+5305	239.3013	53.0949	1.24	50	II	0.61	0.03	p	SDSS J155712.32+530541.5	G	20.85r'	0.50
J1557+5442	239.3131	54.7131	0.58	90	II	0.928		s	SDSS J155715.14+544247.2	G	22.31r'	0.27
J1557+5409	239.3297	54.1571	1.87	122	II	0.81	0.32	p	DESI J239.3297+54.1571	G	22.85r	0.85
J1557+5440	239.3392	54.6711	11.20	154	I	0.047		s	SDSS J155721.39+544015.9	G	13.95r'	0.62
J1557+5448	239.3770	54.8036	1.08	34	II	0.76	0.28	p	PSO J155730.480+544812.94	G	20.68r	0.48
J1557+5402	239.4011	54.0334	0.50	11	II	1.06	0.06	p	DESI J239.4011+54.0334	G	24.37r	0.24
J1557+5622	239.4081	56.3710	0.70	178	II	1.50		e	CWISE J155737.93+562215.6	Qc	17.94W1	0.36
J1557+5527	239.4508	55.4624	0.83	122	I	0.462		s	SDSS J155748.18+552744.5	G	19.69r'	0.29
J1557+5327	239.4540	53.4701	1.64	73:	I/II	0.67	0.02	p	SDSS J155748.96+532812.3	G	21.39r'	0.69
J1557+5508	239.4560	55.1401	0.65	111	I/II	1.90		e	CWISE J155749.44+550824.5	Qc	19.04W1	0.33
J1557+5343	239.4594	53.7261	0.83	100	II	0.312		s	SDSS J155750.24+534334.0	G	17.82r'	0.23
J1558+5403	239.5270	54.0549	0.33	137	II	1.03	0.12	p	DESI J239.5270+54.0549	G	23.51r	0.16
J1558+5554	239.5512	55.9047	0.68	68	II	1.21	0.19	p	DESI J239.5512+55.9047	G	25.00r	0.34
J1558+5633	239.5623	56.5503	0.63	92	II	0.92	0.01	p	DESI J239.5623+56.5503	G	23.42r	0.30
J1558+5558	239.5700	55.9836	0.85	48	II	0.50	0.09	p	SDSS J155816.81+555900.9	G	21.91r'	0.31
J1558+5349	239.5759	53.8298	0.50	33	II	1.03	0.16	p	DESI J239.5759+53.8298	Qc	23.46r	0.24
J1558+5303	239.6051	53.0636	1.77	40	I	0.687		s	SDSS J155825.22+530348.8	G	20.94r'	0.75
J1558+5609	239.7018	56.1579	0.45	115	I/II	1.28		p	DESI J239.7018+56.1579	Qc	19.84r	0.23
J1558+5441	239.7042	54.6902	1.08	52	I	0.27	0.03	p	SDSS J155849.00+544124.8	G	18.36r'	0.27
J1558+5317	239.7399	53.2952	0.53	161	II	0.472		s	SDSS J155857.57+531742.6	G	20.13r'	0.19
J1559+5527	239.7540	55.4503	0.40	136	II	1.16	0.64	p	SDSS J155900.96+552701.0	G	22.86r'	0.20
J1559+5704	239.7827	57.0779	1.30	172	II	0.592		s	SDSS J155907.84+570440.4	G	20.31r'	0.52
J1559+5448	239.8707	54.8169	0.70	5:	II	0.85	1.17	p	SDSS J155928.96+544900.8	G	19.86r	0.32
J1559+5341	239.9018	53.6960	0.90	165	II	1.09	1.06	p	DESI J239.9018+53.6960	G	21.32r	0.44
J1559+5708	239.9340	57.1458	0.87	113	II	0.50	0.01	p	SDSS J155944.17+570844.9	G	20.84r'	0.32
J1559+5556	239.9753	55.9342	0.38	31	II	1.50		e	CWISE J155954.08+555603.2	Qc	18.03W1	0.19

[a] Col. (1), name of the ERG. A "C" appended to the ERG name indicates that it is a candidate, meaning that either the host itself, or its redshift, or its LAS are uncertain. Col. (2) and Col. (3), right ascension and declination (J2000) of the host galaxy in degrees. Col. (4), largest angular size in arcminute. Col. (5) Radio position angle of the ERG in degrees; a colon appended to the RPA indicates that the measurement is uncertain. Col. (6), classification of the ERG according to the Fanaroff–Riley classification. Col. (7), redshift of the host galaxy. Col. (8), redshift error when available. Errors of the spectroscopic redshifts are not reported since they are generally more accurate than the precision we can achieve on the linear sizes. Col. (9), type of the redshift: p for photometric, s for spectroscopic and e if estimated. Col. (10), name of the host galaxy. Col. (11) type of host galaxy: galaxy (G) or QSO (Q) or candidate quasars (Qc). Col. (12), magnitude of the host galaxy in the r-band if available from the DESI DR9 photometric catalogue (r) or SDSSDR12 (r'); the label W1 and W2 indicates that the magnitude is taken from either WISEA (Cutri & et al. 2012; Cutri et al. 2013) or CWISE (Marocco et al. 2021) catalogue. Col. (13), largest linear size in Mpc.